

111
102
1004

Leibniz
Universität
Hannover

Gravitational curvature and relativistic effects in atom interferometers

Von der Fakultät für Mathematik und Physik
der Gottfried Wilhelm Leibniz Universität Hannover
genehmigte Dissertation zur Erlangung des Grades

Doktor der Naturwissenschaften

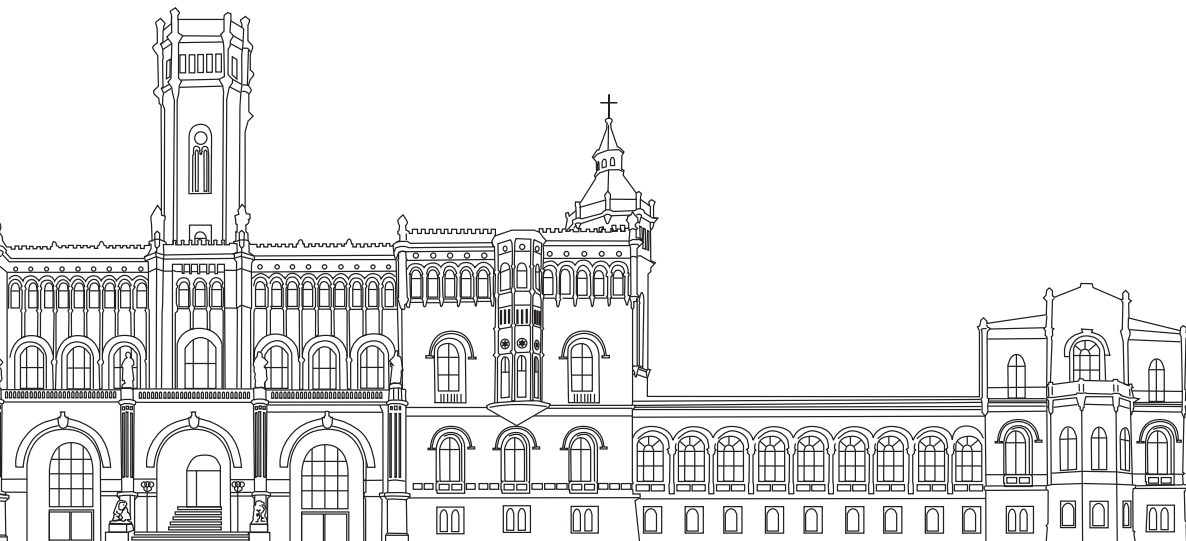
Dr. rer. nat.

von

M.Sc. Michael Werner,

geboren am 07.12.1994 in Bückeburg

2025



Referent: Prof. Dr. Klemens Hammerer
Leibniz Universität Hannover

Korreferent: Dr. Naceur Gaaloul
Leibniz Universität Hannover

Korreferent: Prof. Dr. Claus Lämmertzahl
ZARM, Universität Bremen

Tag der Promotion: 15. Januar 2025

Zusammenfassung

Diese Arbeit widmet sich der theoretischen Untersuchung von Atominterferometern in komplexen Gravitationsfeldern. Die zugrunde gelegten Gravitationsmodelle umfassen einerseits nicht-triviale Korrekturen im Gravitationspotenzial im Rahmen der klassischen Newtonschen Mechanik, die über die Annahme eines idealisierten oder vollständig homogenen Gravitationsfeldes hinausgehen. Andererseits wird die allgemeine Relativitätstheorie herangezogen, um insbesondere im Bereich schwacher Gravitationsfelder eine post-newtonsche Beschreibung zu ermöglichen. Diese Herangehensweise erlaubt es, die dominanten Auswirkungen einer Raumzeitkrümmung systematisch zu erforschen. Die in dieser Arbeit behandelten quantenoptischen Systeme sind Atominterferometer, Experimente, die kalte Atome bzw. Bose-Einstein-Kondensate zur Interferenz bringen. Diese Beschreibung bietet einen möglichen Ansatz, um die Grenzen der modernen Physik auszutesten, und erkundet Regionen, in denen Effekte der Quantengravitation zum Vorschein kommen könnten, die sich von denen der Hochenergiephysik unterscheiden.

Wir beginnen mit einer Einführung in die (allgemeine) Relativitätstheorie und die Theorie der Atominterferometer in idealisierten, Newton'schen Gravitationsfeldern. Um das Gravitationsmodell schrittweise zu erweitern und zusätzliche Effekte wie die Raumzeitkrümmung zu integrieren, führen wir eine kompaktere Notation ein. Diese ermöglicht es uns, die Komplexität durch relativistische Effekte systematisch zu berücksichtigen. In dieser neuen Notation präsentieren wir den aktuellen Forschungsstand auf diesem Gebiet, sodass wir direkt darauf aufbauen und die neuesten Entwicklungen integrieren können. Des Weiteren stellen wir eine neue Interferometergeometrie vor, die besonders gut zur Detektion gravitativer Krümmungen geeignet ist. Wir führen eine detaillierte Analyse durch, um zu untersuchen, wie sich ein solches Interferometer in idealisierten Gravitationsfeldern verhält, und vergleichen dies mit einer numerischen Simulation desselben Interferometers im VLBAI Hannover, welches das neueste und größte Atominterferometer-Experiment in Hannover darstellt. Wir nutzen dieses Beispiel, da uns in diesem Experiment ein präzises Modell des Gravitationsfeldes zur Verfügung steht.

Die durch nicht-triviale Gravitationsfelder und die Relativitätstheorie verursachten Korrekturen treten an vielen Stellen in der theoretischen Beschreibung auf. Dies führt dazu, dass die Endergebnisse, insbesondere bei komplexen Interferometergeometrien, schnell unübersichtlich werden. Um das Risiko zu verringern, Terme und Effekte zu übersehen, war es ein wesentlicher Teil dieser Arbeit, einen Computer-Algorithmus zu entwickeln, der die Berechnung dieser Terme automatisiert. Dadurch können wir in kurzer Zeit zuverlässig Ergebnisse auch für sehr komplexe Experimente modellieren. Die Kombination aus einem Computer-Algorithmus, der uns algebraische Resultate liefert, und einem numerischen Modell für ein explizit gemessenes Gravitationsfeld ermöglicht es uns, Theorie und Experiment besonders detailliert zu vergleichen. Darüber hinaus können wir neue Resultate für zukünftige Experimente im VLBAI Hannover und in anderen Atominterferometern weltweit ableiten.

Schlagwörter: Atominterferometrie, Quantensysteme in Gravitation, Relativistische Effekte in Atominterferometern, Post-Newton'sche Gravitation

Abstract

This work is a theoretical investigation of atom interferometers in complex gravitational fields. The underlying gravitational models include non-trivial corrections in the gravitational potential within the framework of classical Newtonian mechanics, which go beyond the assumption of an idealised or even completely homogeneous gravitational field. On the other hand, the theory of general relativity is used to enable a post-Newtonian description, particularly in the area of weak gravitational fields. This approach makes it possible to systematically investigate the main effects of spacetime curvature. The quantum optical systems discussed in this work are atom interferometers, highly accurate experiments that cause cold atoms or Bose-Einstein condensates to interfere. This description offers a potential approach to testing the boundaries of modern physics and explores regions where quantum gravity may emerge, distinct from the realm of high-energy physics.

We start with an introduction to the theory of (general) relativity and the theory of atomic interferometers in idealised Newtonian gravitational fields. In order to gradually extend the gravitational model and integrate additional effects such as spacetime curvature, we introduce a more compact and versatile notation. This allows us to systematically take into account the additional complexity due to relativistic effects. With this new notation, we present the current state of research in this field, enabling us to directly build upon it and seamlessly incorporate our own developments. Furthermore, we present a new interferometer geometry that is particularly well suited for the detection of gravitational curvature. We perform a detailed analysis to investigate how such an interferometer behaves in idealised gravitational fields and compare this with a numerical simulation of the same interferometer at the VLBAI facility in Hannover, which is the newest large scale atom interferometer experiment in Hannover. We use this example because this experiment provides us with a precise model of the gravitational field.

The corrections caused by non-trivial gravitational fields and the theory of relativity occur at many levels in the theoretical description. This means that the final results quickly become unwieldy, especially in the case of more complex interferometer geometries. To reduce the risk of overlooking terms and effects, an essential part of this work was to develop a computer algorithm that automates the calculation of this algebra. This enables us to reliably model results even for very complex experiments in a short time. The combination of a computer algorithm that provides us with algebraic results and a numerical model for an explicitly measured gravitational field enables us to compare theory and experiment in great detail. In addition, we can derive new results for future experiments in the VLBAI Hannover and in other atom interferometers worldwide.

Key words: Atom interferometry, Quantum systems in gravity, Relativistic effects in atom interferometers, post-Newtonian gravity

*“The best that most of us can hope to achieve in physics
is simply to misunderstand at a deeper level.”*

- Wolfgang Pauli to Jagdish Mehra¹
Berkeley California in May 1958

¹In "The Historical Development of Quantum Theory – Volume 6" by Jagdish Mehra and Helmut Rechenbach.

Author Contributions

Parts of this thesis have appeared elsewhere as peer-reviewed publications or on preprint servers. Here, I summarise my personal contributions to these works in chronological order. Please note that the contributions of other authors without my involvement are not explicitly listed.

1. **M. Werner** and K. Hammerer. *Dataset: Atom interferometers in weakly curved spacetimes using Bragg diffraction and Bloch oscillations.* [1]

Author contribution: **Michael Werner (MW)** and KH developed the main idea behind the algorithm. **MW** implemented this into a scalable and automatised procedure using Python.

2. **M. Werner**, P. Schwartz, J.-N. Kirsten-Siemß, N. Gaaloul, D. Giulini, and K. Hammerer. *Atom interferometers in weakly curved spacetimes using Bragg diffraction and Bloch oscillations.* [2]

Author contribution: **MW** implemented the computer algorithm (see first reference) and created the plots and tables. **MW** and KH came up with the idea to introduce dimensionless parameters. **MW** calculated the algebraic formulas for each phase shift contribution and was assisted by PS and JNKS. **MW** interpreted the results with all authors. **MW** and KH wrote the manuscript with contributions from all authors.

3. **M. Werner** and K. Hammerer. *Local Measurement Scheme of Gravitational Curvature using Atom Interferometers [Data set].* [3]

Author contribution: **MW** build the code upon the previous algorithm (see first reference) and included finite speed of light effects, single photon transitions, internal state changes and the gravitational field of the VLBAI Hannover. **MW** and KH analysed the runtime and interpreted the numerical results.

4. **M. Werner**, A. Lezeik, D. Schlipert, E. M. Rasel, N. Gaaloul and K. Hammerer. *Local Measurement Scheme of Gravitational Curvature using Atom Interferometers.* [4]

Author contribution: **MW**, KH, NG, DS, and ER initiated the research direction, **MW** and KH developed the analytical and numerical modelling, **MW** created the figures and drafted the initial manuscript. All authors actively participated in discussing the results and contributed to the final manuscript.

Abbreviations and Acronyms

In alphabetical order:

AIF Atom Interferometer	9
ARBI Asymmetric Ramsey-Bordé Interferometer	22
BCG Background Coulomb Gauge	81
BEC Bose Einstein Condensate	13
CGI Co-located Gradiometric Interferometer	46
CODATA Committee on Data for Science and Technology	68
COM Centre of Mass	12
DF Dual Frequency	16
EEP Einstein Equivalence Principle	2
ELE Euler-Lagrange Equation	13
EM Electromagnetic	5
EOM equations of motion	15
ER Eddington-Robertson	10
FSL Finite Speed of Light	22
GCG Geometric Coulomb Gauge	81
GNSS Global Navigation Satellite System	2
GPS Global Positioning System	2
GR General Relativity	1
JGM Joint Earth Gravity Model	55
LG Lorenz Gauge	81
LIGO Laser Interferometer Gravitational-Wave Observatory	2

LKB Laboratoire Kastler Brossel	69
LLI Local Lorentz Invariance	3
LMT Large Momentum Transfer	56
LPI Local Position Invariance	3
MZI Mach-Zehnder Interferometer	22
ODE Ordinary Differential Equation	25
PPN Parametrised Post-Newtonian	10
QED Quantum Electrodynamics	12
QM Quantum Mechanics	1
ROI Region of Interest	57
SDDI Symmetric Double Diffraction Interferometer	22
SF Single Frequency	16
SR Special Relativity	6
SRBI Symmetric Ramsey-Bordé Interferometer	22
UCR Universality of Clock Rates	4
UFF Universality of Free Fall	3
UGR Universality of Gravitational Redshift	4
VLBAI Very Long Baseline Atom Interferometer	46
WEP Weak Equivalence Principle	3

Contents

1	Introduction	1
1.1	General Relativity	1
1.1.1	Equivalence Principle	2
1.1.2	Mathematical Formulation	5
1.1.3	Flat Spacetime	6
1.1.4	Newtonian Spacetime	8
1.1.5	Post-Newtonian Spacetime	10
1.2	Quantum Mechanics and Atom Interferometry	11
1.2.1	Motional Hamiltonian	13
1.2.2	Internal Hamiltonian	14
1.2.3	Light Hamiltonian	15
1.2.4	Atom-Light Hamiltonian	16
2	Atom Interferometers in Newtonian Spacetime	21
2.1	Basic Interferometer Geometries	22
2.1.1	Phase Shifts of Free Propagation	24
2.1.2	Dimensionless Parameters	25
2.1.3	Interaction Times	28
2.1.4	Atom-Light Interactions	30
2.1.5	Phase Shift Summary	33
2.2	Advanced Description of Interferometers	35
2.2.1	Comparison to Hamiltonian Approach	37
2.2.2	Comparison to Bordé’s Midpoint Theorem	40
2.2.3	Gravity Gradient Mitigation Schemes	41
2.2.4	Rotating Reference Frames – Coriolis and Centrifugal Forces	42
2.3	Interferometer Geometries to Measure Gravitational Curvature	44
2.3.1	FSL Effect and Mitigation Scheme	50
2.4	Revisiting Assumptions	54
2.4.1	Global Gravitational Variations: Geopotential Model	54
2.4.2	Local Gravitational Variations: VLBAI Hannover	56
2.5	Summary and Outlook	64
3	Atom Interferometers in Curved Spacetimes	67
3.1	Naïve Approach: Fine-Structure Experiments	68
3.1.1	Interferometer Geometries to Measure the Fine-Structure Constant	68
3.1.2	Relativistic motional correction	70
3.2	Transformation to Adapted Coordinates	73
3.3	Relativistically Corrected Hamiltonian	75

3.4	Motional Hamiltonian	77
3.5	Relativistic Light Hamiltonian	80
3.5.1	Wave Equations in the Geometric Coulomb Gauge:	81
3.5.2	Geometric Optics Approximation	84
3.6	Atom-Light Hamiltonian	91
3.6.1	Doppler Effect and Kick Phase	94
3.7	Relativistic Phase Shifts in Interferometers	96
3.8	Outlook: Relativistic Description of Stationary Spacetimes	98
4	Computer Algorithm for Phase Calculations	105
4.1	Code Structure and Preliminaries	106
4.2	Initialisation	109
4.3	Atomic Trajectories	110
4.4	Phase Calculation	113
4.4.1	Propagation Phase	113
4.4.2	Separation Phase	115
4.4.3	Kick Phase	115
4.4.4	Simplified FSL Phase	117
4.5	Visualisation	118
5	Summary and Outlook	120
	Appendix A Differential Geometry	122
	Index	127
	Bibliography	143

Chapter 1

Introduction

"Die im nachfolgenden dargelegte Theorie bildet die denkbar weitgehendste Verallgemeinerung der heute allgemein als 'Relativitätstheorie' bezeichneten Theorie; die letztere nenne ich im folgenden zur Unterscheidung von der ersten 'spezielle Relativitätstheorie' und setze sie als bekannt voraus."

Albert Einstein, 20.03.1916

Introduction from „Die Grundlage der allgemeinen Relativitätstheorie“

General Relativity (GR) and Quantum Mechanics (QM) are the foundational theories in modern physics, providing essential frameworks for understanding the behaviour of matter and energy at both microscopic and cosmic scales. QM has revolutionised technology, leading to advancements in electronics, computing, and medical imaging, while GR has reshaped our understanding of gravity, space, and time, influencing cosmology and astrophysics. Together, these theories form the basis for much of the contemporary scientific research and technological innovation, driving progress across multiple disciplines. Both theories will be introduced in this chapter.

1.1 General Relativity

GR, formulated by Albert Einstein in 1915 [5], revolutionised our understanding of the universe and profoundly altered the course of modern science and technology. This groundbreaking theory redefined gravity, not as a force between masses as Newton had described in the late 17th century in his "Philosophiæ Naturalis Principia Mathematica,"¹ but as a manifestation of the curvature of spacetime caused by mass and energy. The complexity and counter intuitive nature of the theory of GR is often masked by the simplistic looking field equations

$$R_{\mu\nu} - \frac{1}{2}g_{\mu\nu}R + \Lambda g_{\mu\nu} = \frac{8\pi G}{c^4}T_{\mu\nu}, \quad (1.1)$$

which we will elaborate on in the following. GR has produced novel scientific discoveries for more than a century, none of which gave rise to possible extensions beyond the scope of the theory. Testing the validity of GR on even broader length and energy scales therefore becomes ever more interesting.

¹Often only referred to as the "Principia".

One of the most significant contributions of GR was its impact on our understanding of cosmology. The theory predicted the expansion of the universe, a concept that was later confirmed by Edwin Hubble's observations of distant galaxies [6]. This laid the groundwork for the Big Bang theory, which describes the origin and evolution of the universe and was initially proposed by Georges Lemaître² in 1931. GR also predicted the existence of black holes, regions of spacetime with gravitational fields so strong that not even light can escape them [8]. These predictions were initially met with scepticism [9, 10] but have since been confirmed through numerous observations, including the recent imaging of a black hole by the Event Horizon Telescope [11]. The influence of GR extends beyond theoretical physics into practical applications. One of the most notable examples are the Global Navigation Satellite System (GNSS) and Global Positioning System (GPS). The precise functioning of GNSS/GPS satellites depends on the accurate consideration of relativistic time dilation effects predicted by general relativity. Without these corrections, the synchronisation of satellite clocks would drift, rendering the system ineffective for navigation and timing.

GR has also enhanced our understanding of extreme astrophysical phenomena. The theory explains the behaviour of light in strong gravitational fields, leading to the prediction and observation of gravitational lensing, where light from distant stars is bent around massive objects. This phenomenon has become a crucial tool in astronomy for studying dark matter and distant galaxies [12]. Furthermore, the detection of gravitational waves in 2015 by the Laser Interferometer Gravitational-Wave Observatory (LIGO) and Virgo collaborations [13] provided direct evidence of one of GR's most remarkable predictions. These ripples in spacetime, generated by cataclysmic events such as the merger of black holes, have opened a new window for observing the universe and have initiated the field of gravitational wave astronomy. GR's impact on our world-view extends to philosophical and conceptual realms as well. It has challenged our perceptions of space and time, revealing them to be dynamic and interwoven entities rather than fixed and separate absolutes. This paradigm shift has influenced a wide range of disciplines, from philosophy to literature, and has inspired a deeper appreciation for the intricate and interconnected nature of the universe.

In conclusion, GR has profoundly changed the world by reshaping our understanding of gravity, the cosmos, and the nature of reality itself. Its theoretical predictions have been confirmed through groundbreaking observations and experiments, leading to technological advancements and new scientific fields. The legacy of GR continues to inspire and drive scientific inquiry, solidifying its place as one of the most important scientific achievements of the 20th century. In the following we introduce the pillars of GR, namely the equivalence principle, and introduce the mathematical notation.

1.1.1 Equivalence Principle

The Einstein Equivalence Principle (EEP) encompasses three distinct hypotheses and forms the cornerstone of GR. In this section, we will briefly explain each of these hypotheses, drawing on explanations similar to those found in Ref. [14]. Additionally, we will highlight the various methods and experiments used to test each of these assumptions, illustrating their critical roles in validating the foundations of GR.

²Lemaître, who was a Catholic priest and an exceptionally skilled relativist, proposed this theory in response to the emergence of a new theory at that time, quantum mechanics, quoting "If we go back in the course of time we must find fewer and fewer quanta, until we find all the energy of the universe packed in a few or even in a unique quantum." [7]

Universality of Free Fall

The Universality of Free Fall (UFF) states that the motion of "test particles" depends solely on their initial position and velocity in spacetime. This principle implies that gravity couples universally to matter, irrespective of the mass and internal structure of the objects. A famous demonstration of this natural law occurred during the Apollo 15 mission in 1971, when astronaut David Scott simultaneously dropped a hammer and a feather on the Moon. In the vacuum of space, both objects fell at the same rate and hit the ground simultaneously, vividly illustrating the validity of UFF to a wide audience. The UFF is also commonly referred to as the Weak Equivalence Principle (WEP); however, for consistency, we will use the term UFF throughout this thesis. Nevertheless, when analysing this specific example more carefully, it is important to emphasise that the UFF explicitly refers to *point particles*. This means that higher-order mass moments or spin could alter the actual trajectories, even though these interactions are purely gravitational. Consequently, a more detailed examination of the experiment would reveal deviations in the trajectories of the feather and hammer due to their non-trivial mass moments, which – to emphasise this once more – is in accordance with UFF.

This peculiar fact raises the question of which substances actually constitute reasonable candidates for point particles, revealing that the answer is highly context-dependent. On cosmological scales, the Earth serves as an excellent test mass, whereas it lacks this qualification for experiments conducted in its orbit. For Earthbound experiments, the best candidates are typically atoms, as they are indistinguishable from one another, can be electrically neutral, and have a trivial mass compared to most experimental setups and the Earth itself.

Deviations from UFF are usually measured using the Eötvös factor, which is defined as

$$\eta(A, B) = 2 \frac{|a(A) - a(B)|}{a(A) + a(B)}, \quad (1.2)$$

where A, B are systems made of different materials and $a(A), a(B)$ are the local gravitational accelerations of them. The current best UFF test was performed using the MICROSCOPE mission [15] and resulted in a lower bound of $\eta(\text{Pt}, \text{Be}) < [-1.5 \pm 2.3 \text{ (stat)} \pm 1.5 \text{ (syst)}] \times 10^{-15}$ for Platinum and Titanium.

Local Lorentz Invariance

The Local Lorentz Invariance (LLI) principle states that any local, non-gravitational experiment should exhibit no preferred direction in spacetime. Phrased equivalently: One can transform the chosen frame of reference using an arbitrary Lorentz transformation and obtain the same physical observables. A typical example is testing whether the speed of light c varies in different spatial directions [16]. Deviations of LLI are therefore tested by – for example – measuring the quantity

$$\frac{\Delta c}{c} < 3.2 \times 10^{-16}. \quad (1.3)$$

Another approach is to measure potential shifts of atomic spectra over the course of a year due to Earth's orbital velocity in different spatial directions around the Sun. Experiments like those constrain parameters that would describe physics beyond the standard model to the 10^{-21} level [17].

Local Position Invariance

The Local Position Invariance (LPI) principle states that the outcome of any experiment is independent of where and when it is performed. This principle is often expressed through

two equivalent formulations: the Universality of Clock Rates (UCR) and the Universality of Gravitational Redshift (UGR). The UCR states that two different standard clocks³ will display the same time after travelling along identical worldlines. The UGR states that standard clocks, travelling along different worldlines and inter-comparing their times using electromagnetic signals, will exhibit the expected gravitational redshift [18].

A schematic depiction of a UGR experiment can be seen in Fig. 1.1. Each observer measures the frequency of the light field k in their frame of reference and denotes it to be ν_i . This frequency is measured with respect to the proper time of each observer on the respective worldline γ_i . For details, see the mathematical formulation of GR in Sec. 1.1.2. The UGR can then be expressed as

$$\frac{\nu_1}{\nu_2} = \frac{g(u_1, k)|_{\gamma_1}}{g(u_2, k)|_{\gamma_2}}, \quad (1.4)$$

where g denotes the metric tensor and u_i are the respective four-velocities of each observer. Note that, without additional structure, there is no way to distinguish between a gravitational redshift and a kinematic redshift, i.e. the Doppler effect, since there is no preferred frame of reference in GR that can a priori be called "to be at rest". Eq. (1.4) therefore includes both effects simultaneously. The UCR, on the other hand, could also be tested by Eq. (1.4), but using two observers on the same trajectory each carrying a standard clock composed of different materials. The UCR therefore ensures that all clocks, independent of their physical realisation, are equivalent and that the concept of time itself is a property emerging from the geometry of spacetime.

Tests of the UCR/UGR are performed by searching for possible deviations of the value ν_1/ν_2 by multiplying Eq. (1.4) with the quantities $(1 + \alpha_{\text{UGR}})$ or $(1 + \alpha_{\text{UCR}})$, therefore parametrising possible deviations of the LPI by test parameters α_{UGR} and α_{UCR} . Experiments like the "Gravity Probe A" [19] compared two identical hydrogen maser clocks – one of which was at rest on Earth's surface and the other one being on board of a ballistic rocket, travelling nearly two hours around Earth with an altitude of up to 10.000 km, resulting in an upper bound for UGR of

$$\alpha_{\text{UGR}} < 7 \times 10^{-5}, \quad (1.5)$$

whereas comparing two clocks based on different atomic species on (nearly) identical worldlines gave an upper bound for the UCR parameter of

$$\alpha_{\text{UCR}} < 5.8 \times 10^{-6}, \quad (1.6)$$

see Ref. [20].

In summary, Einstein's equivalence principle is a cornerstone of GR, highlighting the indistinguishability of gravitational and kinematic accelerations and leading to the revolutionary concept of gravity as the curvature of spacetime. Testing these assumptions with

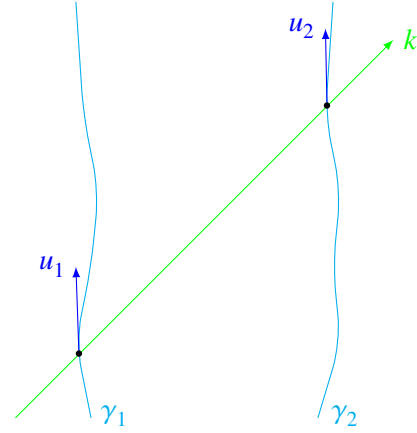


Figure 1.1: Simplified visualisation of a setup to test the UGR with two observers on their respective worldlines γ_1 , γ_2 and corresponding four-velocities u_1 , u_2 interchanging a light ray k for the case of a two-dimensional spacetime.

³Viewed as idealised theoretical devices measuring proper time along any timelike curve.

even greater accuracy is an important task of modern fundamental science and its relevance cannot be overstated.

1.1.2 Mathematical Formulation

We assume that the reader is familiar with the basic mathematical description of relativity. If not, one can find a summary of the basic concepts of differential geometry in Appendix A, which are needed to understand all the mathematics presented in this thesis. We adopt the following convention: Greek indices range from 0 to 3, whereas Latin indices range from 1 to 3. Bold letters like x and R will always represent three-dimensional quantities, like elements in \mathbb{R}^3 or 3-tuples of operators.

In Einstein's GR the universe is modelled to be a smooth four-dimensional Lorentzian manifold with metric tensor field, defined as a section in the tensor bundle of degree (0, 2) that can be written using the canonical co-vector basis fields as

$$g = \sum_{\mu, \nu=0}^3 g_{\mu\nu} dx^\mu \otimes dx^\nu = g_{\mu\nu} dx^\mu dx^\nu = ds^2. \quad (1.7)$$

We shortened the expressions by using abstract index notation with Einstein sum convention and by omitting the tensor product symbol. Additionally, we have written g as a "line element" ds^2 – both conventions will be used interchangeably. The $g_{\mu\nu}$ are the component functions of g for the specific choice of coordinates. The metric tensor is assumed to be symmetric $g_{\mu\nu} = g_{\nu\mu}$ and has – in our convention – one negative and three positive eigenvalues. The inverse of the metric tensor will be denoted by $g^{\mu\nu}$ and satisfies $g^{\mu\nu} g_{\nu\lambda} = \delta^\mu_\lambda$, where δ^μ_λ denotes the Kronecker delta. Using the inverse of the metric tensor one is able to "lift the index" of tensor components, e.g. $x^\mu = g^{\mu\nu} x_\nu$. If spacetime admits a time-independent metric we call it "stationary" – if it is also irrotational we say that the spacetime is "static".

Having a metric tensor grants the possibility to measure lengths and enables us to describe GR as a Lagrangian field theory using a corresponding extremisation of an action functional. A Lagrangian, describing a point particle of mass m , travelling on a worldline $x^\mu(t)$ is defined as

$$L = -mc^2 dt = -mc \sqrt{-g_{\mu\nu} \frac{dx^\mu}{dt} \frac{dx^\nu}{dt}}, \quad (1.8)$$

where t is the "time coordinate"⁴ and dt is an infinitesimal increment of proper time, i.e., the time an ideal clock would tell travelling on the same path through spacetime. In the description of fields, such as the Electromagnetic (EM) field, one encounters Lagrange densities \mathcal{L} , which connect to a Lagrangian via the square root of the determinant of $g_{\mu\nu}$ via $L = \sqrt{g} \mathcal{L}$.

Having a notion of lengths and angles one is able to define a new derivative – the covariant derivative – which generalises directional derivatives and enables to analyse the "straightness" of curves. Its action on vector fields $\mathfrak{X} = \mathfrak{X}^\nu \partial_\nu$ and covector fields $\mathfrak{U} = \mathfrak{U}_\nu dx^\nu$ is given by

$$\nabla_\mu \mathfrak{X}^\nu = \partial_\mu \mathfrak{X}^\nu + \Gamma^\nu_{\mu\lambda} \mathfrak{X}^\lambda \quad \text{and} \quad \nabla_\mu \mathfrak{U}_\nu = \partial_\mu \mathfrak{U}_\nu - \Gamma^\lambda_{\mu\nu} \mathfrak{U}_\lambda, \quad (1.9)$$

with the Christoffel symbols

$$\Gamma^\mu_{\nu\sigma} = \frac{1}{2} g^{\mu\lambda} (\partial_\sigma g_{\lambda\nu} + \partial_\nu g_{\lambda\sigma} - \partial_\lambda g_{\nu\sigma}). \quad (1.10)$$

⁴For simplicity we refer to the zeroth-coordinate in each chart as the time coordinate.

This notion of a covariant derivative is canonical to each manifold which admits a metric tensor and is usually called a *Levi-Civita connection*. To shorten notation even more we will from now on use commas to indicate partial differentiation, whereas semicolons abbreviate covariant derivatives, that is, $A_{\mu,\nu} = \partial_\nu A_\mu$ and $A_{\mu;\nu} = \nabla_\nu A_\mu$. Finally one can define three different notions of curvature

$$\text{Riemann curvature: } R^\alpha_{\beta\gamma\delta} = \partial_\gamma \Gamma^\alpha_{\beta\delta} - \partial_\delta \Gamma^\alpha_{\beta\gamma} + \Gamma^\epsilon_{\beta\delta} \Gamma^\alpha_{\epsilon\gamma} - \Gamma^\epsilon_{\beta\gamma} \Gamma^\alpha_{\epsilon\delta} \quad (1.11a)$$

$$\text{Ricci curvature: } R_{\alpha\beta} = R^\gamma_{\alpha\gamma\beta} \quad (1.11b)$$

$$\text{Ricci scalar: } R = g^{\alpha\beta} R_{\alpha\beta}. \quad (1.11c)$$

Each of these different curvature definitions plays a different – but equally important – role in Einstein's GR, which becomes ultimately apparent in the field equations $R_{\mu\nu} - \frac{1}{2}g_{\mu\nu}R + \Lambda g_{\mu\nu} = \frac{8\pi G}{c^4}T_{\mu\nu}$, where Λ is the cosmological constant and $T_{\mu\nu}$ is the energy-momentum tensor that describes the distribution of energy and matter in spacetime. We say that "spacetime is curved" if there are non vanishing component functions of the Riemann tensor $R^\alpha_{\beta\gamma\delta}$. John Archibald Wheeler's famous quote "*Spacetime tells matter how to move; matter tells spacetime how to curve*" sums up the idea behind GR quite well. So far, we have only described the second part of this quote. We now describe how matter – or to be more precise, test particles, move through spacetime.

Which worldline $x^\mu(t)$ matter takes through spacetime is described by the geodesic equation

$$\frac{d^2x^\lambda}{dt^2} + \Gamma^\lambda_{\mu\nu} \frac{dx^\mu}{dt} \frac{dx^\nu}{dt} = 0, \quad (1.12)$$

which can be derived from the EEP. A geodesic can be thought of as the "straightest possible path" in a curved spacetime and is achieved by a worldline whose infinitesimal (four-) velocity vector is always constant along its path and points in the direction of travel. Note that this concept can be thought of as the direct generalisation of a vanishing acceleration into the framework of differential geometry.

We will continue to introduce three different spacetimes, each including more corrections to describe gravitational interactions with an increasing level of complexity; each step including more relativistic effects – starting from (empty) Minkowski space.

1.1.3 Flat Spacetime

The cornerstone of Einstein's theory of relativity is the fact that the speed of light in vacuum

$$c = 299.792.458 \frac{\text{m}}{\text{s}}, \quad (1.13)$$

is constant, as manifested in the LLI. The sheer amount of trust physicists lay upon this fundamental aspect becomes evident in the SI-redefinition of the metre in 2019 – making c a defined constant, without any measurement uncertainties. The geometry of spacetime, even in the absence of matter, therefore inherits a causal structure, which is defined using the speed of light and results in the framework of Special Relativity (SR). To see how this structure arises we need to set some notation.

For flat, Minkowski spacetime⁵ $\mathcal{M} = (\mathbb{R}^4, \eta)$, we can define a trivial global chart with

⁵The notions of "flat spacetime", "Minkowski spacetime", and "Minkowski space" are often used synonymously. The latter name is justified because this spacetime is additionally equipped with a vector space structure.

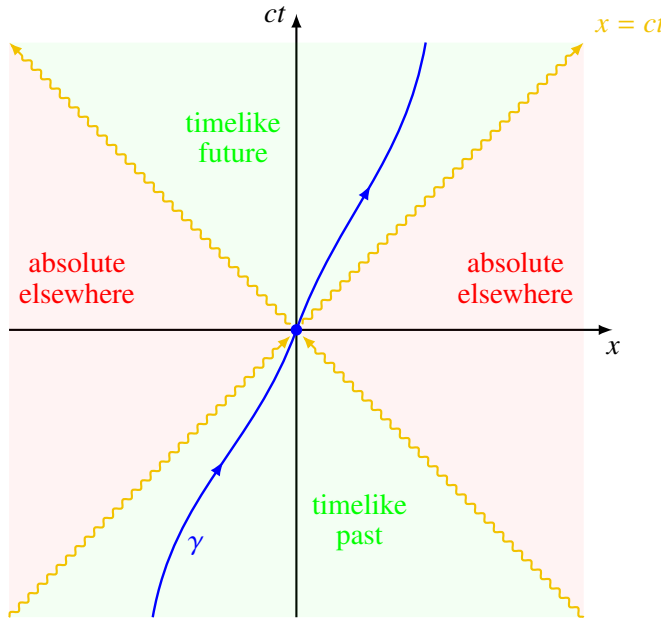


Figure 1.2: Two-dimensional depiction of a spacetime diagram of an observer travelling along the timelike curve γ in Minkowski space (blue) with indicated light cone structure (yellow) and corresponding regions of future, past and the absolute elsewhere.

domain $U = \mathcal{M} = \{(ct, x, y, z) \mid -\infty < t, x, y, z < \infty\}$ and metric tensor

$$\eta : \mathbb{R}^4 \times \mathbb{R}^4 \longrightarrow \mathbb{R}, \quad \text{with component functions} \quad \eta_{\mu\nu} = \text{diag}(-1, 1, 1, 1). \quad (1.14)$$

The line element can then be written as

$$ds^2 = \eta_{\mu\nu} dx^\mu dx^\nu = -c^2 dt^2 + dx^2 + dy^2 + dz^2. \quad (1.15)$$

Note that the four components of an event do not constitute a four-vector in the sense that it transforms covariantly under Lorentz transformations. The difference between two events x_1, x_2 , called a "displacement four-vector", on the other hand, is a four-vector and the sign of its length carries information about the possibility of a causal connection of both events. By defining

$$ds^2 = \eta_{\mu\nu} dx_1^\mu dx_2^\nu < 0 \iff x_1 \text{ and } x_2 \text{ are timelike separated}, \quad (1.16a)$$

$$ds^2 = \eta_{\mu\nu} dx_1^\mu dx_2^\nu = 0 \iff x_1 \text{ and } x_2 \text{ are lightlike separated}, \quad (1.16b)$$

$$ds^2 = \eta_{\mu\nu} dx_1^\mu dx_2^\nu > 0 \iff x_1 \text{ and } x_2 \text{ are spacelike separated}, \quad (1.16c)$$

one can divide Minkowski space into three distinct regions as shown in Fig. 1.2, where the region of spacelike separated events is commonly called the "absolute elsewhere"

Alternatively one can also define a spherical coordinate system with chart domain $\tilde{U} = \{(ct, r, \theta, \varphi) \mid -\infty < t < \infty, r > 0, 0 < \theta < \pi, 0 < \varphi < 2\pi\}$, such that one leaves out a single half-great circle of infinitesimal thickness between the poles in this chart. Most non-trivial, but spherically symmetric, spacetimes use this chart domain, however, one has to keep in mind to use a second chart to describe the whole spacetime. The Minkowski metric takes the following form in these coordinates

$$\tilde{\eta}_{\mu\nu} = \text{diag}(-1, 1, r^2, r^2 \sin^2(\theta)), \quad (1.17)$$

such that the line element reads

$$ds^2 = \tilde{\eta}_{\mu\nu} d\tilde{x}^\mu d\tilde{x}^\nu = -c^2 dt^2 + dr^2 + r^2 d\theta^2 + r^2 \sin^2(\theta) d\varphi^2. \quad (1.18)$$

Next, we examine the dominant gravitational effects that can be added onto Minkowski spacetime to develop a theory similar to Newtonian gravity.

1.1.4 Newtonian Spacetime

We have now seen how gravity arises in GR as the geodetic motion of particles in curved spacetimes. One can ask how Newtonian gravity would fit into this description, or more general "Can we interpret Newton's axioms also in a geometrical framework via a space curvature?" The following description is based on Frederic Schuller's introduction to GR [21]. To do this, let us summarise the axioms of Newtonian gravity

- Axiom 1: *A body on which no force acts moves uniformly along a straight line.*
- Axiom 2: *Deviation of a body's motion from such uniform straight motion is effected by a force, reduced by a factor of the body's reciprocal mass.*

We now introduce a mathematical framework to formalise those concepts.

Let $\mathbf{x} : \mathbb{R} \rightarrow \mathbb{R}^3$ be a particle's trajectory with mass m and $\mathbf{F} = m\mathbf{g} : \mathbb{R}^3 \rightarrow \mathbb{R}^3$ the (time independent) gravitational force field. Let $\phi(\mathbf{x})$ be the corresponding gravitational potential, i.e., $\mathbf{g}(\mathbf{x}) = -\nabla\phi(\mathbf{x})$, which satisfies Poisson's equation

$$\Delta\phi(\mathbf{x}) = 4\pi G\rho(\mathbf{x}) \implies \phi(\mathbf{x}) = -G \int d\mathbf{x}' \frac{\rho(\mathbf{x}')}{|\mathbf{x} - \mathbf{x}'|}, \quad (1.19)$$

where $\rho(\mathbf{x})$ is the gravitational mass density. Newton's second axiom can now be rewritten as

$$\ddot{\mathbf{x}} = \frac{1}{m}\mathbf{F}(\mathbf{x}) \iff \ddot{x}^a - \frac{1}{m}F^a(\mathbf{x}) = 0 \quad (1.20)$$

and we continue to ask whether this formula can be written as a (three-dimensional) geodesic equation, i.e.,

$$\ddot{x}^i + \Gamma_{jk}^i \dot{x}^j \dot{x}^k = 0 \quad (1.21)$$

for a suitable choice of Christoffel symbols. Unfortunately one cannot choose Christoffel symbols Γ_{jk}^i for a given force field \mathbf{F} , such that Eq. (1.21) holds, because of the non-trivial dependence on $\dot{x}^j \dot{x}^k$. We can, nevertheless, lift the description from three to four dimensions by defining a worldline as

$$X : \mathbb{R} \rightarrow \mathbb{R}^4, \quad t \mapsto (ct, \mathbf{x}(t)) \quad (1.22)$$

and see that $\partial_t X^0 = \dot{X}^0 = c$. We can then trivially rewrite Eq. (1.20) by multiplying twice with $\dot{X}^0/c = 1$ to obtain

$$\dot{X}^0 = 0, \quad \dot{X}^a - \frac{1}{mc^2} F^a(\mathbf{x}) \dot{X}^0 \dot{X}^0 = 0 \quad (1.23)$$

and one might ask what the point in the whole derivation was, since we get the same equation as before, but trivially rewritten and with the additional constraint $\dot{X}^0 = 0$. However, since $\dot{X}^0 = c$, one can now – in this four-dimensional description – actually choose Christoffel

symbols $\Gamma^0_{jk} = \Gamma^i_{jk} = 0 \forall i, j, k \in \{1, 2, 3\}$ and $\Gamma^a_{00} = -\frac{1}{mc^2}F^a$, such that the geodesic equation

$$\ddot{X}^\alpha + \Gamma^\alpha_{\mu\nu}\dot{X}^\mu\dot{X}^\nu = 0 \quad (1.24)$$

holds and one can interpret Newton's first axiom to be satisfied.

From the knowledge of all Christoffel symbols one can deduce the form of the metric tensor and its inverse

$$g_{\mu\nu} = \begin{pmatrix} -1 - 2\frac{\phi(\mathbf{r})}{c^2} & 0 \\ 0 & \mathbb{1}_3 \end{pmatrix}, \quad g^{\mu\nu} = \begin{pmatrix} -1 + 2\frac{\phi(\mathbf{r})}{c^2} & 0 \\ 0 & \mathbb{1}_3 \end{pmatrix}, \quad (1.25)$$

where $\mathbb{1}_3$ denotes the three-dimensional unity matrix and we assumed – for simplicity – that the frame of reference does not move with respect to the matter distribution, resulting in a static spacetime.

A spacetime which admits a metric tensor defined by Eq. (1.25) will be called "Newtonian spacetime". Note that this nomenclature should be taken with a few additional thoughts, i.e., if a universe is modelled to be a Newtonian spacetime this is *not* equivalent to Newton's classical theory of gravity, because the notions of "absolute space" and "absolute time" are replaced by a four-dimensional description on spacetime and is – by definition – Lorentz covariant. A better picture would be to see this spacetime as a first order Newtonian extension to special relativity, which can also be motivated by calculating the Lagrangian, defined in Eq. (1.8), corresponding to the metric tensor in Eq. (1.25)

$$L(\mathbf{r}, \dot{\mathbf{r}}) = -mc^2 + \frac{m\dot{\mathbf{r}}^2}{2} - m\phi(\mathbf{r}) + \mathcal{O}(c^{-2}), \quad (1.26)$$

where we used a Taylor expansion of the square root. This is the usual, non-relativistic, Lagrangian for a point particle, up to post-Newtonian corrections of $\mathcal{O}(c^{-2})$ that we will discuss in the next section. The Newtonian spacetime therefore combines the framework of (special) relativity with the dominant effects of Newtonian gravity and will be a helpful intermediate step in the transition from Minkowski to post-Newtonian spacetimes.

An important point we want to highlight is that even this Newtonian spacetime has non-vanishing spacetime curvature. One can calculate Riemann curvature Eq. (1.11a) whose only non-vanishing components are

$$R^a_{0b0}(\mathbf{x}) = -\frac{1}{mc^2} \frac{\partial}{\partial x^b} F^a(\mathbf{x}). \quad (1.27)$$

From here one can calculate the Ricci curvature Eq. (1.11b) as

$$R_{00}(\mathbf{x}) = R^a_{0a0}(\mathbf{x}) = -\frac{1}{mc^2} \frac{\partial}{\partial x^a} F^a(\mathbf{x}) = \frac{1}{c^2} \partial_a \partial^a \phi(\mathbf{x}) = \frac{4\pi G}{c^2} \rho(\mathbf{x}), \quad (1.28)$$

which is non-zero by Poisson's law in the presence of matter. Note that this is not a curvature of space, but a curvature of spacetime.

The notion of spacetime curvature is often used in experiments using Atom Interferometers (AIFs) [22] – but its definition may vary. Often, spacetime curvature is defined to be a non-vanishing second order derivative of $\phi(\mathbf{r})$, i.e., a gravity gradient. Relativistically, however, the mere existence of a non-vanishing gravitational potential manifests as spacetime curvature, independent of whether this potential admits non-trivial second order derivatives, making the above mentioned alternative definition of spacetime curvature not wrong, but potentially ambiguous.

1.1.5 Post-Newtonian Spacetime

We are going to model gravity by a *metric theory* in which test bodies follow geodesics with respect to the corresponding Levi-Civita connection and to which matter couples by the standard minimal scheme. This scheme may be extended to scalar-tensor [23] and vector-tensor theories [24], which we will not consider here.

To perform a Newtonian *weak-field* and *slow-motion* expansion of the physics in a relativistic spacetime, one first has to introduce a background structure with respect to which these notions can be defined [25, Sec. 16.2.1]. This background structure consists of a Minkowskian metric and the worldline of a preferred observer. Then one can implement the Newtonian expansion by a power series expansion in small parameters: The Newtonian gravitational potential $\phi/c^2 \ll 1$ and $v^2/c^2 \ll 1$, where v is a typical velocity of the matter sourcing gravity. With respect to the background structure, the metric tensor g then splits into the sum of a Newtonian spacetime and post-Newtonian corrections, special to each metric theory. This approach gives rise to a 10-parameter class of different metric theories and is described in the Parametrised Post-Newtonian (PPN) formalism [26]. The low-order post-Newtonian behaviour of each metric theory is then uniquely determined by those ten PPN parameters.

In the following, we only consider two out of those ten possible parameters, namely, the Eddington-Robertson (ER) parameters $\beta, \gamma \in \mathbb{R}$, that correspond to the biggest relativistic corrections of static spacetimes. In a local coordinate system $x^\mu = \{ct, \mathbf{r}\}$ the covariant PPN metric tensor components can be written using the line element

$$ds^2 = g_{\mu\nu} dx^\mu dx^\nu = -\left(c^2 + 2\phi(\mathbf{r}) + 2\beta \frac{\phi(\mathbf{r})^2}{c^2}\right) dt^2 + \left(1 - 2\gamma \frac{\phi(\mathbf{r})}{c^2}\right) d\mathbf{r}^2 + O(c^{-4}), \quad (1.29)$$

and ϕ is, again, the gravitational potential that arises from solving Poisson's equation⁶ in Eq. (1.19) for a given matter distribution $\rho(\mathbf{r})$. The coefficient functions of the inverse metric take the form

$$g^{\mu\nu} = \begin{pmatrix} -1 + 2\frac{\phi(\mathbf{r})}{c^2} + (2\beta - 4)\frac{\phi(\mathbf{r})^2}{c^4} + O(c^{-6}) & O(c^{-5}) \\ O(c^{-5}) & \left(1 + 2\gamma \frac{\phi(\mathbf{r})}{c^2}\right) \mathbb{1}_3 + O(c^{-4}) \end{pmatrix}. \quad (1.30)$$

In standard GR, the ER parameters are unity. Upper bounds for the ER parameters are long known to be on the orders $|\gamma - 1| \approx |\beta - 1| \lesssim 10^{-5}$ obtained by tracking, e.g., the trajectory of the Cassini mission or measuring perihelion shifts of Mercury and Mars (cf. [28–31]). For now we model Earth as a point source at the origin with mass M_\oplus , such that the Newtonian gravitational potential takes the form

$$\rho(\mathbf{r}) = M_\oplus \delta(\mathbf{r}) \implies \phi(\mathbf{r}) = -\frac{GM_\oplus}{|\mathbf{r}|}. \quad (1.31)$$

A consideration of more complex gravitational potentials can be found in Sec. 2.4.1 and Sec. 2.4.2. Notice that the metric tensor is asymptotically flat in these coordinates, since $\phi(\mathbf{r}) \rightarrow 0$ for $|\mathbf{r}| \rightarrow \infty$, which means that metric tensor is not Minkowskian at the point of an earthbound experiment.

⁶See, e.g., the discussion in Chapter 6 of Ref. [27] and Eq. (6.2.14) therein.

One can now calculate the Lagrangian as defined in Eq. (1.8), similarly to the case of the Newtonian spacetime before, to obtain

$$\begin{aligned} L(\mathbf{r}, \dot{\mathbf{r}}) &= -mc \sqrt{c^2 + 2\phi(\mathbf{r}) + 2\beta \frac{\phi(\mathbf{r})^2}{c^2} - \left(1 - 2\gamma \frac{\phi(\mathbf{r})}{c^2}\right) \dot{\mathbf{r}}^2 + O(c^{-4})} \\ &= -mc^2 + \frac{m\dot{\mathbf{r}}^2}{2} - m\phi(\mathbf{r}) + \frac{m\dot{\mathbf{r}}^4}{8c^2} - \frac{2\beta - 1}{2c^2} m\phi(\mathbf{r})^2 - \frac{2\gamma + 1}{2c^2} m\phi(\mathbf{r})\dot{\mathbf{r}}^2 + O(c^{-4}), \end{aligned} \quad (1.32)$$

which shows three additional (general) relativistic corrections of order c^{-2} . The first novel contribution is the special relativistic correction to the kinetic energy, the second term is a quadratic correction to the gravitational potential and the last term is a mixture of kinetic and potential contributions.

For the most part of this thesis we will deal with the Newtonian (Chapter 2) and the post-Newtonian (Chapter 3) spacetimes and explain how AIF experiments should be theoretically modelled in such gravitational backgrounds. Nevertheless, as an outlook we will analyse the next order post-Newtonian corrections that describe rotations and the relativistic effect of "gravitomagnetism" in Sec. 3.8. For now we will conclude with the introduction of GR and continue with a short introduction to QM and the interferometry of matter waves.

1.2 Quantum Mechanics and Atom Interferometry

QM, developed in the early 20th century has transformed our understanding of the physical world and led to technological innovations that have reshaped modern society. This branch of physics, which describes the behaviour of particles on the atomic and subatomic scales, challenged classical notions of reality and introduced concepts that have revolutionised science and technology. One of the most significant impacts of QM is its role in the development of modern electronics. The principles of QM are foundational to the design and function of semiconductors, the essential components of transistors and integrated circuits. These components form the backbone of all modern electronic devices, including computers, smartphones, and digital cameras. The miniaturisation and performance improvements in electronics, driven by an understanding of QM, have catalysed the digital revolution and transformed communication, entertainment, and information processing.

QM has also led to profound changes in our philosophical understanding of reality. Concepts such as wave-particle duality, superposition, and entanglement challenge classical intuitions about the nature of matter and energy. The famous thought experiment "Schrödinger's cat" [32] and the Heisenberg uncertainty principle [33] illustrate the counter-intuitive nature of quantum phenomena and have sparked debates in philosophy regarding the nature of reality, observation, and information [34].

Matter waves, the concept integral to the experiments described in this thesis, describe the wave-like behaviour of particles such as electrons, protons, and atoms. This phenomenon was first proposed by Louis de Broglie in 1924 [35], who postulated that every particle with mass also exhibits wave-like properties, characterised by a wavelength inversely proportional to its momentum. This groundbreaking idea was experimentally confirmed by the electron diffraction experiments of Davisson and Germer in 1927 [36], which showed that electrons can produce interference patterns, akin to light waves, and was further improved by Colella, Overhauser and Werner with neutrons in 1975 [37]. Matter waves also play a crucial role in the development of technologies such as electron microscopy and – integral to this thesis – atom interferometry. These applications leverage the wave nature of particles to achieve high-precision measurements and imaging at atomic and subatomic scales. By understanding

and utilising matter waves, scientists can probe the fundamental properties of matter and explore the quantum realm with unprecedented accuracy, as recently demonstrated in the measurement of the fine-structure constant [38, 39].

In an AIF, neutral atoms are first cooled and slowed down to reduce thermal noise and improve coherence. The particles are then split into two or more paths using techniques such as diffraction through a grating or interaction with laser beams. These wave packets travel in coherent spatial superposition and are subsequently recombined. At the point of recombination, the overlapping waves interfere with each other, creating an interference pattern. The nature of this pattern – constructive or destructive interference – depends on the relative phase difference accumulated by the waves along their different paths. By precisely measuring this interference pattern, information about the environment through which the particles travelled, such as gravitational fields, rotation rates, or electromagnetic fields, can be extracted with high sensitivity.

We continue to describe the physics behind an AIF mathematically and introduce the necessary notation. An atom is modelled to be a system of two electromagnetically bound spinless point particles with masses m_1, m_2 , positions $\mathbf{r}_1, \mathbf{r}_2$ and charges q_1, q_2 , coupled to an external EM field. The corresponding Hamilton operator \hat{H} consists of the Hamiltonian for Centre of Mass (COM) motion \hat{H}_{COM} , the Hamiltonian for the internal degrees of freedom \hat{H}_{I} , the Hamiltonian for the external EM field \hat{H}_{EM} and the interaction Hamiltonian of the atom with the EM field $\hat{H}_{\text{A-L}}$, i.e.,

$$\hat{H} = \hat{H}_{\text{COM}} + \hat{H}_{\text{A-L}} + \hat{H}_{\text{I}} + \hat{H}_{\text{EM}}. \quad (1.33)$$

The external EM field is assumed to be a classical solution to the source-free Maxwell equations and will therefore not exhibit any Quantum Electrodynamics (QED) effects. In the following the canonical position and momentum operators of COM and relative motion will be denoted by $\hat{\mathbf{R}}, \hat{\mathbf{P}}$ and $\hat{\mathbf{r}}, \hat{\mathbf{p}}$, respectively, whereas the total mass of the atom will be denoted by $m = m_1 + m_2$, and the reduced mass by $\mu = m_1 m_2 / m$.

Given an initial state $|\psi(0)\rangle$ one can calculate the time evolved state of the system via $|\psi(t)\rangle = e^{-i\hat{H}t/\hbar} |\psi(0)\rangle$, if the external potentials affecting the atom are time independent, which we assume for now. This can be calculated directly from the Schrödinger equation

$$i\hbar \frac{\partial}{\partial t} |\psi\rangle = \hat{H} |\psi\rangle. \quad (1.34)$$

Upon recombination of the atomic paths, interference between both wavefunctions will occur. The probability of the atom to be in a certain state at the end of the experiment, either defined by the amount of photon momenta imparted to the COM or the internal state, is given by

$$P(t) = \langle \psi(t) | \psi(t) \rangle = \frac{1}{2}(1 + C(t) \cos(\Delta\Phi(t))), \quad (1.35)$$

where $C(t)$ is the contrast and $\Delta\Phi(t)$ is the phase difference between the two arms of the interferometer.⁷ The main objective of this thesis is to obtain formulas for the phase difference $\Delta\Phi(t)$ in complex gravitational fields, including general relativistic effects. We continue by analysing each of the terms in the Hamiltonian in Eq. (1.33) separately in more detail.

⁷We omit the time dependence of the phase shift from now on, since the time intervals of the interferometers of interest will be fixed anyway, such that the time instance where the phase shift is measured is clear by context.

1.2.1 Motional Hamiltonian

The motional Hamiltonian \hat{H}_{COM} , i.e., the Hamiltonian for the COM degree of freedom \mathbf{R}, \mathbf{P} , is given by

$$\hat{H}_{\text{COM}} = \frac{\hat{\mathbf{P}}^2}{2m} + m\phi(\hat{\mathbf{R}}), \quad (1.36)$$

with the gravitational potential $\phi(\hat{\mathbf{R}})$. To solve the Schrödinger equation we follow the introduction to atom interferometry from Ref. [40], which makes use of the stationary phase approximation and assumes that the atoms can be attributed with the notion of a well-defined worldline, which can be motivated by a narrow wave packet size using cold atoms, or potentially Bose Einstein Condensates (BECs) [41–46]. The stationary phase approximation states that the wavefunction of an atom, initialised as a wave packet at a time t_a , can be approximated at $t_b > t_a$ using the classical path of the atom $\mathbf{R}(t)$, which minimises the action

$$S(\mathbf{R}(t), \dot{\mathbf{R}}(t)) = \int_{t_a}^{t_b} L(\mathbf{R}(t), \dot{\mathbf{R}}(t)) dt, \quad (1.37)$$

where $L(\mathbf{R}, \dot{\mathbf{R}})$ is the Lagrangian corresponding to the Hamiltonian in Eq. (1.36). Note that $L(\mathbf{R}, \dot{\mathbf{R}})$ coincides with the Lagrangian of Newtonian spacetime from Eq. (1.26) that we have seen in the introduction, up to order $\mathcal{O}(c^{-2})$, i.e.,

$$L(\mathbf{R}, \dot{\mathbf{R}}) = \frac{m}{2} \dot{\mathbf{R}}^2 - m\phi(\mathbf{R}). \quad (1.38)$$

A solution $\mathbf{R}(t)$ to the corresponding Euler-Lagrange Equation (ELE)

$$\frac{d}{dt} \nabla_{\dot{\mathbf{R}}} L(\mathbf{R}, \dot{\mathbf{R}}) - \nabla_{\mathbf{R}} L(\mathbf{R}, \dot{\mathbf{R}}) = 0, \quad (1.39)$$

minimises the action functional in Eq. (1.37) and can be interpreted as the classical trajectory of a point-particle of mass m moving freely in the potential $\phi(\mathbf{R})$, provided two initial conditions: the position $\mathbf{R}(t_a) = \mathbf{R}_a$ and the velocity $\dot{\mathbf{R}}(t_a) = \dot{\mathbf{R}}_a$ at the initial time t_a . The ELE in the Newtonian case evaluates to $\ddot{\mathbf{R}}(t) = -\nabla\phi(\mathbf{R})$ and can analytically be solved, given an explicit form of $\phi(\mathbf{R})$.⁸ The COM wavefunction at the time t_b is then given by

$$|\psi(\mathbf{R}_b, t_b)\rangle = \iint d^3\mathbf{R}_a K(\mathbf{R}_b, t_b; \mathbf{R}_a, t_a) |\psi(\mathbf{R}_a, t_a)\rangle, \quad (1.40a)$$

where \mathbf{R}_b is the position of the atomic wave packet at t_b . This position is acquired using the solution of the ELE from Eq. (1.39), and

$$K(\mathbf{R}_b, t_b; \mathbf{R}_a, t_a) = \int_{t_a}^{t_b} e^{\frac{iS(\mathbf{R}(t), \dot{\mathbf{R}}(t))}{\hbar}} \mathcal{D}X(t) \mathcal{D}Y(t) \mathcal{D}Z(t), \quad (1.40b)$$

is a propagator between the spacetime events $A = (t_a, \mathbf{R}_a)$ and $B = (t_b, \mathbf{R}_b)$. The abstract differentials $\mathcal{D}X(t) \mathcal{D}Y(t) \mathcal{D}Z(t)$ indicate a Feynman path integral and should be taken with respect to all paths connecting A and B . Note that the stationary phase approximation is exact for Lagrangians, which depend at most quadratically on position and velocity, therefore limiting the number of gravitational potentials that can be described by this approach without

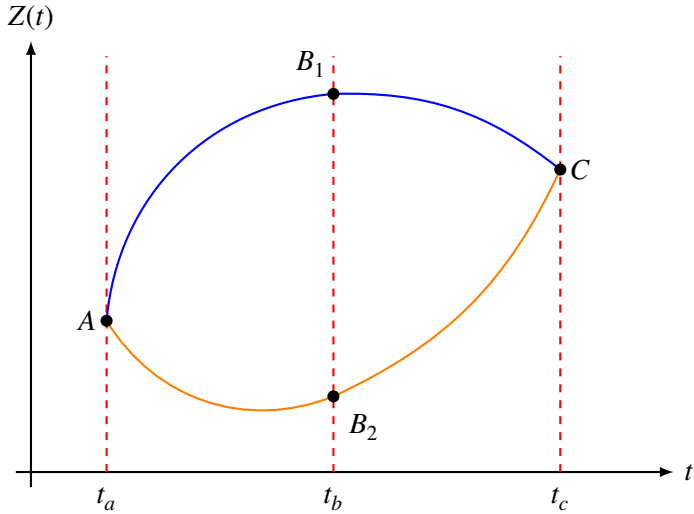


Figure 1.3: Schematic depiction of an interferometer consisting of two atomic paths, which are the solutions to the ELE for the different initial conditions set by the spacetime events A, B_1, B_2 and C . The upper path $A \rightarrow B_1 \rightarrow C$ is depicted in blue and the lower path $A \rightarrow B_2 \rightarrow C$ in orange.

any perturbation. To ease up notation we will always align the local z -axis \mathbf{e}_z with the atomic trajectory, such that we essentially describe a one-dimensional system for the COM motion.⁹

The explicit form of the wavefunction will not be needed, but only the accumulated phase along the atom's path. Considering an interferometer consisting of two distinct atomic paths that start and end at the same position, as depicted in Fig. 1.3, one can calculate the *relative phase* $\Delta\Phi$ acquired between both paths as

$$\Delta\Phi = \Delta\Phi_{A \rightarrow B_1} + \Delta\Phi_{B_1 \rightarrow C} - \Delta\Phi_{A \rightarrow B_2} - \Delta\Phi_{B_2 \rightarrow C}. \quad (1.41)$$

Here the phase between two spacetime events $\Delta\Phi_{A \rightarrow B}$ is the (one-dimensional) action functional evaluated along the classical path $Z_{A \rightarrow B}(t)$ connecting the initial and final heights Z_a, Z_b , i.e.,

$$\Delta\Phi_{A \rightarrow B} = \frac{1}{\hbar} S_z(Z_b, t_b; Z_a, t_a) = \frac{1}{\hbar} \int_{t_a}^{t_b} dt L(Z_{A \rightarrow B}(t) \mathbf{e}_z, \dot{Z}_{A \rightarrow B}(t) \mathbf{e}_z). \quad (1.42)$$

A phase contribution like this will be called a *propagation phase* and is a key element for the upcoming analysis. We continue by setting some notation for the internal degrees of freedom and the external EM fields.

1.2.2 Internal Hamiltonian

The internal Hamiltonian is of lesser importance for this analysis, as the interactions with the EM field are modelled to be instantaneous and perfect, ensuring that no additional phase shifts arise from internal dynamics. Nevertheless, we need to establish some notation for

⁸ $\phi(\mathbf{R})$ is assumed to be *well behaved* enough to guarantee analytical solutions of the ELE.

⁹Corrections to this assumption are discussed in Sec. 2.2.4, where rotating reference frames and Coriolis corrections are included into the analysis.

the atom-light interactions, so we will briefly discuss the form of the Hamiltonian and its eigenstates. The internal Hamiltonian is assumed to have the form of a hydrogen-like system

$$\hat{H}_I = \frac{\hat{\mathbf{p}}^2}{2\mu} - \frac{q_1 q_2}{4\pi\epsilon_0 |\hat{\mathbf{r}}|} \quad (1.43)$$

and is solved by the known electronic orbitals. Depending on the atom-light interaction of interest we define an excited state $|e\rangle$ and a single ground state $|g\rangle$ for the case of Bragg interactions and single photon transitions, see Sec. 1.2.4. For Raman interactions, we define the excited state $|e\rangle$ and two ground states $|g_1\rangle, |g_2\rangle$. The internal Hamiltonian can then be written in the corresponding eigenbasis as

$$\text{Bragg \& Single photon: } \hat{H}_I = \hbar\omega_g |g\rangle\langle g| + \hbar\omega_e |e\rangle\langle e|, \quad (1.44a)$$

$$\text{Raman: } \hat{H}_I = \hbar\omega_1 |g_1\rangle\langle g_1| + \hbar\omega_2 |g_2\rangle\langle g_2| + \hbar\omega_e |e\rangle\langle e|, \quad (1.44b)$$

depending on the interaction process of interest. We also define the transition frequencies $\omega_{eg} = \omega_e - \omega_g$ and $\omega_{12} = \omega_1 - \omega_2$, which will become important in the following discussions.

1.2.3 Light Hamiltonian

Classical EM fields can be described by the Hamilton function

$$H_{\text{EM}} = \frac{\epsilon_0}{2} \int d^3\mathbf{R} [\hat{\mathbf{E}}(\mathbf{R})^2 + c^2 \hat{\mathbf{B}}(\mathbf{R})^2], \quad (1.45)$$

whose equations of motion (EOM) are equivalent to Maxwell's equations of electrodynamics. Canonically quantising Eq. (1.45) results in a full QED description of light fields and the interactions with matter. The vacuum eigenfunctions of this quantised Hamiltonian are plane waves and we are going to expand each solution of the EM field in this eigenbasis. For the sake of simplicity we focus, for now, on the electric field $\hat{\mathbf{E}}(\mathbf{R})$, one could, however, equivalently analyse the magnetic flux density $\hat{\mathbf{B}}(\mathbf{R})$. The general solution for the electric field is then given by

$$\hat{\mathbf{E}}(\hat{\mathbf{R}}) = \sum_{\epsilon=1,2} \int d^3k i\mathcal{E}_\omega \left[\hat{a}_\epsilon(\mathbf{k}) \mathbf{e}_\epsilon(\mathbf{k}) e^{i\mathbf{k}\hat{\mathbf{R}}} - \text{H.c.} \right] \quad \text{with} \quad \mathcal{E}_\omega = \sqrt{\frac{\hbar\omega}{(2\pi)^3 2\epsilon_0}}, \quad (1.46)$$

where $\hat{a}_\epsilon(\mathbf{k}), \hat{a}_\epsilon^\dagger(\mathbf{k})$ are the bosonic creation and annihilation operators for a photon with wave vector \mathbf{k} , polarisation ϵ and frequency $\omega = c|\mathbf{k}|$. The set $\{\mathbf{e}_1(\mathbf{k}), \mathbf{e}_2(\mathbf{k}), \mathbf{k}\}$ constitutes an orthonormal basis of \mathbb{R}^3 for each \mathbf{k} . As indicated before, we always assume propagation of the EM field parallel to the atomic trajectory, i.e., along the z-axis. Furthermore we only consider a single mode, i.e., $\mathbf{k} = \pm k \mathbf{e}_z$ and choose to align the transverse directions with the x and y axes ($\mathbf{e}_1 = \mathbf{e}_x, \mathbf{e}_2 = \mathbf{e}_y$). The whole description can be extended to multiple frequencies in a straightforward manner, because of the linearity of Maxwell's equations.

Evolving the field in Eq. (1.46) in time with respect to the free field Hamiltonian and applying the aforementioned assumptions results in an electric field operator

$$\hat{\mathbf{E}}(\hat{Z}, t) = \sum_{\epsilon=1,2} i\mathcal{E}_\omega \left[\hat{a}_\epsilon(k, t) \mathbf{e}_\epsilon e^{i(k\hat{Z} - \omega t)} - \text{H.c.} \right] \quad \text{with} \quad \hat{a}_\epsilon(k, t) = \hat{a}_\epsilon(k) e^{-i\omega t}. \quad (1.47)$$

The quantum properties of the EM field are encoded in the creation and annihilation operators, allowing to create non-classical light fields and enabling effects like entanglement and squeezing [47–50]. Nevertheless, since we assume the light fields of interest to be classical,

we omit the creation and annihilation operators, treating them as \mathbb{C} -numbers. We furthermore combine the polarisation vector \mathbf{e}_ϵ with the field amplitude \mathcal{E}_ω to a vector-valued amplitude and define two distinct light fields, which will be important for the different atom-light interactions: firstly a Single Frequency (SF) field

$$\hat{\mathbf{E}}_{\text{SF}}(\hat{Z}, t) = \mathcal{E}(t) e^{i(k\hat{Z} - \omega t)} - \text{H.c.}, \quad (1.48)$$

used for interaction processes using single photon transitions and secondly a Dual Frequency (DF) field with counter propagating light fields

$$\hat{\mathbf{E}}_{\text{DF}}(\hat{Z}, t) = \left[\mathcal{E}_a(t) e^{i(k_a \hat{Z} - \omega_a t)} + \mathcal{E}_b(t) e^{i(-k_b \hat{Z} - \omega_b t)} \right] - \text{H.c.}, \quad (1.49)$$

used to describe Raman and Bragg interactions, which rely on two-photon transitions. We take a closer look at these interaction processes in the next section.

1.2.4 Atom-Light Hamiltonian

In order to create an interferometer using atoms, we need to coherently split and recombine atomic wave packets with high accuracy. Essentially, every AIF experiment can be broken down into a sequence of beam splitting operations, which coherently split a single wave packet into a 50 : 50 superposition of momentum states, and mirror operations, which completely flip the momentum of a single wave packet. We describe four of these operations, which can be efficiently performed with classical light fields: Bragg diffraction, Raman transitions, single-photon transitions, and Bloch oscillations. Each of those processes, apart from the Bloch oscillations, can be described using the interaction Hamiltonian between an (external) light field and an atom given by

$$\hat{H}_{\text{A-L}} = -\hat{\mathbf{d}} \cdot \hat{\mathbf{E}}(\hat{Z}, t) \quad \text{with} \quad \hat{\mathbf{d}} = \sum_{\alpha=1,2} q_\alpha \hat{\mathbf{r}}_\alpha = \sum_{i,j} \mathbf{d}_{ij} |i\rangle\langle j|. \quad (1.50)$$

The electric field $\hat{\mathbf{E}}(\hat{Z}, t)$ in Eq. (1.50) is either the SF field from Eq. (1.48) or the DF field from Eq. (1.49). Furthermore, the internal states $|i\rangle$ in the dipole operator $\hat{\mathbf{d}}$ depend on the atomic species and desired interaction process, as in Eqs. (1.44). In most modern experiments either Alkali, or Earth-Alkali metals are used, see Refs. [51–55].

Consider a Bragg interaction as an example, i.e., we have a dipole operator corresponding to the internal Hamiltonian in Eq. (1.44a)

$$\hat{\mathbf{d}}_{\text{Bragg}} = \mathbf{d}_{eg} |e\rangle\langle g| + \text{H.c.}, \quad (1.51)$$

and the DF light field from Eq. (1.49). The interaction Hamiltonian can then be written as

$$\hat{H}_{\text{A-L}} = -\hat{\mathbf{d}}_{\text{Bragg}} \cdot \hat{\mathbf{E}}_{\text{DF}}(\hat{Z}, t) = \left(\hbar \Omega_a(t) e^{i(k_a \hat{Z} - \omega_a t)} + \hbar \Omega_b(t) e^{i(-k_b \hat{Z} - \omega_b t)} \right) |e\rangle\langle g| + \text{H.c.}, \quad (1.52)$$

with individual Rabi frequencies for each light field $i = a, b$ of

$$\Omega_i(t) = -\frac{1}{\hbar} \langle e | \hat{\mathbf{d}}_{\text{Bragg}} \cdot \mathcal{E}_i(t) | g \rangle. \quad (1.53)$$

The exponential of the position operator \hat{Z} acts as a momentum translation, i.e.,

$$e^{\pm i k \hat{Z}} = \int_{-\infty}^{\infty} dP |P \pm \hbar k \rangle\langle P|, \quad (1.54)$$

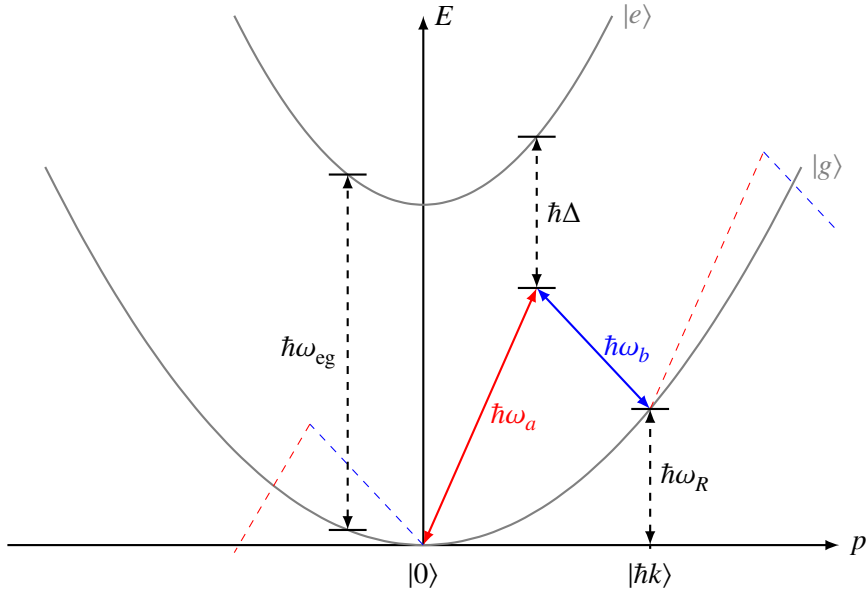


Figure 1.4: Schematic depiction of Bragg diffraction using an effective two-level atom with states $|g\rangle$, $|e\rangle$ and two counter propagating light fields with frequencies ω_a (red) and ω_b (blue), namely a DF field \hat{E}_{DF} . The resonant two photon transition (thick red and blue arrows) results in an effective momentum transfer of $\hbar k = \hbar(k_a + k_b)$, where $\omega_R = \frac{\hbar k^2}{2m} = \omega_a - \omega_b$ denotes the corresponding recoil frequency. The dashed lines correspond to off resonant transitions. Both laser frequencies ω_a , ω_b are detuned by Δ to $|e\rangle$, such that there is no coupling to the excited state.

where $|P\rangle$ denotes a momentum eigenstate of the COM motion. One can therefore see how it is possible to construct a resonant two-photon process inducing a momentum kick of $\hbar k = \hbar(k_a + k_b)$, as depicted in Fig. 1.4. In a nutshell, the atom absorbs a photon with frequency ω_a gaining momentum $\hbar k_a$ in the process and directly emits a photon with frequency ω_b in the other light field, losing a momentum of $-\hbar k_b$, therefore gaining a total amount of $\hbar(k_a + k_b)$. Note that we have depicted the transition process in Fig. 1.4 for the case of an atom initially at rest, i.e., initialised in the momentum state $|0\rangle$. For moving atoms, the Doppler effect needs to be taken care of, one can, however, always transform into the atomic rest frame and interpret the laser frequencies accordingly.

The quantity distinguishing between a beam splitter and a mirror operation is given by the effective Rabi frequency $\Omega_{\text{eff}}(t)$, which is defined as

$$\Omega_{\text{eff}}(t) = 2 \left| \frac{\Omega_a(t)\Omega_b(t)^*}{\Delta} \right|, \quad (1.55)$$

where we neglected the Doppler and AC-Stark effect. Choosing the amplitudes of the light fields and pulse length δt such that the pulse area θ , defined as the time integral over the effective Rabi frequency, evaluates to be multiples of $\pi/2$ or π distinguishes a beam splitter from a mirror, i.e., more formally

$$\theta = \int_0^{\delta t} dt \Omega_{\text{eff}}(t) = \begin{cases} \frac{\pi}{2} + n\pi, & \text{Beam splitter} \\ n\pi, & \text{Mirror} \end{cases} \quad \text{for } n \in \mathbb{N}. \quad (1.56)$$

Equivalently one can describe the interaction process as a unitary scattering matrix, written

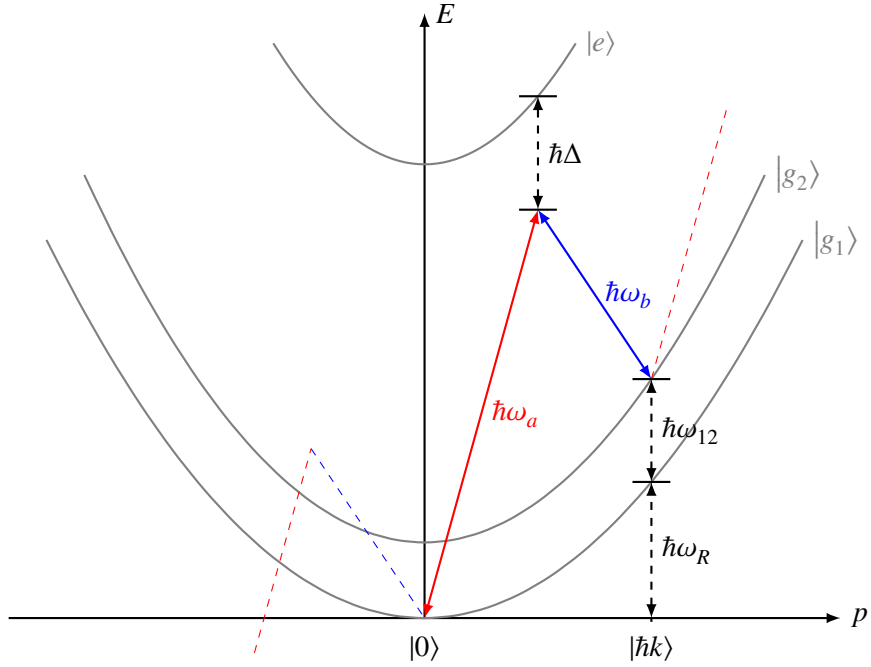


Figure 1.5: Level scheme of a two-photon Raman diffraction for an effective three-level atom and two counter propagating light fields with frequencies ω_a (red) and ω_b (blue). The resonant transition $|g_1\rangle \rightarrow |e\rangle \rightarrow |g_2\rangle$ is indicated with thick arrows. The dashed lines correspond to off resonant transitions. Both light fields are far detuned from the excited state $|e\rangle$.

in a basis of momentum states $|0\rangle, |\hbar k\rangle$, as

$$\hat{U}^{(\theta)}(t) = \frac{1}{\sqrt{2}} \begin{pmatrix} \cos(\theta) & i \sin(\theta) e^{i\Phi_L(t)} \\ i \sin(\theta) e^{-i\Phi_L(t)} & \cos(\theta) \end{pmatrix}, \quad (1.57)$$

where $\Phi_L(t) = \arg\left(\frac{\Omega_a(t)\Omega_b^*(t)}{\Delta}\right)$ is the laser phase of the two-photon process, imparted to the atom [56–62]. The time dependence of the effective Rabi frequency and the laser phase are usually omitted. If one includes a second set of counter propagating lasers and adjusts the polarisations cleverly one can also infer momentum into the positive and negative z-direction simultaneously, which is known as "double Bragg diffraction", see Refs. [63–67].

Similarly to the case of Bragg scattering one can perform Raman transitions, which make use of two ground states as indicated in Eq. (1.44b) and Fig. 1.5. One therefore includes an additional degree of freedom, namely the atom's internal state $|g_1\rangle, |g_2\rangle$ in each path segment of the interferometry sequence. Compared to fully elastic scattering processes, where any excited state is only virtually populated, such a system exhibits far more possibilities for interferometer geometries. Raman transitions are famously used to describe so called *clock interferometers*, where the atoms are travelling in an internal superposition – additional to their spatial superposition – and can therefore be thought of a quantum mechanical analogue of a clock on two worldlines, see Sec. 1.1.1. The definition of clock is here taken very abstractly as an oscillating two-level system and should not be confused with an atomic clock in the frequency metrological sense.

Clock interferometers that utilise Raman transitions have therefore gained interest as po-

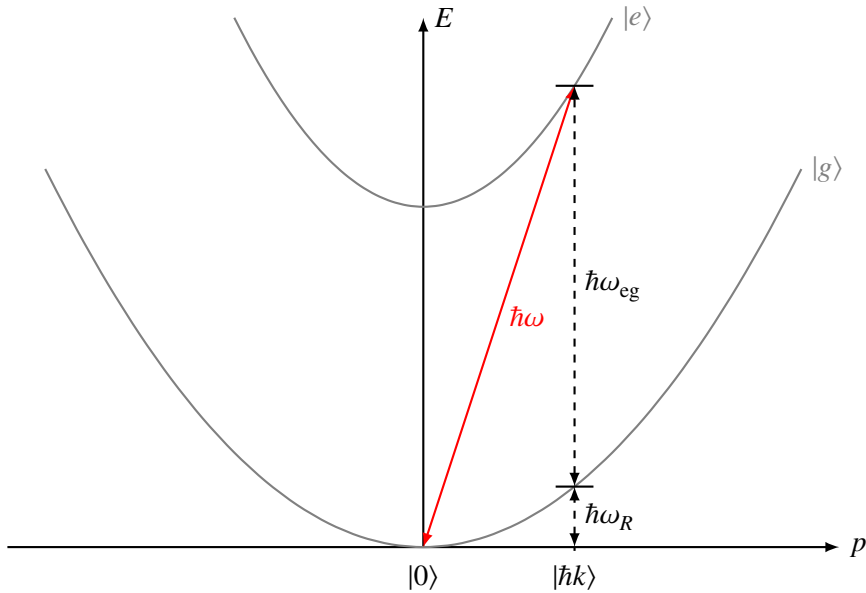


Figure 1.6: Level scheme of a single photon transition for an effective two-level atom and a single light field (red) with frequency ω and wave vector $|k| = \omega/c$.

tential measurement devices for UCR and UGR [68–70] by extracting the "clock frequency" ω_{12} as a potential measurement signal. Due to this fact, clock interferometers could be feasible to rule out certain dark matter models or even measure gravitational waves in a much needed mid-frequency band [71–73]. Since many contributions have already been published in this field and extensions of gravity by dark matter have also been considered [74], we will focus in the following on interferometers with elastic scattering processes such as the Bragg scattering described above. To complete the picture, we continue to mention the last two light field interactions, that can be used to build large scale AIF experiments.

Single photon transitions only use a one mode of the EM field, i.e., a field as in Eq. (1.48) and the internal atomic structure from Eq. (1.44a). The corresponding level scheme and transition is shown in Fig. 1.6. One positive and straightforward aspect of this process is that only a single light field is required, potentially minimizing error sources due to a reduced experimental setup. On the other hand, however, is the flight time of the atom in the excited state $|e\rangle$ limited by its lifetime, which rules out a certain number of atomic species capable for long flight times. Additionally, there is the necessity to find a suitable excited state with good availability for stable and powerful lasers in the corresponding frequency regime of $\omega = \omega_{eg} + \omega_R$. Note that single photon transitions can also be utilised for clock interferometry [75–77].

The last atom-light interaction which is commonly used in AIF experiments are accelerated optical lattices, utilizing Bloch oscillations, used to manipulate the trajectories of atoms with unprecedented speed and accuracy. Bloch oscillations are not based on the dipole Hamiltonian in Eq. (1.50), but rather trap the atoms in a standing EM wave, i.e., an optical lattice, and accelerate it [38, 39, 78, 79] – together with the trapped atoms – in the spatial direction of interest. The COM Hamiltonian for Bloch oscillations can be written in a position basis as

$$\hat{H}_{\text{COM}} = \frac{\hat{\mathbf{P}}^2}{2m} + m\phi(\hat{\mathbf{R}}) + \underbrace{2\hbar\Omega \cos^2(\mathbf{k}\hat{\mathbf{R}})}_{\text{Optical lattice}}, \quad (1.58)$$

where the $|\mathbf{k}| = k = \frac{2\pi}{\lambda}$ defines the width of the lattice λ . A detailed analysis of how Bloch oscillations are implemented in experiments and more details about their theoretical description can be found in Refs. [80, 81]. In the context of this thesis, we will only consider Bloch oscillations in a highly idealised manner, assuming that they instantaneously impart a momentum of $\hbar k$, corresponding to the frequency of the light field and add their phase to the atoms.

We have now summarised the essential tools used for modern AIF experiments and introduced the notation of its mathematical framework. With this, one is now able to calculate phase shifts for a variety of different interferometer geometries, interaction processes and gravitational backgrounds, as we will analyse in the rest of this thesis.

Chapter 2

Atom Interferometers in Newtonian Spacetime

"We physicists are always checking to see if there is something the matter with the theory. That's the game, because if there *is* something the matter, it's interesting! But so far, we have found nothing wrong with the theory of quantum electrodynamics. It is, therefore, I would say, the jewel of physics – our proudest possession."

Richard Feynman, 1985

From "QED – The strange theory of light and matter"

We now analyse various explicit interferometer geometries within the context of a Newtonian spacetime gravitational background, i.e. a metric tensor from Eq. (1.25). Initially, we make several key assumptions to simplify the analysis and establish a foundational understanding of basic interferometers in Sec. 2.1 and discuss more advanced topics in Sec. 2.2. The basic interferometers and the theoretical description behind this has been known before, however, we are going to present it in the dimensionless form we introduced in Werner et al., *Atom interferometers in weakly curved spacetimes using Bragg diffraction and Bloch oscillations* [2]. We continue in Sec. 2.3 with a novel interferometer geometry that we introduced in Werner et al., *Local Measurement Scheme of Gravitational Curvature using Atom Interferometers* [4] to measure gravitational curvature. In Sec. 2.4, we systematically revisit these assumptions to evaluate their validity and impact on our results. By refining or modifying the initial assumptions, we aim to achieve a more accurate and comprehensive understanding of the interferometer geometries in relation to the gravitational background.

The assumptions we are going to include initially are:

1. We start by modelling the mass density of Earth to be spherically symmetric. A more accurate model, known as the "Geopotential model" is discussed in Sec. 2.4.1.
2. We omit local masses, which alter the gravitational background, given by Earth in a non trivial way. Masses disturbing the experiment can be either time independent, like the gravitational acceleration of the building and the lab equipment, or time varying like ground water, air density fluctuations and seismic waves. We discuss an AIF experiment in the vicinity of an experimentally measured gravitational field, including non trivial gravitational gradients in Sec. 2.4.2.

We start to analyse the most basic interferometer geometries, because they produce interesting phase shift signals in their own regard and more elaborate AIF geometries can be thought of

as combinations of those basic interferometers.

2.1 Basic Interferometer Geometries

The most prominent example of an AIF geometry is the Mach-Zehnder Interferometer (MZI). The MZI consists of a beam-splitter pulse to create a coherent spatial superposition, followed by a mirror pulse that inverts the momentum states, and concludes with a final beam splitter that closes the interferometer. Between these pulses, the atoms propagate freely for a duration denoted as Ramsey time, T_R . A graphical depiction of the MZI within the freely falling frame is presented in Fig. 2.1a, where we introduce the pictorial conventions that will be employed throughout this thesis. The freely falling frame is defined as a reference frame that is initially aligned with the atoms before the first beam splitter and subsequently follows a geodesic, behaving as if it were a point particle. In our diagrams, we represent beam splitter and mirror pulses with red dashed lines, atom-light interactions with black dots, and Bloch oscillations with thick purple bars.

It is important to note that in these schematic illustrations, we assume the speed of light to be infinite. This assumption serves two purposes: it allows for clearer and more intuitively understandable graphical representations, and it enables faster identification of symmetry axes. Furthermore, it permits us to depict single and two-photon transitions within the same framework. Despite this illustrative simplification, phase shift contributions resulting from the Finite Speed of Light (FSL) are incorporated into our calculations. The type of atom-light interaction cannot be determined solely from the pictorial representation of the interferometer. However, the resulting phase shift is strongly dependent on the specific interaction process chosen. Therefore, simply defining an interferometer geometry, as shown in Fig. 2.1, does not suffice for accurate phase shift calculations. From this point forward, unless otherwise specified, we will assume the use of Bragg interactions for the beam splitter and mirror operations. These interactions imprint a momentum of $\pm\hbar k_R$ and a recoil frequency of ω_R . Additionally, we consider optional intermediate Bloch oscillations, which impart a momentum transfer of $\hbar k_B$.

By splitting the mirror pulse of a MZI into two consecutive beam splitter pulses and inserting Bloch oscillations between them, one creates a Symmetric Ramsey-Bordé Interferometer (SRBI), as shown in Fig. 2.1b. Maintaining the overall structure of the laser pulses but altering the direction of the induced momentum kicks results in the creation of a Symmetric Double Diffraction Interferometer (SDDI) and an Asymmetric Ramsey-Bordé Interferometer (ARBI), depicted in Figs. 2.1c and 2.1d, respectively. We always assume that the atoms are initialised in a wave packet localised at a coordinate height z_0 with a vertical velocity v_0 . The free propagation time before and after the Bloch oscillations is denoted as T_B , which we refer to as the Bloch time. We opt for a symmetrical time decomposition (T_R, T_B, T_R) to achieve compact final results, although it is straightforward to describe asymmetrical pulse sequences as well. These fundamental AIF geometries can be regarded as representatives of different AIF classes, each exhibiting distinct symmetry axes. It is important to note that Bloch oscillations are optional within these setups. The defining characteristic of an interferometer geometry lies in the arrangement of beam splitters and mirrors.

We now proceed to solve the Schrödinger equation for these fundamental AIF geometries, depicted in Fig. 2.1, assuming Bragg interactions for the beam splitter and mirror pulses. Our analysis will focus on the COM motion along the vertical direction. Henceforth, we denote the vertical coordinate – i.e., the direction pointing radially upwards in Earth’s gravitational field – as Z . For the Earth-bound interferometer geometries considered here, we assume height differences ΔZ on the order of 10 metres, as demonstrated in previous studies [82–84].

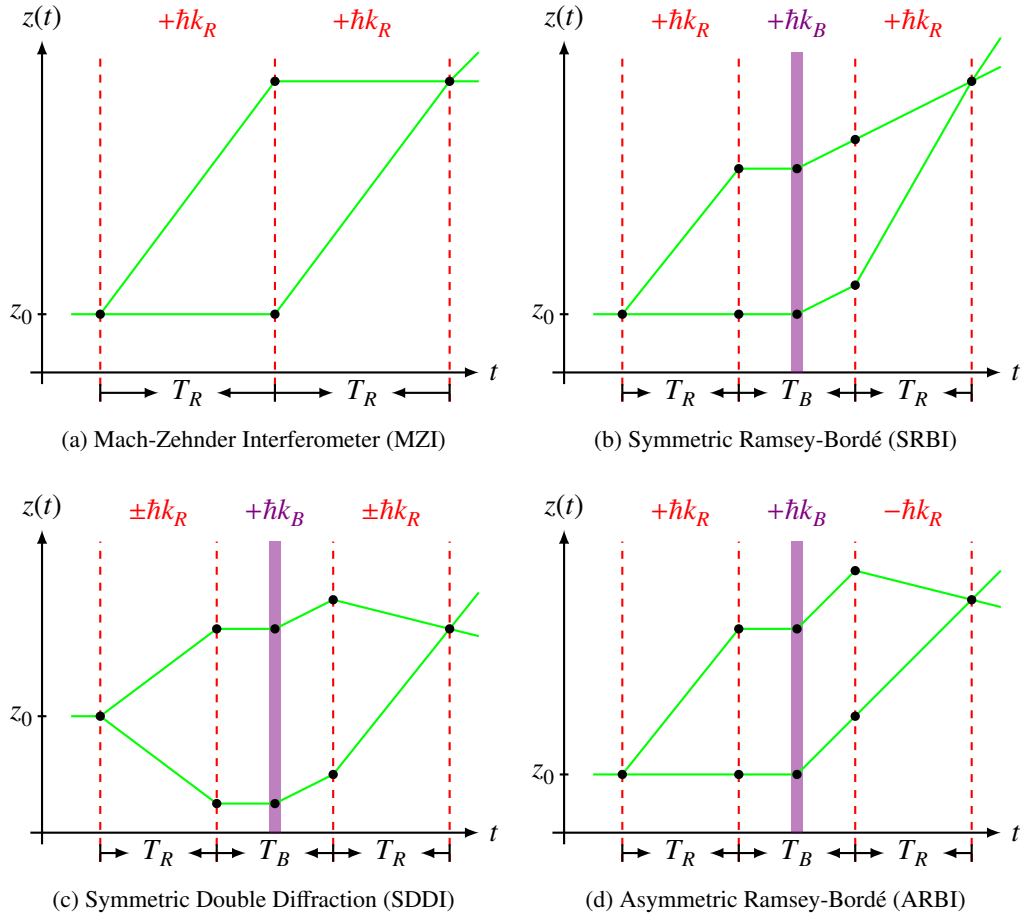


Figure 2.1: Schematic pictures of atomic trajectories (green lines) for four different AIF geometries in the freely falling frame. Interferometry laser (beam splitter/mirror) pulses are depicted in red dashed with a momentum transfer of $\pm\hbar k_R$ and Bloch oscillations in violet with a momentum transfer of $\hbar k_B$. The speed of light is set to infinity for this picture. (a) Mach-Zehnder interferometer (MZI) (b) Symmetric Ramsey-Bordé interferometer (SRBI), (c) Symmetric Double Diffraction interferometer (SDDI), (d) Antisymmetric Ramsey-Bordé interferometer (ARBI). For the case of Bragg scattering (a), (b) and (d) can be realised using single Bragg diffraction, whereas (c) relies on double Bragg diffraction.

Note that 100-metre baselines are also in construction [85, 86]. Therefore, the gravitational potential at a height Z above the ground can be expressed as

$$\phi(\mathbf{R}_\oplus + Z \mathbf{e}_z) = \phi_0 + g Z - \frac{1}{2} \Gamma Z^2 + \mathcal{O}(\partial_r^3 \phi). \quad (2.1)$$

Here, $\phi_0 \approx 60 \text{ MJ/kg}$ represents the constant offset of the gravitational potential. This value corresponds to the energy required for a test object with a mass of 1 kg to escape Earth's gravitational field, equivalent to half of the squared escape velocity for the object. The linear gravitational acceleration is $g \approx 9.81 \text{ m/s}^2$, and the gravity gradient $\Gamma \approx 2.7 \times 10^{-6} \text{ Hz}^2$. To clarify this quantity: the gravity gradient Γ describes the spatial change of g and can be defined as $\Gamma \approx 2.7 \times 10^{-7} \frac{\text{g}}{\text{m}}$, or alternatively as $\Gamma \approx 2.7 \times 10^3 \text{ E}$. Here, we use the unit *Eötvös* (E), defined as $1 \text{ E} = 10^{-9} \text{ Hz}^2$.

We choose to expand the gravitational potential $\phi(\mathbf{r})$ to second order to enable a comparison of our results with those in Refs. [87–89]. This expansion also prepares us for the

analysis of relativistic effects in Chapter 3, where we will incorporate the third order of the potential. With this expansion, the Hamiltonian for COM motion along the vertical z -axis in Eq. (1.36) becomes

$$\hat{H}_{\text{COM}} = \frac{\hat{P}^2}{2m} + mg\hat{Z} - \frac{m}{2}\Gamma\hat{Z}^2 + O(\partial_r^3\phi, c^{-2}), \quad (2.2)$$

with position and momentum operators $\hat{Z}|\psi(Z)\rangle = Z \cdot |\psi(Z)\rangle$, $\hat{P}|\psi(Z)\rangle = -i\hbar\partial_Z|\psi(Z)\rangle$.

2.1.1 Phase Shifts of Free Propagation

We begin solving the motional Schrödinger equation by calculating the accumulated phase shift that the atoms acquire between interactions with the light fields. Since we focus on the free propagation of wave packets in a well-defined internal state, and since interactions with the light field can be effectively modelled using a scattering matrix, we can neglect the internal dynamics of the atoms. Focussing on this allows us to concentrate on the external motion and the resulting phase shifts without the complexity of internal state dynamics. For convenience and readability, we will denote the trajectory of the atoms using lowercase symbols, such as $z(t)$ instead of $Z(t)$.

To solve the Schrödinger equation with the Hamiltonian from Eq. (2.2) for the COM wavefunction $|\psi(z, t)\rangle$ – as indicated in Sec. 1.2.1. – we consider wave packets that remain localised around the classical trajectories corresponding to the paths of the AIFs depicted in Fig. 2.1. It is important to evaluate these atomic paths in the lab frame, rather than the freely falling frame shown in the figure. For such localised wave packets, it is sufficient to determine the *propagation phase*, which is the relative phase accumulated along the two paths. This approach was employed in studies like those conducted by Kasevich and Chu, as well as Storey and Cohen-Tannoudji [40, 90]. The propagation phase takes the form

$$\Delta\Phi_{\text{Prop}} = \frac{1}{\hbar} \int [L(z_{\text{up}}(t), \dot{z}_{\text{up}}(t)) - L(z_{\text{low}}(t), \dot{z}_{\text{low}}(t))] dt, \quad (2.3a)$$

with the Lagrangian of Newtonian spacetime (cf. Eq. (1.26))

$$L(z, \dot{z}) = \frac{m}{2}\dot{z}^2 - mgz + \frac{m}{2}\Gamma z^2 + O(\partial_r^3\phi, c^{-2}). \quad (2.3b)$$

By focusing on the propagation phase, we can effectively describe the interference pattern resulting from the two paths of the interferometer, providing insights into the underlying physical processes and gravitational effects. In the following analysis, we will systematically expand the propagation phase with respect to small, quadratic terms in the Lagrangian. Corrections beyond the stationary phase approximation are expected to contribute only at higher orders, which are negligibly small for our purposes. We will discuss these contributions in more detail at a later stage to ensure a comprehensive understanding of their impact and relevance to the overall analysis.

To determine the classical trajectories of the upper and lower arms of the AIF, we need to solve the geodesic equation or, equivalently, the ELE corresponding to Eq. (2.3b). Instead of deriving the exact trajectories, we focus on constructing approximate solutions to the ELE, which are accurate in the leading orders of the gravity gradient Γ . This approach provides a balance between computational simplicity and the ability to capture essential physical effects, enabling us to analyse the interferometer's behaviour under typical experimental conditions while factoring in the influence of the gravity gradient. To begin, we calculate the derivatives of the Lagrangian as follows:

$$\frac{\partial L}{\partial z} = -m\partial_z\phi(z) + O(c^{-2}), \quad \frac{d}{dt} \frac{\partial L}{\partial \dot{z}} = m\ddot{z} + O(c^{-2}). \quad (2.4a)$$

The ELE then evaluates to

$$\frac{d}{dt} \frac{\partial L}{\partial \dot{z}} - \frac{\partial L}{\partial z} = 0 \iff \ddot{z}(t) = -\partial_z \phi(z(t)) + O(c^{-2}).$$

We now incorporate the approximation of the gravitational potential to the relevant order from Eq. (2.1) into the Lagrangian of Newtonian spacetime Eq. (1.26), which results in the Ordinary Differential Equation (ODE)

$$\ddot{z}(t) = -g + \Gamma z(t) + O(\partial_r^3 \phi). \quad (2.5)$$

This ODE is accompanied by two initial conditions $z(0) = z_0$ and $\dot{z}(0) = v_0 + N_R \frac{\hbar k_R}{m} + N_B \frac{\hbar k_B}{m}$, where z_0 and v_0 are the initial position and velocity of the wave packet, respectively. N_R and N_B denote the number of imprinted Bragg and Bloch momenta in the corresponding laser interaction. Solving this ODE subject to the given initial conditions will yield the approximate classical trajectories for the atoms in the interferometer's arms, incorporating the leading effects of the gravity gradient.

2.1.2 Dimensionless Parameters

Before proceeding to solve the ELE, we would like to express the major steps of the upcoming calculation in a dimensionless form, as introduced in [2]. We start by introducing a dimensionless position and time as

$$\tau = \frac{t}{T_R}, \quad \xi(\tau) = \frac{z(\tau)}{cT_R}. \quad (2.6)$$

In this context, we select $T_R \neq 0$ as the natural time scale of the AIF sequences under consideration. In doing so, we obtain dimensionless terms in the atomic trajectory $\xi(\tau)$, such as $\mathcal{Z}_0 = \frac{z_0}{cT_R}$ and $\mathcal{V}_0 = \frac{v_0}{c}$ for the two initial conditions. Additionally, we identify recoil-related dimensionless parameters $\mathcal{R}_R = \frac{\hbar k_R}{mc}$ and $\mathcal{R}_B = \frac{\hbar k_B}{mc}$ for the Bragg and Bloch momenta, respectively. Similarly, a dimensionless parameter related to the recoil frequency, $\mathcal{F}_R = \frac{\hbar \omega_R}{mc^2}$, can be defined.¹ Finally, we derive two dimensionless parameters related to the gravitational potential, namely $\mathcal{G}_{1,R} = \frac{g T_R}{c}$ and $\mathcal{G}_{2,R} = \Gamma T_R^2$, which will become evident after solving the ELE below.²

One might wonder why it is worthwhile to rewrite everything in dimensionless form. However, as we will demonstrate in Chapter 4, this formalism allows for the systematic and efficient programming of an algorithm that incorporates these parameters. The main advantage of this formalism is that each phase shift contribution possible in an atom interferometer can be expressed as a product of these dimensionless parameters and the term $\omega_C T_R$, where ω_C represents the atomic Compton frequency

$$\omega_C = \frac{mc^2}{\hbar}. \quad (2.7)$$

In typical AIF experiments, the latter term is quite large, on the order of 10^{25} for interferometer times of a second, while the other dimensionless parameters are several orders of magnitude smaller than one. For typical values in 10 m interferometers, we have compiled these parameters in Table 2.1 and illustrated their relative sizes for the cases of Bragg

¹This becomes particularly relevant in the context of the Doppler effect discussed below in Sec. 2.1.4.

²Analogously, one can also define those gravitational dimensionless parameters using the Bloch time T_B and denote them as $\mathcal{G}_{1,B}$ and $\mathcal{G}_{2,B}$.

Parameter	Definition	Magnitude for 10 m baseline AIF	
		$i = R$ (Bragg)	$i = B$ (Bloch)
\mathcal{Z}_0	$\frac{z_0}{cT_R}$	0	
\mathcal{V}_0	$\frac{v_0}{c}$	4.3×10^{-8}	
\mathcal{F}_R	$\frac{\hbar\omega_R}{mc^2}$	8.1×10^{-20}	
$\mathcal{G}_{1,i}$	$\frac{gT_i}{c}$	4.2×10^{-8}	1.3×10^{-8}
$\mathcal{G}_{2,i}$	ΓT_i^2	5.2×10^{-6}	4.9×10^{-7}
\mathcal{R}_i	$\frac{\hbar k_i}{mc}$	3.9×10^{-11}	1.2×10^{-9}

Table 2.1: Definitions of dimensionless parameters for an AIF. As a case study, we give the magnitudes for a 10 m baseline Rubidium AIF assuming the following values: $T_R = 1.3$ s, $T_B = 0.4$ s, $z_0 = 0$, $v_0 = 13$ m/s, $m = 87$ u, $\omega_R = 10^7$ Hz, $k_R = 16 \times 10^6$ m $^{-1}$, $k_B = 5 \times 10^8$ m $^{-1}$, $g = 9.81$ m/s 2 and $\Gamma = 2.7 \times 10^{-6}$ Hz $^2 = 2.7 \times 10^3$ E.

transitions and Bloch oscillations. The magnitude of each phase shift contribution is thus determined by the number of parameters listed in Table 2.1, allowing for a systematic and algebraic description using a computer algorithm.

We now continue with solving the ELE in this dimensionless form. Expressed in terms of the dimensionless variables τ and $\xi(\tau)$, and the dimensionless parameters from Table 2.1, the ELE from Eq. (2.5) becomes

$$\ddot{\xi}(\tau) = -\mathcal{G}_{1,R} + \mathcal{G}_{2,R}\xi(\tau) + \mathcal{O}(3), \quad (2.8)$$

with initial conditions $\xi(\tau_0) = \mathcal{Z}_0$, $\dot{\xi}(\tau_0) = \mathcal{V}_0 + N_R \mathcal{R}_R + N_B \mathcal{R}_B$. Here, the notation $\mathcal{O}(n)$ is used to represent terms that are of at least n -th order in the small dimensionless parameters listed in Table 2.1. Using the example of a drop tower with a height of 10 m, we demonstrate in Table 2.1 that the dimensionless parameters are small for the AIFs depicted in Fig. 2.1. We exploit this fact to consistently construct an approximate solution of the ELE. For instance, the trajectory of the path segment beginning at $\tau_0 = 0$ can be expressed, up to the fourth order in these small parameters, as

$$\xi(\tau) = \xi(0) + \dot{\xi}(0)\tau - \frac{1}{2}\mathcal{G}_{1,R}\tau^2 + \mathcal{G}_{2,R}\left(\frac{1}{2}\xi(0)\tau^2 + \frac{1}{6}\dot{\xi}(0)\tau^3 - \frac{1}{24}\mathcal{G}_{1,R}\tau^4\right) + \mathcal{O}(3). \quad (2.9)$$

We obtain an expression for the propagation phase integral in terms of dimensionless parameters as

$$\int dt \frac{L(\xi(t), \dot{\xi}(t))}{\hbar} = \int d\tau \omega_C T_R \left(\frac{\dot{\xi}(\tau)^2}{2} - \mathcal{G}_{1,R}\xi(\tau) + \frac{\mathcal{G}_{2,R}}{2}\xi(\tau)^2 \right) + \mathcal{O}(4). \quad (2.10)$$

If we denote each time instance of light-matter interactions along the paths by τ_i with $i \in \mathbb{N}$, as indicated by the black dots in Fig. 2.1, we can define $\xi(\tau)$ piecewise by a set of functions $\xi_i(\tau)$ on the time intervals $[\tau_i, \tau_{i+1}]$. Note that due to the FSL one has to actively calculate the τ_i , as shown in Fig. 2.2, for two-photon transitions. A unique solution therefore

requires the knowledge of two initial conditions for each segment of propagation. The initial conditions can be constructed iteratively for $i > 0$ via

$$\xi_i(\tau_i) = \xi_{i-1}(\tau_i), \quad \dot{\xi}_i(\tau_i) = \dot{\xi}_{i-1}(\tau_i) + N_R^{(i)}\mathcal{R}_R + N_B^{(i)}\mathcal{R}_B, \quad (2.11)$$

whereas the first two initial conditions are

$$\xi_0(\tau_0) = \mathcal{Z}_0, \quad \dot{\xi}_0(\tau_0) = \mathcal{V}_0 + N_R^{(0)}\mathcal{R}_R + N_B^{(0)}\mathcal{R}_B. \quad (2.12)$$

$N_R^{(i)}$ and $N_B^{(i)}$ represent the number of photon recoils imprinted at the time τ_i as a result of Bragg or Bloch interactions, respectively. The dot in Eq. (2.11) indicates differentiation with respect to τ . The \mathcal{Z}_0 parameter can play a significant role in differential measurements between different AIFs, such as those conducted in tests of the UFF. In these experiments, an uncertainty in the relative difference in initial height between the interferometers can lead to non-negligible phase contributions, potentially affecting the precision of the results [91].

Using this solution strategy, we calculate each of the AIF paths, specifically $\xi_{\text{up}}(\tau)$ and $\xi_{\text{low}}(\tau)$ for all AIF geometries depicted in Fig. 2.1. Once these trajectories are determined, the propagation phase in Eq. (2.3a) can be computed in dimensionless form, which is achieved by

$$\Delta\Phi_{\text{Prop}} = \int d\tau \omega_C T_R \left[\frac{L(\xi_{\text{up}}(\tau), \dot{\xi}_{\text{up}}(\tau))}{mc^2} - \frac{L(\xi_{\text{low}}(\tau), \dot{\xi}_{\text{low}}(\tau))}{mc^2} \right]. \quad (2.13)$$

The propagation phase has to be consistently expanded in terms of the small dimensionless parameters up to the desired order. If the trajectory is known to $\mathcal{O}(2)$ one can calculate the propagation phase to $\mathcal{O}(3)$, since the Lagrangian depends on the velocity to second order and on the trajectory to first order after multiplication with $\mathcal{G}_{1,R}$ and additional higher-order terms. Similarly, to evaluate the propagation phase to $\mathcal{O}(4)$, the trajectory should first be determined to $\mathcal{O}(3)$. Although the required integrals over the segments of the full AIF sequence are conceptually straightforward, they often lead to tedious and error-prone calculations. This complexity arises from managing the intricacies of higher-order expansions while ensuring accuracy in the resulting phase contributions.

Thus far, our focus has been solely on the propagation phase described in Eq. (2.13). However, when considering the effects of the gravity gradient, Γ , and the FSL on the trajectory, a complication arises: the AIF will not perfectly close at the output port without implementing specific mitigation strategies [92–95]. In this context, it is also crucial to consider the *separation phase*, typically calculated as the product of the spatial separation at the output port and the average momentum of the two atomic paths [87, 89]. Expressed directly in terms of the previously defined dimensionless trajectory, we can define the output port separation³ as $\Delta\xi = \xi_{\text{low}}(\tau_f) - \xi_{\text{up}}(\tau_f)$ and the average output velocity as $\dot{\xi}_{\text{aver.}} = \frac{1}{2}(\dot{\xi}_{\text{low}}(\tau_f) + \dot{\xi}_{\text{up}}(\tau_f))$. Consequently, the separation phase can be expressed as

$$\Delta\Phi_{\text{Sep}} = \omega_C T_R \Delta\xi \cdot \dot{\xi}_{\text{aver.}}. \quad (2.14)$$

To calculate the separation phase, the quantities $\Delta\xi$ and $\dot{\xi}_{\text{aver.}}$ must be evaluated to the desired order of precision. Trajectory separations arise from non-linear gravitational and FSL effects, which become significant at second order in the trajectory. Consequently, $\Delta\xi$ is, at minimum, a $\mathcal{O}(2)$ quantity in the absence of any mitigation strategies [92–95]. Meanwhile, $\dot{\xi}_{\text{aver.}}$ is a $\mathcal{O}(1)$ -term. Therefore, the separation phase, as a result, is at least of order $\mathcal{O}(3)$.

³Note the sign convention in this expression, as it is defined as the lower path position minus the upper path position, which might seem counter-intuitive initially.

Due to the FSL, the interaction times between the upper and lower paths of the interferometer will differ slightly, consequently affecting the integration times in the propagation phase. These FSL effects naturally occur at $O(c^{-1})$, meaning any supplementary gravitational effects would appear at $O(c^{-3})$. Additionally, FSL-related effects are highly dependent on the specific experimental setup. They are particularly influenced by factors such as the initial laser positions and the presence of additional mirrors or other optical components. As a result, these effects will be described using various assumptions about the experimental configuration. We analyse this effect in the following section.

2.1.3 Interaction Times

As previously mentioned, the timing of the atom-light interactions is more complex than what is illustrated in Fig. 2.1, being influenced by the FSL. An accurate – but, for clarity, somewhat exaggerated – representation of a MZI using two-photon transitions is displayed in Fig. 2.2. The key point is that the light field emission times, denoted as t_{E1}, t_{E2}, t_{E3} , do not coincide with the interaction times at the beam splitters $t_{BS1}, t_{B2.1}, t_{BS2.2}$ and the mirrors, t_{UM}, t_{LM} . These need to be accurately computed to correctly determine the atomic trajectory and the imprinted laser phase. It is important to note that for the laser phase, it is irrelevant whether the laser source is positioned at height z_U and reflected by a mirror on z_L , or if it is placed directly at z_L . To enhance clarity and readability, we will present the following equations in their dimensional form, which facilitates a clearer understanding of each effect.

To derive analytical expressions for the interaction times, we need to iteratively solve the atomic ELE alongside considering the light propagation dynamics. The process begins with atoms that are released at the "launch time" t_0 , starting from position z_0 with an initial velocity v_0 . At time t_{E1} , the light fields propagate along the interferometer baseline. It takes a time L/c for the light to reach the mirror at z_U and reverse its direction. To find the interaction time of the first beam splitter, t_{BS1} , one needs to solve

$$z_U + c(t_{BS1} - (t_{E1} + \Delta t_L)) + O(c^{-1}) = z_0 + v_0(t_{BS1} - t_0) - \frac{1}{2}g(t_{BS1} - t_0)^2 + O(\Gamma) \quad (2.15)$$

with the constraint $t_{BS1} > t_0, t_{E1}$. A solution to Eq. (2.15), expressed as a function of the experimentally controllable parameters t_{E1}, t_0, z_U, L and z_0 is given by

$$\begin{aligned} t_{BS1}(t_{E1}, t_0, z_U, L, z_0) = & t_{E1} + \frac{L}{c} + \frac{z_0 - z_U}{c} + \frac{v_0}{c} \left(t_{E1} + \frac{L}{c} - t_0 \right) \\ & - \frac{g}{2c} \left(t_{E1} + \frac{L}{c} - t_0 \right)^2 + O(\Gamma c^{-1}, c^{-3}). \end{aligned} \quad (2.16)$$

It is important to note that, depending on the specific sequence of launch and emission times, one must select the appropriate solution to Eq. (2.15). This equation is quadratic, resulting in two potential solutions, of which only one is physically meaningful. Selecting the correct solution ensures that the calculations accurately reflect the physical interactions occurring in the setup.

The beam splitter pulse creates a coherent superposition of the atomic wave packets, forming what we refer to as the lower and upper paths. Our current focus is on the upper path, although the same principles and processes apply analogously to the lower path. The height at which the interaction occurs is given by the expression $z_{up}(t_{BS1}) = cT_R\xi(\tau_{BS1})$, where $\tau_{BS1} = t_{BS1}/T_R$, and $\xi(\tau)$ is the dimensionless solution to the ELE from Eq. (2.9). This point acts as the initial condition for the ELE that governs the next segment of free propagation. At this instance, the velocity is altered on the upper path by the beam splitter, resulting in

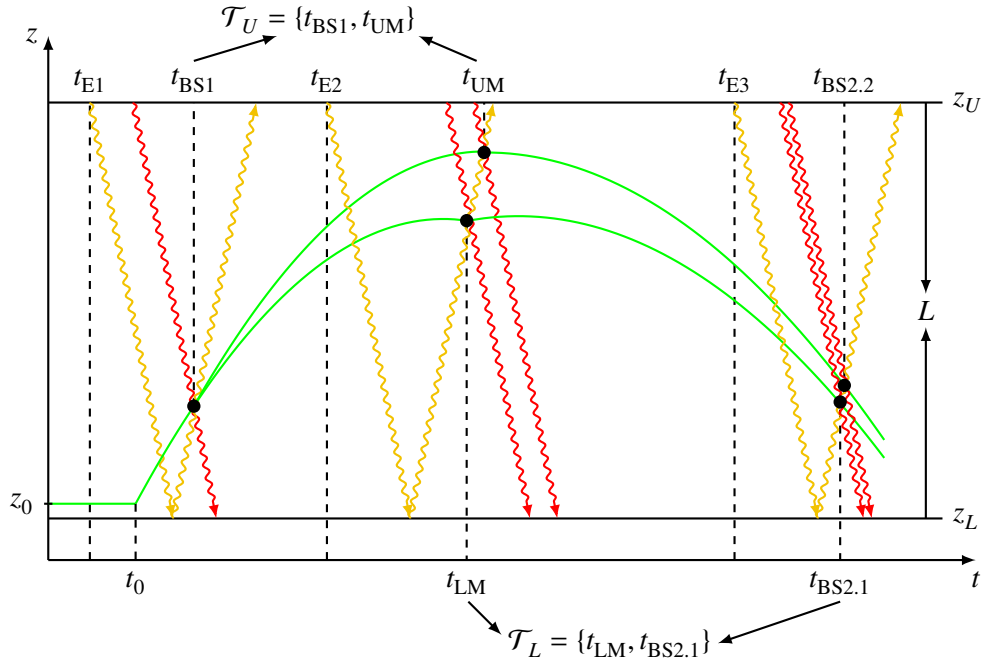


Figure 2.2: Schematic picture of how the finite light speed effects a MZI, which uses two-photon transitions (black dots). The atomic trajectory (green) interacts with two light fields (red, orange), originating by a light sourced at height z_U and retroreflected at z_L . The picture is not to scale in order to highlight the FSL effect. The atoms are launched out of a trap at a time t_0 from a height z_0 with an initial velocity v_0 . At the time t_{BS1} the atomic wave packet is split into a coherent spatial superposition. The mirror interactions happen for the upper path at t_{UM} and for the lower path at t_{LM} . Since gravitational gradients can result in a non-vanishing separation at the output port one can have two distinct time instances $t_{BS2.1}$ and $t_{BS2.2}$ for each atomic path to interact with the light fields.

a velocity change expressed as $\dot{z}_{\text{up}}(t_{BS1}) + N_R \hbar k_R / m$. This modification distinguishes the initial conditions of the ELE for both interferometer paths, enabling differentiation of the trajectories.

Analogous to Eq. (2.16), the time at which the upper mirror interaction occurs, denoted as t_{UM} , can be calculated via

$$t_{UM} = t_{E2} + \frac{L}{c} + \frac{z_{\text{up}}(t_{BS1}) - z_U}{c} + \left(\frac{\dot{z}_{\text{up}}(t_{BS1})}{c} + \frac{N_R \hbar k_R}{mc} \right) \left(t_{E2} + \frac{L}{c} - t_{BS1} \right) - \frac{g}{2c} \left(t_{E2} + \frac{L}{c} - t_{BS1} \right)^2 + O(\Gamma c^{-1}, c^{-3}) \quad (2.17)$$

By performing this procedure iteratively for each laser interaction on both the upper and lower paths, we define the set \mathcal{T}_U containing all interaction times of the upper path, and \mathcal{T}_L analogously for the lower path.⁴ In Chapter 4, we demonstrate how this iterative process can be automated using computer algebraic methods. The interaction times calculated in this way, together with the atomic initial conditions, are then utilised to determine the propagation phase, as given by Eq. (2.13), and the separation phase, according to Eq. (2.14). This

⁴We use the dimensionless form of the time instances interchangeably with the dimensional quantities, as the notation of t and τ provides sufficient clarity.

approach ensures precise and efficient computation of the phases relevant to the system's dynamics.

2.1.4 Atom-Light Interactions

As previously discussed, we are analysing Bragg interactions and Bloch oscillations in greater detail. We begin with an in-depth examination of the Bragg processes. These processes involve the coherent scattering of atoms by a light field, resulting in a change in momentum that is central to their interaction dynamics. By studying Bragg processes first, we can establish a foundation for understanding more complex phenomena such as Bloch oscillations.

Bragg Interactions

Starting from Eq. (1.57) we can express the scattering matrix for a series of N_R Bragg diffraction processes that transfer a total momentum of $N_R \hbar k_R$ as

$$U^{(\theta)}(t) = \frac{1}{\sqrt{2}} \begin{pmatrix} \cos(\theta) & i \sin(\theta) e^{iN_R \Phi_L(t)} \\ i \sin(\theta) e^{-iN_R \Phi_L(t)} & \cos(\theta) \end{pmatrix}.$$

This matrix is expressed in the basis of the momentum eigenstates $|0\hbar k_R\rangle$ and $|N_R\hbar k_R\rangle$. Here, Φ_L represents the phase imprinted during each two-photon process. This formulation captures the cumulative effect of multiple Bragg processes and the corresponding momentum transfer and phase transformation involved in these interactions. The phase of each individual light field is given by

$$\Phi_a(t) = k_a z(t) - \omega_a t \quad \text{and} \quad \Phi_b(t) = -k_b z(t) - \omega_b t \quad (2.18)$$

and is either added or subtracted to the phase of the atom, depending on whether a photon is absorbed from the corresponding field or emitted into it. The effective laser phase imprinted on the atoms in a two-photon process is then given by

$$\Phi_L(t) = \pm(\Phi_a(t) - \Phi_b(t)) = \pm(k_R z(t) - \omega_R t), \quad (2.19)$$

where we used that $k_R = k_a + k_b$ and $\omega_R = \omega_a - \omega_b$ for Bragg scattering. The sign corresponds to a net gain or loss in momentum, respectively. Before proceeding with a deeper analysis of the laser phase, it is essential to include the Doppler effect and its implications into the description. The Doppler effect, which arises from the relative motion between the light source and the atoms, can significantly influence the observed frequency and, consequently, the phase of the laser field.

Doppler effect

To transfer the momentum $\hbar k_R = \hbar(k_a + k_b) = \hbar(\omega_a + \omega_b)/c$, it is necessary to account for the (first order⁵) Doppler effect, as the light fields generally interact with moving atoms. Assuming the atoms have a velocity of v_{int} (or written dimensionless as $\xi_{\text{int}} = v_{\text{int}}/c$) when interacting with the light fields, they experience a first-order Doppler shift, as illustrated in Fig. 2.3. By transforming the interaction Hamiltonian from Eq. (1.52) into the interaction

⁵We are going to include the second order Doppler effect in Chapter 3, when we include relativistic effects.

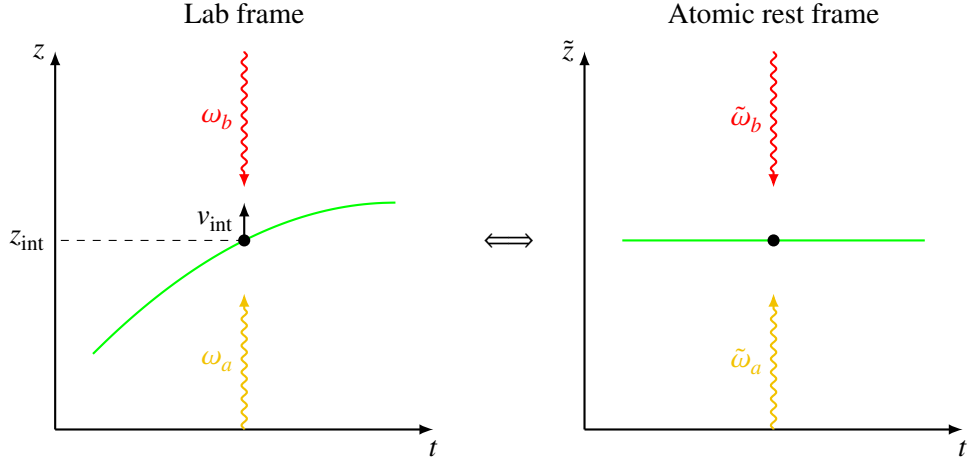


Figure 2.3: Schematic picture of how the Doppler effect is perceived by an atomic trajectory (green line) for two counter propagating light fields (red, orange). Left: Depicted in the lab frame, where the laser sources rest and the atoms move non-trivially. Right: Atomic rest frame, which is co-accelerated with the atoms are each time instance.

picture with respect to the motional Hamiltonian given in Eq. (1.36), the frequencies of the light fields become first-order Doppler shifted by

$$\tilde{\omega}_a = \left(1 - \frac{v_{\text{int}}}{c}\right) \omega_a + O\left(\dot{\xi}_{\text{int}}^2\right), \quad \tilde{\omega}_b = \left(1 + \frac{v_{\text{int}}}{c}\right) \omega_b + O\left(\dot{\xi}_{\text{int}}^2\right). \quad (2.20)$$

This means that, to transfer the momentum $\hbar k_R$, one must shift the frequency of each light field in opposite directions to compensate for the Doppler shift, i.e., one tunes each light field, prior to the interaction with a frequency chirp according to

$$\omega_a \mapsto \left(1 + \frac{v_{\text{int}}}{c}\right) \omega_a + O\left(\dot{\xi}_{\text{int}}^2\right), \quad \omega_b \mapsto \left(1 - \frac{v_{\text{int}}}{c}\right) \omega_b + O\left(\dot{\xi}_{\text{int}}^2\right). \quad (2.21)$$

Note that the imparted momentum is often altered by additional frequency chirps, e.g. for the case of gravity gradient mitigation schemes [92, 94], as we elaborate further in Sec. 2.2.3.

Even though the Doppler detuning in Eq. (2.21) ensures that the atomic trajectories align with the descriptions provided earlier, it is crucial to account for changes in the imprinted laser phase. This consideration is necessary because the Doppler effect modifies the frequency and, consequently, the phase evolution of the light interacting with the atoms. The imprinted phase, originally described by Eq. (2.19), will additionally experience a Doppler shift, resulting in an adjusted expression given by

$$\begin{aligned} \Phi_L(t) &= \pm \left(\left((1 + \dot{\xi}_{\text{int}}) k_a + (1 - \dot{\xi}_{\text{int}}) k_b \right) z(t) - \left((1 + \dot{\xi}_{\text{int}}) \omega_a - (1 - \dot{\xi}_{\text{int}}) \omega_b \right) t \right) + O\left(\dot{\xi}_{\text{int}}^2\right) \\ &= \pm \left(\left(k_a + k_b + \dot{\xi}_{\text{int}}(k_a - k_b) \right) z(t) - \left(\omega_a - \omega_b + \dot{\xi}_{\text{int}}(\omega_a + \omega_b) \right) t \right) + O\left(\dot{\xi}_{\text{int}}^2\right) \\ &= \pm \left(\left(k_R + \dot{\xi}_{\text{int}} \frac{\omega_R}{c} \right) z(t) - (\omega_R + v_{\text{int}} k_R) t \right) + O\left(\dot{\xi}_{\text{int}}^2\right). \end{aligned} \quad (2.22)$$

The recoil frequency ω_R appears in this formula due to the Doppler effect affecting each light field with opposite signs. Since this is the only part of the theoretical model, at least for two-photon Bragg transitions, where this occurs, one can infer from the phase shift's dependence on ω_R , or more precisely \mathcal{F}_R from Table 2.1, that this term originates from the first-order Doppler effect.

For later reference, we rewrite this laser phase contribution in a dimensionless form, similar to the propagation phase Eq. (2.13) and the separation phase Eq. (2.14) as

$$\Phi_L(\tau) = \pm \omega_C T_R \left((\mathcal{R}_R + \dot{\xi}_{\text{int}} \mathcal{F}_R) \xi(\tau) - (\mathcal{F}_R + \dot{\xi}_{\text{int}} \mathcal{R}_R) \tau \right) + O(4). \quad (2.23)$$

One can also choose not to actively detune the light fields, assuming that each atom-light interaction is resonant, as described in Refs. [87, 89]. In this scenario, the laser phase remains undetuned, but each interaction process imparts a momentum kick with a different effective wave vector. This changes the atomic trajectory in such a way that the resulting overall phase shift remains unchanged. If the light fields are not detuned, the imprinted laser phase would indeed change. However, this change would be exactly offset by corresponding alterations in the propagation and separation phases, effectively leaving the sum of the phase shifts unchanged. This balance ensures that the overall phase contribution to the system is consistent, regardless of whether active detuning is used to address the Doppler effect. To elaborate further, assume that the laser frequency is not detuned at all, yet the interaction process of interest still occurs resonantly. In this scenario, atoms will interact with Doppler-shifted light fields in their respective rest frames, as described by Eq. (2.20). Given that this process is assumed to be resonant, the effective momentum transferred to the atoms will be Doppler-shifted, although the laser phase will not be. This results in Doppler-shifted trajectories due to the altered imparted momentum, but not in Doppler-shifted wave vectors in the kick phase. In our formalism, the situation is reversed, ultimately leading to the same net phase. Whether one chooses to actively detune the light fields for Doppler effects in the theoretical framework is optional and varies across different descriptions in the literature.

In summary, the overall *relative* laser phase accumulated from the two-photon Bragg interactions along the upper and lower AIF paths, commonly referred to as the kick phase [96], is given by

$$\Delta\Phi_{\text{Bragg}} = \sum_{\tau_i \in \mathcal{T}_U} \Phi_L(\tau_i) - \sum_{\tau_i \in \mathcal{T}_L} \Phi_L(\tau_i), \quad (2.24)$$

with $\Phi_L(\tau)$ from Eq. (2.23). Here, the sums extend over the time instances τ_i of all Bragg pulses transferring momenta along the two paths, see Fig. 2.1.

Bloch Oscillations

For completeness, we also allow for accelerations of the atomic ensemble common to both AIF arms using Bloch oscillations. In the experiment, the atoms are initially loaded into an optical lattice which is then accelerated. After unloading the atoms they have gained an effective momentum, which we will denote by $\pm \hbar k_B$ the sign of the momentum transfer depends on whether momentum was gained in the positive or negative z-direction. We adopt here a highly simplified description by assuming that Bloch oscillations only impart the desired momentum of $\pm \hbar k_B$, that the interaction is infinitely short, i.e., negligibly short compared to the time scale of the AIF, and that the whole process is lossless. A microscopic description of the underlying physics [80, 97] and its relativistic corrections are beyond the scope of this thesis. Indeed, for the regime of large-momentum transfer [59, 60], the theoretical description of Bloch oscillations is the subject of current investigations [81]. In analogy to the case of Bragg pulses treated before, we will denote the imprinted laser phase during one Bloch interaction as $\Phi_L(t) = \pm k_B z(t)$, or written dimensionless, as $\Phi_L(\tau) = \pm \omega_C T_R \mathcal{R}_B \xi(\tau)$. Hence, the relative Bloch laser phase can be written in terms of dimensionless

quantities as

$$\Delta\Phi_{\text{Bloch}} = \omega_C T_R \mathcal{R}_B \left(\sum_{\tau_i \in \mathcal{T}_U} \xi_{\text{up}}(\tau_i) - \sum_{\tau_i \in \mathcal{T}_L} \xi_{\text{low}}(\tau_i) \right), \quad (2.25)$$

where the summation is taken over all interaction times τ_i that imprint a Bloch momentum. The overall kick phase is defined as the sum of the phases contributed by each individual process, i.e.,

$$\Delta\Phi_{\text{Kick}} = \Delta\Phi_{\text{Bragg}} + \Delta\Phi_{\text{Bloch}}. \quad (2.26)$$

2.1.5 Phase Shift Summary

We are now prepared to summarise the various phase shifts associated with the interferometer geometries illustrated in Fig. 2.1. These include the propagation phase from Eq. (2.13), the separation phase shown in Eq. (2.14), and the laser phases described by Eqs. (2.24) and (2.25), corresponding to Bragg and Bloch pulses, respectively. Presenting the results for the MZI separately is unnecessary, as its phase contributions can be inferred from the SRBI by considering the scenario in which Bloch oscillations are absent. This can be achieved by setting the parameters T_B and k_B to zero.

We devise a computer algorithm specifically designed for this task, as detailed in Chapter 4, with several objectives in mind: (i) The phase should be determined algebraically, similar to the results for the MZI presented by Dimopoulos et al. [87] and Hogan et al. [89]. (ii) The algebraic expressions should maintain accuracy to a specified order⁶ in the small parameters from Table 3.1. (iii) The phase calculation routine should be adaptable to a broad class of AIFs, including arbitrary sequences of Bragg and Bloch pulses. Table 2.2 summarises the 23 phase shift contributions of orders $\mathcal{O}(2)$ and $\mathcal{O}(3)$ for the SRBI, SDDI, and ARBI. The three $\mathcal{O}(2)$ -terms are the well known non-relativistic phases due to linear gravitational acceleration and Bragg as well as Bloch recoils, see rows #1 – #3 in Table 2.2. The 20 remaining $\mathcal{O}(3)$ terms can be categorised into two primary sources: i) Terms #4 – #11 originate from the gravity gradient, as indicated by their dependence on the parameters $\mathcal{G}_{2,R}$ or $\mathcal{G}_{2,B}$. ii) Terms #12 – #23 stem from the Doppler effect, as is evident from the dependence on \mathcal{F}_R . The only remaining phase shifts of order $\mathcal{O}(3)$ are the FSL terms, which we will analyse below. Higher-order derivatives of the gravitational potential, such as phases proportional to $\partial_z^3 \phi(z)$, naturally emerge at the $\mathcal{O}(4)$ level. These are similar to relativistic effects and will be discussed in detail in Chapter 3.

Comparing the phases across the three AIF geometries, it becomes evident that most terms are identical between the SRBI and ARBI, while they differ from the SDDI by a factor of two. This difference arises because the enclosed spacetime area in the SDDI is twice as large as that in the other two AIFs. The relationship between the enclosed spacetime area and the AIF phases has been thoroughly examined by McDonald et al. [98]. Terms like #2 and #8, however, differ quite significantly between the different AIF geometries. The first of those terms was described in Ref. [96] via a special relativistic proper time difference, whereas the latter was phrased as a "1st gradient recoil" effect in Ref. [87] and was explained in the Appendix F of Ref. [69]. We will give a more detailed description of both terms in the context of differential measurement setups in the Sec. 3.1.1 and Sec. 2.3. Phases #18 to #23, associated with the Doppler effect resulting from the transferred Bragg momentum \mathcal{R}_R , also

⁶In this chapter, this means up to order $\mathcal{O}(3)$. When we include relativistic effects in Chapter 3, the accuracy will be increased to include order $\mathcal{O}(4)$.

Phases in units of ω_C							
#	Order	Proportionality	SRBI	SDDI	ARBI	α	Origin
1	$O(2)$	$\mathcal{G}_{1,R}\mathcal{R}_R$	$T_B + T_R$	$2T_B + 2T_R$	$T_B + T_R$	2	Non-relativistic
2		\mathcal{R}_R^2	0	0	T_R	1	
3		$\mathcal{R}_R\mathcal{R}_B$	$-T_R$	$-2T_R$	$-T_R$	1	
4	$O(3)$	$\mathcal{R}_R\mathcal{Z}_0\mathcal{G}_{2,R}$	$-T_B - T_R$	$-2T_B - 2T_R$	$-T_B - T_R$	2	Gravity gradient
5		$\mathcal{R}_R\mathcal{V}_0\mathcal{G}_{2,R}$	$-\frac{3}{2}T_B - T_R$	$-3T_B - 2T_R$	$-\frac{3}{2}T_B - T_R$	3	
6		$\mathcal{R}_R\mathcal{R}_B\mathcal{G}_{2,R}$	$-\frac{1}{4}T_B - \frac{1}{6}T_R$	$-\frac{1}{2}T_B - \frac{1}{3}T_R$	$-\frac{1}{4}T_B - \frac{1}{6}T_R$	4	
7		$\mathcal{R}_R\mathcal{G}_{1,R}\mathcal{G}_{2,R}$	$\frac{7}{6}T_B + \frac{7}{12}T_R$	$\frac{7}{3}T_B + \frac{7}{6}T_R$	$\frac{7}{6}T_B + \frac{7}{12}T_R$	4	
8		$\mathcal{R}_R^2\mathcal{G}_{2,R}$	$-\frac{1}{2}T_B - \frac{1}{2}T_R$	0	$-\frac{1}{2}T_B - \frac{1}{3}T_R$	3	
9		$\mathcal{R}_R\mathcal{V}_0\mathcal{G}_{2,B}$	$-\frac{1}{2}T_R$	$-T_R$	$-\frac{1}{2}T_R$	3	
10		$\mathcal{R}_R\mathcal{R}_B\mathcal{G}_{2,B}$	$-\frac{1}{8}T_R$	$-\frac{1}{4}T_R$	$-\frac{1}{8}T_R$	3	
11		$\mathcal{R}_R\mathcal{G}_{1,R}\mathcal{G}_{2,B}$	$\frac{1}{6}T_B + \frac{3}{4}T_R$	$\frac{1}{3}T_B + \frac{3}{2}T_R$	$\frac{1}{6}T_B + \frac{3}{4}T_R$	4	
12		$\mathcal{F}_R\mathcal{G}_{1,R}^2$	$-\frac{9}{2}T_B - 3T_R$	$-9T_B - 6T_R$	$-\frac{9}{2}T_B - 3T_R$	3	Doppler effect
13		$\mathcal{F}_R\mathcal{G}_{1,R}\mathcal{V}_0$	$3T_B + 3T_R$	$6T_B + 6T_R$	$3T_B + 3T_R$	2	
14		$\mathcal{F}_R\mathcal{G}_{1,R}\mathcal{G}_{1,B}$	$-\frac{3}{2}T_B$	$-3T_B$	$-\frac{3}{2}T_B$	3	
15		$\mathcal{F}_R\mathcal{R}_B\mathcal{G}_{1,R}$	$\frac{5}{2}T_B + \frac{7}{2}T_R$	$5T_B + 7T_R$	$\frac{5}{2}T_B + \frac{7}{2}T_R$	2	
16		$\mathcal{F}_R\mathcal{R}_B^2$	$-T_R$	$-2T_R$	$-T_R$	1	
17		$\mathcal{F}_R\mathcal{R}_B\mathcal{V}_0$	$-2T_R$	$-4T_R$	$-2T_R$	1	
18		$\mathcal{F}_R\mathcal{R}_R^2$	0	$2T_R$	T_R	1	
19		$\mathcal{F}_R\mathcal{R}_R\mathcal{G}_{1,B}$	$\frac{1}{2}T_B$	0	$-\frac{1}{2}T_B$	2	
20		$\mathcal{F}_R\mathcal{R}_R\mathcal{G}_{1,R}$	$3T_B - \frac{5}{2}T_R$	0	$-3T_B + \frac{9}{2}T_R$	2	
21		$\mathcal{F}_R\mathcal{R}_R\mathcal{R}_B$	$-\frac{1}{2}T_B + 2T_R$	0	$\frac{1}{2}T_B - 2T_R$	1	
22		$\mathcal{F}_R\mathcal{R}_R\mathcal{V}_0$	$-T_B - T_R$	0	$T_B + 5T_R$	1	
23		$\mathcal{F}_R\mathcal{R}_R\mathcal{Z}_0$	0	0	$2T_R$	1	

Table 2.2: List of phases of the SRBI, SDDI, ARBI geometries written in terms of dimensionless parameters of order $O(2)$ (# 1 – # 3) and $O(3)$ (# 4 – # 23), excluding FSL terms. To extract this phase for one of the AIF geometries, one has to multiply the factor in the column "proportionality" by the time given in the column of the respective AIF and the atomic Compton frequency ω_C in Eq. (2.7). For example, phase shift # 1 for the SRBI $\mathcal{R}_R\mathcal{G}_{1,R}\omega_C(T_R + T_B)$ which translates into $gk_R(T_R^2 + T_R T_B)$, see Table 2.1. Written out in terms of dimensionful quantities, each contribution is a polynomial in T_R and T_B , i.e., is proportional to $T_R^{\alpha_R} T_B^{\alpha_B}$. The overall exponent $\alpha = \alpha_R + \alpha_B$ determines the scaling of each phase with AIF time.

Parameter	Definition	Magnitude for 10 m baseline AIF
\mathcal{Z}_L	$\frac{z_L}{cT_R}$	2.6×10^{-9}
\mathcal{Z}_U	$\frac{z_U}{cT_R}$	2.8×10^{-8}
\mathcal{H}	$\frac{z_U - z_L}{cT_R}$	3.1×10^{-8}

Table 2.3: Definitions of additional dimensionless parameters connected to the FSL effect. The magnitude is calculated using the following numerical values: $T_R = 1.3$ s, $z_L = -1$ m and $z_U = 11$ m. Note that only two of those parameters are linearly independent.

exhibit non-trivial differences among the AIF geometries. In particular, the phases that are linear in \mathcal{R}_R cancel out in the SDDI due to its inherent symmetry; nevertheless, they remain non-zero in the ARBI and SRBI.

To analyse the FSL phases, we need to introduce a few additional dimensionless parameters related to the heights of the light sources. These parameters are detailed in Table 2.3. With these additional parameters defined, the FSL phases of orders $\mathcal{O}(2)$ and $\mathcal{O}(3)$ can be calculated. These phases are summarised in Table 2.4, based on the specific experimental setup illustrated in Fig. 2.2, where Bloch oscillations are disregarded. To extract phase shifts, that solely arise from the FSL effect, we compare the output of our first computer algorithm [1] with the latter one [3], where this effect was included. Similar to the case of the Doppler effect, one can see how phases resulting from the FSL effect sometimes scale linear with the enclosed spacetime area (terms # 24, 29, 30 – 34, 36, 37), whereas other terms change non-trivially between the interferometer geometries. It is important to note that, unlike previous cases, there are now phase shift contributions with $\alpha = 0$, meaning they remain constant in time. These constant terms are in contrast to other phase shifts that typically depend on the interferometer’s temporal parameters and highlight specific effects intrinsic to the experimental setup. Furthermore, phases # 40 – # 44 arise from the FSL effect, as well as from the Doppler effect, which can lead to ambiguities in naming those terms.

In Fig. 2.4, we plot the phase shifts of $\mathcal{O}(2)$ and the leading contributions of $\mathcal{O}(3)$ evaluated for a 10 m baseline AIF. The resulting list of phase shifts can be grouped into two: Figs. 2.4 (a), (c), (e) show phases that are maximal for $T_B = 0$ and therefore would preferably be analysed in an AIF without Bloch pulses (vanishing Bloch time T_B). Figs. 2.4 (b), (d), (f) display phases that are functions of the Bloch recoil and therefore are maximal for a non-trivial combination of T_R and T_B , since the corresponding phase shift will vanish in both limiting cases, i.e., $T_B = 0$ and $T_R = 0$. It can be observed that the curves of $\mathcal{O}(2)$ and $\mathcal{O}(3)$, respectively, cluster with a gap of several orders of magnitude between them.

2.2 Advanced Description of Interferometers

After considering a theoretical model for the phase shift calculation in basic interferometers, we can now compare it to alternative approaches described in the literature, as we do in Sec. 2.2.1 and Sec. 2.2.2. We then proceed to explore more advanced topics. These include the mitigation of unwanted gravity gradient effects, discussed in Sec. 2.2.3, and the effects of rotating reference frames, with a particular focus on the Coriolis effect, in Sec. 2.2.4.

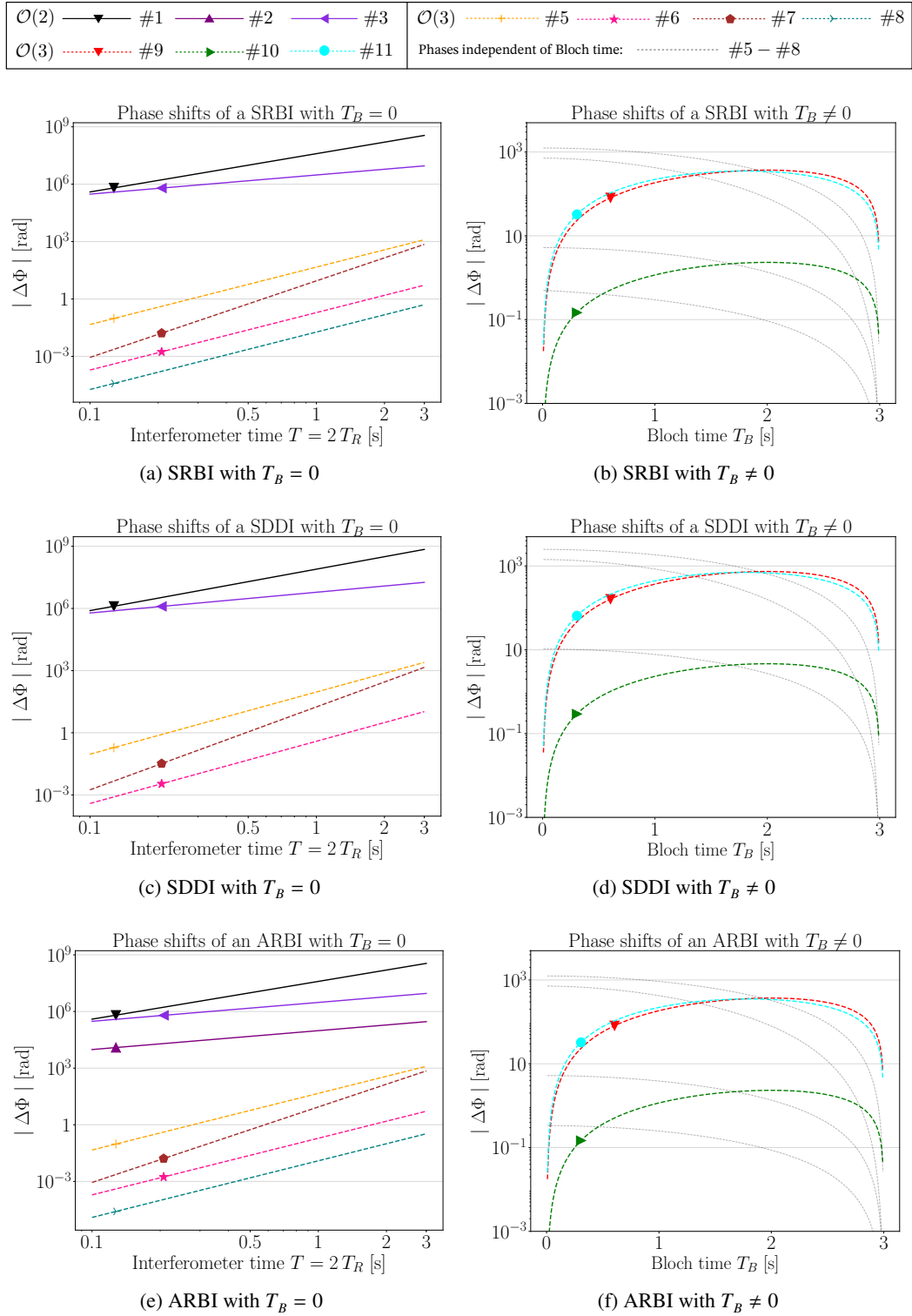


Figure 2.4: Phase shift contributions in the three AIF geometries SRBI, SDDI, ARBI for a 10 m baseline. Solid curves correspond to phase shifts of order $\mathcal{O}(2)$ and dashed curves to $\mathcal{O}(3)$. (a) (c), (e): The Bloch time T_B is set to zero and all non-zero phase shift contributions above $1 \mu\text{rad}$ are plotted w.r.t. time $T = 2T_R$. (b), (d), (f): Coloured phase shift contributions depend non-trivially on T_B and are plotted against T_B for fixed time $T = 2T_R + T_B$ of 3 seconds; the grey curves correspond to the Bloch-time independent phase contributions from (a), (c), (e). Assumed numerical values can be found in Table 2.1.

FSL phases in units of ω_C – without Bloch oscillations							
#	Order	Proportionality	SRBI	SDDI	ARBI	α	Comment
24	$O(2)$	$\mathcal{F}_R \mathcal{G}_{1,R}$	T_R	$2T_R$	T_R	2	
25		$\mathcal{F}_R \mathcal{R}_R$	0	0	$2T_R$	1	
26	$O(3)$	$\mathcal{H} \mathcal{R}_R^2$	$-\frac{1}{2}T_R$	0	$\frac{1}{2}T_R$	0	
27		$\mathcal{Z}_0 \mathcal{R}_R^2$	$-\frac{1}{2}T_R$	0	$\frac{7}{2}T_R$	0	
28		$\mathcal{Z}_L \mathcal{R}_R^2$	$\frac{1}{2}T_R$	0	$-\frac{1}{2}T_R$	0	
29		$\mathcal{H} \mathcal{R}_R \mathcal{G}_{1,R}$	$2T_R$	$2T_R$	$2T_R$	1	
30		$\mathcal{G}_{1,R} \mathcal{R}_R \mathcal{Z}_0$	$2T_R$	$4T_R$	$2T_R$	1	
31		$\mathcal{G}_{1,R} \mathcal{R}_R \mathcal{Z}_L$	$-2T_R$	$-4T_R$	$-2T_R$	1	
32		$\mathcal{H} \mathcal{R}_R \mathcal{V}_0$	$-T_R$	$-2T_R$	$-T_R$	0	
33		$\mathcal{R}_R \mathcal{Z}_0 \mathcal{V}_0$	$-T_R$	$-2T_R$	$-T_R$	0	
34		$\mathcal{R}_R \mathcal{Z}_L \mathcal{V}_0$	T_R	$2T_R$	T_R	0	
35		$\mathcal{R}_R \mathcal{G}_{1,R}^2$	$-6T_R$	$-12T_R$	$-6T_R$	3	
36		$\mathcal{R}_R \mathcal{G}_{1,R} \mathcal{V}_0$	$6T_R$	$12T_R$	$6T_R$	2	
37		\mathcal{R}_R^3	0	$4T_R$	$2T_R$	1	
38		$\mathcal{R}_R^2 \mathcal{G}_{1,R}$	$4T_R$	0	$-8T_R$	2	
39		$\mathcal{R}_R^2 \mathcal{V}_0$	$-T_R$	0	$9T_R$	1	
40		$\mathcal{F}_R \mathcal{G}_{1,R}^2$	$2T_R$	$6T_R$	$5T_R$	3	Adds to # 12.
41		$\mathcal{F}_R \mathcal{R}_R^2$	0	$2T_R$	T_R	1	Adds to # 18.
42		$\mathcal{F}_R \mathcal{R}_R \mathcal{G}_{1,R}$	$7T_R$	0	$-\frac{27}{2}T_R$	2	Adds to # 20.
43		$\mathcal{F}_R \mathcal{R}_R \mathcal{V}_0$	0	0	$5T_R$	1	Adds to # 22.

Table 2.4: List of FSL phases of the SRBI, SDDI, ARBI geometries written in terms of dimensionless parameters. Here, we set $T_B = 0$, since the FSL-effect won't affect the Bloch oscillations in our idealised treatment of this process. α denotes again the exponent of the overall time scaling of each phase.

2.2.1 Comparison to Hamiltonian Approach

An alternative theoretical framework for calculating phase shifts in AIFs is provided in Ref. [99]. This approach is rooted in a Hamiltonian description utilising perturbation theory. In Ref. [99] an AIF was modelled using a Hamiltonian

$$\hat{H} = \hat{H}_0 + \hat{V}(t), \quad (2.27)$$

where \hat{H}_0 represents the dominant Hamiltonian, comprised of the kinetic energy, linear gravitational acceleration, and electromagnetic field interactions, while $\hat{V}(t)$ denotes a perturbation

potential, such as one that might arise from the gravitational gradient, Γ .⁷ The key takeaway is that both the laser phase and the propagation phase of the AIF can be calculated using the *unperturbed* atomic paths. Specifically, for the propagation phase, this implies that the action functional corresponding to the full Hamiltonian \hat{H} must be evaluated along the atomic paths that are classically determined by the dynamics of \hat{H}_0 . This approach might appear to contrast with Eq. (2.13), where the propagation integral is calculated – encompassing what Utrecht et al. would describe as a perturbation – and the functional is evaluated along the *perturbed* atomic paths.

To further analyse this, we must express the perturbative approach in the Lagrangian framework introduced earlier. Consider a Lagrangian $L = L_0 + \varepsilon L_1$, where L_0 represents the dominant contribution and εL_1 is the perturbation term, with $\varepsilon \ll 1$. We denote the solution of the ELE for the complete Lagrangian L over the time interval $[t_a, t_b]$ as $x(t)$ and the solution from L_0 as $x_0(t)$. Without loss of generality, we can express $x(t) = x_0(t) + \varepsilon x_1(t)$, where $x_1(t_a) = 0$. However, we have that $x_1(t_b) \neq 0$, since the perturbation non-trivially influences the atomic motion. In the specific case where the perturbation is the gravitational gradient,⁸ i.e., $\varepsilon = \Gamma$, these quantities become

$$L_0 = \frac{m}{2} \dot{x}(t)^2 - mgx(t), \quad \varepsilon L_1 = \frac{m}{2} \Gamma x(t)^2 \quad (2.28a)$$

$$x_0(t) = x(0) + \dot{x}(0)t - \frac{1}{2}gt^2, \quad \varepsilon x_1(t) = \Gamma \left(\frac{1}{2}x(0)t^2 + \frac{1}{6}\dot{x}(0)t^3 - \frac{1}{24}gt^4 \right). \quad (2.28b)$$

The action functional corresponding to this Lagrangian then splits into two contributions: one from the dominant part of the Lagrangian, S_0 , and another from the perturbative part, S_ε , i.e.,

$$\begin{aligned} S(t_a, t_b) &= \int_{t_a}^{t_b} dt L(x(t), \dot{x}(t)) = \int_{t_a}^{t_b} dt L_0(x(t), \dot{x}(t)) + \varepsilon \int_{t_a}^{t_b} dt L_1(x(t), \dot{x}(t)) \\ &= \int_{t_a}^{t_b} dt L_0(x(t), \dot{x}(t)) + \varepsilon \int_{t_a}^{t_b} dt L_1(x_0(t), \dot{x}_0(t)) + \mathcal{O}(\varepsilon^2) \\ &= S_0(t_a, t_b) + S_\varepsilon(t_a, t_b) + \mathcal{O}(\varepsilon^2). \end{aligned} \quad (2.29)$$

Further analysis of the first action functional, S_0 , reveals

$$\begin{aligned} S_0(t_a, t_b) &= \int_{t_a}^{t_b} dt L_0(x(t), \dot{x}(t)) = \int_{t_a}^{t_b} dt L_0(x_0(t) + \varepsilon x_1(t), \dot{x}_0(t) + \varepsilon \dot{x}_1(t)) \\ &= \int_{t_a}^{t_b} dt \left(L_0(x_0(t), \dot{x}_0(t)) + \frac{\partial L_0(x_0(t), \dot{x}_0(t))}{\partial x_0} \varepsilon x_1(t) + \frac{\partial L_0(x_0(t), \dot{x}_0(t))}{\partial \dot{x}_0} \varepsilon \dot{x}_1(t) \right). \end{aligned} \quad (2.30)$$

⁷In [99], the perturbation potential $\hat{V}(t)$ is considered to potentially be branch-dependent, meaning that it can have different effects on the upper and lower atomic paths.

⁸To be precise: One should set $\varepsilon = \mathcal{G}_{2,R}$, because a perturbation variable should be dimensionless.

	Pert. trajectory	Unpert. trajectory	Pert. trajectory	Unpert. trajectory
	$\mathcal{R}_R \mathcal{G}_{1,R} \mathcal{G}_{2,R}$		$\mathcal{R}_R \mathcal{Z}_0 \mathcal{G}_{2,R}$	
$\Delta\Phi_{\text{Prop}}$	-2	$-\frac{7}{12}$	0	1
$\Delta\Phi_{\text{Sep}}$	2	0	0	0
$\Delta\Phi_{\text{Kick}}$	$-\frac{7}{12}$	0	1	0
	$\mathcal{R}_R \mathcal{V}_0 \mathcal{G}_{2,R}$		$\mathcal{R}_R^2 \mathcal{G}_{2,R}$	
$\Delta\Phi_{\text{Prop}}$	1	1	$\frac{1}{2}$	$\frac{1}{2}$
$\Delta\Phi_{\text{Sep}}$	-1	0	0	0
$\Delta\Phi_{\text{Kick}}$	1	0	0	0

Table 2.5: Comparison of phase shifts contributions using the elaborated procedure with perturbed atomic trajectories and the description presented by Ufrecht et al., which uses the unperturbed atomic trajectories. FSL phases are omitted, as they also not included in [99]. One can see how the sum of propagation, separation and kick phases are the same in each description, which was also expected, since the stationary phase approximation is exact for quadratic potentials, such as the gravitational gradient.

We now perform partial integration on the latter two terms to obtain

$$S_0(t_a, t_b) = L_0(x_0(t), \dot{x}_0(t)) \quad (2.31a)$$

$$+ \varepsilon \int_{t_a}^{t_b} dt x_1(t) \left(\frac{\partial L_0(x_0(t), \dot{x}_0(t))}{\partial x_0} - \frac{d}{dt} \frac{\partial L_0(x_0(t), \dot{x}_0(t))}{\partial \dot{x}_0} \right) \quad (2.31b)$$

$$+ \varepsilon \left[\frac{\partial L_0(x_0(t), \dot{x}_0(t))}{\partial x_0} x_1(t) \right]_{t_a}^{t_b}, \quad (2.31c)$$

where the contribution from Eq. (2.31b) vanishes, since $x_0(t)$ is a solution of the ELE of L_0 . The last part, namely the boundary terms, can be rewritten as

$$\begin{aligned} \varepsilon \left[\frac{\partial L_0(x_0(t), \dot{x}_0(t))}{\partial x_0} x_1(t) \right]_{t_a}^{t_b} &= \varepsilon \frac{\partial L_0(x_0(t_b), \dot{x}_0(t_b))}{\partial x_0} x_1(t_b) - \varepsilon \frac{\partial L_0(x_0(t_a), \dot{x}_0(t_a))}{\partial x_0} x_1(t_a) \\ &= \varepsilon m \dot{x}_0(t_b) x_1(t_b), \end{aligned} \quad (2.32)$$

where the last term vanishes, since $x_1(t_a) = 0$. These boundary terms include a non-vanishing contribution from $x_1(t_b)$, which contrasts with the approach in Ref. [99].

It is evident that only phase shifts that involve the perturbation ε are influenced by the two different descriptions. In the case of the MZI, there are four such phase shift terms: these are the products of $\mathcal{R}_R \mathcal{G}_{2,R}$ with $\mathcal{G}_{1,R}$, \mathcal{Z}_0 , \mathcal{V}_0 , and \mathcal{R}_R . A comprehensive comparison of these terms, as calculated using the two different methods, is provided in Table 2.5. The table shows that the final result remains unchanged, irrespective of the theoretical framework employed,

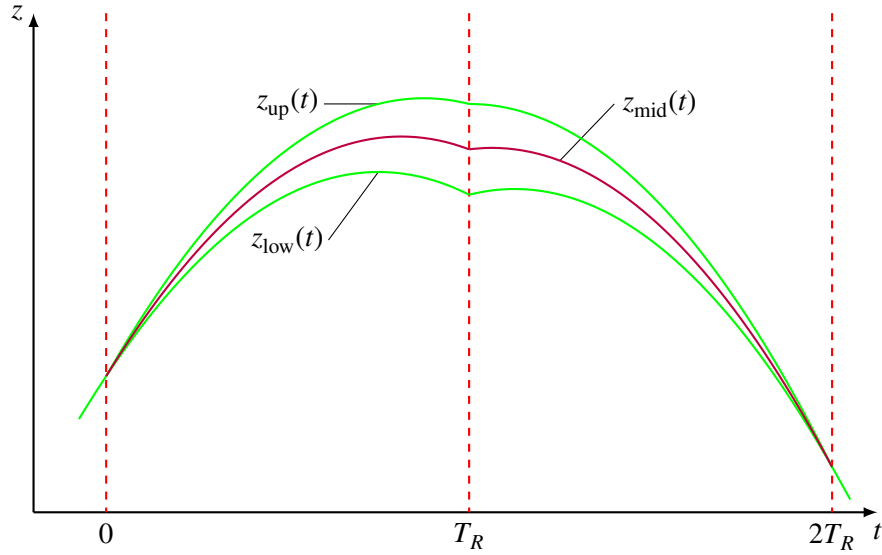


Figure 2.5: Upper and lower atomic trajectories of a MZI $z_{\text{up}}(t)$, $z_{\text{low}}(t)$ (green) in the lab frame and unpopulated midpoint trajectory $z_{\text{mid}}(t)$ (purple), which is used in the midpoint theorem.

which is anticipated in the case of a constant gravity gradient where the stationary phase approximation is exact. However, differences between the two descriptions are expected to emerge when dealing with cubic and higher-order perturbation potentials. Even though the stationary phase approximation loses its exact validity in this case, we do not see why this description should lose its accuracy. The Hamiltonian approach also encounters the problem that the interferometer will not close, necessitating the application of a non-trivial shift operator to maintain the formalism. Determining which description proves correct will be an intriguing question to explore. Testing this idealised model will, however, be complicated, as other effects are likely to arise at such high levels of accuracy [100]. The leading order differences will be explored in the comparison to Dimopoulos et al. [88] in Sec. 3.7.

2.2.2 Comparison to Bordé’s Midpoint Theorem

Another theoretical framework for phase shift calculations is provided by Bordé’s midpoint theorem [101]. This approach approximates the phase shift of an AIF by considering the (unpopulated) midpoint trajectory

$$z_{\text{mid}}(t) = \frac{1}{2}(z_{\text{up}}(t) + z_{\text{low}}(t)). \quad (2.33)$$

This method offers a distinct perspective by focusing on the central path of the interferometer system, potentially simplifying the evaluation of phase shifts under certain conditions. A schematic depiction of such a midpoint trajectory can be found in Fig. 2.5. This approach has been validated for second-order gravitational potentials, such as constant gravitational gradients, as demonstrated in Ref. [102]. Bordé’s midpoint theorem has the advantage of being easily applicable. However, it lacks the ability to straightforwardly incorporate imperfections and more complex gravitational treatments, as the midpoint trajectory lacks a direct physical interpretation. Therefore, we prefer the Lagrangian approach, particularly for novel gravitational backgrounds that have not been previously analysed, as it provides a more flexible and comprehensive framework for such investigations.

The midpoint theorem can be stated as follows: The phase shift of an interferometer, $\Delta\Phi = \Delta\Phi_{\text{Prop}} + \Delta\Phi_{\text{Kick}} + \Delta\Phi_{\text{Sep}}$, is approximately given by

$$\Delta\Phi \approx \Delta\Phi_{\text{MP}} = \sum_{t_i \in \mathcal{T}_U} [k_{\text{eff}} z_{\text{mid}}(t_i) - \omega_{\text{eff}} t_i] - \sum_{t_i \in \mathcal{T}_L} [k_{\text{eff}} z_{\text{mid}}(t_i) - \omega_{\text{eff}} t_i]. \quad (2.34)$$

In this formulation, the sums extend over the instances of atom-light interactions, allowing the phase shift to be perceived as a Kick phase calculation along the hypothetical midpoint trajectory. This approach simplifies the phase shift evaluation by focusing on a central, though hypothetical, path that theoretically experiences all relevant phase contributions. For the case of an MZI based on Bragg transitions, and under the assumption of infinite light speed, this expression can be rewritten as

$$\Delta\Phi_{\text{MP}} = k_R z_{\text{mid}}(0) - 2k_R z_{\text{mid}}(T_R) + k_R z_{\text{mid}}(2T_R). \quad (2.35)$$

This theorem is an approximation and is sufficient when both arms of the interferometer experience similar external forces. Consider a scenario where one of the interferometer arms comes into close proximity to an external potential, which is spatially localised on the scale of the separation between the interferometer arms, as demonstrated in Ref. [103] with a lead block. To first order, the lead block will predominantly affect one of the interferometer arms, with atoms moving in its gravitational potential, thus imprinting a non-trivial propagation phase. Despite this, the atomic trajectory along the affected path will remain nearly unchanged because the gravitational acceleration affecting the atoms is much smaller compared to the potential's effect, as noted in Ref. [102].⁹ Note that FSL effects are only averaged in Eq. (2.34), which is itself an approximation. This is because the actual photon paths can become quite complex in long-baseline interferometers, especially when multiple atomic sources and differential measurements are involved. Consequently, the midpoint theorem may not fully capture the intricate effects that arise from these complications.

2.2.3 Gravity Gradient Mitigation Schemes

The presence of a gravitational gradient, indicated by $\Gamma \neq 0$, introduces phase shifts to an AIF that are dependent on the initial conditions z_0 and v_0 , as shown in Table 2.2, particularly in terms #4 and #5. Due to thermal fluctuations and suboptimal initialisation, these parameters can carry significant measurement uncertainty, which contributes to the overall estimation uncertainty of the desired signal. Another consequence is a loss of contrast, as the atoms' wavefunctions no longer overlap perfectly at the output port, resulting from the differing local accelerations experienced on the upper and lower paths of the interferometer.

For the example of an MZI and the light-field configuration shown in Fig. 2.2, the separation at the output port can be calculated as

$$z_{\text{up}}(t_{\text{BS2.2}}) - z_{\text{low}}(t_{\text{BS2.1}}) = \Delta z_{\Gamma} + \Delta z_{\text{Dop}} + \mathcal{O}(3). \quad (2.36a)$$

The first contribution is due to the gravity gradient

$$\Delta z_{\Gamma} = \frac{N_R \hbar k_R \Gamma T_R^3}{m}, \quad (2.36b)$$

⁹This is primarily due to the fact that the atomic trajectory is largely governed by Newton's law, $\ddot{z} = -\nabla\phi(z)$. Consequently, any change in gravitational acceleration is only manifested in the atomic trajectory through the derivative of the additional gravitational potential. Alternatively, larger signals can be obtained by positioning an atom for an extended period of time (several seconds) near this gravitational perturbation potential, which allows for the accumulation of a significantly larger phase shift.

and the latter term contains contributions related to the Doppler effect

$$\Delta z_{\text{Dop}} = \frac{N_R^2 \hbar^2 k_R \omega_R}{m^2 c^2} T_R - 2 \frac{N_R \hbar \omega_R g T_R^2}{mc^2}. \quad (2.36c)$$

Assuming the numerical values from Table 2.1, we find that $|\Delta z_{\Gamma}| \approx 4.3 \text{ nm} \cdot N_R$ and $\Delta z_{\text{Dop}} \approx 7.7 \times 10^{-23} \text{ m} \cdot N_R^2 - 2.7 \times 10^{-18} \text{ m} \cdot N_R$. Due to the relatively high magnitude of Δz_{Γ} , it is often necessary to mitigate this separation in modern AIF experiments. Techniques for addressing this issue are described in [92–94, 104].

The main idea involves applying a frequency chirp to one or more of the interferometry lasers. This technique alters the momentum imparted to the atoms, enabling them to recombine perfectly at the output port. By carefully tuning the frequency of the laser chirps, the differential phase shifts caused by gravitational gradients can be effectively compensated, ensuring that the atomic wavefunctions overlap as intended. This approach helps maintain the contrast and accuracy in the measurements of modern AIF experiments. In theory, this can be achieved by altering the mirror pulse in a conventional three-pulse interferometer by

$$k_R \mapsto k_R + \Delta k_R \quad \text{with} \quad \Delta k_R = \frac{\mathcal{G}_{2,R}}{2} k_R \quad (2.37)$$

to cancel $\Delta z_{\Gamma} = 0$, thereby achieving high contrast. In a nutshell, it is not essential to know the exact frequency chirp *a priori*. Instead, one can scan through different frequencies experimentally, measuring the resulting contrast at each setting. By identifying the frequency chirp that produces the highest contrast, the interferometer can be optimised to operate effectively, compensating for the gravitational gradient effect without requiring precise pre-calculations of the ideal chirp settings.

2.2.4 Rotating Reference Frames – Coriolis and Centrifugal Forces

In the next section, we will incorporate rotating reference frames into our analysis and examine the potential challenges that may arise. We will use Earth's rotation as our primary example, disregarding any additional rotations to avoid added complexity. Defining rotation itself necessitates establishing what it means to be at rest, which we do in relation to the fixed star background. We align Earth's rotation axis with the North-South axis. In this context, we represent a vector in the co-rotating frame of reference on Earth's surface, denoted as Σ , using $\mathbf{r}(t)$. Similarly, we denote a vector in the fixed rotating frame of the AIF experiment on Earth's surface, denoted as Σ' , by $\mathbf{r}'(t)$. The setup is depicted in Fig. 2.6(a).

The transformation law between the two frames of reference is given by

$$\mathbf{r}'(t) \mapsto \mathbf{r}(t) = R_z(-\omega_{\oplus} t) \mathbf{r}'(t) \quad \dot{\mathbf{r}}'(t) \mapsto \dot{\mathbf{r}}(t) = \dot{\mathbf{r}}'(t) + \omega_{\oplus} \times \mathbf{r}'(t), \quad (2.38)$$

where $\omega_{\oplus} = (0, 0, \omega_{\oplus})^T$ represents the angular velocity vector of Earth's rotation, and R_z is the rotation matrix about the North-South axis. Applying this transformation results in a Lagrangian expressed in the rotating frame as

$$L(\mathbf{r}, \dot{\mathbf{r}}) = \frac{m}{2} \dot{\mathbf{r}}^2 + \underbrace{m \dot{\mathbf{r}} \cdot (\omega_{\oplus} \times \mathbf{r})}_{\text{Coriolis}} + \underbrace{\frac{m}{2} (\omega_{\oplus} \times \mathbf{r})^2}_{\text{Centrifugal}} - m\phi(\mathbf{r}), \quad (2.39)$$

where the ω_{\oplus}^2 -dependent centrifugal term is frequently omitted for simplicity [40]. Since we assumed constant rotations, i.e., $\dot{\omega}_{\oplus} = 0$, the Euler force does not appear; this force would be

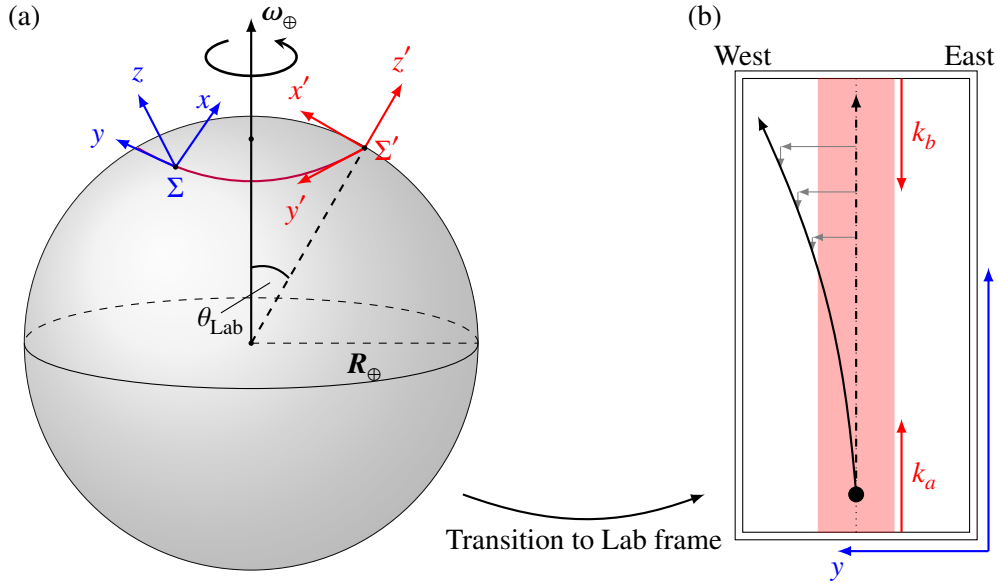


Figure 2.6: (a) Illustration of a reference frame, Σ (blue), which is fixed to Earth's surface, thus rotating with the planet, alongside a stationary reference frame, Σ' (red), which does not rotate relative to the distant stars. Relative to each other, the origins of these two reference frames trace a circle of latitude θ_{Lab} (purple). (b) A two-dimensional cross-section of a vertical AIF within the Earth-fixed reference frame Σ . Laser pulses, depicted by the red shaded region, are associated with light fields k_a, k_b and are aligned with the z -axis. The Earth's rotation causes the initially vertical atomic trajectories (black dashed arrow) to deviate due to fictitious forces (grey arrows), resulting in a curved path that may lead the atoms out of the laser beam. The effect is exaggerated for illustrative purposes.

the third and final fictitious force in classical physics. When rewriting the Lagrangian from Eq. (2.39) in spherical coordinates $\{r, \theta, \varphi\}$, it transforms to

$$L(\mathbf{r}, \dot{\mathbf{r}}) = \frac{m}{2} \dot{r}^2 + \frac{m}{2} r^2 \dot{\varphi}^2 \sin^2(\theta) + m\omega_{\oplus} r^2 - m\phi(\mathbf{r}) \quad (2.40)$$

and gives rise to the ELE

$$\ddot{r} = -r\dot{\theta}^2 - r\dot{\varphi}^2 \sin^2(\theta) - \partial_r \phi(\mathbf{r}) \quad (2.41a)$$

$$\ddot{\theta} = -2\frac{\dot{r}}{r}\dot{\theta} - \dot{\varphi}^2 \sin(\theta) \cos(\theta) - \partial_{\theta} \phi(\mathbf{r}) \quad (2.41b)$$

$$\ddot{\varphi} = -2\frac{\dot{r}}{r}\dot{\varphi} - 2\dot{\theta}\dot{\varphi} \cot(\theta) - \partial_{\varphi} \phi(\mathbf{r}), \quad (2.41c)$$

which are now three coupled ODEs. A complete analytical solution of these equations is typically unnecessary because the primary motion of the atomic ensemble remains predominantly vertical (i.e., along the radial trajectory). Any deviations are generally minor and are corrected or compensated for. However, the Coriolis and centrifugal forces introduce perturbative corrections to this motion. These corrections are more effectively described using a local Cartesian coordinate system $\{x, y, z\}$, which rotates with an effective frequency $\omega_{\text{eff}} = \omega_{\oplus} \sin(\theta_{\text{Lab}})$, specific to the latitude of the experiment, θ_{Lab} . The action functional, still, depends solely on the initial conditions of the atomic trajectory, such that the propagation phase evaluates to

$$\hbar\Delta\Phi_{\text{Prop}}(\mathbf{r}_b, t_b; \mathbf{r}_a, t_a) = S_z(z_b, t_b; z_a, t_a) + S_{xy}(x_b, y_b, t_b; x_a, y_a, t_a), \quad (2.42)$$

see Ref. [40]. Here, the first component represents the propagation phase shift from Eq. (1.42), calculated between the initial height z_a and the final height z_b . The second part accounts for the transverse motion of the atoms and can be explicitly evaluated as

$$S_{xy}(x_b, y_b, t_b; x_a, y_a, t_a) = \frac{m}{2(t_b - t_a)} \left[(x_b - x_a)^2 + (y_b - y_a)^2 \right] + m\omega_{\text{eff}}(x_a y_b - x_b y_a). \quad (2.43)$$

Given the initial conditions x_a and y_a at time t_a , it is only necessary to determine the corresponding positions of the atomic ensemble at time $t = t_b$. Assuming an initially vertical upward motion with velocity v_z , the Coriolis force will cause a westward acceleration (as depicted in Fig. 2.6, in the positive y -direction) given by $a_y = 2\omega_{\text{eff}}v_z$. Motion in the East-West plane, when considered to second order of ω_{\oplus} , leads to what is known as the Eötvös effect. This effect causes a subtle alteration in the vertical acceleration, represented as $a_z = -2\omega_{\text{eff}}v_y$. Specifically, this results in an increased effective gravitational acceleration for particles moving eastward, and a reduced gravitational acceleration for those moving westward. Both of these fictitious accelerations are represented by grey arrows in Fig. 2.6(b). Moreover, any residual velocity components in the transverse directions will lead to further perturbations in the trajectories, caused by the Coriolis and centrifugal effects.

In summary, rotating reference frames do not pose significant theoretical challenges in describing the interferometer, as the propagation integral remains quadratic and can be solved analytically. Determining the classical trajectories of the atoms, while more complex due to the coupled nature of the equations of motion, is still manageable. Experimentally it is crucial to consider that such effects can cause atoms to drift out of the laser beam's focus, leading to a significant loss of contrast. Even when the beam waist is broad enough to ensure the atoms remain within its diameter, various mitigation strategies are typically employed. This is because transverse positional shifts of the atoms within a beam can result in unwanted phase shifts due to wavefront aberrations. Mitigating the Coriolis effect is most effectively achieved by rotating the lasers with Earth, ensuring that the local z -axis – and consequently the beam waist – remains aligned with the vertical motion of the atoms. This is conveniently accomplished using rotating tip-tilt mirrors placed at the start of the atomic baseline [51, 82, 105–107]. For higher baselines extending beyond 10 meters, an additional consideration is required: the rotation of the interferometry laser around a single pivot point can result in a significant transverse offset of the lasers, potentially causing them to collide with the walls of the baseline confinement. For such expansive baselines, more sophisticated laser geometries must be considered [107].

We have now completed an overview of the theoretical framework of AIFs, including some advanced topics that have emerged in recent years. We will now proceed to discuss novel findings, unless states otherwise. We focus mostly on the analyses that were made in Refs. [2, 4].

2.3 Interferometer Geometries to Measure Gravitational Curvature

The most widespread application of AIFs is in the precise measurement of the gravitational field using gravimeters, which provide information about the linear gravitational acceleration, g , along the atomic trajectory. To measure the gravitational gradient, a gradiometric setup is employed, where g -measurements from two spatially separated AIFs are compared. One can see in Table 2.2 how the SRBI and the SDDI share roughly the same phase shifts, only differing by an overall factor of two, related to the smaller spacetime area of the SRBI, apart from term #8 and some smaller FSL and Doppler/FSL related terms. The idea of

doubling the area of the SRBI and taking the differential signal with the SDDI appears to be promising for extracting the differing phase shift # 8. For the sake of simplicity we will omit the Bloch oscillations.¹⁰ An illustration of the resulting interferometer geometry can be found in Fig. 2.7. In the context of the idealised gravitational potential described in Eq. (2.1),

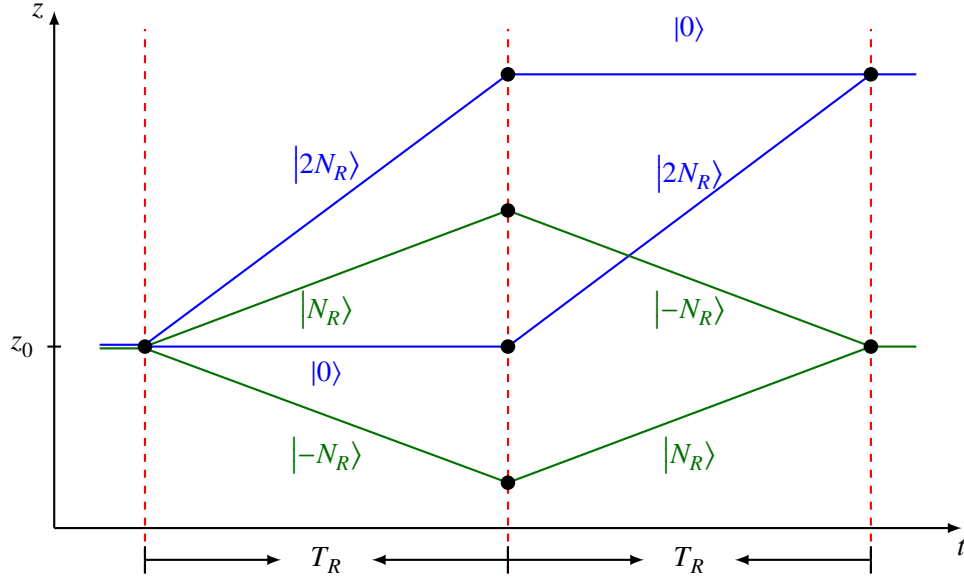


Figure 2.7: A schematic illustration of an interferometer's geometry, designed to isolate phases related to gravity gradients [4]. The atomic paths of the SDDI are depicted in green, while those of the MZI, with a doubled amount of imprinted momenta, are shown in blue. FSL effects are neglected in the picture for illustrative purposes.

the differential phase shift of this novel AIF geometry is expressed by

$$\Delta\Phi = \Delta\Phi_{\text{MZI}} - \Delta\Phi_{\text{SDDI}} = \Delta\Phi_{\text{Curv}} + \Delta\Phi_{\text{FSL/Doppler}} + \mathcal{O}(4), \quad (2.44a)$$

including a contribution denoted as $\Delta\Phi_{\text{Curv}}$, which we refer to as the "curvature phase" or "tidal phase" for reasons that will become clear later and is essentially a rescaled version of term # 8 from Table 2.2.

In this context, $\Delta\Phi_{\text{FSL/Doppler}}$ represents the combined FSL and Doppler phases. As we will show below, sizeable contributions to $\Delta\Phi_{\text{FSL/Doppler}}$ can be mitigated, while other phase shift contributions can be effectively neglected due to their relatively small magnitudes compared to the curvature phase.¹¹ Consequently, we will first concentrate on this dominant phase shift, given by

$$\Delta\Phi_{\text{Curv}} = -2N_R^2 \mathcal{G}_{2,R} \mathcal{R}_R^2 = f_{\text{ideal}} \Gamma \quad \text{with} \quad f_{\text{ideal}} = -\frac{2N_R^2 \hbar k_R^2 T_R^3}{m}. \quad (2.44b)$$

Here, we introduce an idealised scale factor, f_{ideal} , which translates the phase shift to the (idealised) gravity gradient. Consequently, the phase resulting in Eq. (2.44a) depends solely on the gravity gradient Γ and f_{ideal} . This scale factor is known with high precision due to its dependence on the effective wave vector k_R , the interferometer time T_R , and the atomic recoil

¹⁰The SRBI without Bloch oscillations corresponds to the MZI. However, the SDDI without Bloch oscillations will still be referred to as a SDDI.

¹¹As already indicated in Table 2.4, there is an ambiguity in naming terms # 40 – # 44. To address this, and in comparison to Ref. [4], we have collected all Doppler and FSL-related terms into a single contribution.

\hbar/m , making this interferometer geometry a promising candidate for measuring gravitational fields beyond linear acceleration.

Since this phase shift is directly proportional to the gravitational gradient $\mathcal{G}_{2,R}$, it can be used to extract a gradiometric signal directly, thereby eliminating the need to conduct two consecutive experiments at different heights to compare their g -measurements. Due to this co-located setup, we refer to the geometry depicted in Fig. 2.7 as a Co-located Gradiometric Interferometer (CGI) [4]. Consequently, the measurement resolution of such a CGI is determined solely by the signal magnitude and is not limited by the spatial separation between the constituent AIFs. A phase of a similar form to $\Delta\Phi_{\text{Curv}}$, arising from a different experimental setup, was referred to as a "tidal phase" in the work of Asenbaum et al. [108]. In that study, the gravitational gradient, denoted as T_{zz} , referred to a lead block acting as a gravitational test mass. In Hogan et al. [89], [Table 1, Term 9], this phase also appears within a Mach-Zehnder configuration, where the gravity gradient T_{zz} refers to Earth's gravitational field. The different factor of -4 in comparison to [89, 108] arises from the doubled amount of imprinted momentum used in the MZI, combined with the quadratic scaling of $N_R k_R$ and a distinct overall sign factor. In Ref. [87, Table I, Term 6], this term is also present and phrased as a "1st gradient recoil". One can also aim to interpret the tidal phase as a "gradient correction" of the dimensionless quantity $\mathcal{G}_{2,R} = \Gamma T_R^2$ to the recoil phase

$$\Delta\Phi_{\text{Recoil}} = \frac{\hbar N_R^2 k_R^2 T_R}{m}, \quad (2.45)$$

which is used in measurements of the fine-structure constant [38, 39], see Sec. 3.1.1. Consequently, this geometry may be ideally suited for calibrating complex gravitational potentials in novel experimental setups. For this purpose, we also simulate this AIF in gravitational fields that extend beyond the idealised model described in Eq. (2.1). An example of such an application is the Very Long Baseline Atom Interferometer (VLBAI) facility in Hannover, where we utilise its accurately characterised gravitational field [83, 109], as detailed in Sec. 2.4.2.

With the analytic form of this phase shift provided in Eq. (2.44b), one can estimate the magnitude of an (idealised) output signal.¹² Assuming typical values of a launch mode 10 metre interferometer of $T_R = 1.4$ s, $N_R = 1$, $k_R = 10^6 \text{ m}^{-1}$, and a mass of $m = 87 \text{ u}$ (for Rubidium), the resulting atomic wave-packet separation is approximately $N_R \hbar k_R T_R / m \approx 4 \text{ mm}$. In comparison, the CGI setup will result in a dominant phase shift of approximately $|\Delta\Phi_{\text{Curv}}| \approx 0.16 \text{ rad}$. To put this in perspective, consider a MZI using the same numerical values as above to measure the phase $\Delta\Phi = g N_R k_R T_R^2$. Given that the gravitational acceleration g decreases by roughly $\delta g = 2.7 \mu\text{m/s}^2$ per metre, this would result in a differential – gradiometric – signal between two MZIs separated by δh , of approximately

$$\frac{\delta\Phi}{\delta h} = \frac{\delta g N_R k_R T_R^2}{\delta h} = 200 \frac{\text{rad}}{\text{m}}. \quad (2.46)$$

A height difference of $\delta h = 4 \text{ mm}$ would result in a phase difference of approximately $\delta\Phi \approx 0.8 \text{ rad}$. One can therefore observe that the geometry depicted in Fig. 2.7 produces phase shifts of the same order of magnitude as a gradiometric measurement with a height separation equivalent to the path separation of typical AIFs. However, this approach also introduces challenges related to co-location [91] and the fact that both $\delta\Phi$ and δh are subject to measurement uncertainties.

Note that we did not implement any gravity gradient mitigation techniques [92–95], so each constituent AIF will exhibit a non-trivial wave-packet separation at the output port,

¹²Excluding the FSL and Doppler phases, for the moment.

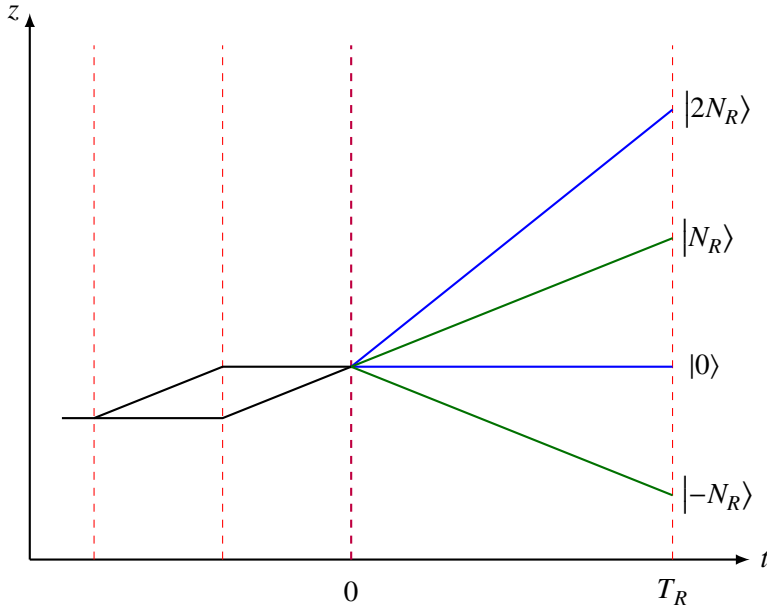


Figure 2.8: A schematic representation of the experimental implementation of the first beam splitter pulse (shown in purple), which is based on an initial MZI. It uses the output ports of this initial system as the inputs for the desired interferometer. Traditional beam splitter pulses are depicted in red.

similar to that described in Eq. (2.36a). Applying the same frequency shift to the mirror pulse in both interferometers will not alter the differential phase shift. As long as both the MZI and SDDI experience the same pulse detuning at the mirror, the measurement setup will continue to function correctly.

Experimental Realisation

An experimental implementation of the first beam splitter of the CGI, as illustrated in Fig. 2.7, could involve preparing an atomic cloud that contains a mixture of two different hyperfine states. This strategy would enable the individual addressing of both atomic subsystems in the MZI and SDDI geometries. Nevertheless, it may also introduce a risk of unwanted effects due to fluctuations in the (then needed) magnetic field. Another approach could be to perform a short Mach-Zehnder sequence just before the first beam splitter and use its output ports as Doppler-selective inputs for the new interferometer geometry. This configuration would allow one to perform the operations

$$|0\rangle \mapsto \frac{1}{\sqrt{2}}(|0\rangle + |-N_R\rangle), \quad |N_R\rangle \mapsto \frac{1}{\sqrt{2}}(|N_R\rangle + |2N_R\rangle) \quad (2.47)$$

within a composite pulse setup, as illustrated in Fig. 2.8. The first setup offers the advantage of ideal "co-location" control [91], as the atoms in each AIF exhibit very narrow uncertainties in their initial conditions due to being initialised in a common trap. On the other hand, the latter setup benefits from excellent coherence between the two input states.

Given that Bragg scattering is inherently a multi-port process, composite pulses can be utilised to produce an effective four-way beam splitter as required in this context. Such generalised beam splitters are developed in the laboratory by applying analytical methods [56] as outlined in Ref. [110], or by employing optimal quantum control techniques [111, 112].

Interpretation of the Phase

To gain a better understanding of the curvature, or tidal, phase, it is beneficial to analyse the origins of this phase contribution. We proceed by reviewing the propagation, separation, and kick phases in the context of the idealised gravitational potential described by Eq. (2.1). Subsequently, we compile all terms, excluding the FSL phases, in Table 2.6.

In an AIF, most phase shifts scale with the enclosed spacetime area, which is identical in both the MZI and SDDI configurations depicted in Fig. 2.7. However, the phase shift $\Delta\Phi_{\text{Curv}}$ arises exclusively from the MZI and is absent in the SDDI. This indicates that this specific phase contribution remains uncancelled in the differential setup. Solving the ELE in the context of the potential from Eq. (2.1) yields an expression for the atomic trajectory of

$$z(t) = z_0 + v_0 t - \frac{1}{2} g t^2 - \frac{\Gamma}{2} \left(z_0 t^2 + \frac{1}{3} v_0 t^3 - \frac{1}{12} g t^4 \right), \quad (2.48)$$

with initial conditions z_0 and v_0 , as we have seen in Eq. (2.9). The Γ -dependent part of the trajectory is not essential for interpreting the curvature phase. Therefore, we will subsume those contributions into $\mathcal{O}(\Gamma)$.

Evaluating these solutions at the time of the mirror pulse ($t = T_R$) for the upper and lower AIF paths of the MZI and SDDI yields atomic heights of

$$z_{\text{up}}^{\text{MZI}}(T_R) = z_0 + v_0 T_R + 2N_R \frac{\hbar k_R T_R}{m} - \frac{1}{2} g T_R^2 + \mathcal{O}(\Gamma), \quad (2.49\text{a})$$

$$z_{\text{low}}^{\text{MZI}}(T_R) = z_0 + v_0 T_R - \frac{1}{2} g T_R^2 + \mathcal{O}(\Gamma), \quad (2.49\text{b})$$

$$z_{\text{up}}^{\text{SDDI}}(T_R) = z_0 + v_0 T_R + N_R \frac{\hbar k_R T_R}{m} - \frac{1}{2} g T_R^2 + \mathcal{O}(\Gamma), \quad (2.49\text{c})$$

$$z_{\text{low}}^{\text{SDDI}}(T_R) = z_0 + v_0 T_R - N_R \frac{\hbar k_R T_R}{m} - \frac{1}{2} g T_R^2 + \mathcal{O}(\Gamma). \quad (2.49\text{d})$$

Calculating the propagation phases for each AIF leads to the following statement

$$\Delta\Phi_{\text{Prop}}^{\text{SDDI}} = \frac{m}{\hbar} \int_0^{2T_R} \left[L(z_{\text{up}}^{\text{SDDI}}(t)) - L(z_{\text{low}}^{\text{SDDI}}(t)) \right] dt, \quad (2.50\text{a})$$

$$\Delta\Phi_{\text{Prop}}^{\text{MZI}} \approx -\frac{m\Gamma}{2\hbar} \int_{T_R}^{2T_R} \left(2N_R \frac{\hbar k_R T_R}{m} \right)^2 dt + \Delta\Phi_{\text{Prop}}^{\text{SDDI}}, \quad (2.50\text{b})$$

where the additional phase in the MZI arises from the propagation phase during the time interval $[T_R, 2T_R]$. This occurs along the $\frac{m}{2}\Gamma z(t)^2$ part of the Lagrangian, particularly due to a non-vanishing photon-recoil asymmetry in the initial heights of $z(t)$, as seen in Eq. (2.49). Note that this contribution vanishes in the SDDI, as both $z_{\text{up}}^{\text{SDDI}}(T_R)^2$ and $z_{\text{low}}^{\text{SDDI}}(T_R)^2$ exhibit identical photon-recoil dependent phase contributions, thereby nullifying any output signal. In a differential measurement setup one is therefore left with the idealised tidal phase

$$\Delta\Phi_{\text{Prop}}^{\text{MZI}} - \Delta\Phi_{\text{Prop}}^{\text{SDDI}} \approx \Delta\Phi_{\text{Curv}} = -2N_R^2 \mathcal{G}_{2,R} \mathcal{R}_R^2 = -\frac{2\Gamma N_R^2 \hbar k_R^2 T_R^3}{m}. \quad (2.51)$$

We will now examine each phase shift contribution in detail to identify the origins of the other terms.

Separation phase

We begin with examining the separation phase of each AIF, which can be calculated using

$$\Delta\Phi_{\text{Sep}} = \frac{m}{\hbar} \Delta z v_{\text{aver}}, \quad (2.52)$$

where Δz is the separation at the output port, and v_{aver} is the average output velocity of the two output ports. For the MZI and SDDI, we obtain the separation phases of

$$\Delta\Phi_{\text{Sep}}^{\text{MZI}} = \Delta\Phi_{\text{Sep}}^{\text{SDDI}} = 2N_R \mathcal{R}_R \mathcal{V}_0 \mathcal{G}_{2,R} - 4N_R \mathcal{G}_{1,R} \mathcal{G}_{2,R} \mathcal{R}_R + 8N_R \mathcal{F}_R \mathcal{G}_{1,R}^2 - 4N_R \mathcal{F}_R \mathcal{G}_{1,R} \mathcal{V}_0, \quad (2.53)$$

which result in no relative phase shift at this level. A differential phase shift between the separation phases will only arise through the FSL effect, which we will include into the analysis below.

Kick phase

The spatial part¹³ of Kick phase can be calculated by the weighted sum of light field phases $\pm\Phi(t_{\text{int}}, z_{\text{int}})$ at each interaction time t_{int} and height z_{int} , counted positively if a photon is absorbed in the process and negatively if a photon is emitted. Calculating this for the MZI and SDDI yields

$$\begin{aligned} \Delta\Phi_{\text{Kick}}^{\text{MZI}} = \Delta\Phi_{\text{Kick}}^{\text{SDDI}} = & 2N_R \mathcal{R}_R \mathcal{G}_{1,R} - 2N_R \mathcal{R}_R \mathcal{Z}_0 \mathcal{G}_{2,R} - 2N_R \mathcal{R}_R \mathcal{V}_0 \mathcal{G}_{2,R} + \frac{7}{6} N_R \mathcal{R}_R \mathcal{G}_{1,R} \mathcal{G}_{2,R} \\ & - 6N_R \mathcal{F}_R \mathcal{G}_{1,R}^2 + 6N_R \mathcal{F}_R \mathcal{V}_0 \mathcal{G}_{1,R}, \end{aligned} \quad (2.54)$$

therefore given a vanishing differential phase shift. Similar to before, there will be FSL phase contributions, that break this symmetry, as discussed below.

Propagation phase

The most interesting contribution to the phase shift is the propagation phase, as introduced in Eq. (2.3a). We will now demonstrate in greater detail how all phases, including those due to linear gravitational acceleration, cancel out, thereby proving Eq. (2.50). The evaluation of the propagation phases yields

$$\Delta\Phi_{\text{Prop}}^{\text{SDDI}} = 4N_R \mathcal{G}_{1,R} \mathcal{G}_{2,R} \mathcal{R}_R - 2N_R \mathcal{R}_R \mathcal{V}_0 \mathcal{G}_{2,R} - 8N_R \mathcal{F}_R \mathcal{G}_{1,R}^2 + 4N_R \mathcal{F}_R \mathcal{G}_{1,R} \mathcal{V}_0 \quad (2.55a)$$

$$\Delta\Phi_{\text{Prop}}^{\text{MZI}} = \Delta\Phi_{\text{Prop}}^{\text{SDDI}} - 2N_R^2 \mathcal{G}_{2,R} \mathcal{R}_R^2 \quad (2.55b)$$

leading to a differential signal that is equivalent to the discussed phase. It is noteworthy that this phase was observed in several previous studies of the MZI [88, 89]. However, the remarkable aspect is that the symmetric momentum imprint of the SDDI effectively nullifies this phase contribution. We have reproduced all the terms in Table 2.2 and demonstrated their respective origins. In Table 2.6, we, again, collect all the non-zero phase contributions relevant to the analysis presented above. For the moment, we have disregarded the FSL terms to simplify the analysis and focus on understanding the origin of this tidal phase. However, FSL phases are also present in the CGI. We will elaborate more on this in the context of two-photon Bragg transitions in the following.

¹³The temporal component of the Kick phase is directly influenced by the FSL effect, as it requires the explicit consideration of the atom's emission and absorption times, as discussed below. Since all the terms presented here are several orders of magnitude below any measurable signal, these contributions will be omitted anyway. The interested reader can find a comprehensive list of the phases affecting both interferometers in a different way in Table 2.7.

Phase comparison of a MZI and a SDDI in a CGI configuration (no FSL phases)					
MZI	SDDI	Phase	Phase	Magnitude [rad]	Differential signal
2	2	$N_R k_R g T_R^2$	$N_R \mathcal{R}_R \mathcal{G}_{1,R}$	1.4×10^7	0
-2	-2	$N_R k_R z_0 \Gamma T_R^2$	$N_R \mathcal{Z}_0 \mathcal{G}_{2,R} \mathcal{R}_R$	20	0
-2	-2	$N_R k_R v_0 \Gamma T_R^3$	$N_R \mathcal{V}_0 \mathcal{G}_{2,R} \mathcal{R}_R$	14	0
$\frac{7}{6}$	$\frac{7}{6}$	$N_R k_R g \Gamma T_R^4$	$N_R \mathcal{G}_{1,R} \mathcal{G}_{2,R} \mathcal{R}_R$	14	0
-2	0	$\frac{N_R^2 \hbar k_R^2 \Gamma T_R^3}{m}$	$N_R^2 \mathcal{G}_{2,R} \mathcal{R}_R^2$	1.5×10^{-2}	-2
-12	-12	$\frac{N_R \omega_R g^2 T_R^3}{c^2}$	$N_R \mathcal{G}_{1,R}^2 \mathcal{F}_R$	2.3×10^{-9}	0
12	12	$\frac{N_R \omega_R g v_0 T_R^2}{c^2}$	$N_R \mathcal{F}_R \mathcal{G}_{1,R} \mathcal{V}_0$	2.4×10^{-9}	0

Table 2.6: Comparison of phases in the MZI and SDDI used for a CGI, as depicted in Fig. 2.7, split into different proportionalities. Pure FSL phases are discarded in this list. The first two columns describe the prefactor of phase shift contributions given in the third and fourth column, which is present in each AIF phase output. The magnitude denotes the absolute value of the expression in the "Phase" columns with assumed numerical values: $N_R = 1$, $\omega_R = 10^7$ Hz, $k_R = 4 \times 10^6$ m⁻¹, $m = 87$ u, $T_R = 0.6$ s, $z_0 = 5$ m, $v_0 = 6$ m/s, $g = 9.81$ m/s² and $\Gamma = 2.7 \times 10^3$ E. The last column comprises the prefactor of the phase expression in a differential measurement setup between MZI and SDDI.

2.3.1 FSL Effect and Mitigation Scheme

Up to this point, we have assumed infinitely fast laser beams and perfectly simultaneous interactions occurring at times $t = 0, T_R, 2T_R$ for each AIF path. Nevertheless, as previously mentioned, the FSL phases are influenced by various experimental conditions, including photon path lengths, mirror positions, and, most importantly, the type of laser interaction used for beam splitting and reflection. Therefore, we will consider a specific experimental setup and choose again the setup depicted in Fig. 2.2. In the case of two-photon Bragg transitions, this phase shift evaluates to

$$\begin{aligned} \Delta\Phi_{\text{FSL}} &= 4N_R^2 \mathcal{R}_R^2 (4\mathcal{G}_{1,R} - \mathcal{V}_0 - \mathcal{R}_R) + \Delta\Phi_0 \\ &= \frac{4\hbar N_R^2 k_R^2 T_R}{mc} \left(4g T_R - v_0 - \frac{N_R \hbar k_R}{m} \right) + \Delta\Phi_0, \end{aligned} \quad (2.56)$$

along with an additional time-independent component

$$\begin{aligned} \Delta\Phi_0 &= 2N_R^2 \mathcal{R}_R^2 (2\mathcal{Z}_L - \mathcal{Z}_0 - \mathcal{Z}_U) = 2N_R^2 \mathcal{R}_R^2 (\mathcal{Z}_L - \mathcal{H} - \mathcal{Z}_0) \\ &= \frac{2\hbar N_R^2 k_R^2}{mc} (2z_L - z_0 - z_U) \end{aligned} \quad (2.57)$$

and some other phase shift contributions of similar magnitude to those previously neglected. The time-independent part is not inherently problematic, as it remains constant across each AIF and can be used to precisely calculate the desired quantities from the output phase shift, provided its magnitude is known. The T_R dependence of the first part can pose challenges,

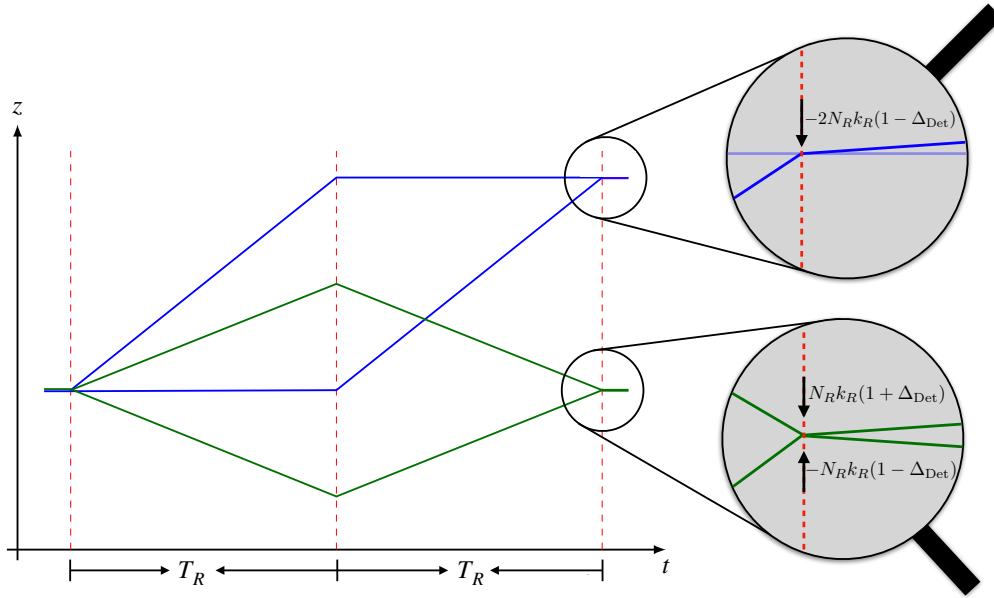


Figure 2.9: A schematic illustration that presents the mitigation scheme, which involves applying a detuning Δ_{Det} to the final interferometry pulse. By precisely adjusting the frequency of the last pulse in the AIF, a carefully calculated detuning is introduced to cancel out unwanted phases related to the FSL effect.

since T_R (as well as v_0) are variable parameters within the experiment. We summarised how each phase shift contribution of the MZI and SDDI are altered due to the FSL effect in Table 2.7. We therefore only consider phase shifts with a magnitude bigger than 2×10^{-11} rad. Note that we only show phase shifts, that not appear universally in the MZI and SDDI.

Mitigation of FSL terms If one modifies the last AIF laser pulse according to $N_R \hbar k_R \mapsto (1 + \Delta_{\text{Det}})N_R \hbar k_R$, where Δ_{Det} is a dimensionless detuning parameter with $\Delta_{\text{Det}} \ll 1$, this results in an additional dominant phase shift at the output port of

$$\Delta\Phi_{\text{Additional}} = 2N_R k_R T_R \Delta_{\text{Det}} \left(v_0 + \frac{N_R \hbar k_R}{m} - g T_R \right). \quad (2.58)$$

It is crucial to emphasise that this detuning parameter, Δ_{Det} , must be kept small to ensure a significant overlap at the final output ports of each constituent AIF. Maintaining a small detuning parameter helps preserve the fidelity and coherence of the system's output. An illustration of this process is given in Fig. 2.9.

Note that the term in the brackets in Eq. (2.58) is usually small, as setting this term to zero corresponds to the constraint equation involving T_R and v_0 for achieving optimal motion in a launch-mode AIF. This happens because the apex of the atomic trajectory ideally occurs after half of the interferometer's duration, at $t = T_R$. If the initial velocity is $v_0 + \frac{N_R \hbar k_R}{m}$, this precisely leads to the equation

$$v_0 + \frac{N_R \hbar k_R}{m} - g T_R = 0. \quad (2.59)$$

When applying this mitigation strategy, it is essential to ensure that v_0 and T_R are selected in such a way that Eq. (2.59) is not satisfied. Otherwise, there would be no additional phase shift that could be tuned to cancel the unwanted phase contributions.

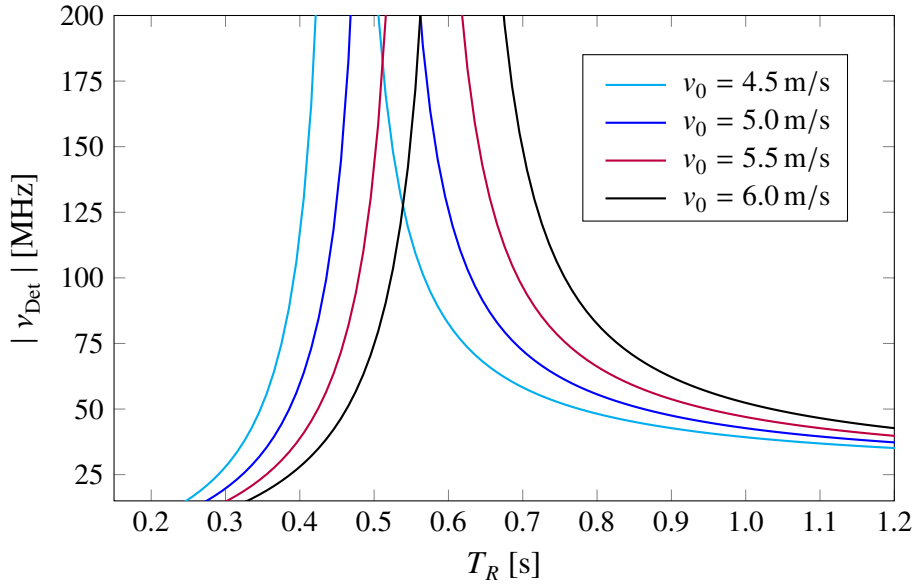


Figure 2.10: Optimal detuning frequency $v_{\text{Det}}(v_0, T_R) = ck_R\Delta_{\text{Det}}(v_0, T_R)$ as a function of T_R for fixed values of v_0 . Notably, the optimal detuning approaches infinity for pairs (v_0, T_R) that satisfy Eq. (2.59).

The described detuning enables the calculation of an appropriate form of Δ_{Det} such that the additional phase cancels out the time-dependent part of $\Delta\Phi_{\text{FSL}}$. This cancellation occurs if we choose

$$\Delta_{\text{Det}}(N_R, v_0, T_R) = 2 \frac{v_0 + \frac{N_R\hbar k_R}{m} - 4gT_R}{v_0 + \frac{N_R\hbar k_R}{m} - gT_R} \frac{N_R\hbar k_R}{mc}. \quad (2.60)$$

In Fig. 2.10, the optimal detuning frequency $v_{\text{Det}} = ck_R\Delta_{\text{Det}}$ of the last AIF pulse is depicted as a function of T_R for a given initial velocity and number of imprinted photon momenta. One can see that the detuning frequency is approximately on the order of hundreds of MHz for usual 10 m interferometers, which is achievable in the laboratory without significant problems. It is worth noting that instead of detuning only the last interferometry pulse, one could also apply a small detuning to each pulse individually. By carefully selecting the corresponding detuning parameters for each pulse, along with adjusting the other relevant variables, one can achieve a more flexible and potentially more effective mitigation of unwanted phase shifts. Another approach to mitigate FSL effects is to adjust the photonic path lengths in such a way that additional FSL phase shifts are introduced, ideally cancelling out the unwanted phase shifts. In our calculations of the various FSL effects, we have assumed that all laser sources are positioned at the same, fixed, heights z_U and z_L . By altering the height of certain lasers for specific pulses, or by combining two-photon and single-photon transitions, it may be possible to mitigate the FSL effects. However, this strategy relies on the specific capabilities and flexibility available within the experimental setup. Such adjustments would need to be carefully considered in the context of the experimental conditions and apparatus constraints.

In conclusion, there are numerous strategies available to mitigate unwanted FSL phases in the CGI. These strategies enable us to safely disregard these effects in our theoretical description. This is particularly crucial for the more detailed analysis presented in Sec. 2.4.2.

Detailed analysis of FSL phases in the CGI in units of $\omega_C T_R$										
Interferometer	MZI				SDDI				CGI	
Origin	Propagation	Separation	Temporal Kick	Spatial Kick	Propagation	Separation	Temporal Kick	Spatial Kick	Phase	Magnitude of CGI phase (with prefactor)
$\mathcal{F}_R \mathcal{R}_R \mathcal{G}_{1,R}$	12	-8	8	6	0	0	0	0	18	2×10^{-11}
$\mathcal{F}_R \mathcal{R}_R \mathcal{V}_0$	-4	4	0	-4	0	0	0	0	-4	5×10^{-12}
$\mathcal{R}_R^2 \mathcal{G}_{1,R}$	-2	0	10	8	0	0	0	0	16	2×10^{-3}
$\mathcal{R}_R^2 \mathcal{H}$	2	0	0	-4	0	0	0	0	-2	1×10^{-3}
$\mathcal{R}_R^2 \mathcal{Z}_0$	2	0	0	-4	0	0	0	0	-2	4×10^{-4}
$\mathcal{R}_R^2 \mathcal{Z}_L$	-2	0	0	4	0	0	0	0	2	8×10^{-5}
$\mathcal{F}_R \mathcal{R}_R^2$	0	0	0	0	4	0	0	0	-4	2×10^{-15}
$\mathcal{F}_R^2 \mathcal{G}_{1,R}$	0	0	-4	0	0	0	0	0	-4	4×10^{-20}
$\mathcal{F}_R \mathcal{R}_R \mathcal{H}$	0	0	-4	0	0	0	0	0	-4	2×10^{-11}
$\mathcal{F}_R \mathcal{R}_R \mathcal{Z}_0$	0	0	-4	0	0	0	0	0	-4	7×10^{-12}
$\mathcal{F}_R \mathcal{R}_R \mathcal{Z}_L$	0	0	4	0	0	0	0	0	4	1×10^{-12}
$\mathcal{R}_R^2 \mathcal{V}_0$	0	0	-4	0	0	0	0	0	-4	6×10^{-4}
\mathcal{R}_R^3	0	0	0	0	0	0	4	0	-4	3×10^{-7}
$\mathcal{F}_R^2 \mathcal{R}_R$	0	0	0	0	0	0	-4	0	4	2×10^{-23}

Table 2.7: FSL phases in the CGI, assuming the setup in Fig. 2.2. The first column collects the phase shift contributions. The next eight columns denote the origin of this phase shift contribution for the MZI and SDDI, respectively. The last two columns denote the prefactor in the CGI and its magnitude. Numerical values: $N_R = 1$, $\omega_R = 10^7$ Hz, $k_R = 4 \times 10^6$ m $^{-1}$, $m = 87$ u, $T_R = 0.6$ s, $z_0 = 5$ m, $v_0 = 6$ m/s, $g = 9.81$ m/s 2 , $z_L = -1$ m and $z_U = 11$ m.

2.4 Revisiting Assumptions

In this section, we will revisit the assumptions about the gravitational field discussed in the introduction of this chapter. Adopting a top-down approach, we first analyse the deviations of the gravitational field from the idealised model on a global scale, which is crucial for AIF experiments conducted on satellites. Subsequently, we examine gravitational anharmonicities on a local scale, using a 10 metre interferometer facility in Hannover as an example.

2.4.1 Global Gravitational Variations: Geopotential Model

Initially, the analysis assumed a spherically symmetric Earth as the source of the gravitational background field. However, acknowledging the limitations of this simplification, we have now incorporated a more realistic geopotential model. By adopting this approach, we aim to capture the complexities and irregularities of Earth's gravitational field, on a global scale, providing deeper insights into potential experiments with AIF in Earth's orbit [42, 113–115]. On one hand, experimental setups of this nature can be viewed as supporting missions like GRACE Follow-On for purposes of relativistic geodesy. On the other hand, they are utilised to measure gravitational waves and investigate dark matter. Since our goal is to incorporate and understand effects arising from GR, particularly spacetime curvature, it is essential to know Earth's static gravitational field with high precision. This accuracy allows us to distinguish inhomogeneities in the gravitational field from potential signals of new physics.

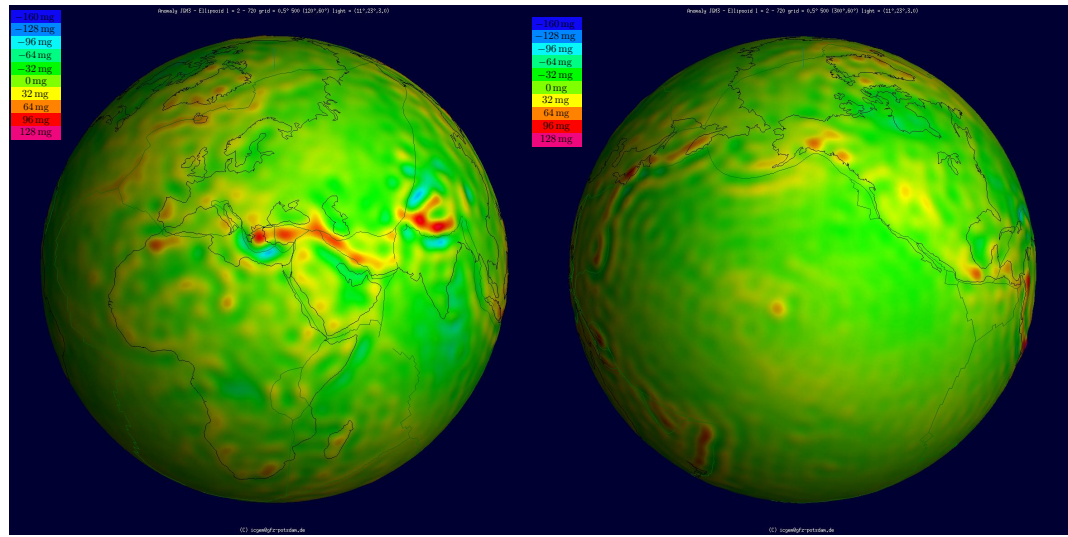


Figure 2.11: Deviation of the local gravitational acceleration from the mean, based on the JGM-3 model. The figure was created using the open source 3D visualisation tool of the International Centre for Global Earth Models (ICGEM) at the GFZ in Potsdam, see Ref. [116]. The legend has been adapted for better readability.

To begin, it is important to consider that Earth's radius is not constant; instead, it varies depending on the observer's latitude. This results in a deviation of approximately 0.3 % from the average, or about ± 10.5 km. We use the radius formula for a spheroid

$$R(\theta) = \sqrt{\frac{R_e^4 \cos^2(\theta) + R_p^4 \sin^2(\theta)}{R_e^2 \cos^2(\theta) + R_p^2 \sin^2(\theta)}}, \quad (2.61)$$

where R_e and R_p represent the equatorial and polar radii of the Earth, respectively. For all calculations, we select the Earth's radius at the laboratory to be R_\oplus , while keeping in mind that this value implicitly depends on the latitude. In the second step, a multipole expansion of the gravitational potential is performed, expressed in the following form

l	J_l	n	m	C_n^m	S_n^m
2	$1.75 \times 10^{10} \text{ km}^5/\text{s}^2$	2	1	$5638 \text{ km}^5/\text{s}^2$	$-26518 \text{ km}^5/\text{s}^2$
3	$-2.62 \times 10^{11} \text{ km}^6/\text{s}^2$		2	$-2.55 \times 10^7 \text{ km}^5/\text{s}^2$	$1.46 \times 10^7 \text{ km}^5/\text{s}^2$
4	$-1.07 \times 10^{15} \text{ km}^7/\text{s}^2$	3	1	$-2.27 \times 10^{11} \text{ km}^6/\text{s}^2$	$-2.77 \times 10^{10} \text{ km}^6/\text{s}^2$
5	$-9.58 \times 10^{17} \text{ km}^8/\text{s}^2$		2	$-3.20 \times 10^{10} \text{ km}^6/\text{s}^2$	$2.19 \times 10^{10} \text{ km}^6/\text{s}^2$
6	$1.45 \times 10^{22} \text{ km}^8/\text{s}^2$		3	$-1.04 \times 10^{10} \text{ km}^6/\text{s}^2$	$-2.05 \times 10^{10} \text{ km}^6/\text{s}^2$

Table 2.8: Table of the first zonal and tesseral coefficients according to the JGM-3 model.

$$\phi(r, \theta, \varphi) = -\frac{GM_\oplus}{r} + \sum_{l=2}^{\infty} Z_l(r, \theta) + \sum_{n=2}^{\infty} \sum_{m=1}^n T_{n,m}(r, \theta, \varphi) \quad (2.62a)$$

with

$$Z_l(r, \theta) = \frac{J_l P_l^0(\sin(\theta))}{r^{l+1}}, \quad (2.62b)$$

$$T_{n,m}(r, \theta, \varphi) = P_n^m(\sin(\theta)) \frac{C_n^m \cos(m\varphi) + S_n^m \sin(m\varphi)}{r^{n+1}}. \quad (2.62c)$$

Here Z_l are "zonal" and $T_{n,m}$ are "tesseral" corrections. The J_l, C_n^m, S_n^m are constants, with the most significant ones listed in Table 2.8. The $P_n^m(x)$ are the associated Legendre polynomials. To maintain axial symmetry, the tesseral terms would need to be disregarded, meaning one would set $C_n^m = S_n^m = 0 \forall l, m$. In this model, the Newtonian gravitational potential would take the form

$$\begin{aligned} \phi(r, \theta, \varphi) = & -\frac{GM_\oplus}{r} + \frac{J_2}{2r^3} (3 \sin^2(\theta) - 1) + \frac{J_3 \sin(\theta)}{2r^4} (5 \sin^2(\theta) - 3) \\ & + \frac{J_4}{8r^5} (35 \sin^4(\theta) - 30 \sin^2(\theta) + 3) + O(C_n^m, S_n^m, J_5). \end{aligned} \quad (2.63)$$

Explicit values for the correction constants can be found, for example, in the Joint Earth Gravity Model (JGM), such as the JGM-3 catalogue (see Ref. [117]). Because water and other liquids are continually moving on Earth, the matter distribution is inherently a dynamic quantity. A graphical representation of the anomaly in local gravitational acceleration, as described by the JGM-3 model, can be seen in Fig. 2.11. This figure uses colour codes to represent deviations from the mean gravitational acceleration. Figure 2.12 illustrates the significant effect of the zonal coefficients compared to the dominant (constant) contribution of the gravitational potential on Earth's surface. The zonal coefficient Z_2 has the largest impact, being roughly three orders of magnitude greater than Z_n for $n \geq 3$. The effects

of the tesseral contributions are of the same order of magnitude as the higher-order zonal coefficients, as demonstrated in Figure 2.13. This is shown at Earth's surface and a fixed latitude of $\theta = \pi/4$, which corresponds approximately to the regions of North America, Southern Europe, or Central Asia.

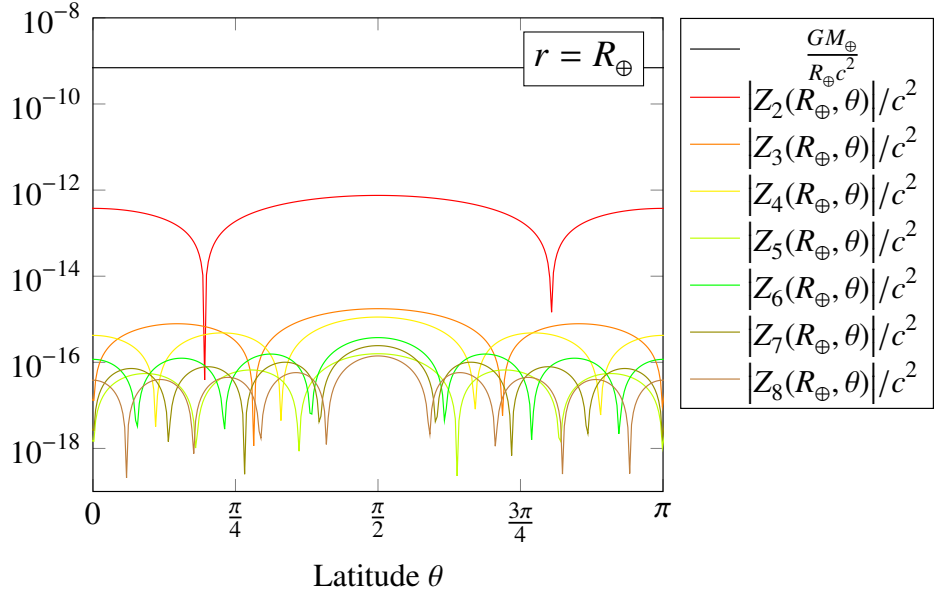


Figure 2.12: Comparison of the (dimensionless) magnitudes of several components of the effective gravitational potential as functions of latitude θ from 0 (north pole) to π (south pole): i) constant gravitational potential of a sphere (black) and ii) zonal correction terms from Eq. (2.62b) for different $l \geq 2$ (coloured).

In earthbound experiments, this analysis is not crucial for local setups because the local value of g remains constant across the transverse dimensions. The movement in the local x and y directions is too small to detect any inhomogeneities at this scale. However, for such locally confined experiments, the analysis in the next section becomes important as it incorporates local inhomogeneities in the radial direction. For space borne AIF experiments, the scenario differs. Zonal and tesseral corrections decrease with higher orders of r , reducing their impact on AIF experiments conducted in Earth's orbit. This topic is further explored in the outlook of Chapter 3, particularly in Sec. 3.8.

2.4.2 Local Gravitational Variations: VLBAI Hannover

State-of-the-art AIF are being developed with increasingly longer baselines [85, 86, 118, 119] and more efficient Large Momentum Transfer (LMT) techniques [60, 120, 121] all over the world. These advancements are pushing the potential wave packet separation beyond the region where the assumption of an idealised local gravitational field as in Eq. (2.1) remains valid. The transition to non-trivial fields presents not only a challenge for large baseline interferometers but also an opportunity for experiments utilising gravitational test masses. By deliberately introducing non-trivial gravitational fields, researchers can measure phases along the atomic trajectory to probe this non-linearity. This approach has been exploited in studies such as [108, 122], leading to the proposed gravitational Aharonov-Bohm effect [103]. Measuring anomalies in the gravitational gradient is also employed to detect inhomogeneities in the gravitational field [123] and is becoming increasingly important for applications in

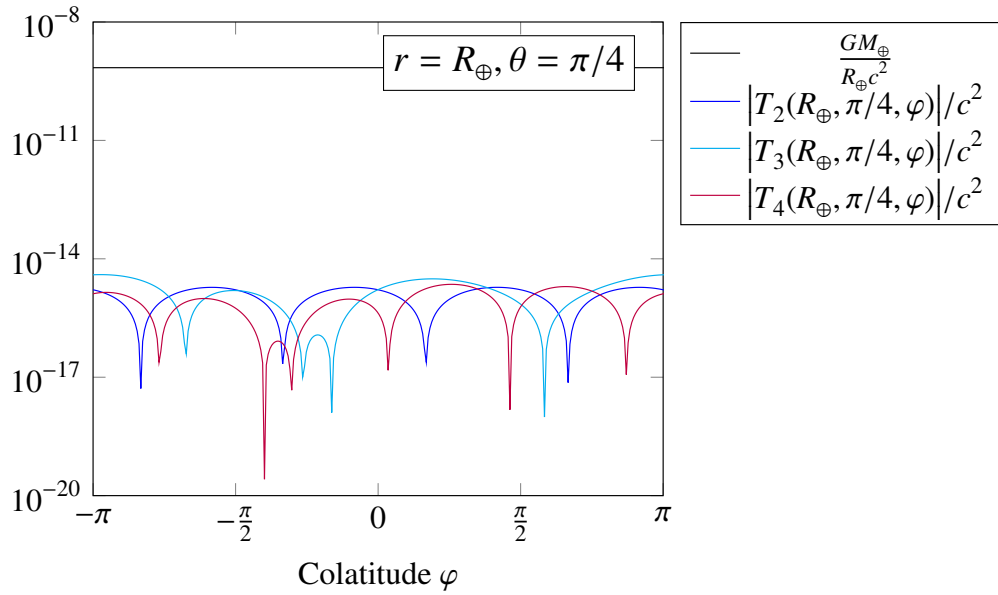


Figure 2.13: Comparison of the (dimensionless) magnitudes of several components of the effective gravitational potential as functions of colatitude φ for fixed $\theta = \pi/4$: i) constant gravitational potential of a sphere (black) and ii) summed tesselation correction terms $T_n = \sum_{m=1}^n T_{n,m}$ from Eq. (2.62c) (coloured).

civil engineering and quantum metrology. Resolving a spatially varying gravity gradient with high accuracy using a gradiometric AIF setup involves comparing g -measurements in close proximity. This process is prone to increasing errors due to the relative uncertainty in the positions of the atomic ensembles compared to the separation between the two constituent AIFs.

At the VLBAI facility in Hannover, a high-precision measurement campaign was conducted to understand the gravitational background and its fluctuations along the 10 metre baseline of the interferometer [83, 109], particularly within its Region of Interest (ROI). As shown in Fig. 2.14, the gravitational gradient's non-linearity varies with height, ranging around 10^{-7} s^{-2} , or equivalently 10^{-6} g/m . This variation appears to correlate with the large masses of concrete and steel in the ground and first floors. Given that the newly proposed CGI was shown to be especially sensitive to gravitational curvature – terms beyond linear acceleration – we will use this interferometer geometry to analyse the VLBAI in Hannover in greater detail. We simulate the CGI scheme for the VLBAI facility in Hannover, using its precisely known gravitational field from Refs. [83, 109], as depicted in Fig. 2.14. The measured values of g have been interpolated with a polynomial of degree 10, which results in a gravitational potential represented by a polynomial of degree 11 after integration. The measurement data was collected before the magnetic shielding of the VLBAI was in place. Since the shielding is a spherically symmetric and homogeneous mass, significant deviations from the presented model would only be expected at the top and bottom of the shielding.

Throughout this analysis, we will assume one-dimensional movement of the AIF atoms along the z -axis of a local coordinate system originating at a fixed height of the experiment, while disregarding Earth's rotation. By expanding the gravitational potential, $\phi(z)$, in the

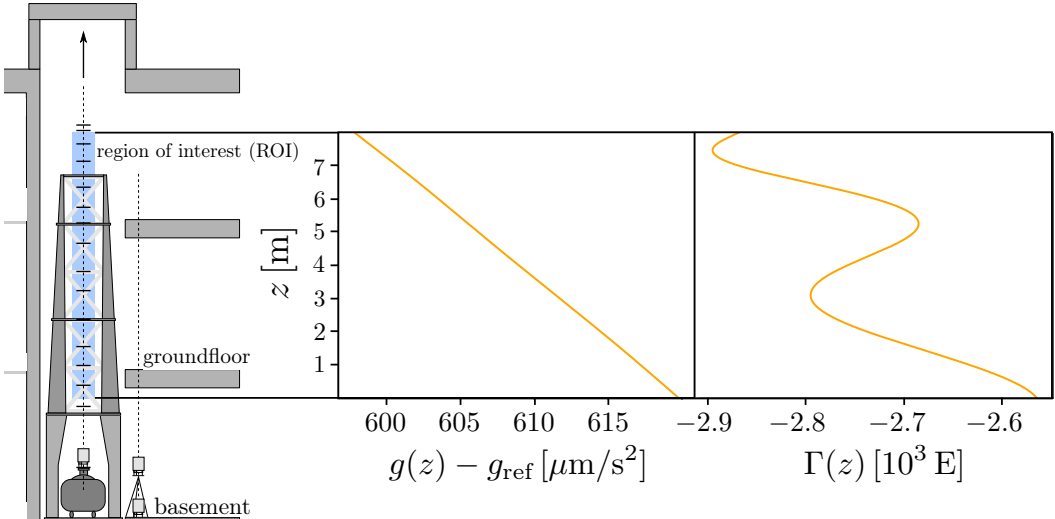


Figure 2.14: Gravitational acceleration $g(z)$ and gravitational gradient $\Gamma(z)$ as functions of height in the ROI of the VLBAI Hannover with a reference acceleration of $g_{\text{ref}} = 9.812 \text{ m/s}^2$. $g(z)$ is interpolated by a polynomial fit. Building cross-section taken from Ref. [83] and adapted.

vicinity of the origin of this local coordinate system using a Taylor series, we obtain

$$\phi(z) = \phi_0 + g z + \sum_{n=2} \frac{\phi^{(n)}}{n!} z^n. \quad (2.64)$$

Note that, in comparison to Eq. (2.1), we have $\phi^{(2)} = -\Gamma$ and we define gravitational curvature as

$$\Gamma(z) = \frac{\partial^2 \phi(z)}{\partial z^2}, \quad (2.65)$$

The summation in Eq. (2.64) must be carried out to a considerable order, depending on the complexity of the gravitational environment. In our case, this extends to order 11, as described above. To highlight this once more: we refer to all terms in $\Gamma(z)$ as gravitational curvature, including the gravity gradient and higher-order derivatives of the potential. In a general relativistic context, curvature is defined through components of the Riemann curvature tensor, which – at first order – are second derivatives of the gravitational potential, as is the case here.¹⁴ We will focus on the CGI depicted in Fig. 2.7, which consists of a MZI with a $2N_R \hbar k_R$ momentum transfer and a SDDI with an initial photon kick of $N_R \hbar k_R$ in each direction.

To address the challenge of inferring gravitational curvature at a specific height from a measured phase shift, given that atoms sample a substantial section of the gravitational field during their flight, effectively averaging it, we begin by analysing multiple CGI sequences as shown in Fig. 2.7. Each sequence spans a height difference of Δh with varying initial heights z_0 , as illustrated in Fig. 2.15. The apex of each atomic trajectory occurs at time $t = T_R$, which

¹⁴Geodesists refer to gravitational curvature as third-order derivatives of the gravitational potential, i.e., the spatial variation of the gravity gradient.

is achieved by setting

$$v_0 = gT_R \quad \text{and} \quad T_R = \sqrt{\frac{2\Delta h}{g}}. \quad (2.66)$$

Note that each atomic sub-trajectory experiences different momentum kicks and therefore will not reach its apex at exactly the same time. However, since the atomic recoils are small compared to the initial launch velocity, this intricacy can be safely ignored for the moment. For simplicity, in this section, we will always illustrate trajectories in this way, such that Δh and T_R can be viewed interchangeably.

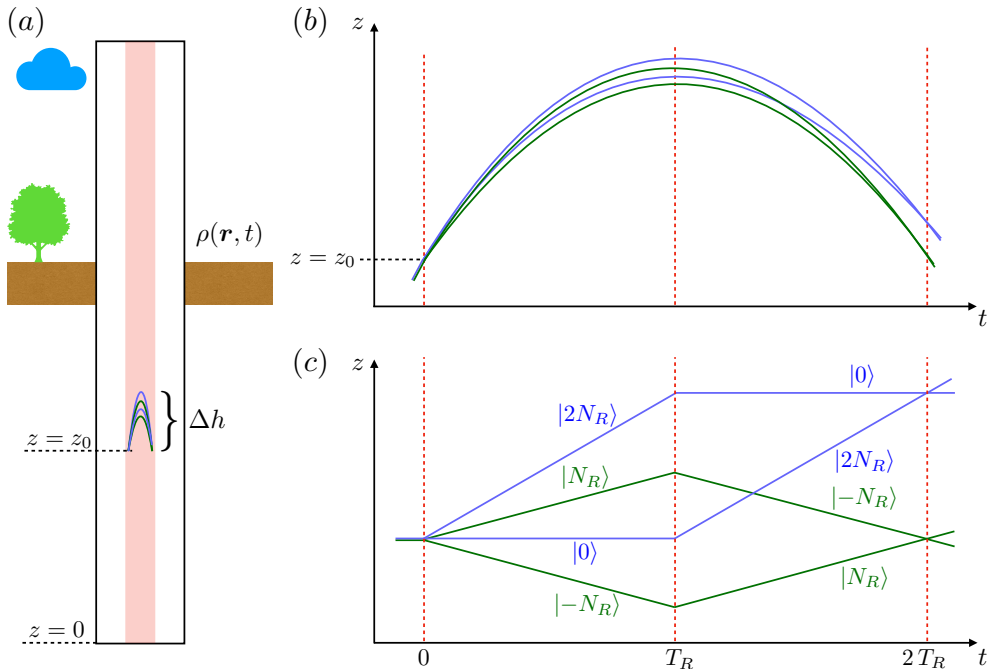


Figure 2.15: (a) Graphical depiction of a CGI within the baseline of a large-scale interferometry facility, where the initial height z_0 can be chosen freely. (b) Detailed depiction of the CGI in the laboratory frame. (c) Illustration of the CGI in the freely falling frame, with the current momentum state of each interferometer arm indicated.

Numerical Simulation of the CGI in Non-trivial Gravitational Fields

Having developed a numerical model of the gravitational field at VLBAI Hannover, we can now simulate any AIF interferometer by implementing the preceding theoretical model. We simulate the CGI from Fig. 2.7 in the gravitational field of the VLBAI from Fig. 2.14. The numerics are done in Python [3] and use a time discretisation of the interval $[0, 2T_R]$ into a certain number of sub-intervals. For the VLBAI gravity profile we have seen that a number of 20.000 time steps is sufficient for convergence. By simulating the CGI as outlined in Fig. 2.15, we demonstrate the link between gravitational curvature and the phase shift, as illustrated in Fig. 2.16. It is intriguing to observe that the gravitational curvature depicted in Fig. 2.14 directly correlates with the CGI phase $\Delta\Phi$, after a shift along the horizontal axis, as shown in Fig. 2.16.

In fact, this behaviour is logical because the atoms effectively explore the gravitational curvature along their entire trajectory, which changes non-trivially from its initial value.

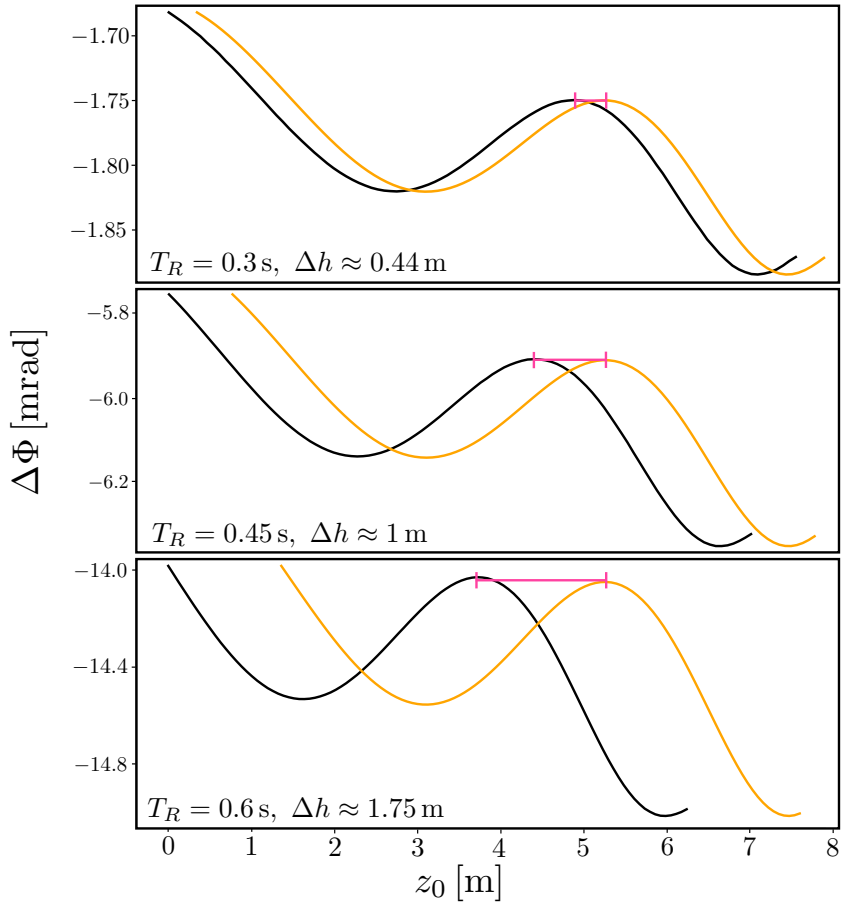


Figure 2.16: Comparison of the measured phase shift $\Delta\Phi$ (black) and the gravitational curvature Γ from Fig. 2.14 (orange), as a function of the initial height z_0 in the ROI for three different values of T_R (and therefore Δh), i.e., different choices of measurement resolution. The pink line highlights the offset between the phase shift and the gravitational curvature.

Consequently, the output signal of the interferometer is based on a carefully chosen average value of $\Gamma(z)$. This implies that the phase shift, along with the information it contains about $\Gamma(z)$, can be correlated to a precisely averaged height within the interval $[z_0, z_0 + \Delta h]$, i.e., the phase shift directly reflects the gravitational curvature at that specific height. This raises the question of the magnitude of this shift and, more importantly, whether there is any underlying systematic or universality that could be discovered. A reasonable ansatz for this shift stems from the aforementioned thought, that the atoms average gravity along their trajectory. Thus, we define the n -th mean of the atomic position along its trajectory using

$$\|z(t)\|_n = \left(\frac{1}{2T_R} \int_0^{2T_R} |z(t) - z_0|^n dt \right)^{1/n}, \quad (2.67)$$

where the trajectory $z(t)$ is adjusted to exclude the initial height z_0 . A collection of various different for the trajectory means and their connection to the interferometer baseline can be found in Table 2.9.

n	1	2	3	4	5
$\ z(t)\ _n$	$0.66 \Delta h$	$0.73 \Delta h$	$0.77 \Delta h$	$0.79 \Delta h$	$0.82 \Delta h$

Table 2.9: Comparison of different trajectory means, $\|z(t)\|_n$, for the first five of values for n . Here, we assumed an initial height of $z_0 = 0$, a baseline $\Delta h = 10$ m, and corresponding values of v_0 and T_R , given by Eq. (2.66).

Consequently, we define a shifted version of the phase shift using the n -th trajectory mean as

$$\Delta\Phi_{\text{shift}}(z_0, n) = \Delta\Phi(z_0 - \|z(t)\|_n). \quad (2.68)$$

Furthermore, we introduce a series of exact scale factors, f_n , analogous to the idealised scale factor f_{ideal} , established in Eq. (2.44b), as

$$f_n \cdot \Gamma(z_0) = \Delta\Phi_{\text{shift}}(z_0, n). \quad (2.69)$$

For small baselines, the exact scale factors f_n should naturally align with the idealised scale factor. Comparing the shifted phase $\Delta\Phi_{\text{shift}}(z_0, n)$ for various values of n with the gravitational curvature – each as a function of height – results in the finding, that the case $n = 3$ exhibits particularly good agreement. This can also be physically motivated, as the tidal phase, in its idealised form, is cubic in the interferometer time T_R . In the following, we examine the connection between the shifted phase and the gravitational curvature for $n = 3$, and we define an estimator for the gravitational curvature, as demonstrated in Ref. [4].

Defining an Estimator for Gravitational Curvature

We begin by comparing the scale factor f_3 with the idealised one f_{ideal} in Fig. 2.18(a), and indeed, observe that they coincide in the limit as $\Delta h \rightarrow 0$, as anticipated. However, even as the baseline increases beyond 2 metres, the idealised scale factor continues to approximate the exact one with an accuracy better than one per mill. Although we lack an analytical expression for f_3 , we observe that the idealised scale factor provides a promising approximation. Thus, we define an estimator for the gravity curvature by

$$\hat{\Gamma}(z_0) = \frac{\Delta\Phi_{\text{shift}}(z_0, 3)}{f_{\text{Ideal}}}. \quad (2.70)$$

Fig. 2.17 demonstrates that this estimator is in excellent agreement with the exact gravitational curvature $\Gamma(z_0)$ for small baselines Δh , corresponding to high spatial resolutions. It is noteworthy that this averaging process appears to be universal for this particular geometric configuration. Increasing the baseline results in a noticeable reduction in estimation accuracy. This aspect requires more detailed quantification. For this we define the root mean-square error as

$$\Delta\hat{\Gamma} = \sqrt{\frac{1}{2T_R} \int_0^{2T_R} dz (\Gamma(z) - \hat{\Gamma}(z))^2}. \quad (2.71)$$

Fig. 2.18(b) illustrates that increasing the baseline – and consequently the average phase shift – leads to a higher root mean square error, $\Delta\hat{\Gamma}$, in the estimation of the gravitational

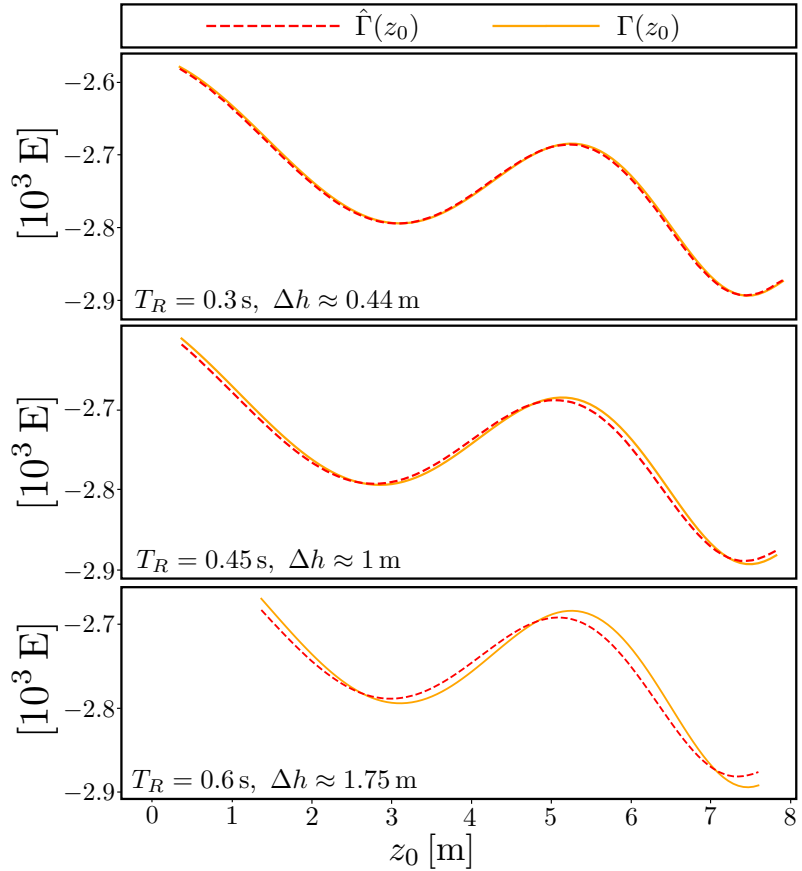


Figure 2.17: Comparison of the gravitational curvature Γ from Fig. 2.14 (orange) and the estimator for the gravity gradient $\hat{\Gamma}$ from Eq.(2.70) (red dashed) for three different values of T_R (and therefore Δh), i.e., different choices of measurement resolution.

curvature. These findings underscore the critical importance of thoroughly understanding the gravitational environment in VLBAI facilities, as the link between measured phases and their corresponding heights was previously unclear. This knowledge is particularly crucial when aiming to detect signals from additional test masses or even gravitational waves. Given that the tidal phase remains robust when transitioning to complex gravitational fields, our objective is to derive an approximate expression for the dominant phase shift in a CGI under these conditions.

Defining a Formula for the Tidal Phase in Complex Gravitational Fields

Utilising the Taylor series expansion of the gravitational potential in Eq. (2.64), we can deduce the dominant phase shift contribution in the CGI. We find that the tidal/curvature phase can be reformulated as

$$\Delta\Phi_{\text{Curv}} = -\frac{m}{\hbar} \sum_{n=2} \frac{\phi^{(n)}}{n!} [\mathcal{A}_{\text{MZI}}(n) - \mathcal{A}_{\text{SDDI}}(n)]. \quad (2.72)$$

Here $\mathcal{A}_{\text{MZI}}(n)$, $\mathcal{A}_{\text{SDDI}}(n)$ are geometry dependent quantities. Denoting the classical solutions of the atomic trajectories on the upper and lower AIF path of the MZI as $z_{\text{up/low}}^{\text{MZI}}(t)$ respectively,

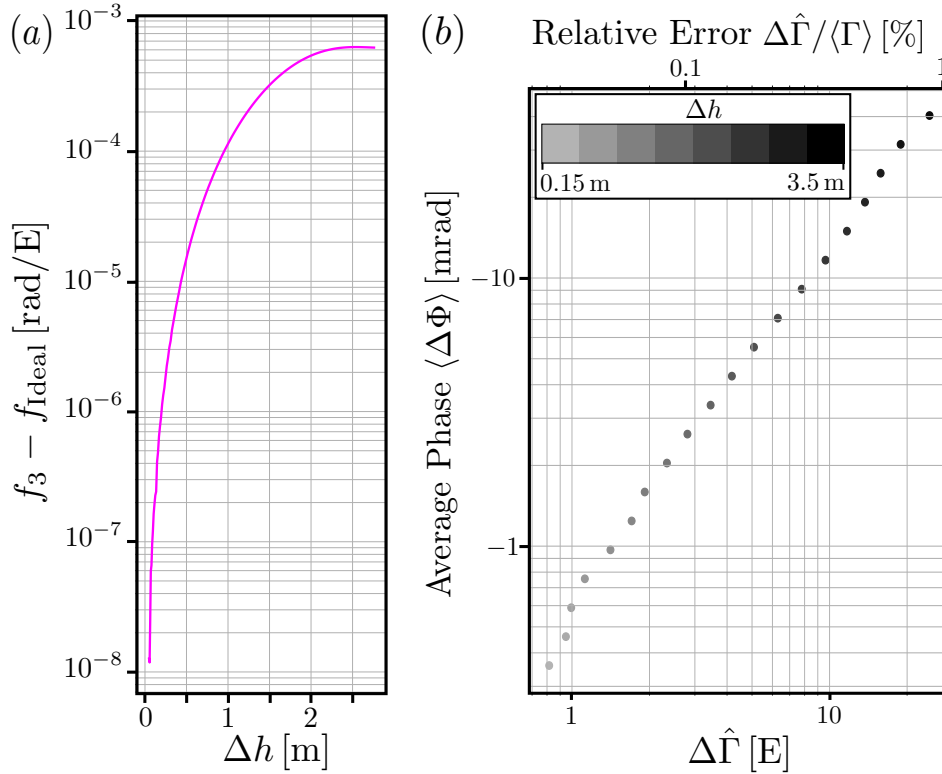


Figure 2.18: (a) Difference between the exact scale factor f_3 and the idealised one, f_{ideal} , as a function of the interferometer baseline Δh . (b) Phase shift magnitude for CGIs with varying baselines Δh and corresponding root mean-square error in the estimation of the gravity gradient. $\Delta\hat{\Gamma}$ is averaged over all possible initial heights in the ROI obtainable with a baseline of Δh and $\langle\Gamma\rangle = 2.75 \times 10^3$ E is the magnitude of the mean gravitational gradient of the facility.

one can write $\mathcal{A}_{\text{MZI}}(n)$ as

$$\mathcal{A}_{\text{MZI}}(n) = \int_0^{2T_R} \left(z_{\text{up}}^{\text{MZI}}(t)^n - z_{\text{low}}^{\text{MZI}}(t)^n \right) dt, \quad (2.73)$$

which coincides with the spacetime area of the MZI for $n = 1$. The formula for the SDDI is completely analogous. Note that there is no $n = 1$ contribution of $\Delta\Phi_{\text{Curv}}$, i.e., phase shifts resulting from linear gravitational acceleration g , cancel to leading order.

In a nutshell: It has been previously demonstrated how the tidal phase emerges from the propagation integral involving the higher-order potential terms of the Lagrangian and the macroscopic height difference at the mirror pulse of the MZI of $2N_R\hbar k_R T_R/m$. For a non-trivial gravitational potential, the propagation phase will consequently always take the form

$$\Delta\Phi_{\text{Prop}}^{\text{MZI}} \approx \frac{m\phi^{(2)}}{2\hbar} \left(\frac{2N_R\hbar k_R T_R}{m} \right)^2 + \frac{m\phi^{(3)}}{6\hbar} \left(\frac{2N_R\hbar k_R T_R}{m} \right)^3 + \dots,$$

whereas $\Delta\Phi_{\text{Prop}}^{\text{SDDI}}$ lacks those kind of terms. However, the kick phase depends only on the atomic positions, and both paths of the CGI are influenced by gravity in a similar manner due to the small spatial separation between the two arms, which is on the order of $2N_R\hbar k_R T_R/m$.

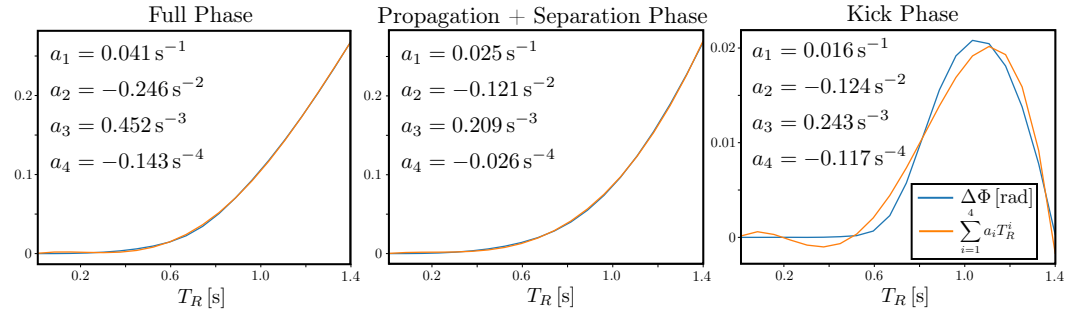


Figure 2.19: Numerical phase shift simulation (blue) of the CGI in the gravitational field of the VLBAI from Fig. 2.14 as a function of T_R for fixed $N_R = 1$, $z_0 = 0$, and $v_0 = 13.8 \text{ m/s}$. A polynomial of fourth order (orange) is fitted to the phase shift. One can observe that the phase shift is primarily dominated by the propagation and separation phases, with the kick phase contributing at most one order of magnitude lower.

The expression for the tidal phase in Eq. (2.72) is essentially given by the propagation phase, where the kinetic and the linear gravitational part of the Lagrangian drop out, as we have seen for the case of the idealised potential.

We support this theoretical argument with a numerical analysis. Figure 2.19 illustrates how the total phase shift – and its constituent phase shifts, namely the propagation, separation and kick phase¹⁵ – scale as a function of T_R . FSL phases are excluded from this simulation, meaning all atom-light interactions occur at time instances $t = 0, T_R, 2T_R$. This simplification avoids the additional complexity introduced by the FSL effect, which can be mitigated in any case. The approximation in Eq. (2.44a) fails under certain conditions. First, in a rather unique scenario, if the separation phase becomes excessively large, it may grow larger than the propagation integral from Eq. (2.44a). This situation is experimentally trivial, as a large separation phase would result in zero contrast anyway. Second, if the gravitational potential is configured¹⁶ to accelerate one interferometer arm significantly differently from the other, this would yield non-trivial effects in both the propagation and kick phases. Of course, this scenario is also quite artificial, as the atomic paths are required to interfere at the output port regardless.

2.5 Summary and Outlook

We introduced a novel AIF geometry designed to exhibit high sensitivity in the measurement of gravitational curvature [4]. In addition, we performed numerical simulations to analyse the behaviour of this AIF sequence in the gravitational field of the VLBAI facility in Hannover, Germany. Our results provide new insights into the interpretation of phase shift data in complex gravitational environments. This analysis serves as a case study for VLBAI, highlighting the critical role of accurate gravitational models in state-of-the-art atom interferometry experiments with baselines longer than 10 metres. It should be noted that we idealised the atom-light interaction by assuming instantaneous and lossless processes. Here, we also disregarded Earth's rotation, which was analysed in Sec. 2.2.4.

¹⁵It was shown in Ref. [87] how the separation phase can be viewed as the "missing part" of the closed propagation phase integral. Whenever we have a substantial separation at the output port it will therefore make sense to analyse the sum of the propagation and separation phase, since they arise from the same intrinsic mechanism.

¹⁶Potentially, by using cleverly positioned macroscopic test masses.

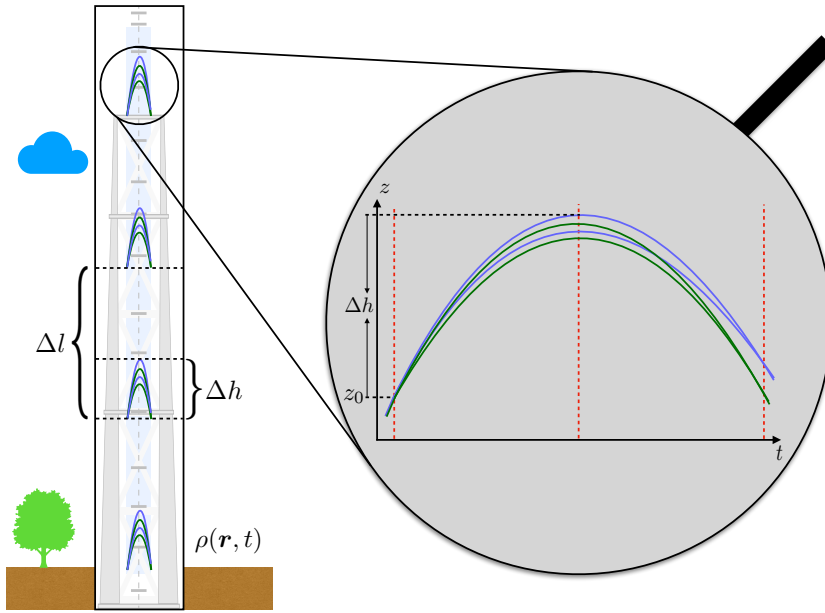


Figure 2.20: Schematic depiction of a measurement sequence to obtain a time resolved model of the gravitational curvature. Here, the separation between the initial heights of each CGI, Δl , are shown equally spaced, in order to achieve a higher spatial resolution, one can decrease the separation between neighbouring interferometers in certain areas.

An additional strategy to measure the gravity gradient involves the gradient mitigation techniques, see Sec. 2.2.3. By scanning through different pulse detunings and identifying the highest contrast of the interference signal, one can infer the value of the (dominant) gravitational curvature from the optimal detuning frequency. This approach is experimentally simple but requires multiple AIF experiments to scan various detuning frequencies. The repetition poses a challenge, particularly for time-varying gravitational fields. Additionally, one must further analyse the appropriate estimator for $\Gamma(z)$ for a non-trivial gravitational field based on the optimal detuning of the AIF laser, possibly similar to this analysis, i.e., one needs to analyse which averaging procedure for $\Gamma(z)$ is involved for the detuning parameter that results in the highest contrast.

Until now, we have assumed the gravitational background near the interferometric baseline to be constant in time. This assumption, however, is not valid, especially for large experimental setups with baselines of 100 metres or more [124, 125]. Variations in ground and surface water $\rho_{\text{Water}}(t)$, seismic activity $\rho_{\text{Earth}}(t)$, and even air pressure differentials $\rho_{\text{Air}}(t)$ can significantly impact the experimental outcomes. It could therefore be beneficial to include an array of these newly described AIFs with an extension of Δh and separation Δl along the baseline of a large scale experiment, as depicted in Fig. 2.7. Ideally, this array would be located in a parallel shaft, measuring the gravitational field in real time, while other interferometric experiments are done in the main experimental facility. This array of CGIs should be seen as an integral part of the experimental setup and would be used to gauge and interpret the phase shifts of the other measurements.

Depending on the frequency of variations in the gravitational potential, Δh and Δl can be adjusted suitably to obtain a time- and height-resolved measurement of the gravitational field along the baseline. The temporal fluctuations of the gravitational field can – a priori – span a broad frequency domain. Consider, for the moment, that one wants to resolve changes in the gravitational field with a frequency centred around ν , and that each AIF run takes a

time $2T_R = 2\sqrt{2\Delta h/g}$. Firstly, we know that $\nu^{-1} > 2T_R$, which constrains T_R , i.e., Δh . This can be challenging for very high frequencies ν , as a smaller T_R results in a smaller phase shift, which must still be greater than the measurement uncertainty. Assuming a minimal phase resolution of 1 mrad, $N_R = 4$, and the phase output of the CGI being dominantly given by Eq. (2.44b), this would require a minimal interferometer time of $T_R \geq 0.3$ s, corresponding to a maximum variation frequency of the gravitational field of $\nu \leq 3.3$ Hz. Secondly, the choice of Δl depends on the complexity of the (static) gravitational potential and the measurement uncertainties of $g(z)$ and $\Gamma(z)$ given by the previously determined value of Δh . The separation between each interferometer height should be chosen such that it resolves the spatial and temporal changes, possibly by choosing non-uniform separations between each interferometer, i.e., tighter spacing, when the gravitational field is especially non-trivial in space or time.

Extending this concept, one could strategically position gravitational inhomogeneities, such as test masses, near the AIF baseline to explore the intricate interplay between quantum mechanics and gravity with greater precision. Phenomena such as the "gravitational Aharonov-Bohm" effect [103] and the fundamental interaction between quantum matter and (classical) gravitational fields require a precise interpretation of phase shifts, possibly reaching sub-mrad scales. Therefore, the analysis presented here serves as a crucial preliminary step towards achieving such goals.

Chapter 3

Atom Interferometers in Curved Spacetimes

"Die Quantenmechanik ist sehr achtung-gebietend. [...] Die Theorie liefert viel, aber dem Geheimnis des Alten bringt sie uns kaum näher. Jedenfalls bin ich überzeugt, daß *der* nicht würfelt."

Albert Einstein, 04.12.1926
in a letter to Max Born

It is now time to incorporate the effects of relativity into quantum mechanics, focusing on at least its first-order effects. By doing so, we aim to address higher order kinematic effects or effects arising from a post-Newtonian and non-linear description of gravity. Integrating relativity into quantum mechanics allows us to develop a more comprehensive framework that accounts for both the principles of quantum systems and the constraints imposed by relativity. Theories such as SR and classical mechanics rely on a class of preferred reference frames, specifically inertial frames. In these frames, the laws of motion can be expressed without the need for fictitious forces, and particles will continue to move uniformly unless subjected to an external force. In contrast, GR does not have any preferred frames of reference. For instance, it is entirely valid to select a local Cartesian coordinate system within a spatial hypersurface¹ of spacetime that contracts over time. In such a frame, the spatial coordinates of a particle considered to be at rest can diverge. This scenario exemplifies a coordinate singularity, which can occur quite frequently in GR. The takeaway here is that while tensors themselves remain invariant across all reference frames, their components – such as k_μ , z^μ , or $R_{\mu\nu}$ – are frame-dependent and do not inherently represent physically observable quantities.

Relativity and its often perplexing implications, such as gravitational time dilation and redshift, pose significant challenges when integrating into QM. This complexity can lead to intense debates about the possibility of measuring relativistic quantities using quantum sensors. An example of this is the proposed measurement schemes for gravitational redshift using matter wave interference [14, 126–130]. These discussions highlight the intricate interplay between relativity and quantum mechanics and underscore the ongoing efforts to develop methods that bridge the gap between these two foundational pillars of modern physics.

¹In a stationary spacetime with a timelike Killing vector field k , this would involve choosing three vectors that are mutually orthonormal to k and to each other.

3.1 Naïve Approach: Fine-Structure Experiments

We will now show how a simplistic or unrefined integration of relativity into the phase calculation framework of AIFs, as discussed in the previous chapter, can easily lead to incorrect results of a potentially significant order of magnitude. This simplified argument stems from a particular observation: In non-relativistic quantum optics, the Hamiltonian uses metres and seconds to measure length and time coordinates, respectively. However, in the post-Newtonian Hamiltonian derived from the Lagrangian in Eq. (1.32) for the motional case, these variables are no longer restricted to metres and seconds. This is evident when we calculate the metric tensor from Eq. (1.29) at the Earth's surface, which reveals a spacetime modified by the gravitational potential at that height, ϕ_0 , rather than a flat Minkowski spacetime. In simpler terms, an AIF experiment defines length and time scales using a laser that is locally at rest in the vicinity of the experiment. However, the time and length variables in the metric tensor, and hence in the Hamiltonian and Schrödinger equation of Eqs. (1.33) and (1.34), correspond to the time and lengths measured for an observer at spatial infinity.

To construct a Hamiltonian description that accurately represents these local length and time variables as operators, we must adjust our coordinate system so that the spacetime near the laser is Minkowskian in this reference frame. To show how much error can result from not transforming into adapted coordinates and not including all relativistic effects in the phase calculation, we (erroneously!) apply the framework of Chapter 2 to the relativistic motional Hamiltonian and see how large the resulting phase shifts become. To achieve this, we apply the aforementioned formalism to the currently most precise set of experiments utilising AIFs, specifically the measurements of the fine-structure constant using atomic recoils. We begin by introducing the underlying experimental geometries.

3.1.1 Interferometer Geometries to Measure the Fine-Structure Constant

Measurements of the fine-structure constant, α , using matter wave interferometers rely on determining the atomic recoil, $\frac{\hbar}{m_{\text{At}}}$, where m_{At} is the mass of the atom used in the interferometer. The fine-structure constant is defined as

$$\alpha = \sqrt{\frac{4\pi R_\infty m_{\text{At}}}{c m_e}} \sqrt{\frac{\hbar}{m_{\text{At}}}}, \quad (3.1)$$

where R_∞ is the Rydberg constant and m_e is the mass of an electron. By measuring the factor $\frac{\hbar}{m_{\text{At}}}$, one can derive a value for the fine-structure constant α . This is possible because the Rydberg constant R_∞ is known with a 6 parts-per-trillion (ppt) accuracy [131], and the mass ratios m_{At}/m_e are determined with less than parts-per-billion (ppb) accuracy for various atomic species through mass spectrometry [38]. With such precise knowledge of these constants, it allows for an accurate calculation of α . The official Committee on Data for Science and Technology (CODATA) value from 2018 of the fine-structure constant is $\alpha_{\text{CODATA18}} = 137.035999084^{-1}$. We continue with a more detailed explanation of how this recoil can be measured using AIFs, analysing the two most recent experiments of this kind.

We start by discussing the experiment conducted at Berkeley, which employed two ARBIs using Bragg interactions with Caesium-133 atoms. These interferometers are distinguished by the differing directions of the momentum imprinted by the Bloch oscillations and Bragg pulses, as illustrated in Fig. 3.1. This configuration results in a dominant phase shift

$$\Delta\Phi_{\text{Berkeley}}(\omega_m) = 16N_R(N_R + N_B)\omega_r T_R - 2N_R\omega_m T_R, \quad \text{with} \quad \omega_r = \frac{\hbar k_R^2}{2m_{\text{Cs}}}, \quad (3.2)$$

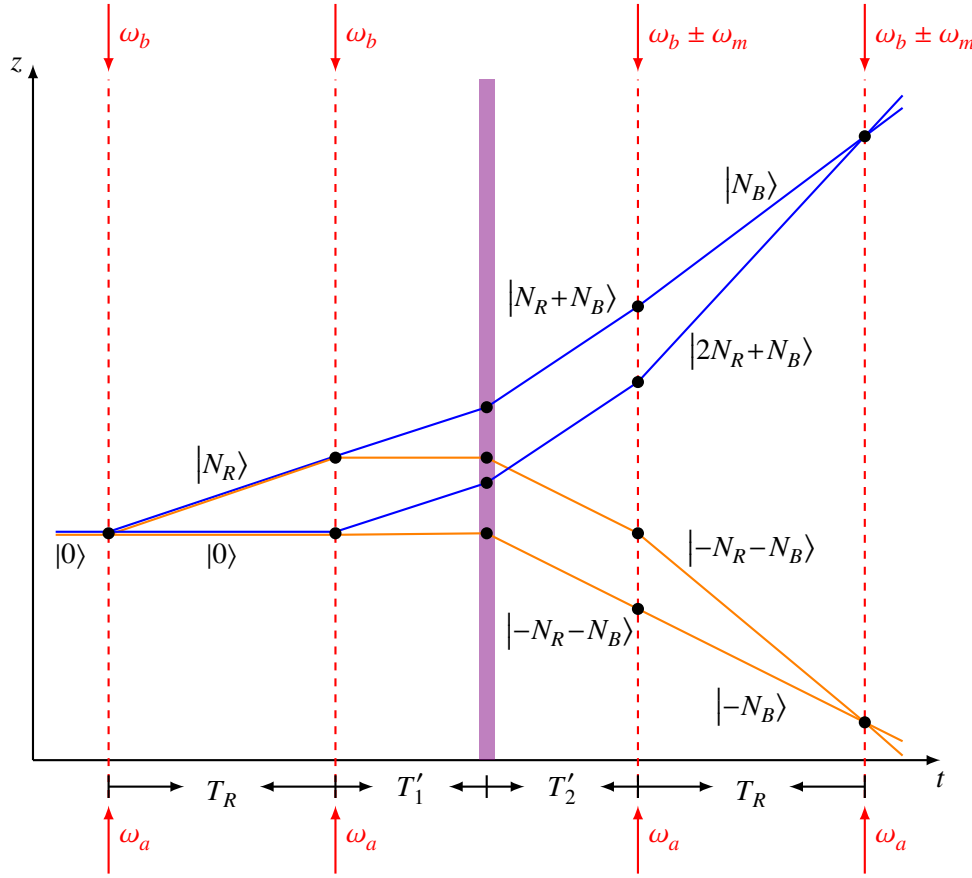


Figure 3.1: A simplified configuration for a double differential measurement involving two ARBI is illustrated in a freely falling reference frame, as similarly presented in Ref. [38]. The illustration includes atomic trajectories (orange and blue), Bloch oscillations (purple), and Bragg lasers (red, dashed). In this setup, the last two Bragg pulses are frequency-detuned by ω_m . The notation used has been adapted for our analysis.

which can be converted into a highly accurate dark-fringe measurement by adjusting the frequency ω_m to the point where $\Delta\Phi_{\text{Berkeley}}(\omega_m) = 0$. This occurs when $\omega_m = 8(N_R + N_B)\omega_r$. By inverting this equation, one can infer information about \hbar/m_{Cs} , and consequently α , resulting in the expression $\hbar/m_{\text{Cs}} = \omega_m/4(N_R + N_B)k_R^2$.

Two years later, a comparable experiment was conducted at Laboratoire Kastler Brossel (LKB) [39], utilising two-photon Raman transitions and Bloch oscillations with Rubidium-87 atoms, as illustrated in Fig. 3.2. The distinct internal levels are represented by solid and dashed lines. Based on the direction of the momentum kicks, four distinct versions of an SRBI can be created, classified by the signs of the parameters ε_R and ε_B . The resulting phase shift is given by

$$\Delta\Phi_{\text{LKB}}(\varepsilon_R, \varepsilon_B, \delta\omega_R) = T_R \left(2\varepsilon_R k_R \left(\frac{2\varepsilon_B \hbar k_B}{m} - g T_R \right) - \delta\omega_R \right) + \Phi_{\text{LS}}, \quad (3.3)$$

where $\delta\omega_R$ is the difference between the Raman laser frequencies of the first and third pulses, and Φ_{LS} denotes the phases originating from parasitic level shifts that cancel out in differential measurements. Similarly to the other fine-structure measurement, the value of $\delta\omega_R$ is adjusted so that the overall phase shift becomes zero. This specific detuning frequency is denoted as $\delta\omega_{R,0}(\varepsilon_R, \varepsilon_B)$. The atomic recoil can then be determined by summing over all

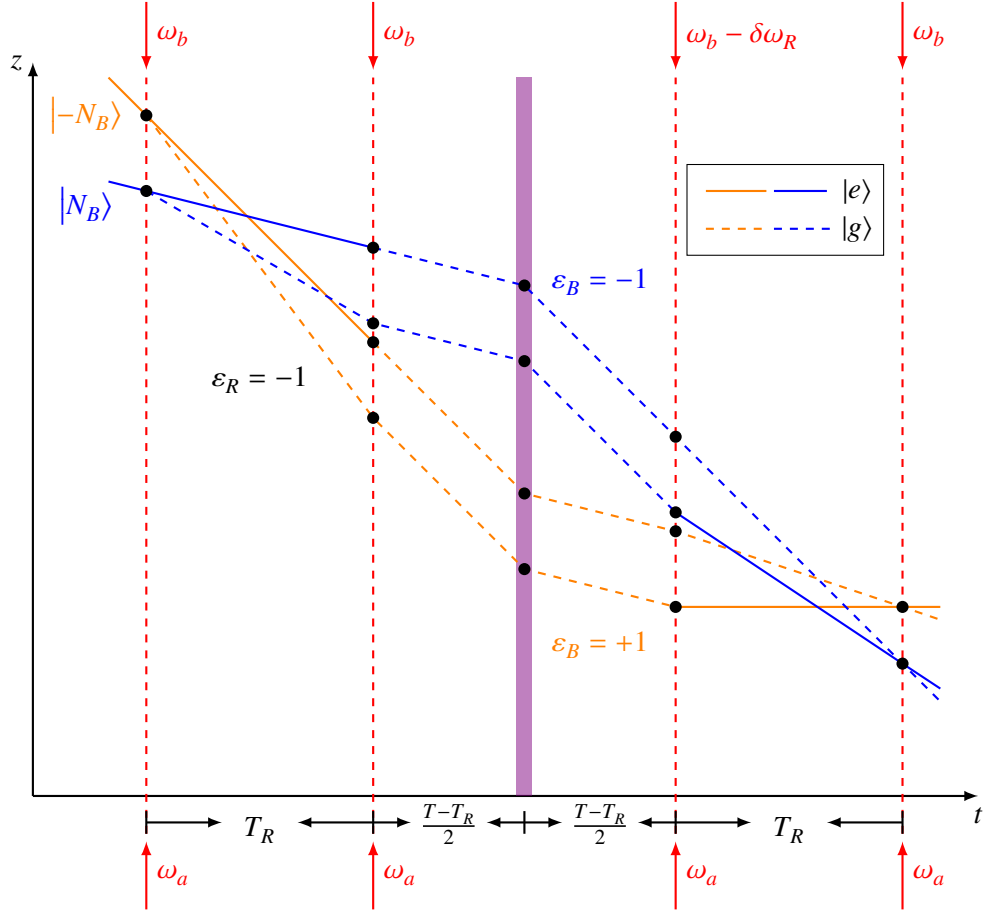


Figure 3.2: Illustration of the interferometer setup described in Ref. [39]. Atomic trajectories are shown in orange and blue, Bloch oscillations in purple, and Raman lasers in red, dashed. The notation has been adapted to suit our analysis. Depending on the orientations of the Bloch and Raman lasers, up to four different interferometer configurations can be realised. In the two depicted AIF configurations, the Raman pulses impart momentum downward to the initial wave packet, indicated by $\varepsilon_R = -1$, while the Bloch oscillations are presented in both orientations, $\varepsilon_B = \pm 1$.

four interferometer configurations

$$\frac{\hbar}{m_{\text{Rb}}} = \frac{1}{16N_R N_B k_R} \sum_{\varepsilon_R, \varepsilon_B = \pm 1} \delta\omega_{R,0}(\varepsilon_R, \varepsilon_B). \quad (3.4)$$

These two experiments were conducted with unprecedented accuracy at the 10^{-10} level, underscoring the significance of this burgeoning field of quantum optics and its potential applications. However, the two values obtained for α differ with a statistical significance of 5.4σ , and the cause of this discrepancy remains unknown.

3.1.2 Relativistic motional correction

We will now demonstrate how including relativistic effects solely based on the previously established manner into the theoretical framework can easily result in incomplete outcomes. These errors can reach a potentially measurable magnitude in the setups measuring the

fine-structure constant, underscoring the importance of a comprehensive and simultaneous consideration of these effects in the analysis.

Relativistic motional correction

Since the entire analysis in the previous chapter centred on the concept of a Lagrangian, we now explore what would occur if we extend this description to the next level, namely the post-Newtonian level. When considering the relativistically correct motional Lagrangian with respect to the metric tensor given by Eq. (1.29) for the previously mentioned description – in particular, Eq. (1.32) in one spatial dimension – one arrives at

$$L(z, \dot{z}) = -mc^2 + \frac{m\dot{z}(t)^2}{2} - m\phi(z(t)) + \frac{m\dot{z}(t)^4}{8c^2} - m\frac{2\beta - 1}{2} \frac{\phi(z(t))^2}{c^2} - m\frac{2\gamma + 1}{2} \frac{\phi(z(t))\dot{z}(t)^2}{c^2} + O(c^{-4}), \quad (3.5)$$

which was also analysed in Ref. [132]. By performing a Legendre transformation on this Lagrangian to obtain the corresponding Hamiltonian, the final term in the expression introduces, to lowest order, a relativistic correction to the kinetic energy of the form $\frac{m\dot{z}(t)^2}{2} \mapsto (1 + (2\gamma + 1)\frac{\phi_0}{c^2}) \frac{m\dot{z}(t)^2}{2}$. This is because the constant contribution of the gravitational potential would give a non-vanishing term to the kinetic energy. In the ARBI setup depicted in Fig. 2.1, where the leading order phase shift is proportional to $\frac{k^2\hbar T_R}{m}$, this relativistic correction would appear to induce an additional phase shift

$$\Delta\Phi_{\text{Old}} \propto \frac{k^2\hbar T_R}{m} \mapsto \Delta\Phi_{\text{New}} \propto \left(1 + (2\gamma + 1)\frac{\phi_0}{c^2}\right) \frac{k^2\hbar T_R}{m} + O(g/c^2), \quad (3.6)$$

when calculating the propagation phase using the action functional. In the Berkeley experiment, the wave vector contribution k^2 is represented as k_R^2 , while in the LKB experiment, it is $k_R k_B$. To keep the expressions short in this gedankenexperiment, we will denote it simply as k^2 . A change of the phase shift would, in turn, correspond to the following shift in the estimation of the fine-structure constant:

$$\begin{aligned} \alpha_{\text{Old}} &\mapsto \alpha_{\text{New}} \propto \alpha_{\text{Old}} \sqrt{1 - (2\gamma + 1)\frac{\phi_0}{c^2}} + O(g/c^2) \\ &\approx \alpha_{\text{Old}} \left(1 - \frac{2\gamma + 1}{2} \frac{\phi_0}{c^2}\right) + O(g/c^2). \end{aligned} \quad (3.7)$$

Assuming $\gamma = 1$, this results in a systematic offset of $\frac{3\phi_0}{2c^2} \approx 10^{-9} = 1 \text{ ppb}$. This offset is significant because it falls within the measurement accuracy of the current state-of-the-art fine-structure constant measurements [38, 39]. Coincidentally, it is also of the same order as the observed discrepancy.

Note that similar effects have been suggested as a potential resolution for a measurement anomaly in the anomalous magnetic moment of the muon [133]. This proposal was corrected by subsequent analyses [134–136]. Essentially, the error in the original proposal stemmed from two main issues: a miscalculation and an incorrect implementation of GR into QM. The arguments presented in [134] regarding why the constant part of the gravitational potential cannot influence any measurable phase shift are largely correct and provide valuable insight into the logical framework of GR. Nevertheless, there is one aspect of his reasoning that is somewhat incomplete. The claim is made that if an experiment generates a measurement

outcome dependent on Earth's ϕ_0 , then by the same reasoning, one would expect the constant contributions of the gravitational potentials from the Sun, the Milky Way, the local group, and so on – which progressively increase – to also affect the final phase shift. In contrast, we argue that there is a flaw in this reasoning. The key issue is that in an AIF experiment, both the atoms and lasers are in free fall relative to the Sun and all other large-scale structures in the universe, making it impossible to locally detect their gravitational influence. Nevertheless, the situation is different with respect to the Earth. While the atoms are in free fall relative to the Earth, the lasers are continuously accelerated at Earth's surface. This breaks the symmetry between Earth's gravitational influence and that of other gravitational sources.

Since the apparent ϕ_0 -dependent phase shift emerged from the relativistically modified Lagrangian in Eq. (3.5), we must consider whether this approach to incorporating relativity into the quantum mechanical framework is valid or if we failed to account for all sources of gravitational influence. Fortunately, it is the latter, and we will elaborate on this further in this chapter. The primary reason the conventional approach in quantum optics leads to this incorrect term is due to the different – and, in certain respects, more flexible – role of space and time in GR, as already mentioned in the introduction of this chapter. A simpler, and possibly more easy to grasp, illustration of this concept would involve altering the spatial basis vectors to be twice their original length, thereby defining a new "coordinate metre". Since the phase shift is a dimensionless quantity, changing the units should not affect any measurable outcomes, as each "coordinate metre" will cancel with its corresponding inverse, similar to how the spatial kick phase is calculated using $k \cdot z$. This underscores the necessity of adjusting the wave vectors, measured in m^{-1} , to account for the new basis vectors and their lengths. In GR, a similar process occurs; however, it is not only the length scales that change but also time, and the coordinate deviation arises from gravity itself.² The additional sources of gravity, therefore, arise from the "gravitational redefinition" of length and time. We will briefly illustrate the implications of this before proceeding with an in-depth analysis of a relativistic treatment.

Wave vector correction

By solving Maxwell's equations in the curved PPN spacetime, we will observe how a wave vector k must be replaced by $k \mapsto (1 - \gamma \frac{\phi_0}{c^2})k$. As k appears quadratically in the phase shift expression, this replacement results in a modification of the entire phase shift of

$$\Delta\Phi_{\text{Old}} \propto \frac{k^2 \hbar T_R}{m} \mapsto \Delta\Phi_{\text{New}} \propto \left(1 - 2\gamma \frac{\phi_0}{c^2}\right) \frac{k^2 \hbar T_R}{m} + O(g/c^2). \quad (3.8)$$

The corresponding correction to the fine-structure constant would be

$$\alpha_{\text{Old}} \mapsto \alpha_{\text{New}} \propto \alpha_{\text{Old}} \sqrt{1 + 2\gamma \frac{\phi_0}{c^2}} + O(g/c^2) \approx \alpha_{\text{Old}} \left(1 + \gamma \frac{\phi_0}{c^2}\right) + O(g/c^2), \quad (3.9)$$

such that it partially mitigates the apparent shift described in Eq. (3.6).

Proper time correction

Lastly, gravity affects the rate at which clocks run. If one wishes to rewrite every expression not in terms of "coordinate time" t but in terms of the proper time τ of a (nearby) resting

²Note that the definitions of the metre and the second are operationally set by the SI-system.

clock, the time coordinate is transformed as $t \mapsto \tau = \left(1 + \frac{\phi_0}{c^2}\right)t + O(g/c^2)$. This transformation reflects how gravitational potential ϕ_0 influences the passing of time, converting the coordinate time t into the proper time τ experienced by the clock at rest in the gravitational field. This would, similarly to before, induce a phase shift

$$\Delta\Phi_{\text{Old}} \propto \frac{k^2 \hbar T_R}{m} \mapsto \Delta\Phi_{\text{New}} \propto \left(1 - \frac{\phi_0}{c^2}\right) \frac{k^2 \hbar T_R}{m} + O(g/c^2), \quad (3.10)$$

which would then alter the α -measurement by

$$\alpha_{\text{Old}} \mapsto \alpha_{\text{New}} \propto \alpha_{\text{Old}} \sqrt{1 + \frac{\phi_0}{c^2} + O(g/c^2)} \approx \alpha_{\text{Old}} \left(1 + \frac{\phi_0}{2c^2}\right) + O(g/c^2). \quad (3.11)$$

If one combines all three of the presented relativistic corrections, the phase expressions given in this section are restored, meaning there are no ϕ_0/c^2 contributions left. This indicates that the combined effect of these corrections effectively cancels the influence of the gravitational potential on the phase shift when considered together, aligning the results with the expected outcomes in the absence of such corrections. As is evident, a more sophisticated approach is necessary to accurately calculate phase shifts in relativistic settings. We will undertake this task for the remainder of the chapter.

3.2 Transformation to Adapted Coordinates

As we have seen, using coordinates where the metric tensor approximates Minkowskian values at spatial infinity highlights asymptotic flatness. However, these coordinates cannot be used directly to represent local measurements of spacetime distances through simple coordinate expressions. Local measurements rely on co-located clocks and spatial length references established by light signals, such as those provided by a laser. These measurements would need to be described by a Hamiltonian operator, with the corresponding clock signal reflecting the metric at the experiment's location. To enable a simpler and more direct interpretation of coordinates as quantities measurable with a local clock and length scale, it is advantageous to transform to coordinates in which the metric components at the reference point of the experiment (set by the clock and laser) simplify to the Minkowski metric. This transformation facilitates clearer and more meaningful measurements by aligning the local coordinate system with the natural geometry of flat spacetime.

To clarify the notation: we denote our previous set of coordinates, introduced in Eq. (1.29), as (ct, \mathbf{r}) , with the components of the metric tensor represented as $g_{\mu\nu}$. We are now going to transform to a new set of coordinates (ct, \mathbf{r}) , where the metric tensor components are denoted as $g_{\mu\nu}$. We will stick to this notation and this choice of coordinates for the remainder of this thesis.

We want to construct a coordinate transformation $(x^\mu) = (ct, \mathbf{r}) \mapsto (x^\mu) = (ct, \mathbf{r})$ that brings the metric tensor to Minkowskian form at the point of the experiment, which we will generically denote by p_0 . Since the asymptotic coordinates in which the metric was originally expressed in Eq. (1.29) are already orthogonal to our order of approximation, in order to bring the metric to Minkowskian form at p_0 , we only have to perform a coordinate transformation such as to normalise the new coordinate basis vectors at this point. This can most easily be realised by globally rescaling the coordinates by the corresponding (constant) normalisation factor: defining the new coordinates according to

$$x^\mu = \sqrt{|g_{\mu\mu}(p_0)|} x^\mu \quad (3.12)$$

(no summation over μ), the new coordinate basis vectors are given by

$$\frac{\partial}{\partial x^\mu} = \frac{1}{\sqrt{|g_{\mu\mu}(p_0)|}} \frac{\partial}{\partial x^\mu}, \quad (3.13)$$

which are normalised at p_0 . Explicitly, defining $\phi_0 = \phi(p_0)$, the metric length of the timelike coordinate basis vector $\frac{\partial}{\partial x^0} \Big|_{p_0} = \frac{1}{c} \frac{\partial}{\partial t} \Big|_{p_0}$ of the asymptotic coordinates is given by

$$\sqrt{-g_{00}(p_0)} = \sqrt{1 + 2\frac{\phi_0}{c^2} + 2\beta\frac{\phi_0^2}{c^4} + O(c^{-6})} = 1 + \frac{\phi_0}{c^2} + \frac{2\beta - 1}{2} \frac{\phi_0^2}{c^4} + O(c^{-6}), \quad (3.14a)$$

while the metric length of the spacelike coordinate basis vector $\frac{\partial}{\partial x^i} \Big|_{p_0}$ of the asymptotic coordinates is (without summation over i)

$$\sqrt{g_{ii}(p_0)} = \sqrt{1 - 2\gamma\frac{\phi_0}{c^2} + O(c^{-4})} = 1 - \gamma\frac{\phi_0}{c^2} + O(c^{-4}). \quad (3.14b)$$

Therefore, we may take the constantly rescaled new coordinates expressed in terms of the old coordinates as

$$t = \left(1 + \frac{\phi_0}{c^2} + \frac{2\beta - 1}{2} \frac{\phi_0^2}{c^4}\right) t, \quad \mathbf{r} = \left(1 - \gamma\frac{\phi_0}{c^2}\right) \mathbf{r}. \quad (3.15a)$$

The inverse transformation is then given by

$$t = \left(1 - \frac{\phi_0}{c^2} - \frac{2\beta - 3}{2} \frac{\phi_0^2}{c^4} + O(c^{-6})\right) t, \quad \mathbf{r} = \left(1 + \gamma\frac{\phi_0}{c^2} + O(c^{-4})\right) \mathbf{r}, \quad (3.16a)$$

which enables us to compute the components of the metric tensor in the new coordinates via

$$g_{\mu\nu} = \frac{\partial x^\lambda}{\partial x^\mu} \frac{\partial x^\sigma}{\partial x^\nu} g_{\lambda\sigma}. \quad (3.17)$$

It will be convenient to define a shifted version of the gravitational potential as

$$\bar{\phi}(\mathbf{r}) = \phi(\mathbf{r}) - \phi_0, \quad (3.18)$$

that vanishes at Earth's radius. With this we obtain the new spatial components

$$g_{ij}(\mathbf{r}) = \left(1 - 2\gamma\frac{\bar{\phi}(\mathbf{r})}{c^2}\right) \delta_{ij} + O(c^{-4}) \quad (3.19)$$

and the new temporal component

$$g_{00}(\mathbf{r}) = -1 - 2\frac{\bar{\phi}(\mathbf{r})}{c^2} - 2\beta\frac{\bar{\phi}(\mathbf{r})^2}{c^4} - 4(\beta - 1)\frac{\phi_0\bar{\phi}(\mathbf{r})}{c^4} + O(c^{-6}) \quad (3.20)$$

of the metric tensor. The line element in the new coordinates reads accordingly as

$$ds^2 = -\left(c^2 + 2\bar{\phi}(\mathbf{r}) + 2\beta\frac{\bar{\phi}(\mathbf{r})^2}{c^2} + 4(\beta - 1)\frac{\phi_0\bar{\phi}(\mathbf{r})}{c^2}\right) dt^2 + \left(1 - 2\gamma\frac{\bar{\phi}(\mathbf{r})}{c^2}\right) d\mathbf{r}^2 + O(c^{-4}), \quad (3.21)$$

which is Minkowskian at the reference point $\mathbf{r} = \mathbf{R}_\oplus$. Note that there are only residual ϕ_0 -dependencies in this metric tensor, if $\beta \neq 1$, which can be interpreted as an additional non-linearity of gravity. The components of the inverse metric are then

$$g^{\mu\nu} = \begin{pmatrix} -1 + 2\frac{\bar{\phi}(\mathbf{r})}{c^2} + (2\beta - 4)\frac{\bar{\phi}(\mathbf{r})^2}{c^4} + 4(\beta - 1)\frac{\phi_0\bar{\phi}(\mathbf{r})}{c^4} + O(c^{-6}) & O(c^{-5}) \\ O(c^{-5}) & \left(1 + 2\gamma\frac{\bar{\phi}(\mathbf{r})}{c^2}\right)\mathbb{1}_3 + O(c^{-4}) \end{pmatrix}, \quad (3.22)$$

where $\mathbb{1}_3 = \text{diag}(1, 1, 1)$ denotes the 3×3 -identity matrix. Using these expressions, we can calculate the Christoffel symbols by applying Eq. (1.10). Given the assumption that the Newtonian gravitational potential is time-independent, i.e., $\partial_t\phi = 0$, we can identify the trivial and non-trivial Christoffel symbols in the chosen coordinate system. The trivial Christoffel symbols are

$$\Gamma^0_{00} = O(c^{-7}), \quad \Gamma^0_{ij} = O(c^{-5}), \quad \Gamma^i_{j0} = O(c^{-5}). \quad (3.23)$$

The non-vanishing Christoffel symbols, which have significant contributions, would typically depend on the spatial derivatives of the gravitational potential and the metric tensor components and are given by

$$\Gamma^0_{i0}(\mathbf{r}) = \Gamma^0_{0i}(\mathbf{r}) = \left(1 + 2(\beta - 1)\frac{\phi(\mathbf{r})}{c^2}\right)\frac{\bar{\phi}_{,i}(\mathbf{r})}{c^2} + O(c^{-6}), \quad (3.24a)$$

$$\Gamma^i_{00}(\mathbf{r}) = \left(1 + 2(\beta + \gamma)\frac{\phi(\mathbf{r})}{c^2} - 2(\gamma + 1)\frac{\phi_0}{c^2}\right)\frac{\delta^{ij}\bar{\phi}_{,j}(\mathbf{r})}{c^2} + O(c^{-6}), \quad (3.24b)$$

$$\Gamma^i_{jk}(\mathbf{r}) = -\gamma\frac{\delta^i_j\bar{\phi}_{,k}(\mathbf{r}) + \delta^i_k\bar{\phi}_{,j}(\mathbf{r}) - \delta_{jk}\delta^{il}\bar{\phi}_{,l}(\mathbf{r})}{c^2} + O(c^{-4}). \quad (3.24c)$$

Using this new set of coordinates, we can derive a relativistic Hamiltonian that incorporates the effects of spacetime curvature on the dynamics of the system. With this Hamiltonian, it is possible to solve the Schrödinger equation for the case of AIFs. In this context, the relativistic Hamiltonian would include terms reflecting the gravitational potential and its derivatives, as well as corrections stemming from relativistic effects encoded in the metric tensor. These contributions would modify the usual quantum mechanical Hamiltonian, typically altering kinetic and potential energy terms to account for relativistic influences.

3.3 Relativistically Corrected Hamiltonian

In our model, similar to the introduction, we consider the Hamiltonian for an atom as a system comprising two electromagnetically bound and spinless point charges. These charges interact with an external electromagnetic field and operate within the weakly curved PPN spacetime metric described in Eq. (1.29). This setup has been detailed in the work by Schwartz et al. [132] within the original asymptotic coordinate system. Here, we aim to replicate this derivation using the new set of coordinates introduced in Eq. (3.15a), where the metric tensor is provided by Eq. (3.21). To zeroth order in $1/c^2$, the Hamiltonian reflects the standard non-relativistic quantum optics description of an atom, as analysed in Section 1.2. However, the terms of order $1/c^2$ represent the leading relativistic corrections. These corrections influence the energies associated with the COM and the internal (electronic) degrees of freedom of the atom. They also affect the interactions between these energies

and the coupling with the external electromagnetic field. This refined approach allows for a more precise representation of the atom's behaviour under both, relativistic and quantum mechanical influences, providing additional insights into atom interferometry applications within a relativistically influenced environment.

This novel Hamiltonian can then be grouped into the distinct components

$$\hat{H} = \hat{H}_{\text{COM}} + \hat{H}_{\text{I}} + \hat{H}_{\text{M-I}} + \hat{H}_{\text{A-L}} + \mathcal{O}(c^{-4}), \quad (3.25)$$

where \hat{H}_{COM} is the Hamiltonian for COM motion, the Hamiltonian for the internal degrees of freedom is \hat{H}_{I} , their relativistic coupling is described by $\hat{H}_{\text{M-I}}$, and the relativistically corrected dipole interaction of the atom with the external EM field is contained in $\hat{H}_{\text{A-L}}$, as before. The external EM field, being a classical solution to the source-free Maxwell equations in our curved spacetime, and the gravitational field itself provide the background interaction fields for the atom's dynamics. To recap, the relativistically corrected canonical position and momentum operators of COM and internal degrees of freedom will be denoted by $\hat{\mathbf{R}}$, $\hat{\mathbf{P}}$ and $\hat{\mathbf{r}}$, $\hat{\mathbf{p}}$, respectively. The total (rest) mass of the atom will be denoted by m , and the reduced mass of the internal degree of freedom by μ . The Hamiltonian for COM motion in the adapted (locally Minkowskian) coordinates is given by

$$\hat{H}_{\text{COM}} = m\bar{\phi}(\hat{\mathbf{R}}) + \frac{\hat{\mathbf{P}}^2}{2m} \quad (3.26a)$$

$$+ \frac{1}{mc^2} \left[\frac{2\gamma + 1}{2} \hat{\mathbf{P}}\bar{\phi}(\hat{\mathbf{R}})\hat{\mathbf{P}} - \frac{\hat{\mathbf{P}}^4}{8m^2} + \frac{2\beta - 1}{2} m^2 \bar{\phi}(\hat{\mathbf{R}})^2 + 2(\beta - 1)m^2 \phi_0 \bar{\phi}(\hat{\mathbf{R}}) \right] + \mathcal{O}(c^{-4}). \quad (3.26b)$$

The terms in the square brackets, i.e., Eq. (3.26b), comprise the relativistic corrections of the COM energy, and will be the most relevant for our analysis. The first of those terms corresponds to the metric correction of the length of the vector $\hat{\mathbf{P}}$ determining the kinetic energy, written in symmetric ordering. The second term is the special relativistic correction to the kinetic energy, the third term describes the relativistic non-linear correction to the Newtonian potential, and the last term corresponds to non-linear GR effects.

The internal Hamiltonian,

$$\hat{H}_{\text{I}} = \frac{\hat{\mathbf{p}}^2}{2\mu} - \frac{e^2}{4\pi\epsilon_0|\hat{\mathbf{r}}|} + \hat{H}_{\text{FS}}, \quad (3.27)$$

consists of the non-relativistic kinetic energy and Coulomb interaction. Additional relativistic corrections are subsumed in the fine-structure Hamiltonian \hat{H}_{FS} , which contains the special relativistic corrections of kinetic and Coulomb energy, as well as spin-orbit interaction etc., if spin was included. We refer to Ref. [132] for the explicit form of \hat{H}_{FS} . In the following, we take these corrections to be accounted for in the internal stationary states and energies, e.g. the ground state $\hat{H}_{\text{I}}|g\rangle = E_g|g\rangle$.

The relativistic coupling of COM and internal degrees of freedom has the form

$$\hat{H}_{\text{M-I}} = \frac{1}{mc^2} \left(m\phi(\hat{\mathbf{R}}) - \frac{\hat{\mathbf{P}}^2}{2m} \right) \otimes \hat{H}_{\text{I}} + \frac{\phi(\hat{\mathbf{R}})}{c^2} \otimes \left(2\gamma \frac{\hat{\mathbf{p}}^2}{2\mu} - \gamma \frac{e^2}{4\pi\epsilon_0|\hat{\mathbf{r}}|} \right). \quad (3.28)$$

The first part of this equation can be interpreted as arising from the correction of the mass of the atom due to internal binding energy, as can be seen by replacing $m \mapsto m + \hat{H}_{\text{I}}/c^2$ in Eq. (3.26a) and expanding in $1/c^2$. The second part describes the metric corrections of the internal kinetic and Coulomb energy, similar to Eq. (3.26b), cf. Ref. [25]. For AIFs

involving elastic scattering processes only, the atom remains in its internal ground state $|g\rangle$ at all times. In this case the terms in Eq. (3.28) contribute only trivially to the dynamics of the problem: As explained above, the effect of the first term can be absorbed in a rescaling of the atomic mass $m \mapsto m + E_g/c^2$. The second term does not contribute at all since it has vanishing matrix elements for stationary states [137] as a consequence of the virial theorem³. However, they can be the main contribution to the phase in quantum clock AIFs with inelastic scattering processes [18, 69, 74, 138].

Finally, the Hamiltonian for the interaction of the atom with the external light field is

$$\hat{H}_{\text{A-L}} = -\hat{\mathbf{d}} \cdot \mathbf{E}^\perp(\hat{\mathbf{R}}) + \frac{1}{2m} [\hat{\mathbf{P}} \cdot (\hat{\mathbf{d}} \times \mathbf{B}(\hat{\mathbf{R}})) + \text{h.c.}], \quad (3.29)$$

where $\hat{\mathbf{d}}$, \mathbf{E} , and \mathbf{B} denote the dipole moment operator and the electric and magnetic fields, respectively. The atom-light interaction in Eq. (3.29) is written in the dipole approximation and includes the Röntgen term as the dominant relativistic correction⁴. In comparison to the Hamiltonian from Ref. [132], only the last term in the motional Hamiltonian is a new contribution. Apart from this new term, the only difference is the dependence on $\bar{\phi}$ instead of ϕ .

3.4 Motional Hamiltonian

In this section, we solve the Schrödinger equation for the basic interferometer geometries outlined in Sec. 2.1, this time considering the gravitational background within the PPN formalism. The previous analysis was accurate up to order $O(3)$. GR effects appear at order $O(4)$, except for a single contribution at order $O(3)$. As a result, we will also incorporate the subsequent Taylor coefficient in the series expansion of the gravitational potential into our formalism. Specifically, we will include the spatial derivative of the gravity gradient, denoted by Λ , into our description by setting

$$\bar{\phi}(z) = \phi(z) - \phi_0 = g z - \frac{1}{2} \Gamma z^2 + \frac{1}{3} \Lambda z^3 + O(\partial_r^4 \phi). \quad (3.30)$$

The corresponding Hamiltonian from Eq. (3.26) for COM motion along the vertical axis then becomes

$$\begin{aligned} \hat{H}_{\text{COM}} = & \frac{\hat{P}^2}{2m} + mg\hat{Z} - \frac{m}{2}\Gamma\hat{Z}^2 + \frac{m}{3}\Lambda\hat{Z}^3 + \frac{2\gamma+1}{2}\frac{g}{mc^2}\hat{P}\hat{Z}\hat{P} \\ & - \frac{\hat{P}^4}{8m^3c^2} + \frac{2\beta-1}{2}\frac{mg^2}{c^2}\hat{Z}^2 + 2(\beta-1)\frac{m\phi_0g}{c^2}\hat{Z} + O(\Gamma c^{-2}). \end{aligned} \quad (3.31)$$

The relativistically corrected Lagrangian for a trajectory in the z -direction, which corresponds to the Hamiltonian given in Eq. (3.31), can be expressed as

$$\begin{aligned} L(z, \dot{z}) = & \frac{m\dot{z}^2}{2} - m\bar{\phi}(z) + \frac{m\dot{z}^4}{8c^2} \\ & - m\frac{2\beta-1}{2}\frac{\bar{\phi}(z)^2}{c^2} - m\frac{2\gamma+1}{2}\frac{\bar{\phi}(z)\dot{z}^2}{c^2} - 2(\beta-1)m\phi_0\frac{\bar{\phi}(z)}{c^2} + O(c^{-4}), \end{aligned} \quad (3.32)$$

³This follows from $\frac{i}{\hbar} [\hat{\mathbf{r}} \cdot \hat{\mathbf{p}}, \hat{H}_1] = 2\frac{\hat{p}^2}{2\mu} - \frac{e^2}{4\pi\epsilon_0} \frac{1}{|\hat{\mathbf{r}}|} + O(c^{-2})$, and taking the matrix element with respect to $|g\rangle$.

⁴We disregard further relativistic corrections relevant in strong magnetic fields, cf. Eq. (5.9) in Schwartz et al. [132].

Parameter	Definition	Magnitude for 10 m baseline AIF	
		$i = R$ (Bragg)	$i = B$ (Bloch)
\mathcal{Z}_0	$\frac{z_0}{cT_R}$	0	
\mathcal{V}_0	$\frac{v_0}{c}$	4.3×10^{-8}	
\mathcal{F}_R	$\frac{\hbar\omega_R}{mc^2}$	8.1×10^{-20}	
\mathcal{G}_0	$\frac{\phi_0}{c^2}$	7×10^{-10}	
\mathcal{Z}_L	$\frac{z_L}{cT_R}$	2.6×10^{-9}	
\mathcal{Z}_U	$\frac{z_U}{cT_R}$	2.8×10^{-8}	
\mathcal{H}	$\frac{z_U - z_L}{cT_R}$	3.1×10^{-8}	
$\mathcal{G}_{1,i}$	$\frac{gT_i}{c}$	4.2×10^{-8}	1.3×10^{-8}
$\mathcal{G}_{2,i}$	ΓT_i^2	5.2×10^{-6}	4.9×10^{-7}
$\mathcal{G}_{3,i}$	$\Lambda c T_i^3$	4.8×10^{-4}	1.4×10^{-5}
\mathcal{R}_i	$\frac{\hbar k_i}{mc}$	3.9×10^{-11}	1.2×10^{-9}

Table 3.1: Complete list of dimensionless parameters for an AIF, including FSL and relativistic effects.

where we deliberately did not expand the gravitational potential to keep the following formulas short. As before, we need to determine the classical trajectories of the upper and lower arms of the AIF, which are derived from the ELE associated with Eq. (3.32). Conducting the analysis in a dimensionless form, as done previously, introduces two new dimensionless parameters: ϕ_0/c^2 and $\Lambda c T_i^3$ for $i = R, B$. These new parameters can be combined with the ones previously defined in Table 2.1 and the ones corresponding to FSL contribution from Table 2.3 and are summarised in Table 3.1. First, we calculate the derivatives of the Lagrangian as

$$\frac{\partial L}{\partial z} = -m\partial_z \bar{\phi}(z) - \frac{m}{c^2} \partial_z \bar{\phi}(z) \left[(2\beta - 1)\bar{\phi}(z) + \frac{2\gamma + 1}{2} \dot{z}^2 + 2(\beta - 1)\phi_0 \right] + O(c^{-4}) \quad (3.33a)$$

$$\frac{\partial L}{\partial \dot{z}} = m\dot{z} + \frac{m}{c^2} \left[\frac{\dot{z}^3}{2} - (2\gamma + 1)\bar{\phi}(z)\dot{z} \right] + O(c^{-4}) \quad (3.33b)$$

$$\frac{d}{dt} \frac{\partial L}{\partial \dot{z}} = m\ddot{z} + \frac{m}{c^2} \left[\frac{3}{2} \dot{z}^2 \ddot{z} - (2\gamma + 1)\dot{z}^2 \partial_z \bar{\phi}(z) - (2\gamma + 1)\bar{\phi}(z)\ddot{z} \right] + O(c^{-4}), \quad (3.33c)$$

where we have used that $\dot{\bar{\phi}}(z)\dot{z} = \dot{z}^2 \partial_z \bar{\phi}(z)$, which holds because $\frac{d}{dt} \bar{\phi}(z(t)) = \frac{\partial \bar{\phi}}{\partial z} \frac{dz}{dt}$. The ELE

$\frac{d}{dt} \frac{\partial L}{\partial \ddot{z}} - \frac{\partial L}{\partial z} = 0$ can then be expressed recursively in terms of \ddot{z} as

$$\ddot{z} = -\partial_z \bar{\phi}(z) + \frac{1}{c^2} \left[(2\gamma + 1) \dot{z}^2 \partial_z \bar{\phi}(z) - \frac{3}{2} \dot{z}^2 \ddot{z} + (2\gamma + 1) \bar{\phi}(z) \ddot{z} - (2\beta - 1) \bar{\phi}(z) \partial_z \bar{\phi}(z) - \frac{2\gamma + 1}{2} z^2 \partial_z \bar{\phi}(z) - 2(\beta - 1) \phi_0 \partial_z \bar{\phi}(z) \right] + O(c^{-4}).$$

Inserting the c^0 -contribution into the \ddot{z} -term on the right-hand side results in

$$\ddot{z} = -\partial_z \left[\left(1 + 2(\beta - 1) \frac{\phi_0}{c^2} \right) \bar{\phi}(z) + \frac{\beta + \gamma}{c^2} \bar{\phi}(z)^2 \right] + \frac{\gamma + 2}{c^2} \dot{z}^2 \partial_z \bar{\phi}(z) + O(c^{-4}). \quad (3.34)$$

We now use the approximation of the gravitational potential to relevant order, i.e., Eq. (3.30), which gives the ELE

$$\ddot{z}(t) = -\left(1 + 2(\beta - 1) \frac{\phi_0}{c^2} \right) g + \left(1 + 2(\beta - 1) \frac{\phi_0}{c^2} \right) \Gamma z(t) - \Lambda z(t)^2 - 2g^2 \frac{\beta + \gamma}{c^2} z(t) + (\gamma + 2) \frac{g}{c^2} \dot{z}(t)^2 + O(\partial_r^4 \phi, \Lambda c^{-2}, c^{-4}), \quad (3.35)$$

with the same initial conditions as before: $z(0) = z_0$, $\dot{z}(0) = v_0 + N_R \frac{\hbar k_R}{m} + N_B \frac{\hbar k_B}{m}$.

Rewriting the ELE in a dimensionless form yields

$$\ddot{\xi}(\tau) = -\mathcal{G}_{1,R} + \mathcal{G}_{2,R} \xi(\tau) - \mathcal{G}_{3,R} \xi(\tau)^2 - 2(\beta + \gamma) \mathcal{G}_{1,R}^2 \xi(\tau) + (\gamma + 2) \mathcal{G}_{1,R} \dot{\xi}(\tau)^2 + 2(\beta - 1) \mathcal{G}_0 \left[-\mathcal{G}_{1,R} + \mathcal{G}_{2,R} \xi(\tau) \right] + O(4), \quad (3.36)$$

with $\xi(0) = \mathcal{Z}_0$, $\dot{\xi}(0) = \mathcal{V}_0 + N_R \mathcal{R}_R + N_B \mathcal{R}_B$ defined as before. The ELE is, up to third order in the dimensionless parameters from Table 3.1, given by

$$\xi(\tau) = \xi(0) + \dot{\xi}(0) \tau - \frac{1}{2} \mathcal{G}_{1,R} \tau^2 + \xi_2(\tau) + \xi_3(\tau) + O(4) \quad (3.37a)$$

with the two contributions

$$\xi_2(\tau) = -(\beta - 1) \mathcal{G}_0 \mathcal{G}_{1,R} \tau^2 + \mathcal{G}_{2,R} \left(\frac{1}{2} \xi(0) \tau^2 + \frac{1}{6} \dot{\xi}(0) \tau^3 - \frac{1}{24} \mathcal{G}_{1,R} \mathcal{G}_{2,R} \tau^4 \right) \quad (3.37b)$$

$$\begin{aligned} \xi_3(\tau) = & \left(\frac{C_3}{2} \mathcal{G}_0 \mathcal{G}_{2,R} \xi(0) - \frac{1}{2} \xi(0)^2 \mathcal{G}_{3,R} - C_4 \mathcal{G}_{1,R}^2 \xi(0) + C_5 \mathcal{G}_{1,R} \dot{\xi}(0)^2 \right) \tau^2 \\ & + \frac{1}{3} \left(\frac{C_3}{2} \mathcal{G}_0 \mathcal{G}_{2,R} \dot{\xi}(0) - \xi(0) \dot{\xi}(0) \mathcal{G}_{3,R} - C_4 \mathcal{G}_{1,R}^2 \dot{\xi}(0) \right) \tau^3 \\ & + \frac{1}{12} \left(\frac{1}{2} \xi(0) \mathcal{G}_{2,R}^2 - \mathcal{G}_{3,R} \dot{\xi}(0)^2 + \xi(0) \mathcal{G}_{1,R} \mathcal{G}_{3,R} + C_6 \mathcal{G}_{1,R}^3 - C_3 \mathcal{G}_0 \mathcal{G}_{1,R} \mathcal{G}_{2,R} \right) \tau^4 \\ & + \frac{1}{20} \left(\frac{1}{6} \dot{\xi}(0) \mathcal{G}_{2,R}^2 + \dot{\xi}(0) \mathcal{G}_{1,R} \mathcal{G}_{3,R} \right) \tau^5 - \frac{\mathcal{G}_{1,R}}{120} \left(\frac{1}{6} \mathcal{G}_{2,R}^2 + \mathcal{G}_{1,R} \mathcal{G}_{3,R} \right) \tau^6. \end{aligned} \quad (3.37c)$$

Here we used the constants

$$C_1 = \frac{2\beta - 1}{2}, \quad C_2 = \frac{2\gamma + 1}{2}, \quad C_3 = 2(\beta - 1), \quad (3.37d)$$

$$C_4 = \beta + \gamma, \quad C_5 = \frac{\gamma + 2}{2}, \quad C_6 = \beta - 2 \quad (3.37e)$$

in order to denote the trajectories as compact as possible. We obtain an expression for the propagation phase integral in terms of dimensionless parameters as

$$\begin{aligned} \frac{1}{\hbar} \int dt L(\xi(t), \dot{\xi}(t)) = \omega_C T_R \int d\tau \left(-\mathcal{G}_{1,R} \xi(\tau) + \frac{1}{2} \mathcal{G}_{2,R} \xi(\tau)^2 - \frac{1}{3} \mathcal{G}_{3,R} \xi(\tau)^3 + \frac{1}{2} \dot{\xi}(\tau)^2 \right. \\ \left. + \frac{1}{8} \dot{\xi}(\tau)^4 - \frac{2\beta - 1}{2} \mathcal{G}_{1,R}^2 \xi(\tau) - \frac{2\gamma + 1}{2} \mathcal{G}_{1,R} \xi(\tau) \dot{\xi}(\tau)^2 \right. \\ \left. - 2(\beta - 1) \mathcal{G}_0 (\mathcal{G}_{1,R} \xi(\tau) - \mathcal{G}_{2,R} \xi(\tau)^2) \right) + O(5), \end{aligned} \quad (3.38)$$

which is correct to order $O(4)$.

3.5 Relativistic Light Hamiltonian

Following Refs. [87, 139], our focus so far has been on the relativistic corrections to the atomic degrees of freedom. Next, we will analyse the EM field and its interaction with atoms in the context of PPN curved spacetime. Our approach will be to first determine the eigenmodes of the wave equation for the light field, incorporating relativistic corrections. In the subsequent section, these eigenmodes will then be used to describe the interaction between atoms and a coherent laser field, using a semi-classical approximation. Specifically, we will consider a coherent laser field expressed in these eigenfunctions, coupled to an atom via the interaction Hamiltonian \hat{H}_{A-L} as presented in Eq. (3.29). A similar approach is described in Ref. [74] and will be mentioned below.

The most straightforward way to obtain the Maxwell equations in general coordinates is to start from the Lagrangian and use the variational principle. The Lagrangian for an EM field in vacuum with EM field strength tensor $F_{\mu\nu}$ is given by

$$L_{EM} = \int \frac{\sqrt{-g}}{4\mu_0} F_{\mu\nu} F^{\mu\nu} d^3x, \quad (3.39)$$

where g is the determinant of the matrix of spacetime metric components, and the field strength tensor is taken as derived from a vector potential A_μ via $F_{\mu\nu} = A_{\nu,\mu} - A_{\mu,\nu} = A_{\nu,\mu} - A_{\mu,\nu}$ (thus, the homogeneous Maxwell equations $dF = 0$, or in components $F_{[\mu\nu;\rho]} = F_{[\mu\nu,\rho]} = 0$, are automatically satisfied). The variational principle, varying with respect to A_μ , then directly leads to the inhomogeneous Maxwell equations (in our case with vanishing source)

$$F^{\alpha\beta}_{;\beta} = \nabla_\beta F^{\alpha\beta} = \nabla_\beta (\nabla^\alpha A^\beta - \nabla^\beta A^\alpha) = 0, \quad (3.40)$$

where we have expressed the field strength tensor in terms of the four-vector potential A^α . Next we commute the covariant derivatives in the first term at the expense of introducing a curvature term, i.e.,

$$A^\beta_{;\beta} - A^{\alpha;\beta}_{;\beta} + R^\alpha_\beta A^\beta = 0. \quad (3.41)$$

The non-commutativity of covariant derivatives therefore introduces curvature terms and deviates from the usual rule of interchanging partial derivatives with covariant ones,⁵ c.f. Ref [140][Box 16.1]. In order to see which magnitude such curvature terms will have we need to calculate the non-zero Christoffel symbols of the PPN spacetime, as already done in

⁵Sometimes referred to as the *comma goes to semicolon* rule.

Eq. (3.24), combined with the assumption $\phi(t, \mathbf{r}) = \phi(z)$, which yields

$$\Gamma_{z0}^0 = \Gamma_{0z}^0 = \left(1 + 2(\beta - 1)\frac{\phi}{c^2}\right) \frac{\bar{\phi}_{,z}}{c^2} + O(c^{-6}), \quad (3.42a)$$

$$\Gamma_{00}^z = \left(1 + 2(\beta + \gamma)\frac{\phi}{c^2} - 2(\gamma + 1)\frac{\phi_0}{c^2}\right) \frac{\bar{\phi}_{,z}}{c^2} + O(c^{-6}), \quad (3.42b)$$

$$\Gamma_{xx}^z = \Gamma_{yy}^z = \gamma \frac{\bar{\phi}_{,z}}{c^2} + O(c^{-4}), \quad (3.42c)$$

$$\Gamma_{zz}^z = \Gamma_{xz}^x = \Gamma_{zx}^x = \Gamma_{yz}^y = \Gamma_{zy}^y = -\gamma \frac{\bar{\phi}_{,z}}{c^2} + O(c^{-4}). \quad (3.42d)$$

From those Christoffel symbols one can calculate the non-vanishing components of the Ricci tensor using

$$R_{\mu\nu} = \partial_\lambda \Gamma_{\mu\nu}^\lambda - \partial_\mu \Gamma_{\nu\lambda}^\lambda + \Gamma_{\sigma\lambda}^\sigma \Gamma_{\mu\nu}^\lambda - \Gamma_{\mu\lambda}^\sigma \Gamma_{\sigma\nu}^\lambda = \partial_\lambda \Gamma_{\mu\nu}^\lambda - \partial_\mu \Gamma_{\nu\lambda}^\lambda + O(c^{-4}), \quad (3.43)$$

which gives rise to the only components of the Ricci curvature at order $O(c^{-2})$ of

$$R_{00} = \partial_z \Gamma_{00}^z = \frac{\partial_z^2 \bar{\phi}(z)}{c^2}, \quad R_{xx} = \partial_z \Gamma_{xx}^z = \gamma \frac{\partial_z^2 \bar{\phi}(z)}{c^2}, \quad (3.44a)$$

$$R_{yy} = \partial_z \Gamma_{yy}^z = \gamma \frac{\partial_z^2 \bar{\phi}(z)}{c^2}, \quad R_{zz} = -2\partial_z \Gamma_{zz}^z - \partial_z \Gamma_{z0}^0 = (2\gamma - 1) \frac{\partial_z^2 \bar{\phi}(z)}{c^2}. \quad (3.44b)$$

The Ricci curvature therefore only contributes at the order $O(c^{-2})$, which we have previously neglected. The curvature contribution in Eq. (3.41) is therefore beyond our approximation level and will be omitted.

For the upcoming calculations it will turn out beneficial to rewrite Maxwell's equations with respect to a covariant EM potential, such that we rather work with

$$F_{\alpha\beta}^{\beta} = \nabla^\beta F_{\alpha\beta} = \nabla^\beta (\nabla_\alpha A_\beta - \nabla_\beta A_\alpha) = 0, \quad (3.45)$$

where we now need to imply a gauge condition. Three different choices arise canonically at this stage, due to the $(3 + 1)$ -split of the metric, namely the fully relativistic Lorenz Gauge (LG) and two additional versions of the Coulomb gauge, i.e., the Geometric Coulomb Gauge (GCG) and Background Coulomb Gauge (BCG), formulated as

$$\text{LG:} \quad \nabla_\beta A^\beta = A^\beta_{;\beta} = A_\beta^{\beta} = 0, \quad (3.46a)$$

$$\text{GCG:} \quad \nabla^i A_i = A_i^{,i} = 0, \quad (3.46b)$$

$$\text{BCG:} \quad \partial^i A_i = A_i^{,i} = 0. \quad (3.46c)$$

The BCG refers to the "usual" Coulomb gauge, commonly employed in quantum optics.

3.5.1 Wave Equations in the Geometric Coulomb Gauge:

The gauge condition, when incorporating the expanded covariant derivative, is expressed as

$$0 = \nabla^i A_i = g^{i\lambda} \nabla_\lambda A_i = \partial^i A_i - g^{i\lambda} \Gamma_{\lambda i}^\sigma A_\sigma, \quad (3.47)$$

to allow for Maxwell's equations to be expanded in a manner that directly contains this term. Starting with Maxwell's equations from Eq. (3.45) we begin to expand all differential terms.

We then colour-code the terms that appear in the gauge condition specified in Eq. (3.47) in order to derive

$$\begin{aligned}
0 &= F_{\nu\mu}^{\mu} = A_{\mu}^{\mu}_{;\nu} - A_{\nu;\mu}^{\mu} \\
&= g^{\mu\lambda} \partial_{\lambda} \partial_{\mu} A_{\nu} - \partial_{\nu} \partial^{\mu} A_{\mu} - g^{\mu\lambda} \Gamma^{\sigma}_{\lambda\mu} (\partial_{\sigma} A_{\nu} + \partial_{\nu} A_{\sigma}) - g^{\mu\lambda} \Gamma^{\sigma}_{\lambda\nu} (\partial_{\mu} A_{\sigma} - \partial_{\sigma} A_{\mu}) \\
&= g^{\mu\lambda} \partial_{\lambda} \partial_{\mu} A_{\nu} - \partial_{\nu} \partial^0 A_0 - \partial_{\nu} \partial^i A_i - g^{\mu\lambda} \Gamma^{\sigma}_{\lambda\mu} \partial_{\sigma} A_{\nu} + \partial_{\nu} g^{0\lambda} \Gamma^{\sigma}_{\lambda 0} A_{\sigma} + \partial_{\nu} g^{i\lambda} \Gamma^{\sigma}_{\lambda i} A_{\sigma} \\
&\quad - (\partial_{\nu} g^{\mu\lambda}) \Gamma^{\sigma}_{\lambda\mu} A_{\sigma} - g^{\mu\lambda} (\partial_{\nu} \Gamma^{\sigma}_{\lambda\mu}) A_{\sigma} - g^{\mu\lambda} \Gamma^{\sigma}_{\lambda\nu} \partial_{\mu} A_{\sigma} + g^{\mu\lambda} \Gamma^{\sigma}_{\lambda\nu} \partial_{\sigma} A_{\mu} \\
&= g^{\mu\lambda} (\partial_{\lambda} \partial_{\mu} A_{\nu} - \Gamma^{\sigma}_{\lambda\mu} \partial_{\sigma} A_{\nu} - (\partial_{\nu} \Gamma^{\sigma}_{\lambda\mu}) A_{\sigma} - \Gamma^{\sigma}_{\lambda\nu} \partial_{\mu} A_{\sigma} + \Gamma^{\sigma}_{\lambda\nu} \partial_{\sigma} A_{\mu}) \\
&\quad - \partial_{\nu} (\partial^0 A_0 - g^{0\lambda} \Gamma^{\sigma}_{\lambda 0} A_{\sigma}) - (\partial_{\nu} g^{\mu\lambda}) \Gamma^{\sigma}_{\lambda\mu} A_{\sigma} - \partial_{\nu} (\partial^i A_i - g^{i\lambda} \Gamma^{\sigma}_{\lambda i} A_{\sigma}) \\
&= g^{00} (\partial_0^2 A_{\nu} - \Gamma^{\sigma}_{00} \partial_{\sigma} A_{\nu} - (\partial_{\nu} \Gamma^{\sigma}_{00}) A_{\sigma} - \Gamma^{\sigma}_{0\nu} \partial_0 A_{\sigma} + \Gamma^{\sigma}_{0\nu} \partial_{\sigma} A_0) \\
&\quad - \partial_{\nu} (\partial^0 A_0 - g^{00} \Gamma^{\sigma}_{00} A_{\sigma}) - (\partial_{\nu} g^{00}) \Gamma^{\sigma}_{00} A_{\sigma} - (\partial_{\nu} g^{ij}) \Gamma^{\sigma}_{ij} A_{\sigma} \\
&\quad + g^{ij} (\partial_i \partial_j A_{\nu} - \Gamma^{\sigma}_{ij} \partial_{\sigma} A_{\nu} - (\partial_{\nu} \Gamma^{\sigma}_{ij}) A_{\sigma} - \Gamma^{\sigma}_{j\nu} \partial_i A_{\sigma} + \Gamma^{\sigma}_{j\nu} \partial_{\sigma} A_i). \tag{3.48}
\end{aligned}$$

Note that the only non-zero Christoffel symbol Γ^{σ}_{00} is Γ^z_{00} (as referenced in Eq. (3.42)). Using this, we proceed to calculate the last remaining non-trivial term in Eq. (3.48) that requires the application of the Leibniz rule, namely

$$\partial_{\nu} g^{00} \Gamma^z_{00} A_z = (\partial_{\nu} g^{00}) \Gamma^z_{00} A_z + g^{00} (\partial_{\nu} \Gamma^z_{00}) A_z + g^{00} \Gamma^z_{00} (\partial_{\nu} A_z).$$

Using this identity, one obtains

$$\begin{aligned}
0 &= g^{00} (\partial_0^2 A_{\nu} - \Gamma^z_{00} \partial_z A_{\nu} - (\partial_{\nu} \Gamma^z_{00}) A_z - \Gamma^{\sigma}_{0\nu} \partial_0 A_{\sigma} + \Gamma^{\sigma}_{0\nu} \partial_{\sigma} A_0) \\
&\quad - g^{00} (\partial_{\nu} \partial_0 A_0 - (\partial_{\nu} \Gamma^z_{00}) A_z - \Gamma^z_{00} (\partial_{\nu} A_z)) - (\partial_{\nu} g^{ij}) \Gamma^{\sigma}_{ij} A_{\sigma} \\
&\quad + g^{ij} (\partial_i \partial_j A_{\nu} - \Gamma^{\sigma}_{ij} \partial_{\sigma} A_{\nu} - (\partial_{\nu} \Gamma^{\sigma}_{ij}) A_{\sigma} - \Gamma^{\sigma}_{j\nu} \partial_i A_{\sigma} + \Gamma^{\sigma}_{j\nu} \partial_{\sigma} A_i) \\
&= g^{00} (\partial_0^2 A_{\nu} - \Gamma^z_{00} \partial_z A_{\nu} - \Gamma^{\sigma}_{0\nu} \partial_0 A_{\sigma} + \Gamma^{\sigma}_{0\nu} \partial_{\sigma} A_0 - \partial_{\nu} \partial_0 A_0 + \Gamma^z_{00} (\partial_{\nu} A_z)) \\
&\quad + g^{ij} (\partial_i \partial_j A_{\nu} - \Gamma^{\sigma}_{ij} \partial_{\sigma} A_{\nu} - (\partial_{\nu} \Gamma^{\sigma}_{ij}) A_{\sigma} + \Gamma^{\sigma}_{j\nu} (\partial_{\sigma} A_i - \partial_i A_{\sigma})) - (\partial_{\nu} g^{ij}) \Gamma^{\sigma}_{ij} A_{\sigma}.
\end{aligned}$$

Inserting the explicit formulas for the metric tensor components from Eq. (3.21), we see that

$$\begin{aligned}
0 &= \left(-1 + 2 \frac{\bar{\phi}}{c^2} \right) [\partial_0^2 A_{\nu} - \Gamma^z_{00} \partial_z A_{\nu} + \Gamma^{\sigma}_{0\nu} (\partial_{\sigma} A_0 - \partial_0 A_{\sigma}) - (\partial_{\nu} \partial_0 A_0 - \Gamma^z_{00} (\partial_{\nu} A_z))] \\
&\quad + \left(\delta^{ij} + 2\gamma \frac{\bar{\phi}}{c^2} \delta^{ij} \right) (\partial_i \partial_j A_{\nu} - \Gamma^{\sigma}_{ij} \partial_{\sigma} A_{\nu} - (\partial_{\nu} \Gamma^{\sigma}_{ij}) A_{\sigma} - \Gamma^{\sigma}_{j\nu} \partial_i A_{\sigma} + \Gamma^{\sigma}_{j\nu} \partial_{\sigma} A_i) \\
&\quad - 2\gamma \left(\frac{\partial_{\nu} \bar{\phi}}{c^2} \right) \delta^{ij} \Gamma^{\sigma}_{ij} A_{\sigma} + O(c^{-4}).
\end{aligned}$$

If we denote the flat Laplace operator by $\Delta_{\text{flat}} = \delta^{ij} \partial_i \partial_j = \partial_x^2 + \partial_y^2 + \partial_z^2$, we find the relativistic corrections to the flat wave equation to be

$$\begin{aligned}
\Delta_{\text{flat}} A_{\nu} &= \left(1 - 2(\gamma + 1) \frac{\bar{\phi}}{c^2} \right) (\partial_0^2 A_{\nu} + \Gamma^z_{00} (\partial_{\nu} A_z - \partial_z A_{\nu}) - \Gamma^{\sigma}_{0\nu} \partial_0 A_{\sigma} + \Gamma^{\sigma}_{0\nu} \partial_{\sigma} A_0 - \partial_{\nu} \partial_0 A_0) \\
&\quad + \sum_{i=1}^3 (\Gamma^{\sigma}_{ii} \partial_{\sigma} A_{\nu} + (\partial_{\nu} \Gamma^{\sigma}_{ii}) A_{\sigma} + \Gamma^{\sigma}_{i\nu} \partial_i A_{\sigma} - \Gamma^{\sigma}_{i\nu} \partial_{\sigma} A_i) + O(c^{-4}). \tag{3.49}
\end{aligned}$$

In this context, considering relativistic corrections, one typically extends the flat wave equation, which involves the flat Laplace operator, by incorporating terms that arise due to

curvature or relativistic effects as described by the metric. Written out explicitly for the four values of ν , this yields

$$\Delta_{\text{flat}} A_0 = (\gamma + 1) \frac{\partial_z \bar{\phi}}{c^2} \partial_z A_0 - \frac{\partial_z \bar{\phi}}{c^2} \partial_0 A_z + O(c^{-4}), \quad (3.50a)$$

$$\begin{aligned} \Delta_{\text{flat}} A_x = & \left(1 - 2(\gamma + 1) \frac{\bar{\phi}}{c^2} \right) \partial_0^2 A_x + \gamma \frac{\partial_z \bar{\phi}}{c^2} \partial_z A_x + (2\gamma + 1) \frac{\partial_z \bar{\phi}}{c^2} (\partial_x A_z - \partial_z A_x) \\ & - \left(1 - 2(\gamma + 1) \frac{\partial_z \bar{\phi}}{c^2} \right) \partial_x \partial_0 A_0 + O(c^{-4}), \end{aligned} \quad (3.50b)$$

$$\begin{aligned} \Delta_{\text{flat}} A_y = & \left(1 - 2(\gamma + 1) \frac{\bar{\phi}}{c^2} \right) \partial_0^2 A_y + \gamma \frac{\partial_z \bar{\phi}}{c^2} \partial_z A_y + (2\gamma + 1) \frac{\partial_z \bar{\phi}}{c^2} (\partial_y A_z - \partial_z A_y) \\ & - \left(1 - 2(\gamma + 1) \frac{\partial_z \bar{\phi}}{c^2} \right) \partial_y \partial_0 A_0 + O(c^{-4}), \end{aligned} \quad (3.50c)$$

$$\begin{aligned} \Delta_{\text{flat}} A_z = & \left(1 - 2(\gamma + 1) \frac{\bar{\phi}}{c^2} \right) \partial_0^2 A_z + \gamma \frac{\partial_z \bar{\phi}}{c^2} \partial_z A_z + \gamma \frac{\partial_z^2 \bar{\phi}}{c^2} A_z \\ & - \left(1 - 2(\gamma + 1) \frac{\partial_z \bar{\phi}}{c^2} \right) \partial_z \partial_0 A_0 + O(c^{-4}). \end{aligned} \quad (3.50d)$$

Before solving these gravitationally modified wave equations, we examine whether the BCG, which is a common gauge condition in quantum optics, results in a set of simpler differential equations.

Comparison to background Coulomb gauge: The BCG condition reads $\partial^i A_i = 0$ and differs from the GCG in Maxwell's equations Eq. (3.48) by the term

$$\begin{aligned} \partial_\nu g^{i\lambda} \Gamma^\sigma_{\lambda i} A_\sigma &= \partial_\nu g^{ii} \Gamma^\sigma_{ii} A_\sigma = (\partial_\nu g^{ii}) \Gamma^\sigma_{ii} A_\sigma + g^{ii} (\partial_\nu \Gamma^\sigma_{ii}) A_\sigma + g^{ii} \Gamma^\sigma_{ii} (\partial_\nu A_\sigma) \\ &= 2\gamma \frac{\bar{\phi}_{,\nu}}{c^2} \Gamma^\sigma_{ii} A_\sigma + \left(1 + 2\gamma \frac{\bar{\phi}}{c^2} \right) [(\partial_\nu \Gamma^\sigma_{ii}) A_\sigma + \Gamma^\sigma_{ii} (\partial_\nu A_\sigma)] \\ &= (\partial_\nu \Gamma^\sigma_{ii}) A_\sigma + \Gamma^\sigma_{ii} (\partial_\nu A_\sigma) + O(c^{-4}) \\ &= (\partial_\nu \Gamma^x_{ii}) A_x + (\partial_\nu \Gamma^y_{ii}) A_y + (\partial_\nu \Gamma^z_{ii}) A_z \\ &\quad + \Gamma^x_{ii} (\partial_\nu A_x) + \Gamma^y_{ii} (\partial_\nu A_y) + \Gamma^z_{ii} (\partial_\nu A_z) + O(c^{-4}) \\ &= (\partial_\nu \Gamma^z_{xx} + \partial_\nu \Gamma^z_{yy} + \partial_\nu \Gamma^z_{zz}) A_z + (\Gamma^z_{xx} + \Gamma^z_{yy} + \Gamma^z_{zz}) (\partial_\nu A_z) + O(c^{-4}) \\ &= \gamma \frac{\bar{\phi}_{,\nu,z}}{c^2} A_z + \gamma \frac{\bar{\phi}_{,\nu,z}}{c^2} (\partial_\nu A_z) + O(c^{-4}) \\ &= \gamma \frac{\bar{\phi}_{,\nu,z}}{c^2} (\partial_\nu A_z) + O\left(\frac{\partial_z^2 \bar{\phi}}{c^2}, c^{-4}\right). \end{aligned} \quad (3.51)$$

This contribution is non-zero, leading to an additional term in the wave equations. Since the term in Eq. (3.51) does not cancel out any other contributions in Eq. (3.50) for $\nu \in \{0, \dots, 3\}$, it results in even more complex wave equations. The LG, turns out to be equivalent to the GCG, as we will demonstrate after solving the wave equations. To achieve this, we introduce the following plane wave approximation scheme.

3.5.2 Geometric Optics Approximation

When solving Maxwell's equations, we set aside issues related to self-interactions (see, for example, Ref. [141]) and focus on geometric optics and plane wave-like solutions. To perform a geometric optics approximation, we follow a method similar to that presented in the textbook by Misner et al. [140][§22.5.]. A similar technique was recently employed by Di Pumbo et al. [74] (within a different coordinate system) to describe light propagation in atom interferometers, including the effects of a non-vanishing Dilaton field. We will compare our approach to that of Di Pumbo et al. at the conclusion of this section. By denoting the wavelength of the light field as λ , we can identify two crucial length scales for the approximation to be

$$\mathcal{R} = \left| \begin{array}{l} \text{typical component of } R''_{\nu\sigma\tau} \text{ as} \\ \text{measured in a local Lorentz frame} \end{array} \right|^{-\frac{1}{2}} \approx \left| \partial_r \frac{\bar{\phi}}{c^2} \right|^{-\frac{1}{2}} \approx 10^8 \text{m}$$

$$\mathcal{L} = \left| \begin{array}{l} \text{radius of curvature} \\ \text{of a wave front} \end{array} \right| \approx 1 \text{mm.}$$

We then define the small expansion parameter

$$\epsilon = \lambda / (2\pi \min(\mathcal{R}, \mathcal{L})) = \lambda / (2\pi \mathcal{L}),$$

which can be conceptualised as the ratio of the wavelength of the light field to the characteristic length scale \mathcal{L} over which the slowly varying envelope of the field changes, divided by 2π . We now make the ansatz that the four-potential to be given by

$$A_\mu = (a_\mu + \epsilon b_\mu + \epsilon^2 c_\mu + \mathcal{O}(\epsilon^3)) e^{i\Phi/\epsilon}, \quad (3.52)$$

where $a_\mu, b_\mu, c_\mu: \mathcal{M} \rightarrow \mathbb{C}$ are complex-valued functions on spacetime and $\Phi: \mathcal{M} \rightarrow \mathbb{R}$ is the real-valued phase. Following Ref. [140, §22.5.], we refer to terms of order up to ϵ^{-1} as "geometric optics", meaning we focus on these leading-order contributions and disregard "post-geometric optics" orders, such as ϵ^0 and higher. This approach simplifies our analysis to include only those components that dominate under this approximation. Given that we impose a gauge condition aligned with the Coulomb gauge to order $\mathcal{O}(c^0)$, we further assume that the time component A_0 of the four-potential contributes only at $\mathcal{O}(c^{-2})$ (in vacuum).

Calculating the wave vector and phase

The relativistic (four-) wave vector is defined as the covariant derivative of the phase

$$k_\mu = \nabla_\mu \Phi = \partial_\mu \Phi. \quad (3.53)$$

Note that here the partial and covariant derivative coincide, since Φ maps into \mathbb{R} and is therefore seen as a $(0, 0)$ -tensor field. In this context, the spatial wave vector \mathbf{k} consists of the spatial components of the four-wave vector

$$k_\mu = (k_0, \mathbf{k}) = (k_0, k_x, k_y, k_z). \quad (3.54)$$

By grouping terms according to their order in ϵ , a condition for the wave vector emerges at the order ϵ^{-2} , i.e.,

$$0 = -\frac{g^{\mu\lambda}}{\epsilon^2} (\partial_\mu \Phi) (\partial_\lambda \Phi) a_\nu + \mathcal{O}(\epsilon^{-1}) = -\frac{k_\mu k^\mu a_\nu}{\epsilon^2} + \mathcal{O}(\epsilon^{-1}). \quad (3.55)$$

This occurs because the only way to derive terms of order ϵ^{-2} is through the term involving two partial derivatives in Maxwell's equations.⁶ We observe that geometric optics dictates that the wave vector k_μ must be light-like. This means it must satisfy the condition $k_\mu k^\mu = g^{\mu\lambda} k_\mu k_\lambda = 0$. We will disregard the k_x and k_y components and concentrate solely on the behaviour of k_0 and k_z , as we are limiting our analysis to EM propagating exclusively in the z-direction. Therefore, we need to solve

$$\begin{aligned} \left(-1 + 2\frac{\bar{\phi}(z)}{c^2} + (2\beta - 4)\frac{\bar{\phi}(z)^2}{c^4} + 4(\beta - 1)\phi_0\frac{\bar{\phi}(z)}{c^4} + O(c^{-6}) \right) k_0^2(z) \\ + \left(1 + 2\gamma\frac{\bar{\phi}(z)}{c^2} + O(c^{-4}) \right) k_z^2(z) = 0, \end{aligned} \quad (3.56)$$

which subsequently leads to a dispersion relation for the free propagation⁷ of

$$k_z^2(z) = \left(1 - 2(\gamma + 1)\frac{\bar{\phi}(z)}{c^2} + O(c^{-4}) \right) k_0^2(z) \quad (3.57a)$$

$$k_z(z) = \pm \left(1 - (\gamma + 1)\frac{\bar{\phi}(z)}{c^2} \right) k_0(z) + O(c^{-4}), \quad (3.57b)$$

where the two solutions reflect the possible propagation directions of the light field. If we express this in the form of a vector in a $(1 + 1)$ -dimensional spacetime – considering only k_0 and k_z – we obtain the wave vector

$$k_\mu(z) = \begin{pmatrix} 1 \\ \pm \left(1 - (\gamma + 1)\frac{\bar{\phi}(z)}{c^2} \right) \end{pmatrix} k_0(z) + O(c^{-4}). \quad (3.58)$$

Taking the covariant derivative of $k_\mu k^\mu = 0$, we obtain

$$k_\mu k^\mu = 0 \implies (k_\mu k^\mu)_{;\alpha} = 0 \implies 2k^\mu k_{\mu;\alpha} = 2k^\mu k_{\alpha;\mu} = 0. \quad (3.59)$$

In the final step, we applied the Leibniz rule and used the fact that $k_\mu = \Phi_{,\mu}$ is the derivative of a scalar function. The expression $k^\mu k_{\alpha;\mu} = 0$ is the propagation equation for the relativistic wave vector, essentially providing a geometric optics analogue of the geodesic equation for light rays. Since we have assumed spacetime to be stationary with a timelike Killing vector field $\partial_0 = c^{-1}\partial_t$, we know that, at the level of approximation we are considering, the wave vector's corresponding timelike component $k_0 = k_\mu(\partial_0)^\mu = c^{-1}\partial_t\Phi$ remains constant along each geodesic or light ray, which are integral curves of the vector field k^μ . If we write out Eq. (3.59) for $\alpha = 0$, $k^\mu k_{0;\mu}$, one can derive that this is equivalent to

$$0 = k^0 \partial_0 k_0 + k^z \partial_z k_0 - \frac{\partial_z \bar{\phi}(z)}{c^2} k^z k_0 - \delta^{zi} \frac{\partial_i \bar{\phi}(z)}{c^2} k^0 k_z. \quad (3.60)$$

We now choose the ansatz $k_0(z) = k_0 + \frac{f(z)}{c^2}$, as we know that, to order c^0 , the frequency of the light field remains constant. Substituting this ansatz into Eq. (3.60), we find that $\partial_z f(z) = 0$,

⁶Specifically, this condition arises from the first term in Eq. (3.48), namely $g^{\mu\lambda} \partial_\lambda \partial_\mu A_\nu$. The other term that contains two derivatives only involves A_0 , which, as we will show in the upcoming calculations, is zero to at least order $O(\epsilon^2)$.

⁷Note how this coincides with Eq. (9) from Ref. [142] with $\gamma = 1$, when one expands the Schwarzschild solution to small heights and uses the original choice of coordinates.

indicating that $k_0(z)$ is constant to order c^{-4} . To determine whether this solution aligns with Eq. (3.59) for $\alpha = z$, i.e. $k^\mu k_{z;\mu}$, we calculate

$$0 = \pm(\gamma + 1)k_0 \frac{\partial_z \bar{\phi}(z)}{c^2} \mp (\gamma + 1)k_0 \frac{\partial_z \bar{\phi}(z)}{c^2} + O(c^{-4}) = O(c^{-4}), \quad (3.61)$$

which holds to the same order of accuracy. This is in agreement with Ref. [142], where the connection was made between the quantity k_0 and the photon energy $E = ck_0$, which is constant throughout its path.⁸ Consequently, we derive a relativistic wave vector

$$k_\mu(z) = \begin{pmatrix} 1 \\ \pm \left(1 - (\gamma + 1) \frac{\bar{\phi}(z)}{c^2}\right) \end{pmatrix} k_0 + O(c^{-4}). \quad (3.62)$$

Since $k_\mu = \Phi_{,\mu}$, we can deduce that the phase of the EM field, to the order of approximation we are considering, is given by

$$\Phi(z, t) = \Phi_0 + k_0 ct \pm \left(1 - \frac{\gamma + 1}{2} \frac{gz}{c^2}\right) k_0 z + O(\Gamma c^{-2}), \quad (3.63)$$

where Φ_0 is an arbitrary offset, which we will set to zero. The contravariant components of the wave vector, defined as $k^\mu = g^{\mu\nu} k_\nu$, are given by

$$k^\mu(z) = \begin{pmatrix} -1 + 2 \frac{\bar{\phi}(z)}{c^2} \\ \pm \left(1 + (\gamma - 1) \frac{\bar{\phi}(z)}{c^2}\right) \end{pmatrix} k_0 + O(c^{-4}). \quad (3.64)$$

Note that k_0 is still a coordinate-dependent object and is, a priori, not an observable frequency. It is possible to express the light field in terms of its *actually measurable* frequency. However, any relativistic concept of measurable frequency necessitates the notion of an observer, whose worldline intersects the photon's path and who measures the frequency of the light field in their own rest frame. To achieve this, we define a family of observers who are at rest (with respect to the laser source) at various heights. The corresponding four-velocities of these observers, denoted as $u^\mu(z)$, must satisfy the condition $u^\mu(z) u_\mu(z) = -c^2$, as this is a fundamental requirement for four-velocities. Let's make an ansatz involving an arbitrary function $\alpha(z)$ to determine the form of $u^\mu(z)$:

$$u^\mu(z) = \alpha(z) \begin{pmatrix} c \\ 0 \end{pmatrix} \implies u^\mu(z) = \left(1 - \frac{\bar{\phi}(z)}{c^2} + O(c^{-4})\right) \begin{pmatrix} c \\ 0 \end{pmatrix}. \quad (3.65)$$

From this, we can express the frequency of the light field as it would be perceived by an observer at rest at a height z as

$$\omega(z) = -k_\mu(z) u^\mu(z) = -\left(1 - \frac{\bar{\phi}(z)}{c^2} + O(c^{-4})\right) c k_0. \quad (3.66)$$

If we assume that the photon is emitted from the laser, positioned at a height $z = 0$ with a frequency of $\omega_{\text{emit}} := \omega(0) = -ck_0$, then this can be rewritten as

$$\omega(z) = \left(1 - \frac{\bar{\phi}(z)}{c^2} + O(c^{-4})\right) \omega_{\text{emit}}. \quad (3.67)$$

⁸In their notation: $k_0 = p_0$ and $k_z = p_r$.

The frequency of a photon "climbing out of the gravitational well" is thus shifted as perceived by observers at rest at different heights. This shift arises from the fact that observers at varying heights experience different rates of time passage due to gravitational time dilation. However, for simplicity, we will continue using the quantity k_0 and assume that the reader is aware of this subtlety.

Calculating the amplitude

To find analytic expressions for the leading-order amplitudes a_μ , we proceed by substituting the ansatz from Eq. (3.52) into the wave equations given in the GCG in Eq. (3.50). By first calculating the second-order partial derivative, we obtain

$$\begin{aligned} \partial_j^2 A_\mu &= \partial_j^2 \left[(a_\mu + \epsilon b_\mu + \epsilon^2 c_\mu + O(\epsilon^3)) e^{i\Phi/\epsilon} \right] \\ &= \partial_j \left[\left[(a_\mu + \epsilon b_\mu + \epsilon^2 c_\mu + O(\epsilon^3)) \frac{i(\partial_j \theta)}{\epsilon} + ((\partial_j a_\mu) + \epsilon(\partial_j b_\mu) + \epsilon^2(\partial_j c_\mu) + O(\epsilon^3)) \right] e^{i\Phi/\epsilon} \right] \\ &= \left[2i\epsilon^{-1}(\partial_j a_\mu)(\partial_j \theta) + i\epsilon^{-1} a_\mu (\partial_j^2 \theta) - (\epsilon^{-2} a_\mu + \epsilon^{-1} b_\mu)(\partial_j \theta)^2 + O(\epsilon^0) \right] e^{i\Phi/\epsilon}. \end{aligned} \quad (3.68)$$

This results in a left-hand side of Eq. (3.50) of

$$\Delta_{\text{flat}} A_\mu = \left[2i\epsilon^{-1}(\nabla a_\mu) \cdot \mathbf{k} + i\epsilon^{-1} a_\mu \nabla \cdot \mathbf{k} - (\epsilon^{-2} a_\mu + \epsilon^{-1} b_\mu) \mathbf{k}^2 + O(\epsilon^0) \right] e^{i\Phi/\epsilon}, \quad (3.69)$$

where we used the notation $\nabla = (\nabla_x, \nabla_y, \nabla_z)$. The right-hand side of Eq. (3.50) varies for each value of μ ; we start with the temporal case.

Temporal wave equation ($\mu = 0$): The temporal equation is given in Eq. (3.50a) and its right-hand side reads

$$\begin{aligned} \text{Eq. (3.50a)} &= (\gamma + 1) \frac{\partial_z \bar{\phi}}{c^2} \partial_z A_0 - \frac{\partial_z \bar{\phi}}{c^2} \partial_0 A_z + O(c^{-4}) \\ &= \left[(\gamma + 1) \frac{\partial_z \bar{\phi}}{c^2} i k_z \epsilon^{-1} a_0 - \frac{\partial_z \bar{\phi}}{c^2} i k_0 \epsilon^{-1} a_z \right] e^{i\Phi/\epsilon} + O(c^{-4}). \end{aligned} \quad (3.70)$$

This implies that at order $O(\epsilon^{-2})$, $a_0 = O(c^{-4})$, since neither the exponential nor \mathbf{k}^2 can be zero. Subsequently, at order $O(\epsilon^{-1})$ one finds that $b_0 = 0$. Consequently, A_0 is zero to order $O(c^{-4}, \epsilon^2)$, as previously indicated.

Spatial wave equation in z -direction ($\mu = z$): Next, we consider Eq. (3.50d) for the case $\mu = z$. By directly applying that $A_0 = O(c^{-4}, \epsilon^2)$, we obtain

$$\begin{aligned} \text{Eq. (3.50d)} &= \left(1 - 2(\gamma + 1) \frac{\bar{\phi}}{c^2} \right) \partial_0^2 A_z + \gamma \frac{\partial_z \bar{\phi}}{c^2} \partial_z A_z + \gamma \frac{\partial_z^2 \bar{\phi}}{c^2} A_z + O(c^{-4}) \\ &= \left(1 - 2(\gamma + 1) \frac{\bar{\phi}}{c^2} \right) \left[2i k_0 \epsilon^{-1} (\partial_0 a_z) + i(\partial_0 k_0) \epsilon^{-1} a_z - k_0^2 (\epsilon^{-2} a_z + \epsilon^{-1} b_z) \right] e^{i\Phi/\epsilon} \\ &\quad + \gamma \frac{\partial_z \bar{\phi}}{c^2} i k_z \epsilon^{-1} a_z e^{i\Phi/\epsilon} + O\left(c^{-4}, \epsilon^0, \frac{\partial_z^2 \bar{\phi}}{c^2}\right). \end{aligned} \quad (3.71)$$

Splitting this equation according to the corresponding powers of ϵ yields, at leading order,

$$O(\epsilon^{-2}): \quad -a_z \mathbf{k}^2 e^{i\Phi/\epsilon} = -\left(1 - 2(\gamma + 1) \frac{\bar{\phi}}{c^2} \right) k_0^2 a_z e^{i\Phi/\epsilon} + O(c^{-4}). \quad (3.72a)$$

Note that this is equivalent to

$$\mathbf{k}^2 = \left(1 - 2(\gamma + 1) \frac{\bar{\phi}}{c^2}\right) k_0^2 + O(c^{-4}) \iff k_\mu k^\mu = 0, \quad (3.72b)$$

as discussed in Eq. (3.57b). At the next geometric optics order, $O(\epsilon^{-1})$, one obtains

$$\begin{aligned} O(\epsilon^{-1}) : \quad 2i(\nabla a_z) \cdot \mathbf{k} + ia_z \nabla \cdot \mathbf{k} - b_z \mathbf{k}^2 &= \gamma \frac{\partial_z \bar{\phi}}{c^2} ik_z a_z \\ &+ \left(1 - 2(\gamma + 1) \frac{\bar{\phi}}{c^2}\right) [2ik_0(\partial_0 a_z) + i(\partial_0 k_0)a_z - k_0^2 b_z] + O\left(\frac{\partial_z^2 \bar{\phi}}{c^2}, c^{-4}\right). \end{aligned} \quad (3.73a)$$

The b_z -dependent part drops out because its prefactor is $k_\mu k^\mu$. The resulting equation is

$$2(\nabla a_z) \cdot \mathbf{k} + a_z \nabla \cdot \mathbf{k} = \gamma \frac{\partial_z \bar{\phi}}{c^2} k_z a_z + \left(1 - 2(\gamma + 1) \frac{\bar{\phi}}{c^2}\right) [2k_0(\partial_0 a_z) + (\partial_0 k_0)a_z] + O\left(\frac{\partial_z^2 \bar{\phi}}{c^2}, c^{-4}\right). \quad (3.73b)$$

Given that the time derivatives of a_z and k_0 vanish by construction and due to spacetime being static, one is left with

$$(\nabla a_z) \cdot \mathbf{k} + \frac{1}{2} a_z \nabla \cdot \mathbf{k} = \gamma \frac{\partial_z \bar{\phi}}{2c^2} k_z a_z + O\left(\frac{\partial_z^2 \bar{\phi}}{c^2}, c^{-4}\right). \quad (3.73c)$$

The left-hand side of this equation is the z -component of the propagation law of the EM amplitudes, given by $\nabla_k a_z = -\frac{1}{2}(\nabla \cdot \mathbf{k})a_z$ (cf. Ref. [140]). The right-hand side contains the relativistic corrections to this identity.

Spatial wave equation in transverse-directions ($\mu = x, y$): The transverse wave equations in Eqs. (3.50b) and (3.50c) are completely symmetric. Therefore, we will only show the solution in the x -direction, which is

$$\begin{aligned} \text{Eq. (3.50b)} &= \left(1 - 2(\gamma + 1) \frac{\bar{\phi}}{c^2}\right) \partial_0^2 A_x + \gamma \frac{\partial_z \bar{\phi}}{c^2} \partial_z A_x + (2\gamma + 1) \frac{\partial_z \bar{\phi}}{c^2} (\partial_x A_z - \partial_z A_x) \\ &\quad - \left(1 - 2(\gamma + 1) \frac{\partial_z \bar{\phi}}{c^2}\right) \partial_x \partial_0 A_0 + O(c^{-4}) \\ &= \left(1 - 2(\gamma + 1) \frac{\bar{\phi}}{c^2}\right) \partial_0^2 A_x + \gamma \frac{\partial_z \bar{\phi}}{c^2} \partial_z A_x + (2\gamma + 1) \frac{\partial_z \bar{\phi}}{c^2} (\partial_x A_z - \partial_z A_x) + O(c^{-4}). \end{aligned} \quad (3.74a)$$

Inserting the geometric optics ansatz then leads to

$$\begin{aligned} \text{Eq. (3.50b)} &= \frac{1}{c^2} \left[\left(1 - 2(\gamma + 1) \frac{\bar{\phi}}{c^2}\right) \left(2 \frac{i}{\epsilon} k_0 (\partial_0 a_x) + \frac{i}{\epsilon} (\partial_0 k_0) a_x - \frac{k_0^2}{\epsilon^2} (a_x + \epsilon b_x)\right) \right. \\ &\quad \left. + (2\gamma + 1) (\partial_z \bar{\phi}) \frac{i}{\epsilon} k_x a_z - (\gamma + 1) (\partial_z \bar{\phi}) \frac{i}{\epsilon} k_z a_x \right] e^{i\Phi/\epsilon} + O(c^{-4}, \epsilon^0). \end{aligned} \quad (3.74b)$$

The $O(\epsilon^{-2})$ condition is, once more, equivalent to $k_\mu k^\mu = 0$. The $O(\epsilon^{-1})$ equation is given by

$$\begin{aligned} 2(\nabla a_x) \cdot \mathbf{k} + a_x \nabla \cdot \mathbf{k} &= \frac{1}{c^2} \left[\left(1 - 2(\gamma + 1) \frac{\bar{\phi}}{c^2} \right) (2k_0(\partial_0 a_x) + (\partial_0 k_0)a_x) \right. \\ &\quad \left. + (2\gamma + 1)(\partial_z \bar{\phi})k_x a_z - (\gamma + 1)(\partial_z \bar{\phi})k_z a_x \right] \\ &= \frac{2\gamma + 1}{c^2} (\partial_z \bar{\phi})k_x a_z - \frac{\gamma + 1}{c^2} (\partial_z \bar{\phi})k_z a_x. \end{aligned} \quad (3.74c)$$

For the y -direction, the process and results work analogously.

To summarise, we arrive at a set of differential equations

$$\text{i) } (\nabla a_x) \cdot \mathbf{k} + \frac{1}{2} a_x \nabla \cdot \mathbf{k} = \frac{2\gamma + 1}{2c^2} (\partial_z \bar{\phi})k_x a_z - \frac{\gamma + 1}{2c^2} (\partial_z \bar{\phi})k_z a_x + O(\epsilon^0, c^{-4}), \quad (3.75a)$$

$$\text{ii) } (\nabla a_y) \cdot \mathbf{k} + \frac{1}{2} a_y \nabla \cdot \mathbf{k} = \frac{2\gamma + 1}{2c^2} (\partial_z \bar{\phi})k_y a_z - \frac{\gamma + 1}{2c^2} (\partial_z \bar{\phi})k_z a_y + O(\epsilon^0, c^{-4}), \quad (3.75b)$$

$$\text{iii) } (\nabla a_z) \cdot \mathbf{k} + \frac{1}{2} a_z \nabla \cdot \mathbf{k} = \frac{\gamma}{2c^2} (\partial_z \bar{\phi})k_z a_z + O(\epsilon^0, c^{-4}). \quad (3.75c)$$

We further impose the boundary conditions $a_i(z = 0) = \mathcal{A}_i$ for $i = x, y$ and $a_z(z = 0) = 0$, indicating that we begin with a transverse wave. We continue by rewriting the ODE for a_z in Eq. (3.75c). By using the relation $\partial_z k_z = -(\gamma + 1) \frac{\partial_z \bar{\phi}}{c^2} k_0 + O(c^{-4})$, we obtain

$$\partial_z a_z + \frac{\partial_z k_z}{2k_z} a_z = \frac{\gamma}{2c^2} (\partial_z \bar{\phi})a_z + O(c^{-4}) \quad (3.76a)$$

$$\iff \partial_z a_z - \frac{\gamma + 1}{2} \frac{\partial_z \bar{\phi}}{c^2} a_z = \frac{\gamma}{2c^2} (\partial_z \bar{\phi})a_z + O(c^{-4}) \quad (3.76b)$$

$$\iff \partial_z a_z = \frac{2\gamma + 1}{2} \frac{g}{c^2} a_z + O\left(\frac{\partial_z^2 \bar{\phi}}{c^2}, c^{-4}\right), \quad (3.76c)$$

which is solved by

$$a_z(z) = \mathcal{A}_z e^{\frac{2\gamma+1}{2} \frac{g z}{c^2}} \implies a_z(z = 0) = 0 \implies \mathcal{A}_z = 0 \implies a_z(z) \equiv 0. \quad (3.77)$$

The amplitude in the z -direction therefore identically vanishes, meaning that the EM wave remains transverse. Substituting this solution into the remaining equations, we obtain (using the example of the x -direction)

$$\partial_z a_x + \frac{\partial_z k_z}{2k_z} a_x = -\frac{\gamma + 1}{2c^2} (\partial_z \bar{\phi})a_x + O(\epsilon^0, c^{-4}) \quad (3.78a)$$

$$\iff \partial_z a_x - \frac{\gamma + 1}{2c^2} (\partial_z \bar{\phi})a_x = -\frac{\gamma + 1}{2c^2} (\partial_z \bar{\phi})a_x + O(\epsilon^0, c^{-4}) \quad (3.78b)$$

$$\iff \partial_z a_x = O(\epsilon^0, c^{-4}), \quad (3.78c)$$

which is trivially solved by the constant amplitude $a_x(z) = \mathcal{A}_x$. In conclusion, at the chosen level of approximation, there are no general relativistic corrections to the amplitudes of EM waves.

Combining this with the phase expression from Eq. (3.63), we arrive at an EM vector potential in the geometric optics approximation, expressed as

$$(A_i) = \mathbf{A} = \mathcal{A} e^{i \left(k_0 c t \pm \left(1 - \frac{\gamma+1}{2} \frac{g z}{c^2} \right) k_0 z \right)} + O(\Gamma c^{-2}), \quad (3.79)$$

where we introduced $\mathcal{A} = (\mathcal{A}_x, \mathcal{A}_y, 0)$. It is important to highlight that we have absorbed the factor ϵ^{-1} from the exponent in the ansatz, Eq. (3.52), into the normalisation of k_0 . Consequently, the angular frequency of the light, as measured by a stationary observer at rest at the origin, is given by $\omega_0 = -ck_0$.

Comparison to Lorenz gauge Note also that the LG condition is, at our level of approximation, equivalent to the GCG. This can be more clearly seen if we calculate the difference between the two gauge conditions, i.e.,

$$\begin{aligned}\nabla^0 A_0 &= \nabla^\beta A_\beta - \nabla^i A_i = \partial^0 A_0 - g^{0\nu} \Gamma_{0\nu}^\mu A_\mu = \partial^0 A_0 - g^{00} \Gamma_{00}^\mu A_\mu \\ &= \partial^0 A_0 - g^{00} \Gamma_{00}^z A_z = \partial^0 A_0 + g^{00} \frac{\bar{\phi}_{,z}}{c^2} A_z + O(c^{-4}).\end{aligned}\quad (3.80)$$

Both contributions vanish at our level of approximation, as A_0 and A_z are also zero. Consequently, both gauge conditions align in this gravitational model.

Comparison to an approach in Fermi normal coordinates Following Ref. [140][§13.6], one can express any metric tensor in the Fermi normal coordinates⁹ of an accelerated observer as

$$g_{00} = -\left(1 + \delta_{ij} \frac{a^i x^j}{c^2}\right)^2 - R_{0i0j} x^i x^j + O(|\mathbf{x}|^3), \quad (3.81a)$$

$$g_{0i} = -\frac{2}{3} R_{0jik} x^j x^k + O(|\mathbf{x}|^3), \quad (3.81b)$$

$$g_{ij} = \delta_{ij} - \frac{1}{3} R_{ikjl} x^k x^l + O(|\mathbf{x}|^3), \quad (3.81c)$$

where a^i represents the local spatial acceleration that the reference frame experiences to maintain the observer's position at the origin of the reference frame. In the case of linear gravitational acceleration in the z-direction, this would imply that $a^i = -g$.

In Di Pumbo et al. [74], these coordinates, along with the assumption of a linear gravitational potential, were employed to derive a metric tensor

$$g_{\mu\nu} = \eta_{\mu\nu} + \delta_\mu^0 \delta_\nu^0 \frac{2gz}{c^2} + O(c^{-4}), \quad (3.82)$$

where no contributions from the Riemann curvature tensor arise, since all of its component functions identically vanish.¹⁰ Following the same steps as before, one then derives a relativistic wave vector

$$k_\mu(z) = \begin{pmatrix} 1 \\ \pm \left(1 - \frac{\bar{\phi}(z)}{c^2}\right) \end{pmatrix} k_0 + O(c^{-4}), \quad (3.83)$$

which differs from Eq. (3.62) in the prefactor of the spatial part. The underlying physics remain unchanged, as the positions of atoms and photons also shift in this frame of reference compared to the aforementioned approach, thereby exactly cancelling any differences in the calculation of scalar quantities. This example serves to illustrate the importance of consistently tracking all coordinate systems used throughout the analysis and avoiding the comparison of quantities that are dependent on these coordinate choices.

⁹Sometimes also referred to as a *proper reference frame*.

¹⁰The components of the Riemann tensor, at least at the c^{-2} level, always involve a second derivative of the gravitational potential, which is by definition zero, assuming only a linear gravitational potential.

3.6 Atom-Light Hamiltonian

We are now prepared to analyse the atom-light interaction to describe beam splitter and mirror pulses, including relativistic corrections. Revisiting the interaction Hamiltonian in Eq. (3.29), we observe no direct gravitational effects at the level of the Hamiltonian. However, since the electromagnetic fields are themselves influenced by gravity, it is essential to examine how these gravitational effects might impact the operations of beam splitter and mirror pulses.

Bragg interactions: Two Counter-propagating Light Fields

In principle, determining the dynamics during a light pulse involves solving the Schrödinger equation using the Hamiltonian from Eq. (3.29), which in its one-dimensional form is expressed as

$$\hat{H}_{\text{A-L}} = -\hat{\mathbf{d}} \cdot \mathbf{E}(\hat{Z}) + \frac{1}{2m} \left[\hat{P} \left(\hat{\mathbf{d}} \times \mathbf{B}(\hat{Z}) \right)_z + \text{h.c.} \right] \quad (3.84)$$

with position and momentum operators \hat{Z}, \hat{P} . We begin by discussing the case of atoms at rest and will incorporate effects due to Doppler shifts in a subsequent step. The \hat{Z} -dependence of the electromagnetic fields, which arise from the vector potential in Eq. (3.79), leads to \hat{Z} -dependent corrections in the electromagnetic phases. This height dependence of the phase is significant for the net interferometric phase and will be the primary focus of the following discussion.

To derive expressions for the electric and magnetic fields, we begin with the vector potential given in Eq. (3.79). We incorporate a time dependence into the amplitudes to facilitate the creation of specific pulse shapes during the experiment. Each of the corresponding vector potentials can then be expressed as

$$\mathbf{A}_i(z, t) = \mathcal{A}_i(t) e^{i\Phi_i(z, t)} + \mathcal{O}(\Gamma c^{-2}), \quad (3.85)$$

where the phase expression is given by

$$\Phi_i(z, t) = -\omega_i t \pm \left(1 - \frac{\gamma + 1}{2} \frac{gz}{c^2} \right) k_i z + \mathcal{O}(\Gamma c^{-2}), \quad (3.86)$$

with $i = a, b$ respectively. Using canonical quantisation, we express every motional variable in terms of the position and momentum operators \hat{Z} and \hat{P} . Utilising the vector potential, we obtain expressions for the electric and magnetic fields via $\mathbf{E}_i(\hat{Z}, t) = -\partial_t \mathbf{A}_i(\hat{Z}, t)$ and $\mathbf{B}_i(\hat{Z}, t) = \nabla \times \mathbf{A}_i(\hat{Z}, t)$. Writing both EM fields explicitly yields

$$\mathbf{E}_i(\hat{Z}, t) = \mathcal{E}_i(t) e^{i\Phi_i(\hat{Z}, t)} + \mathcal{O}(\Gamma c^{-2}), \quad (3.87a)$$

$$\mathbf{B}_i(\hat{Z}, t) = \pm \mathcal{B}_i(t) e^{i\Phi_i(\hat{Z}, t)} + \mathcal{O}(\Gamma c^{-2}), \quad (3.87b)$$

where the amplitudes are given by

$$\begin{aligned} \mathcal{E}_i(t) &= -i\omega_i \mathcal{A}_i(t) - \dot{\mathcal{A}}_i(t), \\ \mathcal{B}_i(t) &= ik_i \mathbf{e}_z \times \mathcal{A}_i(t). \end{aligned}$$

The interaction Hamiltonian Eq. (3.29) then takes the form

$$\hat{H}_{\text{A-L}} = -\hat{\mathbf{d}} \cdot \mathbf{E}_i(\hat{Z}, t) + \frac{1}{2m} \left[\hat{P} \cdot \left(\hat{\mathbf{d}} \times \mathbf{B}_i(\hat{Z}, t) \right) + \text{h.c.} \right]. \quad (3.88)$$

We now transform into the interaction picture corresponding to the internal Hamiltonian \hat{H}_I as given in Eq. (3.27). This transformation modifies the dipole operator $\hat{\mathbf{d}}$ according to

$$\hat{\mathbf{d}}(t) = e^{i\hat{H}_I t/\hbar} \hat{\mathbf{d}} e^{-i\hat{H}_I t/\hbar} = \mathbf{d}_{\text{eg}} |e\rangle\langle g| e^{i\omega_{\text{eg}} t}, \quad (3.89)$$

with $\mathbf{d}_{\text{eg}} = \langle e | \hat{\mathbf{d}} | g \rangle$. To move the \hat{Z} -dependent phase of the magnetic field in the Röntgen term past the \hat{P} , we utilise the relation $e^{\pm ik\hat{Z}} \hat{P} = (\hat{P} \mp \hbar k) e^{\pm ik\hat{Z}}$ (cf. [143]). Additionally, we employ the Graßmann identity to simplify

$$(\mathbf{d}_{\text{eg}} \times (\mathbf{e}_z \times \mathcal{A}_j))_z = \mathbf{d}_{\text{eg}} \cdot \mathcal{A}_j. \quad (3.90)$$

The full Hamiltonian, expressed within the rotating wave approximation and in the interaction picture with respect to \hat{H}_I , takes the form

$$\hat{H} = \hat{H}_{\text{COM}} + \sum_{i=a,b} \frac{\hbar\Omega_i(\hat{Z}, \hat{P}, t)}{2} |e\rangle\langle g| e^{i(\pm k_i(\hat{Z})\hat{Z} - (\omega_i - \omega_{\text{eg}})t)}, \quad (3.91)$$

where the Rabi frequency exhibits an additional dependency on the momentum

$$\frac{\hbar\Omega_i(\hat{P}, t)}{2} = -\mathbf{d}_{\text{eg}} \cdot \boldsymbol{\varepsilon}_i \mathcal{E}_i(t) \pm \left(\hat{P} \mp \frac{\hbar k_i}{2} \right) \frac{\mathbf{d}_{\text{eg}} \cdot \boldsymbol{\varepsilon}_i}{m} \mathcal{B}_i(t),$$

and the coordinate wave vector is given by

$$k_i(\hat{Z}) = \left(1 - (\gamma + 1) \frac{g}{c^2} \hat{Z} \right) k_i + \mathcal{O}(c^{-4}). \quad (3.92)$$

This leads to a quadratic dependence of the position operator in the exponential, which requires further analysis to understand its implications. The non-relativistic part of the \hat{Z} -dependent exponential of Hamiltonian Eq. (3.91) is just the momentum translation

$$e^{\pm ik_i \hat{Z}} = \int dp |p \pm \hbar k_i \rangle \langle p|, \quad (3.93)$$

whereas we now also have an additional contribution $\exp(\pm i\alpha k_i \hat{Z}^2)$ with $\alpha = -(\gamma + 1) \frac{g}{c^2}$ in the interaction Hamiltonian in Eq. (3.91).

Let's further analyse the form of the interaction Hamiltonian when we also transform into the interaction picture with respect to the COM Hamiltonian. It is important to note that the light fields are only activated for a very short period of time. Therefore, it is sufficient to focus on the dominant contribution, which is given by $\hat{P}^2/2m$. Each position operator \hat{Z} will then be transformed according to

$$\hat{Z} \mapsto \hat{Z}(t) = e^{i\frac{\hat{P}^2 t}{2m\hbar}} \hat{Z} e^{-i\frac{\hat{P}^2 t}{2m\hbar}} = \hat{Z} + \frac{\hat{P}}{m} t, \quad (3.94)$$

resulting in an interaction Hamiltonian

$$\hat{H} = \sum_{i=a,b} \frac{\hbar\Omega_i(\hat{Z}(t), \hat{P}, t)}{2} |e\rangle\langle g| e^{\pm i(\hat{Z}(t) - (\gamma + 1) \frac{g}{c^2} \hat{Z}(t)^2) k_i - i(\omega_i - \omega_{\text{eg}})t}. \quad (3.95)$$

Now the question arises, how to deal with the operator $\hat{Z}(t)^2$ in this exponential. For this, we introduce the following theorem.

Theorem: Consider a set of three operators \mathcal{K}_+ , \mathcal{K}_- , and \mathcal{K}_3 , which satisfy the commutation relations

$$[\mathcal{K}_3, \mathcal{K}_\pm] = \pm \mathcal{K}_\pm, \quad [\mathcal{K}_+, \mathcal{K}_-] = -2\mathcal{K}_3. \quad (3.96a)$$

As shown in Barnett et al. [144], the following identity holds:

$$e^{\gamma_+ \mathcal{K}_+ + \gamma_- \mathcal{K}_- + \gamma_3 \mathcal{K}_3} = e^{\Gamma_+ \mathcal{K}_+} e^{\ln(\Gamma_3) \mathcal{K}_3} e^{\Gamma_- \mathcal{K}_-}, \quad (3.96b)$$

where we have defined

$$\Gamma_\pm = \frac{2\gamma_\pm \sinh(\beta)}{2\beta \cosh(\beta) - \gamma_3 \sinh(\beta)}, \quad (3.96c)$$

$$\Gamma_3 = \left(\cosh(\beta) - \frac{\gamma_3}{2\beta} \sinh(\beta) \right)^{-2}, \quad (3.96d)$$

$$\beta^2 = \frac{1}{4} \gamma_3^2 - \gamma_+ \gamma_-. \quad (3.96e)$$

In our case we define $\mathcal{K}_+ = \frac{1}{\sqrt{2}\hbar} \hat{Z}^2$, $\mathcal{K}_- = \frac{1}{\sqrt{2}\hbar} \hat{P}^2$, and $\mathcal{K}_3 = \frac{i}{2\hbar} (\hat{Z}\hat{P} + \hat{P}\hat{Z})$. We use that $[\hat{Z}, \hat{P}^2] = 2i\hbar\hat{P}$ and $[\hat{Z}^2, \hat{P}] = 2i\hbar\hat{Z}$ in order to show that the commutation relations in Eq. (3.96a) are satisfied, i.e.,

$$[\mathcal{K}_3, \mathcal{K}_+] = \frac{i}{2\sqrt{2}\hbar^2} ([\hat{Z}\hat{P}, \hat{Z}^2] + [\hat{P}\hat{Z}, \hat{Z}^2]) = \frac{1}{\sqrt{2}\hbar} \hat{Z}^2 = \mathcal{K}_+, \quad (3.97a)$$

$$[\mathcal{K}_3, \mathcal{K}_-] = \frac{i}{2\sqrt{2}\hbar^2} ([\hat{Z}\hat{P}, \hat{P}^2] + [\hat{P}\hat{Z}, \hat{P}^2]) = -\frac{1}{\sqrt{2}\hbar} \hat{P}^2 = -\mathcal{K}_-, \quad (3.97b)$$

$$[\mathcal{K}_+, \mathcal{K}_-] = \frac{1}{2\hbar^2} (\hat{Z}[\hat{P}^2, \hat{Z}] + [\hat{P}^2, \hat{Z}]\hat{Z}) = -2\mathcal{K}_3. \quad (3.97c)$$

We therefore have the prefactors $\gamma_+ = i\hbar \frac{\alpha k_i}{\sqrt{2}}$, $\gamma_- = i\hbar \frac{\alpha k_i t^2}{\sqrt{2}m^2}$ and $\gamma_3 = i\hbar \frac{\alpha k_i t}{m}$, which lead to the definition of the β parameter

$$\beta^2 = \frac{3}{4} \left(\frac{\gamma+1}{2} \frac{gk_i}{c^2} \right)^2 \frac{t^2}{m^2} \implies \beta = \sqrt{\frac{3}{4}(\gamma+1)\hbar \frac{gk_i}{c^2} \frac{t}{m}}. \quad (3.98)$$

Using this approach, one can determine the values of the Γ 's to the required order of accuracy using

$$\Gamma_+ = \frac{2\gamma_+ \sinh(\beta)}{2\beta \cosh(\beta) - \gamma_3 \sinh(\beta)} = \frac{2\gamma_+}{(2 - \gamma_3)} + O(c^{-4}) = i \frac{\alpha k_i \hbar}{\sqrt{2}} + O(c^{-4}), \quad (3.99a)$$

$$\Gamma_- = \frac{2\gamma_- \sinh(\beta)}{2\beta \cosh(\beta) - \gamma_3 \sinh(\beta)} = \frac{2\gamma_+}{(2 - \gamma_3)} + O(c^{-4}) = i \frac{\alpha k_i \hbar t^2}{\sqrt{2}m^2} + O(c^{-4}), \quad (3.99b)$$

$$\Gamma_3 = \left(\cosh(\beta) - \frac{\gamma_3}{2\beta} \sinh(\beta) \right)^{-2} \approx \left(1 - \frac{\gamma_3}{2} \right)^{-2} \approx 1 + \gamma_3, \quad (3.99c)$$

such that we have $\ln(\Gamma_3) \approx \alpha \hbar \frac{k_i t}{m} + O(c^{-4})$.

Applying the theorem and including the definitions given above, we obtain

$$e^{\pm i\alpha k_i \left(\hat{Z}^2 + \frac{\hat{Z}\hat{P}_z + \hat{P}_z\hat{Z}}{m} t + \frac{\hat{P}_z^2 t^2}{m^2} \right)} = e^{\pm i\alpha k_i \hat{Z}^2} e^{\pm i\alpha k_i \frac{\hat{Z}\hat{P}_z + \hat{P}_z\hat{Z}}{m} t} e^{\pm i\alpha k_i \frac{\hat{P}_z^2 t^2}{m^2}} + O(c^{-4}). \quad (3.100)$$

Since the time span of interest, t , corresponds to the photon flight time and is itself on the order of $\Delta h/c$, we can neglect the latter two exponentials. Consequently, we are left with an operator of the form $e^{\mp ik\hat{Z}^2/c^2}$. Since this operator will act on spatially well-defined Gaussian wave packets, it becomes evident that the full operator $\exp(\pm i(1 + \alpha\hat{Z})k_i\hat{Z})$ will map a momentum eigenstate $|p\rangle$ to $|p \pm \hbar k_i(1 + \alpha z)\rangle$, where z represents the expectation value of \hat{Z} with respect to the initial wave packet.

The wave vector of each laser ($i = a, b$), as depicted in Fig. 1.4, will be gravitationally altered according to

$$\kappa_i(z) = \left(1 - (\gamma + 1)\frac{gz}{c^2}\right)k_i + O(\Gamma c^{-2}). \quad (3.101)$$

To achieve a resonant transition, the goal is to transfer precisely the desired momentum k_i upon interaction. To accomplish this, each laser pulse must be detuned so that the effective wave number $\kappa_i(z_{\text{int}})$ equals k_i , where z_{int} represents the height at which the light pulse interacts with (a component of) the atomic wave packet along the respective path. This condition is fulfilled by mapping the wave vector k_i to $\left(1 + (\gamma + 1)\frac{gz_{\text{int}}}{c^2}\right)k_i$. Using such a frequency chirp, one achieves an effective laser phase imprinted on the atoms during a two-photon process at the interaction height z_{int} given by

$$\Phi_L(z_{\text{int}}) = \pm \left(1 + \frac{\gamma + 1}{2}\frac{gz_{\text{int}}}{c^2}\right)k_R z_{\text{int}} + \Delta\Phi_{\text{FSL}} + O(\Gamma c^{-2}), \quad (3.102)$$

where the sign corresponds to a net gain or loss in momentum, respectively. We absorb the temporal part in $\Delta\Phi_{\text{FSL}}$, since it directly depends on the FSL effect.

As shown in Eq. (1.58), the scattering matrix for Bragg diffraction, which transfers a momentum of $N_R\hbar k_R$, can be represented as

$$U^{(\theta)}(z_{\text{int}}) = \frac{1}{\sqrt{2}} \begin{pmatrix} \cos(\theta) & i \sin(\theta) e^{iN_R\Phi_L(z_{\text{int}})} \\ i \sin(\theta) e^{-iN_R\Phi_L(z_{\text{int}})} & \cos(\theta) \end{pmatrix}, \quad (3.103)$$

in the basis of the momentum eigenstates $|0\hbar k_R\rangle$ and $|N_R\hbar k_R\rangle$. In the experiment, the angle θ is precisely controlled through the manipulation of pulse intensities and durations, as discussed in the works by Müller et al. [145] and Kirsten-Siemß et al. [56]. It is fine-tuned to $\pi/2 + n\pi$ for a beam splitter and $\pi + 2n\pi$ for a mirror pulse with $n \in \mathbb{Z}$. It is important to note that, because of various relativistic effects that influence the Rabi frequency and the detuning, the angle θ can, in principle, also have dependencies on position and momentum. These dependencies are expected to appear at an insignificant level and will likely be overshadowed by factors such as the uncertainty in the electric field magnitude. Thus, while the relativistic corrections can theoretically affect θ , their practical impact on the outcomes of the Bragg diffraction process remains negligible, allowing the angle to be treated as effectively constant for the purposes of high-precision experiments.

3.6.1 Doppler Effect and Kick Phase

In the non-relativistic scenario, as previously discussed, we need to consider the Doppler effect. However, when incorporating relativistic effects, we must account for both, the first-order Doppler shift – which influences the light fields as shown in Eq. (2.20) – and

the second-order Doppler shift. Consequently, the necessary frequency chirp, analogous to Eq. (2.21), is given by

$$\omega_a \mapsto \left(1 + \frac{v_{\text{int}}}{c} - \frac{v_{\text{int}}^2}{2c^2}\right)\omega_a, \quad \omega_b \mapsto \left(1 - \frac{v_{\text{int}}}{c} - \frac{v_{\text{int}}^2}{2c^2}\right)\omega_b. \quad (3.104)$$

From this point onward, consider the frequencies ω_a, ω_b as already detuned as described in Eq. (3.104). The imprinted phase Eq. (3.102) will then be additionally Doppler shifted, and is given by

$$\begin{aligned} \Phi_L(t) = & \pm \left(k_R + \frac{v_{\text{int}}}{c} \frac{\omega_R}{c} - \frac{v_{\text{int}}^2}{2c^2} k_R + \frac{\gamma + 1}{2} \frac{g z_{\text{int}}}{c^2} k_R \right) z_{\text{int}} \\ & \mp \left(\omega_R - v_{\text{int}} k_R + \frac{v_{\text{int}}^2}{c^2} \omega_R \right) t + O(\Gamma c^{-2}). \end{aligned} \quad (3.105)$$

For later reference, we rewrite each laser phase contribution in Eq. (3.105) in a dimensionless form, similar to the propagation phase in Eq. (2.13) and the separation phase in Eq. (2.14) as

$$\begin{aligned} \Phi_L(\tau) = & \pm \omega_C T_R \left(\left(1 - \frac{\dot{\xi}_{\text{int}}^2}{2} + \frac{\gamma + 1}{2} \mathcal{G}_{1,R} \xi_{\text{int}} \right) \mathcal{R}_R + \dot{\xi}_{\text{int}} \mathcal{F}_R \right) \xi_{\text{int}} \\ & \mp \omega_C T_R \left(\mathcal{F}_R - \dot{\xi}_{\text{int}} \mathcal{R}_R + \dot{\xi}_{\text{int}}^2 \mathcal{F}_R \right) \tau + O(5). \end{aligned} \quad (3.106)$$

In this context, the first-order Doppler term, which is proportional to \mathcal{F}_R , contributes to the laser phase at order $O(3)$. On the other hand, both the second-order Doppler term and the recoil term, proportional to \mathcal{R}_R , contribute at order $O(4)$. Additionally, the terms of $O(\Gamma c^{-2})$ in Eq. (3.105) translate to an even higher order, specifically $O(5)$. Given these scaling behaviours, our goal is to consistently determine each phase shift contribution with accuracy up to $O(4)$.

In summary, the overall relative laser phase accumulated along the upper and lower AIF paths $\xi_{\text{up}}(\tau)$ and $\xi_{\text{low}}(\tau)$, due to Bragg interactions, is given by

$$\Delta\Phi_{\text{Bragg}} = \sum_{\tau_i \in \mathcal{T}_U} \Phi_L(\tau_i) - \sum_{\tau_i \in \mathcal{T}_L} \Phi_L(\tau_i). \quad (3.107)$$

Atomic Velocity After a Photon Interaction

Understanding how the Doppler effect and spacetime curvature affect the photon momentum transferred to the atoms undergoing Bragg transitions is necessary to calculate the boundary conditions of the atomic trajectories in Eq. (2.11). Note that calculating the momentum kicks bears a subtlety: The light field's momentum $\hbar k_\mu$ is a covector, whereas the atomic four-velocity u^μ is a (contravariant) vector. Therefore, in order to compute the atomic velocity after the momentum kick, we need to raise the index of $\hbar k_\mu$ using the metric.¹¹

As an example, consider a Bragg pulse interacting with a wave packet at a height z_{int} as before. The additional velocity after the kick will then be given by

$$v_{\text{Kick}} = \frac{N_R \hbar k_R}{m} \left(1 + 2\gamma \frac{g z_{\text{int}}}{c^2} \right) + O(\Gamma c^{-2}). \quad (3.108)$$

¹¹This is also evident from the upper index in Eq. (63) in Dimopoulos et al. [87].

3.7 Relativistic Phase Shifts in Interferometers

Similar to the presentation of phase shifts in Table 2.2 and Table 2.4, we now compile the phase shifts resulting from relativistic effects for the SRBI, SDDI, and ARBI as shown in Fig. 2.1. With one exception, all of these terms will be at least of order $O(4)$. Listing all terms of order $O(4)$ is impractical due to their sheer number, but they can be explicitly obtained from Ref. [1].

Even if we ignore the Bloch oscillations for a moment, we still have seven small parameters from Table 2.1: \mathcal{Z}_0 , \mathcal{V}_0 , \mathcal{G}_0 , $\mathcal{G}_{1,R}$, $\mathcal{G}_{2,R}$, \mathcal{R}_R , and \mathcal{F}_R . These parameters lead to $\binom{7+4-1}{4} = \binom{10}{4} = 210$ possible distinct terms at order $O(4)$, since the order of parameters does not matter. However, since observable phase shifts are constituted only by products of these parameters that include at least one recoil-associated factor¹² \mathcal{R}_R or \mathcal{F}_R , the number of potential phase shifts at order $O(4)$ can be bounded by $2 \cdot \binom{6+3-1}{3} = 112$. Therefore, we present a limited selection of these phase shifts in Table 3.3 and refer the readers to extract any other desired terms from Ref. [1] that are not included in the table. The only relativistic term of order $O(3)$, labelled as number #44, can be seen as a correction to the well known phase shift $\omega_C T_R \mathcal{R}_R \mathcal{G}_{1,R} = g k_R T_R^2$. This term scales with the constant gravitational potential at Earth's surface, ϕ_0 , and $(\beta - 1)$, which would identically vanish in GR. Note that terms #56, 57 are not diverging for $T_R \rightarrow 0$, since $\mathcal{G}_{3,R}$ is cubic in T_R .

For the specific case of a MZI (equivalent to the SRBI with $k_B = 0$, $T_B = 0$) we can compare the results of our treatment to the one of Dimopoulos et al. [87, 88], and find good, although not exact, agreement. A detailed comparison of the terms up to $O(4)$ can be found below. There, we also summarise where our approach differs from that of Refs. [87, 88] in methodology and notation and discuss how these differences affect the final results.

The papers by Dimopoulos et al. [87, 88] discuss a Raman AIF of the Mach-Zehnder type within the PPN spacetime framework. To effectively compare our results with their findings, we need to adapt their notation and sign conventions to match ours. We list all needed differences in sign conventions and notation in Table 3.2. Notably, due to a different sign convention in the phases of the EM waves, it is necessary to redefine the wave vector and frequency as follows: $k_i \mapsto -k_i$ and $\omega_i \mapsto -\omega_i$ for $i = a, b$, which gives an overall sign change in ω_R , but not in k_R .

Dim. et al.	g	$\partial_r g$	$\partial_r^2 g$	T	ω_a	κ_{eff}	ω_{eff}	v_L
Our notation	$-(1 + 2\gamma \mathcal{G}_0) g$	$(1 + 3\gamma \mathcal{G}_0) \Gamma$	$-\frac{1}{2} \Lambda$	T_R	0	k_R	$-\omega_R$	v_0

Table 3.2: Comparison of notation between the analysis by Dimopoulos et al. [87, 88] and this work.

¹²Because there is no atomic recoil, no enclosed spacetime area is generated, which means there are no resulting phase shifts. This scenario would differ in the context of clock interferometry, since there a superposition of internal states can lead to non-vanishing phase shifts even when the atoms travel on the same trajectory.

Phases in units of ω_C							
#	Order	Proportionality	SRBI	SDDI	ARBI	α	Origin
44	$O(3)$	$\mathcal{G}_0 \mathcal{G}_{1,R} \mathcal{R}_R$	$2(\beta - 1)(T_B + T_R)$	$4(\beta - 1)(T_B + T_R)$	$2(\beta - 1)(T_B + T_R)$	2	Post-Newtonian
45	$O(4)$	$\mathcal{R}_R \mathcal{G}_{1,R} \mathcal{V}_0 \mathcal{R}_B$	$-\frac{13\gamma+20}{2} T_B - \frac{20\gamma+41}{2} T_R$	$-(13\gamma + 20)T_B - (20\gamma + 41)T_R$	$-\frac{13\gamma+20}{2} T_B - \frac{20\gamma+41}{2} T_R$	2	Post-Newtonian
46		$\mathcal{R}_R \mathcal{G}_{1,R} \mathcal{V}_0^2$	$-\frac{10\gamma+11}{2} T_B - \frac{8\gamma+11}{2} T_R$	$-(10\gamma + 11)T_B - (8\gamma + 11)T_R$	$-\frac{10\gamma+11}{2} T_B - \frac{8\gamma+11}{2} T_R$	2	
47		$\mathcal{R}_R \mathcal{G}_{1,R}^2 \mathcal{V}_0$	$\frac{8\beta+48\gamma+51}{2} T_B + \frac{4\beta+30\gamma+38}{2} T_R$	$(8\beta + 48\gamma + 51)T_B + (4\beta + 30\gamma + 38)T_R$	$\frac{8\beta+48\gamma+51}{2} T_B + \frac{4\beta+30\gamma+38}{2} T_R$	3	
48		$\mathcal{R}_R \mathcal{G}_{1,R}^2 \mathcal{R}_B$	$\frac{12\beta+165\gamma+264}{12} T_B + \frac{112\gamma+242}{12} T_R$	$\frac{12\beta+165\gamma+264}{6} T_B + \frac{112\gamma+242}{6} T_R$	$\frac{12\beta+165\gamma+264}{12} T_B + \frac{112\gamma+242}{12} T_R$	3	
49		$\mathcal{R}_R \mathcal{G}_{1,R}^3$	$-\frac{36\beta+220\gamma+278}{12} T_B - \frac{4\beta+93\gamma+151}{12} T_R$	$-\frac{36\beta+220\gamma+278}{6} T_B - \frac{4\beta+93\gamma+151}{6} T_R$	$-\frac{36\beta+220\gamma+278}{12} T_B - \frac{4\beta+93\gamma+151}{12} T_R$	4	
50		$\mathcal{R}_R \mathcal{G}_{1,R} \mathcal{R}_B^2$	$-\frac{8\gamma+17}{4} T_B - \frac{10\gamma+35}{4} T_R$	$-\frac{8\gamma+17}{2} T_B - \frac{10\gamma+35}{2} T_R$	$-\frac{8\gamma+17}{4} T_B - \frac{10\gamma+35}{4} T_R$	2	
51		$\mathcal{R}_R \mathcal{G}_{1,R} \mathcal{G}_{1,B}^2$	$\frac{\beta-43\gamma-52}{24} T_B$	$\frac{\beta-43\gamma-52}{12} T_B$	$\frac{\beta-43\gamma-52}{24} T_B$	4	
52		$\mathcal{R}_R \mathcal{G}_{1,R}^2 \mathcal{G}_{1,B}$	$-\frac{6\beta+44\gamma+51}{4} T_B$	$-\frac{6\beta+44\gamma+51}{2} T_B$	$-\frac{6\beta+44\gamma+51}{4} T_B$	4	
53		$\mathcal{R}_R \mathcal{G}_{1,R} \mathcal{G}_{1,B} \mathcal{V}_0$	$\frac{\beta+13\gamma+13}{2} T_B$	$(\beta + 13\gamma + 13)T_B$	$\frac{\beta+13\gamma+13}{2} T_B$	3	
54		$\mathcal{R}_R \mathcal{G}_{1,R} \mathcal{G}_{1,B} \mathcal{R}_B$	$\frac{8\gamma+11}{2} T_B$	$(8\gamma + 11)T_B$	$\frac{8\gamma+11}{2} T_B$	3	
55		$\mathcal{R}_R \mathcal{G}_0 \mathcal{G}_{1,R} \mathcal{G}_{2,R}$	$\frac{57\beta-57}{3} T_B + \frac{25\beta-25}{3} T_R$	$2 \frac{57\beta-57}{3} T_B + 2 \frac{25\beta-25}{3} T_R$	$\frac{57\beta-57}{3} T_B + \frac{25\beta-25}{3} T_R$	4	
\vdots		\vdots	\vdots	\vdots	\vdots	\vdots	
56		$\mathcal{G}_{3,R} \mathcal{R}_R \mathcal{V}_0^2$	$\frac{T_B^3 + 12T_B^2 T_R + 8T_R^2 (3T_B + T_R)}{8T_R^2}$	$\frac{T_B^3 + 12T_B^2 T_R + 8T_R^2 (3T_B + T_R)}{4T_R^2}$	$\frac{T_B^3 + 12T_B^2 T_R + 8T_R^2 (3T_B + T_R)}{8T_R^2}$	4	3rd order grav. potential
57		$\mathcal{G}_{3,R} \mathcal{R}_R^2 \mathcal{V}_0$	$\frac{T_B^2 + 4T_R^2 (2T_B + T_R)}{4T_R}$	0	$\frac{T_B^2 + 4T_R^2 (2T_B + T_R)}{4T_R}$	4	
\vdots		\vdots	\vdots	\vdots	\vdots	\vdots	

Table 3.3: Post-Newtonian list of phases of the SRBI, SDDI, ARBI geometries. The list starts with term number # 44 and should be seen as a continuation of the previous tables. There was no selection method at place to specifically show theses phase contributions, compared to all other terms of order $O(4)$.

Despite aligning the notation between our study and that of Dimopoulos et al., some differences persist. Dimopoulos et al. selected an initial height of $z_0 = 0$. We assumed that the gravitational parameters g, Γ and Λ were obtained by evaluating the gravitational potential and their derivatives in the original (asymptotically flat) coordinate system. This assumption follows the standard practice of using coordinate lengths for such evaluations. It could also be the case that Dimopoulos et al. chose to evaluate those parameters using "metric lengths" and not "coordinate lengths", which would shift those definitions by some factors of $\mathcal{G}_0 = \phi_0/c^2$. We therefore expect deviations of our results in comparison to [87] at order $\mathcal{O}(4)$.

The comparison of our results to Refs. [87, 88] can be found in Table 3.4. To orders $\mathcal{O}(2)$ and $\mathcal{O}(3)$ all terms except # 8, # 9 are reproduced. Term # 8 can result from a different definition of g by Dimopoulos et al., as discussed before. Term # 9 can be reproduced if we omit the contribution of the final interferometry laser when calculating the dominant FSL phase. Setting the imprinted recoil in the last pulse to zero, in this step of the calculation, yields the same output for term # 9 as in Dimopoulos et al. It therefore appears like this contribution might have been omitted in Refs. [87, 88]. For more details, we refer to the analysis in Chapter 4. We have also reproduced all non-zero terms for our system from [89, Table 1]. However, term # 9 was not included in their results. On the other hand, they did include Coriolis and centrifugal terms in their phase shift calculations, as well as the fourth-order differential of the gravitational potential. Another notable set of terms consists of numbers # 10 and # 15. The prefactors in these terms are intentionally expressed in this form because the primary contribution of $\frac{7}{6}$ arises from including the Λ -dependent part of the gravitational potential into the Lagrangian, which influences the propagation phase. The additional contribution¹³ of $-\frac{1}{6}$ results from considering this part of the potential in the ELE, leading to the modified atomic trajectories described in Eq. (3.37c). It appears that this latter effect was omitted in Refs. [87, 88].

3.8 Outlook: Relativistic Description of Stationary Spacetimes

So far, we only considered static spacetimes, which are characterised by time-independent metrics with no cross-terms between space and time. Spacetimes like those offer a straightforward description of gravitational systems in equilibrium, such as a non-rotating star. Transitioning from a static to a stationary spacetime involves accounting for systems where time invariance is maintained, but rotational or additional dynamic effects are present, such as in the case of rotating gravitating objects. This transition requires the introduction of off-diagonal metric components, specifically terms that couple time and angular components, capturing the essence of frame dragging and rotational dynamics introduced by angular momentum. This transition can be viewed as the first step towards understanding even more complex, i.e., non-stationary spacetimes, which are necessary for describing phenomena such as gravitational waves.

¹³Note that we originally wrote that this additional factor is $-\frac{1}{36}$ in Ref. [2], which was a typo.

Comparison to the MZI from Refs. [87, 88]				
#	Term from [87] in our notation	[87] in dim. param. mod ω_C	Our result	$O(n)$
1	$\kappa_R g T_R^2$	$\mathcal{R}_R \mathcal{G}_{1,R} T_R$	$\mathcal{R}_R \mathcal{G}_{1,R} T_R$	2
2	$-\kappa_R \Gamma v_0 T_R^3$	$-\mathcal{R}_R \mathcal{G}_{2,R} \mathcal{V}_0 T_R$	$-\mathcal{R}_R \mathcal{G}_{2,R} \mathcal{V}_0 T_R$	3
3	$\frac{7}{12} \Gamma g \kappa_R T_R^4$	$\frac{7}{12} \mathcal{R}_R \mathcal{G}_{1,R} \mathcal{G}_{2,R} T_R$	$\frac{7}{12} \mathcal{R}_R \mathcal{G}_{1,R} \mathcal{G}_{2,R} T_R$	4
4	$-3 \frac{\kappa_R g^2}{c} T_R^3$	$-3 \mathcal{R}_R \mathcal{G}_{1,R}^2 T_R$	$-3 \mathcal{R}_R \mathcal{G}_{1,R}^2 T_R$	3
5	$3 \frac{\kappa_R g v_0}{c} T_R^2$	$3 \mathcal{G}_{1,R} \mathcal{V}_0 \mathcal{R}_R T_R$	$3 \mathcal{G}_{1,R} \mathcal{V}_0 \mathcal{R}_R T_R$	2
6	$-\frac{\hbar \kappa_R^2}{2m} \Gamma T_R^3$	$-\frac{1}{2} \mathcal{R}_R^2 \mathcal{G}_{2,R} T_R$	$-\frac{1}{2} \mathcal{R}_R^2 \mathcal{G}_{2,R} T_R$	3
7	$\omega_R \frac{g T_R}{c}$	$\mathcal{F}_R \mathcal{G}_{1,R} T_R$	$\mathcal{F}_R \mathcal{G}_{1,R} T_R$	2
8	$(2 - 2\beta + \gamma) \frac{\kappa_R g \phi_0 T_R^2}{c}$	$(2 - 2\beta + \gamma) \mathcal{G}_0 \mathcal{G}_{1,R} \mathcal{R}_R T_R$	$(2 - 2\beta + 2\gamma) \mathcal{G}_0 \mathcal{G}_{1,R} \mathcal{R}_R T_R$	2
9	$\frac{3\hbar \kappa_R^2}{2mc} g T_R^2$	$\frac{3}{2} \mathcal{R}_R^2 \mathcal{G}_{1,R} T_R$	$\frac{5}{2} \mathcal{R}_R^2 \mathcal{G}_{1,R} T_R$	2
10	$\frac{7}{6} \kappa_R v_0^2 \Lambda T_R^4$	$\frac{7}{6} \mathcal{R}_R \mathcal{V}_0^2 \mathcal{G}_{3,R}$	$\left(\frac{7}{6} - \frac{1}{6}\right) \mathcal{R}_R \mathcal{V}_0^2 \mathcal{G}_{3,R}$	4
11	$\frac{35}{4} \frac{\kappa_R \Gamma g v_0}{c} T_R^4$	$\frac{35}{4} \mathcal{R}_R \mathcal{V}_0 \mathcal{G}_{1,R} \mathcal{G}_{2,R} T_R$	$\frac{35}{4} \mathcal{R}_R \mathcal{V}_0 \mathcal{G}_{1,R} \mathcal{G}_{2,R} T_R$	4
12	$-4 \frac{\kappa_R \Gamma v_0^2}{c} T_R^3$	$-4 \mathcal{R}_R \mathcal{V}_0^2 \mathcal{G}_{2,R} T_R$	$-4 \mathcal{R}_R \mathcal{V}_0^2 \mathcal{G}_{2,R} T_R$	3
15	$\frac{7}{6} \frac{\hbar \kappa_R^2}{m} v_0 \Lambda T_R^4$	$\frac{7}{6} \mathcal{R}_R^2 \mathcal{V}_0 \mathcal{G}_{3,R}$	$\left(\frac{7}{6} - \frac{1}{6}\right) \mathcal{R}_R^2 \mathcal{V}_0 \mathcal{G}_{3,R}$	4
16 + 19 [†]	$-(14 - 2\beta - \gamma) \frac{\kappa_R g^2 v_0 T_R^3}{c}$	$-(14 - 2\beta - \gamma) \mathcal{R}_R \mathcal{G}_{1,R}^2 \mathcal{V}_0 T_R$	$(19 + 2\beta + 20\gamma) \mathcal{R}_R \mathcal{G}_{1,R}^2 \mathcal{V}_0 T_R$	3
17 + 23 [*]	$\frac{7}{12} (14 - 2\beta - \gamma) \frac{\kappa_R g^3 T_R^4}{c}$	$\frac{7}{12} (14 - 2\beta - \gamma) \mathcal{R}_R \mathcal{G}_{1,R}^3 T_R$	$-\frac{151+4\beta+117\gamma}{12} \mathcal{R}_R \mathcal{G}_{1,R}^3 T_R$	4
18	$5 \frac{\kappa_R g v_0^2}{c^2} T_R^2$	$5 \mathcal{R}_R \mathcal{G}_{1,R} \mathcal{V}_0^2 T_R$	$-\frac{11+12\gamma}{2} \mathcal{R}_R \mathcal{G}_{1,R} \mathcal{V}_0^2 T_R$	2
20	$\frac{7}{12} (4 - 4\beta - 3\gamma) \frac{\kappa_R \phi_0 \Gamma g}{c^2} T_R^4$	$\frac{7}{12} (4 - 4\beta - 3\gamma) \mathcal{G}_0 \mathcal{G}_{1,R} \mathcal{G}_{2,R} \mathcal{R}_R$	$\frac{100\beta-100-14\gamma}{12} \mathcal{G}_0 \mathcal{G}_{1,R} \mathcal{G}_{2,R} \mathcal{R}_R$	4
21	$-\omega_R \frac{\Gamma v_0 T_R^3}{c}$	$-\mathcal{F}_R \mathcal{G}_{2,R} \mathcal{V}_0 T_R$	$-\mathcal{F}_R \mathcal{G}_{2,R} \mathcal{V}_0 T_R$	3
22	$\frac{7}{12} \omega_R \frac{\Gamma g T_R^4}{c}$	$\frac{7}{12} \mathcal{F}_R \mathcal{G}_{1,R} \mathcal{G}_{2,R} T_R$	$\frac{7}{12} \mathcal{F}_R \mathcal{G}_{1,R} \mathcal{G}_{2,R} T_R$	4
24	$\frac{7\hbar \kappa_R^2}{2mc} \Gamma v_0 T_R^3$	$\frac{7}{2} \mathcal{R}_R^2 \mathcal{G}_{2,R} \mathcal{V}_0 T_R$	$-\frac{19}{6} \mathcal{R}_R^2 \mathcal{G}_{2,R} \mathcal{V}_0 T_R$	3
25	$-\frac{27\hbar \kappa_R^2}{8mc} \Gamma g T_R^4$	$-\frac{27}{8} \mathcal{R}_R^2 \mathcal{G}_{1,R} \mathcal{G}_{2,R} T_R$	$\frac{65}{24} \mathcal{R}_R^2 \mathcal{G}_{1,R} \mathcal{G}_{2,R} T_R$	4
27	$6(2 - 2\beta - \gamma) \frac{\kappa_R \phi_0 g^2 T_R^3}{c^3}$	$6(2 - 2\beta - \gamma) \mathcal{R}_R \mathcal{G}_0 \mathcal{G}_{1,R}^2$	$6(4 - 4\beta + \gamma) \mathcal{R}_R \mathcal{G}_0 \mathcal{G}_{1,R}^2$	3
28	$-3\omega_R \frac{g^2 T_R^3}{c^2}$	$-3 \mathcal{F}_R \mathcal{G}_{1,R}^2 T_R$	$-3 \mathcal{F}_R \mathcal{G}_{1,R}^2 T_R$	3
29	$3\omega_R \frac{g v_0 T_R^2}{c^2}$	$3 \mathcal{F}_R \mathcal{G}_{1,R} \mathcal{V}_0 T_R$	$3 \mathcal{F}_R \mathcal{G}_{1,R} \mathcal{V}_0 T_R$	2
30	$-6(1 - \beta) \frac{\phi_0 g v_0 T_R^2}{c^3} \kappa_{\text{eff}}$	$-6(1 - \beta) \mathcal{G}_0 \mathcal{G}_{1,R} \mathcal{V}_0 \mathcal{R}_R$	$-6(2 - 2\beta + \gamma) \mathcal{G}_0 \mathcal{G}_{1,R} \mathcal{V}_0 \mathcal{R}_R$	2

Table 3.4: Comparison of phase shifts for a MZI of our results and Dimopoulos et al. Factors of \hbar and c are restored and highlighted in orange. One can see that all terms of orders $O(2)$ and $O(3)$ are reproduced apart from terms # 8 and # 9. Terms # 13, # 14 and # 26 are zero for Bragg interferometers and therefore not shown. [†], ^{*}: Terms # 16 + # 19 and # 17 + # 23 can be combined and therefore share a row.

Stationary Case

Based on Ref. [146][Box 13.1], we express the rotating PPN metric of interest using a (3, 1)-decomposition as

$$g_{\mu\nu} = \begin{pmatrix} -1 - 2\frac{\phi(\mathbf{r})}{c^2} - 2\beta\frac{\phi(\mathbf{r})^2}{c^4} + O(c^{-6}) & -\frac{4+4\gamma+\alpha_1}{2c^3} \mathbf{V}(\mathbf{r})^T + O(c^{-5}) \\ -\frac{4+4\gamma+\alpha_1}{2c^3} \mathbf{V}(\mathbf{r}) + O(c^{-5}) & \left(1 - 2\gamma\frac{\phi(\mathbf{r})}{c^2}\right) \mathbb{1}_3 + O(c^{-4}) \end{pmatrix}, \quad (3.109)$$

including an additional PPN parameter α_1 , which vanishes in GR. The novel rotational PPN vector-potential $\mathbf{V}(\mathbf{r})$ can be constructed from the gravitational mass density $\rho(\mathbf{r})$ by

$$\mathbf{V}(\mathbf{r}) = G \int d^3 \mathbf{r}' \frac{\rho(\mathbf{r}') \mathbf{v}(\mathbf{r}')}{|\mathbf{r} - \mathbf{r}'|} \quad \text{with} \quad \mathbf{v}(\mathbf{r}, t) = \frac{d\mathbf{r}}{dt}. \quad (3.110)$$

For nearly spherical bodies, the PPN vector potential $\mathbf{V}(\mathbf{r})$ can be determined as (see Ref. [147][Eq. (9.4)])

$$\mathbf{V}(\mathbf{r}) = \frac{GM_{\oplus}}{r} \mathbf{v}_{\text{COM}} - \frac{G \mathbf{r} \times \mathbf{J}_{\oplus}}{2r^3} + O(r^{-3}), \quad (3.111)$$

where \mathbf{v}_{COM} its COM motion, which we'll neglect for the case of the Earth as the gravitating body. We therefore obtain off-diagonal metric components

$$\begin{aligned} g_{0j}(\mathbf{r}) &= -\frac{4+4\gamma+\alpha_1}{2c^3} V_j(\mathbf{r}) + O(c^{-5}) \\ &= \frac{4+4\gamma+\alpha_1}{4r^3 c^3} G (\mathbf{r} \times \mathbf{J}_{\oplus})_j + O(r^{-3}, c^{-5}). \end{aligned} \quad (3.112)$$

Calculating the Lagrangian $L^{\text{Rot}}(\mathbf{r}, \dot{\mathbf{r}})$ from the metric tensor, in a manner similar to Eq. (1.8), one derives the non-rotating PPN Lagrangian $L(\mathbf{r}, \dot{\mathbf{r}})$ as seen in Eq. (1.32). This result includes contributions from the two fictitious forces, detailed in Sec. 2.2.4, and additional terms related to the so-called Lense-Thirring effect, leading to

$$\begin{aligned} L^{\text{Rot}}(\mathbf{r}, \dot{\mathbf{r}}) &= L(\mathbf{r}, \dot{\mathbf{r}}) + m \dot{\mathbf{r}} \cdot (\omega_{\oplus} \times \mathbf{r}) + \frac{m}{2} (\omega_{\oplus} \times \mathbf{r})^2 \\ &\quad - \frac{4+4\gamma+\alpha_1}{4} \frac{mG}{r^3 c^2} (\mathbf{r} \times \dot{\mathbf{r}}) \cdot \mathbf{J}_{\oplus} + O(c^{-4}). \end{aligned} \quad (3.113)$$

The Lense-Thirring effect, also known as frame dragging, is a relativistic phenomenon predicted by GR. It occurs when a massive rotating object, like a planet or a star, drags the spacetime around it as it rotates. This effect results in the precession of the orbit of nearby particles and gyroscopes. The ELE in their vector form, $\frac{d}{dt} \nabla_{\dot{\mathbf{r}}} L^{\text{Rot}}(\mathbf{r}, \dot{\mathbf{r}}) - \nabla_{\mathbf{r}} L^{\text{Rot}}(\mathbf{r}, \dot{\mathbf{r}}) = 0$, can be calculated to be

$$\begin{aligned} \ddot{\mathbf{r}} &= -\nabla \phi(\mathbf{r}) - \frac{3}{2c^2} \mathbf{r}^2 \ddot{\mathbf{r}} + \frac{2\gamma+1}{c^2} \phi(\mathbf{r}) \ddot{\mathbf{r}} - \frac{2\beta-1}{c^2} \phi(\mathbf{r}) \nabla \phi(\mathbf{r}) \\ &\quad + \frac{4+4\gamma+\alpha_1}{4} \frac{G}{r^3 c^2} \dot{\mathbf{r}} \times \left[\mathbf{J}_{\oplus} - 3 \frac{\mathbf{J}_{\oplus} \cdot \mathbf{r}}{r^2} \mathbf{r} \right] + O(c^{-4}). \end{aligned} \quad (3.114)$$

Substituting the solution for $\ddot{\mathbf{r}}$ back into itself on the right-hand side yields

$$\begin{aligned} \ddot{\mathbf{r}} &= -\nabla \phi(\mathbf{r}) + (2\gamma+1) \frac{\dot{\mathbf{r}}^2 \nabla \phi(\mathbf{r})}{c^2} - 2(\beta+\gamma) \frac{\phi(\mathbf{r}) \nabla \phi(\mathbf{r})}{c^2} \\ &\quad + \frac{4+4\gamma+\alpha_1}{4} \frac{G}{r^3 c^2} \dot{\mathbf{r}} \times \left[\mathbf{J}_{\oplus} - 3 \frac{\mathbf{J}_{\oplus} \cdot \mathbf{r}}{r^2} \mathbf{r} \right] + O(c^{-4}). \end{aligned} \quad (3.115)$$

The *gravitomagnetic field* \mathbf{B}_G can now be defined through its vector potential \mathbf{A}_G , which is given by $\mathbf{A}_G = \frac{4+4\gamma+\alpha_1}{8} \frac{G}{r^3 c} \mathbf{J}_\oplus \times \mathbf{r}$. This definition leads to

$$\mathbf{B}_G = \nabla \times \mathbf{A}_G = \frac{4+4\gamma+\alpha_1}{4} \frac{G}{r^3 c} \left[\mathbf{J}_\oplus - 3 \frac{\mathbf{J}_\oplus \cdot \mathbf{r}}{r^2} \mathbf{r} \right]. \quad (3.116)$$

The Lense-Thirring term in the ELE then reads $\frac{r}{c} \times \mathbf{B}_G$, completely analogous to the magnetic component of the conventional Lorentz force. The gravitomagnetic field is therefore an exact dipole field, allowing it to be treated similarly to standard magnetic fields.

The stationary PPN metric can also be viewed as a post-Newtonian approximation of another well-known rotational solution of Einstein's field equations: the Kerr metric. To illustrate this, we express the triple product in Eq. (3.113) using spherical coordinates, assuming that the mass density $\rho(\mathbf{r})$ is primarily rotating with an angular velocity $\dot{\phi}$. Assuming a "right handed" cross product convention one obtains

$$(\mathbf{r} \times \dot{\mathbf{r}}) \cdot \mathbf{J}_\oplus = -r^2 J_\oplus \sin^2(\theta) \dot{\phi},$$

By inserting a trivial identity of the form M_\oplus/M_\oplus and the Kerr parameter of Earth, $a = J_\oplus/M_\oplus$, we can rewrite the Lagrangian

$$\begin{aligned} L^{\text{Rot}}(\mathbf{r}, \dot{\mathbf{r}}) = L(\mathbf{r}, \dot{\mathbf{r}}) + m \dot{\mathbf{r}} \cdot (\omega_\oplus \times \mathbf{r}) + \frac{m}{2} (\omega_\oplus \times \mathbf{r})^2 \\ + \frac{4+4\gamma+\alpha_1}{4} \frac{ma\dot{\phi}(\mathbf{r}) \sin^2(\theta) \dot{\phi}}{c^2} + O(c^{-4}), \end{aligned} \quad (3.117)$$

which includes the Newtonian gravitational potential. This form is also evident in the Lagrangian of a Kerr black hole.

Ground Based Interferometers

We will now consider the scenario where the interferometric experiment of interest is conducted in an Earth-based interferometer. The Kerr parameter of the Earth is $a \approx 10^9 \frac{m}{s}$. Let us return to the Lagrangian expressed in spherical coordinates, considering a non-corotating frame of reference¹⁴

$$\begin{aligned} L^{\text{Rot}}(\mathbf{r}, \dot{\mathbf{r}}) = \frac{m}{2} \dot{\mathbf{r}}^2 - m\phi(\mathbf{r}) + \frac{4+4\gamma+\alpha_1}{4} \frac{ma\dot{\phi} \sin^2(\theta)}{c^2} \phi(\mathbf{r}) \\ + \frac{m\dot{\mathbf{r}}^4}{8c^2} - \frac{2\beta-1}{2c^2} m\phi(\mathbf{r})^2 - \frac{2\gamma+1}{2c^2} m\phi(\mathbf{r}) \dot{\mathbf{r}}^2 + O(c^{-4}) \end{aligned} \quad (3.118)$$

The velocity in this frame of reference, $\dot{\mathbf{r}}$, can be split into three contributions via $\dot{\mathbf{r}}^2 = v_r^2 + v_\theta^2 + v_\varphi^2$. Here, v_r corresponds to the final velocity, v_θ is the transverse velocity, and $v_\varphi \approx 500 \frac{m}{s}$ is, essentially, the rotational velocity of the Earth, resulting from its angular velocity ω_\oplus . In order to analyse the Lense-Thirring effect further, we define

$$LT(r, \theta, \dot{\phi}) = -\frac{4+4\gamma+\alpha_1}{4} \frac{a\dot{\phi} \sin^2(\theta)}{c^2} \frac{GM_\oplus}{r} \quad (3.119)$$

The respective orders of magnitude for the gravitational potential, its zonal and tesseral corrections, and the Lense-Thirring effect are illustrated graphically in Figs. 3.3 and 3.4. These figures represent the perspective of a ground-based observer, i.e., where $r = R_\oplus$.

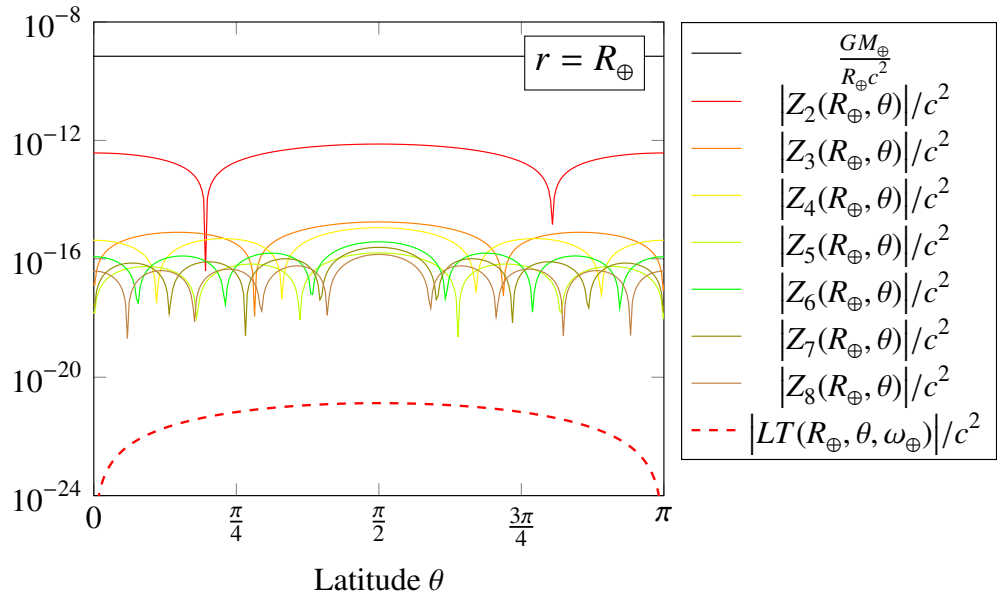


Figure 3.3: Comparison of the (dimensionless) magnitudes of several components of the effective gravitational potential as functions of latitude θ from 0 (north pole) to π (south pole): i) constant gravitational potential of a sphere (black), ii) zonal correction terms from Eq. (2.62b) for different $l \geq 2$ (coloured), and iii) the Lense-Thirring term for an observer fixed on Earth's surface (red dashed). This figure builds upon Fig. 2.12.

Choosing a cut-off for the geopotential corrections in the Lagrangian that allows for the analysis of Lense-Thirring contributions would ultimately require including more than a dozen of gravitational correction terms, rendering any analytical calculation impractical. To effectively measure the Lense-Thirring effect in a ground-based laboratory, seems to be impossible with modern day technology, as even the tesseral correction terms to the potential are considerably larger compared to the frame-dragging effects.

Measuring frame dragging using AIF setups is a challenging task, as indicated by the orders of magnitude shown in Figs. 3.3 and 3.4. Given that the Lense-Thirring contribution depends on r, θ and ϕ , atomic trajectories must be selected to differ in at least one of these degrees of freedom to achieve a non-zero phase shift. If only a radial split of the wavefunction is considered, as is commonly desired in interferometric schemes, the Lense-Thirring term would contribute in a manner similar to gravitational acceleration. This occurs because the Newtonian contribution of the gravitational potential, $\partial_r \phi(\mathbf{r})$ in Eq. (3.120a), would be shifted by a factor $\frac{4+4\gamma+\alpha_1}{4} \frac{ma\dot{\phi} \sin^2(\theta_0)}{c^2}$, where θ_0 represents the latitude of the experiment. This factor is approximately 12 orders of magnitude smaller than g .¹⁴ Since this effect scales identically with g , it is not possible to distinguish between frame dragging and variations in g , through radial separation alone. Therefore, a different approach or additional measurements would be necessary to differentiate between the two effects. Therefore, to measure frame-dragging effects, a more sophisticated experimental geometry is required. This involves constructing spatial superpositions of the atomic wave packets in transverse directions, too. To achieve this, we examine the equations of motion in greater detail. Building on the Newtonian spacetime scenario described in Eq. (2.41), we can express the complete ELE in spherical

¹⁴Thereby, omitting the fictitious forces.

¹⁵Evaluated at the equator, where the Lense-Thirring effect is maximal.

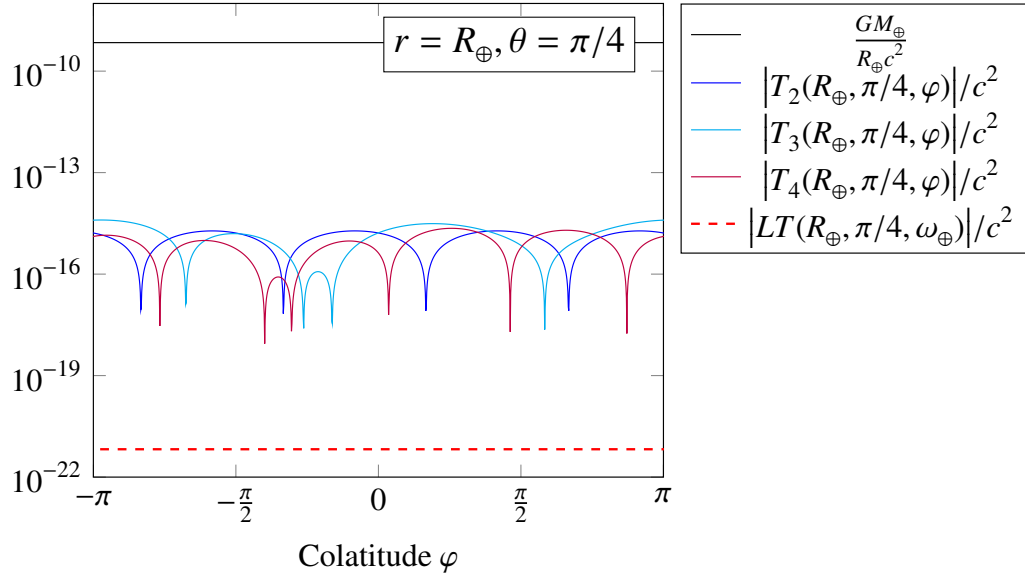


Figure 3.4: Comparison of the (dimensionless) magnitudes of several components of the effective gravitational potential as functions of colatitude φ for fixed $\theta = \pi/4$: i) constant gravitational potential of a sphere (black), ii) summed tesseral correction terms $T_n = \sum_{m=1}^n T_{n,m}$ from Eq. (2.62c) (coloured), and iii) the Lense-Thirring term for an observer fixed on Earth's surface (red dashed). This figure builds upon Fig. 2.13.

coordinates, now incorporating additional relativistic effects, as given by

$$\begin{aligned} \ddot{r} = & -r\dot{\theta}^2 - r\dot{\varphi}^2 \sin^2(\theta) - \partial_r \phi(\mathbf{r}) - \frac{4+4\gamma+\alpha_1}{4} \frac{aGM_{\oplus}\dot{\varphi}\sin^2(\theta)}{c^2 r^2} - \frac{r^3\dot{\varphi}^4 \sin^4(\theta)}{2c^2} \\ & - (2\beta-1) \frac{G^2 M_{\oplus}^2}{r^3 c^2} - \frac{2\gamma+1}{2} \frac{GM_{\oplus}\dot{\varphi}^2 \sin^2(\theta)}{c^2}, \end{aligned} \quad (3.120a)$$

$$\begin{aligned} \ddot{\theta} = & -2\frac{\dot{r}}{r}\dot{\theta} - \dot{\varphi}^2 \sin(\theta) \cos(\theta) - \partial_{\theta} \phi(\mathbf{r}) + \frac{4+4\gamma+\alpha_1}{2} \frac{a\dot{\varphi} \sin(\theta) \cos(\theta) GM_{\oplus}}{c^2 r^3} \\ & - \frac{r^2 \sin^3(\theta) \cos(\theta) \dot{\varphi}^4}{2c^2} - (2\gamma+1) \frac{GM_{\oplus} \sin(\theta) \cos(\theta) \dot{\varphi}^2}{rc^2}, \end{aligned} \quad (3.120b)$$

$$\begin{aligned} \ddot{\varphi} = & -2\frac{\dot{r}}{r}\dot{\varphi} - 2\dot{\theta}\dot{\varphi} \cot(\theta) - \partial_{\varphi} \phi(\mathbf{r}) + \frac{4+4\gamma+\alpha_1}{4} \frac{aGM_{\oplus}}{c^2} \frac{2r\dot{\theta}\cot(\theta) - \dot{r}}{r^4} \\ & - \frac{r\sin(\theta)}{c^2} (\dot{r}\dot{\varphi} \sin(\theta) + r\dot{\theta}\dot{\varphi} \cos(\theta)) + (2\gamma+1) \frac{GM_{\oplus}\dot{r}\dot{\varphi}}{r^2 c^2}. \end{aligned} \quad (3.120c)$$

It becomes evident that finding an exact solution for this set of ODEs is complicated when considering more than just radial motion. The complexity arises from the added degrees of freedom and the interplay between different directions of motion.

The question remains whether the Lense-Thirring effect can even be measured using a ground based interferometer. Since both the dominant component of the gravitational potential and the Lense-Thirring term scale with r^{-1} , while the zonal and tesseral contributions diminish with r^{-l} for $l \geq 3$, the idea of a satellite mission with an onboard AIF presents itself as a promising alternative. Such a mission could benefit from being situated far from Earth's surface, potentially in a highly elliptical orbit, where the Lense-Thirring contribution could be of comparable size to or even larger than the largest zonal correction. From Fig. 3.5, we observe that a radial distance from Earth's centre of at least $10^4 R_{\oplus} - 10^5 R_{\oplus}$ is necessary for

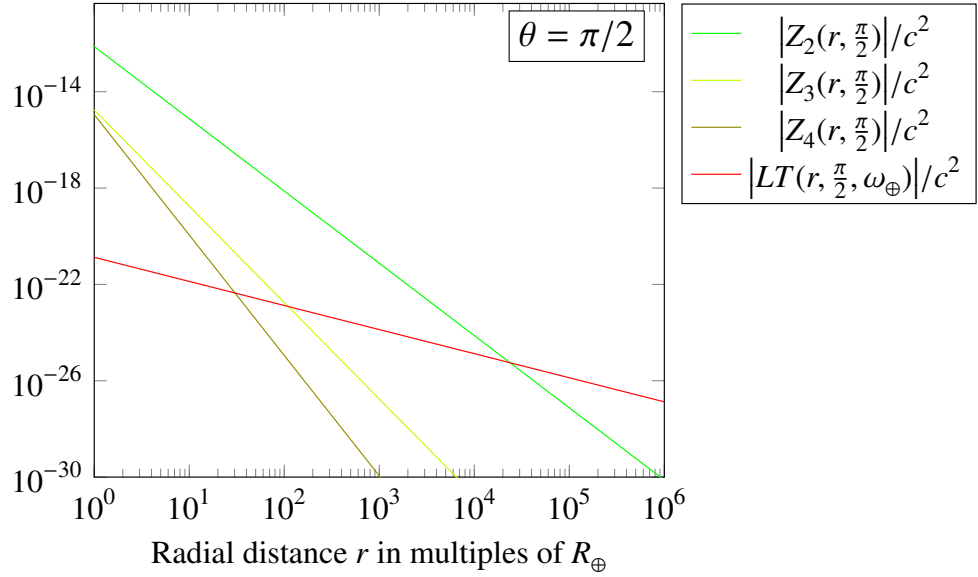


Figure 3.5: Comparison of the dominant zonal correction term (green) to the Lense-Thirring contribution (red) over the radial distance at the equator

the Lense-Thirring contribution to exceed the magnitude of the largest correction terms of the gravitational potential.

In summary, the first significant effect of rotating spacetimes, the Lense-Thirring effect, is unlikely to be measurable with earthbound AIF experiments. However, future setups, which may be designed to measure gravitational waves – a distinct topic on its own – could possess the necessary sensitivity to detect such signals from Earth’s orbit.

Chapter 4

Computer Algorithm for Phase Calculations

"Not only does God definitely play dice, but He sometimes confuses us by throwing them where they can't be seen."

Stephen Hawking in his 1999 lecture "Does God play dice?"

The use of computational tools and programming languages has become an essential component of modern scientific research. In the previous chapters, we analysed how phase shifts in general atomic interferometry frameworks can be calculated and demonstrated that these shifts are always expressed as polynomial functions of time and integrals – both of which can be easily implemented analytically. Previous theoretical descriptions have utilised computer algebra systems, such as **Mathematica**, as referenced in [87, 88]. However, these programs are proprietary and often require expensive software licenses. Moreover, their algorithms can quickly become outdated and are not openly accessible. We believe that modern science should be free and open source, which is why we chose to implement our logic in Python.

Python is known for its versatility, user-friendliness, and extensive library ecosystem that supports various scientific disciplines. However, one area where Python is typically not renowned is analytical and symbolic algebra, a domain where software like **Mathematica** excels. To address this, we employed two significant approaches: i) the use of the library **sympy**, which enables symbolic algebra, and ii) the expansion of phases based on dimensionless parameters from Table 3.1 and the resulting systematic size estimation. Implementing such an algorithm allows us not only to easily compute partial results, but also to trace the origins of certain phase shifts. This is facilitated by the transparency of Python, which is not a black box and provides plenty of opportunities for debugging. Given these innovative methods, we present the essential code snippets and the foundational logic in this dedicated chapter. We hope that the benefits of this approach inspire other researchers to adopt similar phase calculation automation techniques.

The following chapter offers a comprehensive walk-through of the logic behind the Python codes [1] and [3], detailing each important module and function. It will cover the algorithmic approaches, data structures, and libraries utilised, along with examples of input and output. This thorough analysis aims not only to explain how the code functions but also to provide insights into the rationale behind certain aspects of the algorithm. To enhance readability, line breaks will be indicated with a grey hooked arrow "↪".

4.1 Code Structure and Preliminaries

The algorithm is organised into the following files:

- `main.py`: The main file is responsible for calling all relevant functions and initializing the desired plots.
- `interferometer_geometry.py`: This file defines the geometry of the AIF by specifying the number and strength of photon recoils, as well as the time intervals.
- `latex_attributes.py`: This file contains the structure and predefined text blocks used for automatic L^AT_EX file creation. It is only included in the PPN analysis of Ref. [1].
- `parameters_and_functions.py`: This file contains all the definitions of symbols and functions used to obtain partial results in the algorithm. They are organised here to enhance readability.
- `gravity_model.py`: This file reads the numerical model of the gravitational field, if available. It includes all the necessary tools to create a polynomial fit of the measurement data and save it for later use. It is only included in the VLBAI analysis of Ref. [3].

Let's proceed by analysing key code snippets one at a time, in order to gain a deeper understanding of how this algorithm functions internally.

As mentioned above, we aim to perform algebraic operations on purely symbolic expressions and use the Python library `sympy`. This library allows us to define symbols with optional attributes, such as the constant offset of the gravitational field ϕ_0 , which is real and negative.

```
phi_0=symbols("phi_0", negative=True, real=True)
```

Similarly, one can define real but positive constants via:

```
t, hbar, m, c, beta, gamma, g=symbols("t, hbar, m, c, beta, gamma, g", positive=True, real= True)
```

Next, we define the global parameters of the interferometer setup, focusing primarily on the effective recoil momentum, frequency, mass of the atomic species used, and baseline length.

```
# Either 10 or 100
interferometer_height = 10

# in Hz
bragg_recoil_frequency = 10 ** 7

# in 1/m
effective_bragg_k_vector = 16 * 10 ** 6
effective_bloch_k_vector = 5 * 10 ** 8

# in amu
mass_of_atom = 87

# in m/s
# 10m baseline: 15 m/s and 100m baseline: 45 m/s
if interferometer_height == 10:
    initial_velocity = 15
elif interferometer_height == 100:
    initial_velocity = 45

# Complete time of the interferometric sequence (in seconds)
# 10m baseline: full_time = 3 and bragg_time = 1.3
```

```

# 100m baseline: full_time = 9 and bragg_time = 4
if interferometer_height == 10:
    full_time = 3
    bragg_time = 1.3
elif interferometer_height == 100:
    full_time = 9
    bragg_time = 4
else:
    full_time = 9
    bragg_time = 4
print("Choose an interferometer height of 10m or 100m.")
quit()

bloch_time = full_time - 2 * bragg_time

```

A key aspect of the phase calculation is the manipulation of dimensionless parameters, which are defined in Table 3.1. As previously discussed, every phase shift of an arbitrary AIF can be expressed as a linear combination of these terms. The algorithm leverages this principle, which is reflected in its structure and processes as follows. The main object in the algorithm is based on the newly defined class DimPar. This class consists of a prefactor, the name of the dimensionless parameter, a time-order, and a magnitude. It is initialised as follows:

```

class DimPar:
    def __init__(self, prefactor, parameter, time_order: int, magnitude: int):
        self.pre = prefactor
        self.param = parameter
        self.order = time_order
        self.mag = magnitude

```

This implies that a dimensionless parameter, DimPar, possesses four properties: i) A prefactor, which can be an integer, rational, symbolic (such as β or γ), or a float number. ii) A symbol, for example, \mathcal{R}_R or $\mathcal{G}_{1,R}\mathcal{F}_R$. iii) The time order, which is zero for all parameters in Table 3.1, but would be one for a dimensionless time $\tau = t/T_R$. This time order is necessary for the time integrals in the propagation phase. iv) A magnitude, which is an integer that counts the number of small parameters from Table 3.1 present in the symbolic part. The set of dimensionless parameters thus inherits an algebraic structure, as the product of dimensionless parameters with numbers or other dimensionless parameters preserves this structure. When multiplying two such DimPar objects, their prefactors and symbols are multiplied, and their time orders and magnitudes are added.

Within this class definition, you can specify how basic algebraic operations interact with this newly defined class. For example, consider the expression $-\mathcal{R}_R$, which represents the multiplication of a DimPar object by -1 . This operation would map `self.pre` to $-self.pre$, while leaving all other attributes unchanged. This is defined within the class definition using:

```

def __neg__(self):
    return DimPar(-self.pre, self.param, self.order, self.mag)

```

Another, more complicated, operation on this class is given by multiplication, since one needs to define how an operation acts on this class, depending on the object type one wants to multiply the class object to.

```

def __mul__(self, other):
    if isinstance(other, DimPar):
        return DimPar(self.pre*other.pre, self.param*other.param, self.order+other.order
                     , self.mag+other.mag)
    else:
        return DimPar(other*self.pre, self.param, self.order, self.mag)

```

When Python attempts to multiply two quantities it calls the left object's `__mul__()` method. However, if this is not explicitly defined, Python will attempt to determine if the

Generic class object: `DimPar(pre, param, order, mag)`

Multiplication:

$$\begin{aligned} & \text{DimPar}(\text{pre_1}, \text{param_1}, \text{order_1}, \text{mag_1}) * \text{DimPar}(\text{pre_2}, \text{param_2}, \text{order_2}, \text{mag_2}) \\ &= \text{DimPar}(\text{pre_1} * \text{pre_2}, \text{param_1} * \text{param_2}, \text{order_1} + \text{order_2}, \text{mag_1} + \text{mag_2}) \end{aligned}$$

\implies DimPar-class is stable under multiplication

Addition:

$$\begin{aligned} & \text{DimPar}(\text{pre_1}, \text{param_1}, \text{order_1}, \text{mag_1}) + \text{DimPar}(\text{pre_2}, \text{param_2}, \text{order_2}, \text{mag_2}) \\ &= [\text{DimPar}(\text{pre_1}, \text{param_1}, \text{order_1}, \text{mag_1}), \text{DimPar}(\text{pre_2}, \text{param_2}, \text{order_2}, \text{mag_2})] \end{aligned}$$

\implies DimPar-class addition is defined via list concatenation

Figure 4.1: Summary of the algebraic structure within the DimPar-class.

right-hand object has a valid multiplication operation. Since multiplication is not inherently commutative, you must also specify a "right multiplication" procedure using `__rmul__()`. In the case of dimensionless parameters, multiplication is commutative, meaning that the left and right multiplications yield the same result.

```
def __rmul__(self, other):
    return self.__mul__(other)
```

Division is defined in a similar manner, with the additional step of checking to ensure that division by zero does not occur.

```
def __div__(self, other):
    if other != 0:
        return DimPar(self.pre / other, self.param, self.order, self.mag)
    else:
        print("Attempt to divide by zero")
        quit()
```

Lastly, we define how to raise DimPar objects to a certain power, specifying the behaviour of exponentiation for these objects.

```
def __pow__(self, power, modulo=None):
    if power == 0:
        return DimPar(self.pre, 1, 0, 0)
    if isinstance(power, int) and power != 0:
        return DimPar(self.pre**power, self.param**power, self.order*power, self.mag*
                     power)
```

The DimPar class, however, is not closed under addition. To address this, we define the sum of two DimPar objects by placing them into a list. Consequently, addition is handled through list concatenation. We summarise this algebraic structure once more in Fig. 4.1. To keep the lists of terms concise, we define a function that removes all DimPar objects with a magnitude greater than the threshold value, `number_of_small_parameters_kept` defined in the beginning of `main.py`.

```
def mag_cutoff(parameter: DimPar, cutoff: int):
    if cutoff <= 0:
        return 0
    if parameter.mag < cutoff:
        return parameter
    else:
        return 0

def delete_zeros_list(list_of_things):
```

```

new_list = list()
for i_index in range(len(list_of_things)):
    if list_of_things[i_index] != 0:
        new_list.append(list_of_things[i_index])
return new_list

def mag_cutoff_list(list_of_parameters, cutoff: int):
    new_list = list()
    try:
        len(list_of_parameters)
        for i_index in range(len(list_of_parameters)):
            new_list.append(mag_cutoff(list_of_parameters[i_index], cutoff))
    except TypeError:
        return mag_cutoff(list_of_parameters, cutoff)
    return delete_zeros_list(new_list)

```

With the class now defined, we proceed with the definition of an interferometer geometry.

4.2 Initialisation

Initialisation involves defining time segments and their durations, along with specifying the number of imprinted (desired) Bragg and Bloch momenta. We also assign a name to the geometry, which will be used as an abbreviation in the generated files.

```

interferometer_name = "MZI"
time_decomposition = [0,TR,TR]

bragg_quanta_upper_path = [0,1,0,0]
bloch_quanta_upper_path = [0,0,0,0]
bragg_quanta_lower_path = [0,0,1,0]
bloch_quanta_lower_path = [0,0,0,0]

```

From this we define the number of transferred momenta.

```

trans_bragg_upper_path = list()
trans_bragg_lower_path = list()
trans_bloch_upper_path = list()
trans_bloch_lower_path = list()

for i in range(len(time_decomposition)):
    trans_bragg_upper_path.append(bragg_quanta_upper_path[i+1]-
        bragg_quanta_upper_path[i])
    trans_bragg_lower_path.append(bragg_quanta_lower_path[i+1]-
        bragg_quanta_lower_path[i])
    trans_bloch_upper_path.append(bloch_quanta_upper_path[i+1]-
        bloch_quanta_upper_path[i])
    trans_bloch_lower_path.append(bloch_quanta_lower_path[i+1]-
        bloch_quanta_lower_path[i])

```

The initial conditions are always set to be Z0 and V0. We define a set of abstract initial conditions for each AIF path via

```

abstract_init_pos_upper_path = [Z0,ZU1,ZU2,ZU3,ZU4]
abstract_init_vel_upper_path = [V0,VU1,VU2,VU3,VU4]
abstract_init_pos_lower_path = [Z0,ZL1,ZL2,ZL3,ZL4]
abstract_init_vel_lower_path = [V0,VL1,VL2,VL3,VL4]

```

and will be filled with analytic expressions later. To elaborate further: We allow the algorithm to compute abstract phase expressions, such as the propagation phase, starting from a time segment with initial conditions ZU3 and VU3. At a subsequent stage, we substitute this analytical expression, with the given initial conditions, into the final phase expression. Figure 4.2 illustrates how the code progresses from this point, beginning with the calculation of the true atomic trajectories, which include Doppler and gravitational corrections. In this discussion, we have set aside the automatic implementation of the FSL as detailed in Ref. [3]. In that reference, an intermediate step calculates the intersection point between the light rays (in this case, two) and the atomic ensemble, as described in Eq. (2.16).

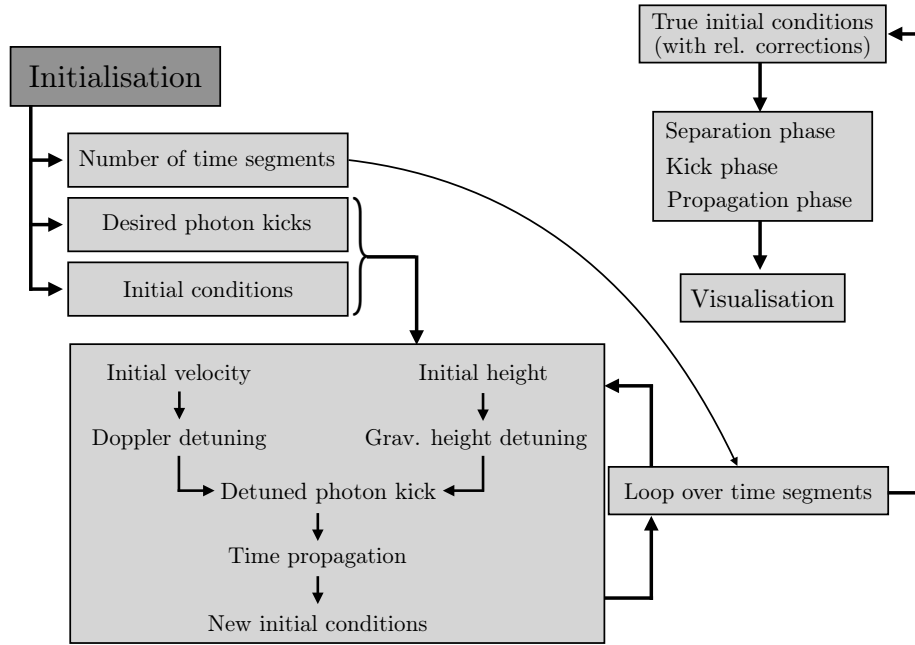


Figure 4.2: Schematic and simplified overview of the algorithm after initialisation.

4.3 Atomic Trajectories

To simplify the calculations, a non-relativistic version of the atomic trajectory and velocity is defined, as relativistic corrections to atomic trajectories, phases, and various intermediate results often depend on the atoms' height or velocity. In that context, only the non-relativistic trajectory is necessary. We start with a purely symbolic definition, which will be needed to visualise the results.

```

def non_relativistic_trajectory_piece(height, velocity, k, time):
    return height + velocity*time + hbar*k*time/m - Rational(1,2)*g*time**2

def non_relativistic_velocity_piece(velocity, k, time):
    return velocity + hbar*k/m - g*time
  
```

We continue with a version consisting of DimPar-objects.

```

def nr_trajectory_dim_param(ramsey_quanta: int, bloch_quanta: int, time,
                           init_height, init_velocity, initial_time):
    time_factor = DimPar(1, time/initial_time, 1, 0)

    next_init_height = list()
    next_init_height.append(init_height)
    next_init_height.append(time_factor*init_velocity)
    next_init_height.append(time_factor*ramsey_quanta*RR)
    next_init_height.append(time_factor*bloch_quanta*RB)
    next_init_height.append(-Rational(1,2)*GIR*time_factor**2)

    return next_init_height
  
```

The first line defines a dimensionless time variable, therefore having a magnitude of zero, but a time order of one. We demonstrate the concept behind this construction with an example, shown in Fig. 4.3.

One of the key functions is the atomic trajectory that incorporates all the corrections elaborated in previous chapters. It will be introduced in multiple steps. We begin with the non-relativistic component of order $O(1)$.

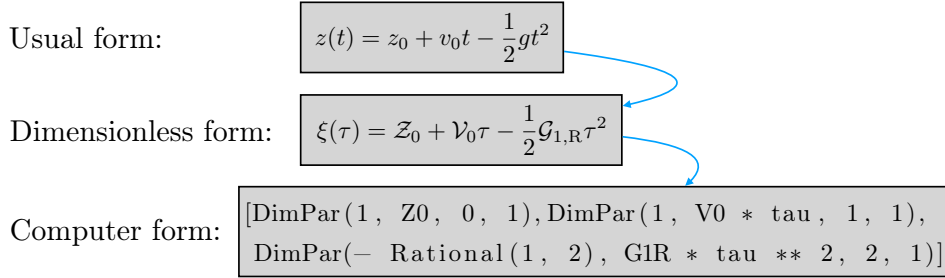


Figure 4.3: Example of the transition between an analytic expression and the computer form in terms of DimPar-class arguments.

```

def trajectory_dim_param(ramsey_quanta: int, bloch_quanta: int, time, init_height,
    ↪ init_vel, nr_init_height, nr_init_vel, init_time, cutoff: int,
    ↪ third_order_gravity: bool, second_order_gravity: bool):
    time_factor = DimPar(1, time/init_time, 1, 0)

    # Initial conditions
    next_init_height = list()
    next_init_height.append(init_height)
    next_init_height.append(time_factor*init_vel)

    # Trajectory due to momentum kicks
    next_init_height.append(time_factor*ramsey_quanta*RR)
    next_init_height.append(time_factor*bloch_quanta*RB)

    # Trajectory due to linear gravity
    next_init_height.append(-Rational(1,2)*G1R*time_factor**2)

```

Next, we include the corrections to the trajectory at order $O(2)$, as defined in Eq. (3.37b).

```

# General second order corrections to the trajectory
next_init_height.append(-C3*G0*G1R*time_factor**2)

# Second order corrections due to the gravity gradient
if second_order_gravity:
    next_init_height.append(Rational(1,2)*G2R*time_factor**2*nr_init_height)
    next_init_height.append(Rational(1,6)*nr_init_vel*G2R*time_factor**3)
    next_init_height.append(Rational(1,6)*ramsey_quanta*RR*G2R*time_factor**3)
    next_init_height.append(Rational(1,6)*bloch_quanta*RB*G2R*time_factor**3)
    next_init_height.append(-Rational(1,24)*G1R*G2R*time_factor**4)

```

At third order, $O(3)$, we include the effects described in Eq. (3.37c). It is important to note that we also include the contribution from Eq. (3.108), which is the first one. We added multiple Boolean variables to the definition to allow for the easy inclusion or exclusion of certain effects. We begin with the general contributions at third order.

```

# Third order corrections to the trajectory
if cutoff >= 5:
    # Third order correction to the momentum kick
    next_init_height.append(2*gamma*time_factor*G1R*init_height*ramsey_quanta*RR)

    # General third order corrections to the trajectory
    next_init_height.append(-C4*G1R**2*nr_init_height*time_factor**2)
    next_init_height.append(C5*G1R*nr_init_vel**2*time_factor**2)
    next_init_height.append(C5*G1R*ramsey_quanta**2*RR**2*time_factor**2)
    next_init_height.append(C5*G1R*bloch_quanta**2*RB**2*time_factor**2)
    next_init_height.append(2*C5*G1R*nr_init_vel*bloch_quanta*RB*time_factor**2)
    next_init_height.append(2*C5*G1R*nr_init_vel*ramsey_quanta*RR*time_factor**2)
    next_init_height.append(2*C5*G1R*ramsey_quanta*RR*bloch_quanta*RB*time_factor
        ↪ **2)
    next_init_height.append(-Rational(1,3)*C4*nr_init_vel*G1R**2*time_factor**3)
    next_init_height.append(-Rational(1,3)*C4*ramsey_quanta*RR*G1R**2*time_factor
        ↪ **3)

```

```
next_init_height.append(-Rational(1,3)*C4*bloch_quanta*RB*G1R**2*time_factor**3)
next_init_height.append(Rational(1,12)*C6*G1R**3*time_factor**4)
```

Next, we include third order corrections resulting from the gravity gradient.

```
# Third order corrections due to the gravity gradient
if second_order_gravity:
    next_init_height.append(Rational(1,2)*C3*G0*G2R*nr_init_height*time_factor**2)
    next_init_height.append(Rational(1,6)*C3*G0*G2R*nr_init_vel*time_factor**3)
    next_init_height.append(Rational(1,6)*C3*G0*G2R*ramsey_quanta*RR*time_factor**3)
    next_init_height.append(Rational(1,6)*C3*G0*G2R*bloch_quanta*RB*time_factor**3)
    next_init_height.append(Rational(1,24)*nr_init_height*G2R**2*time_factor**4)
    next_init_height.append(-Rational(1,12)*C3*G0*G1R*G2R*time_factor**4)
    next_init_height.append(Rational(1,120)*nr_init_vel*G2R**2*time_factor**5)
    next_init_height.append(Rational(1,120)*ramsey_quanta*RR*G2R**2*time_factor**5)
    next_init_height.append(Rational(1,120)*bloch_quanta*RB*G2R**2*time_factor**5)
    next_init_height.append(-Rational(1,720)*G1R*G2R**2*time_factor**6)
```

Lastly, we include corrections to the trajectory that result from the second-order gravity gradient, denoted as Λ . This allows for comparison between our approach and that of Dimopoulos et al. [87, 88], as they appear to have integrated this contribution into the Lagrangian but not into the trajectory.

```
# Third order corrections due to the second gravity gradient
if third_order_gravity:
    next_init_height.append(-Rational(1,2)*G3R*time_factor**2*nr_init_height**2
                           ↪ time_factor**3)
    next_init_height.append(-Rational(1,3)*nr_init_height*nr_init_vel*G3R*
                           ↪ time_factor**3)
    next_init_height.append(-Rational(1,3)*nr_init_height*ramsey_quanta*RR*G3R*
                           ↪ time_factor**3)
    next_init_height.append(-Rational(1,3)*nr_init_height*bloch_quanta*RB*G3R*
                           ↪ time_factor**3)
    next_init_height.append(-Rational(1,12)*nr_init_vel**2*G3R*time_factor**4)
    next_init_height.append(-Rational(1,12)*ramsey_quanta**2*RR**2*G3R*time_factor
                           ↪ **4)
    next_init_height.append(-Rational(1,12)*bloch_quanta**2*RB**2*G3R*time_factor
                           ↪ **4)
    next_init_height.append(-Rational(1,6)*nr_init_vel*ramsey_quanta*RR*G3R*
                           ↪ time_factor**4)
    next_init_height.append(-Rational(1,6)*ramsey_quanta*RR*bloch_quanta*RB*G3R*
                           ↪ time_factor**4)
    next_init_height.append(-Rational(1,6)*nr_init_vel*bloch_quanta*RB*G3R*
                           ↪ time_factor**4)
    next_init_height.append(Rational(1,12)*nr_init_height*G1R*G3R*time_factor**4)
    next_init_height.append(Rational(1,20)*nr_init_vel*G1R*G3R*time_factor**5)
    next_init_height.append(Rational(1,20)*ramsey_quanta*RR*G1R*G3R*time_factor**5)
    next_init_height.append(Rational(1,20)*bloch_quanta*RB*G1R*G3R*time_factor**5)
    next_init_height.append(-Rational(1,120)*G1R**2*G3R*time_factor**6)

return next_init_height
```

Here, we utilised the definitions of the constants C_1 to C_6 from Eqs. (3.37d) and (3.37e). We also define a list of substitutions to eliminate these constants in the final phase calculations.

```
c_substitution = [(C1, Rational(1,2)*(2*beta-1)), (C2, Rational(1,2)*(2*gamma+1)), (C3
                           ↪ , 2*(beta-1)), (C4, beta+gamma), (C5, Rational(1,2)*(gamma+2)), (C6, beta-2)]
```

The velocity is defined in a completely analogous manner and will be omitted here for the sake of readability. With all the necessary components in place, we can now determine the exact atomic trajectories. We begin with the initial conditions and iterate over all time instances. For simplicity, we will present only the trajectories, omitting the velocities, which will be required for calculating the Doppler effect later on.

```
init_pos_upper_path_dim_param = [Z0]
init_vel_upper_path_dim_param = [V0]

for i in range(number_of_time_intervals):
```

```

upper_end_pos_list=trajectory_dim_param(trans_bragg_upper_path[i],
    ↵ trans_bloch_upper_path[i], time_decomposition[i+1],
    ↵ abstract_init_pos_upper_path[i], abstract_init_vel_upper_path[i],
    ↵ abstract_nr_init_pos_upper_path[i], abstract_nr_init_vel_upper_path[i],
    ↵ time_decomposition[1], order_cutoff,
    ↵ include_3rd_order_gravity_in_trajectory,
    ↵ include_2nd_order_gravity_in_trajectory)
init_pos_upper_path_dim_param.append(upper_end_pos_list)

lower_end_pos_list=trajectory_dim_param(trans_bragg_lower_path[i],
    ↵ trans_bloch_lower_path[i], time_decomposition[i+1],
    ↵ abstract_init_pos_lower_path[i], abstract_init_vel_lower_path[i],
    ↵ abstract_nr_init_pos_lower_path[i], abstract_nr_init_vel_lower_path[i],
    ↵ time_decomposition[1], order_cutoff,
    ↵ include_3rd_order_gravity_in_trajectory,
    ↵ include_2nd_order_gravity_in_trajectory)
init_pos_lower_path_dim_param.append(lower_end_pos_list)

```

As previously mentioned, we will substitute the abstract symbolic expressions ZU1 through ZU4 with a simplified version of the calculated initial heights. To achieve this, we define a substitution list as follows:

```

list_of_substitutions = list()
for i in range(number_of_time_intervals-1):
    substitutes = list()
    substitutes.append((abstract_init_pos_upper_path[i+1].parameter,
        ↵ simp_init_pos_upper_path_symbol[i+1]))
    substitutes.append((abstract_init_pos_lower_path[i+1].parameter,
        ↵ simp_init_pos_lower_path_symbol[i+1]))
    list_of_substitutions.append(substitutes)

```

We now have all the relevant data to define the three phase shift contributions individually.

4.4 Phase Calculation

4.4.1 Propagation Phase

To calculate the propagation phase, we need to perform time integrals, as demonstrated in Eq. (2.13). This requires defining the action of an integral on DimPar objects. Thankfully, this is straightforward, as all these objects are polynomials in time. We define the indefinite integral of a single DimPar object via:

```

def custom_integral(parameter: DimPar):
    if parameter == 0:
        return 0
    else:
        time_order = parameter.order
        if time_order == -1:
            return Zero
        else:
            return Rational(1, time_order+1)*parameter

```

Using this we define the Lagrangian in two steps: First, we initialise

```

def lagrangian_list(ramsey_quanta:int, bloch_quanta:int, time, init_height, init_vel,
    ↵ nr_init_height, nr_init_vel, cutoff:int, init_time, third_order_grav_pot:bool,
    ↵ second_order_grav_traj:bool, third_order_grav_traj:bool):
    lagrangian = list()

    traj_3rd_order=trajectory_dim_param(ramsey_quanta, bloch_quanta, time, init_height,
        ↵ init_vel, nr_init_height, nr_init_vel, init_time, 4, third_order_grav_traj,
        ↵ second_order_grav_traj)
    vel_3rd_order=velocity_dim_param(ramsey_quanta, bloch_quanta, time, init_height,
        ↵ init_vel, nr_init_height, nr_init_vel, init_time, 4, third_order_grav_traj,
        ↵ second_order_grav_traj)
    traj_2nd_order=delete_zeros_from_list(trajectory_dim_param(ramsey_quanta,
        ↵ bloch_quanta, time, init_height, init_vel, nr_init_height, nr_init_vel,
        ↵ init_time, 3, third_order_grav_traj, second_order_grav_traj))

```

```

traj_1st_order=delete_zeros_from_list(nr_trajectory_dim_param(ramsey_quanta ,
    ↵ bloch_quanta ,time ,nr_init_height ,nr_init_vel ,init_time ))
vel_1st_order=delete_zeros_from_list(nr_velocity_dim_param(ramsey_quanta ,
    ↵ bloch_quanta ,time ,nr_init_vel ,init_time ))

```

since the relativistic corrections to the Lagrangian at order $O(3)$ do not require dependence on the fully relativistic (also $O(3)$) trajectory. They only need the $O(1)$ trajectory. Similarly, the $O(2)$ contributions to the Lagrangian only require a trajectory that is accurate to the same order ($O(2)$) to achieve an overall accuracy of $O(4)$. The Lagrangian is completed by appending the following contributions to the `lagrangian`-list:

```

#Potential
lagrangian.append(mul_param_to_list(-1*G1R, magnitude_cutoff_list(traj_3rd_order ,
    ↵ cutoff-1)))
lagrangian.append(mul_param_to_list(Rational(1,2)*G2R, magnitude_cutoff_list(
    ↵ mult_list_with_itself(2,traj_2nd_order),cutoff-1)))
if third_order_grav_pot:
    lagrangian.append(mul_param_to_list(-Rational(1,3)*G3R, mult_list_with_itself(3,
        ↵ traj_1st_order)))

#Kinetic
lagrangian.append(magnitude_cutoff_list(mul_param_to_list(Rational(1,2) ,
    ↵ mult_list_with_itself(2,vel_3rd_order)),cutoff))

#Relativistic
lagrangian.append(magnitude_cutoff_list(mul_param_to_list(Rational(1,8) ,
    ↵ mult_list_with_itself(4,vel_1st_order)),cutoff))
lagrangian.append(mul_param_to_list(-C1*G1R**2,mult_list_with_itself(2,
    ↵ traj_1st_order)))
lagrangian.append(mul_param_to_list(-C2*G1R,multiply_two_lists(traj_1st_order ,
    ↵ mult_list_with_itself(2,vel_1st_order))))
lagrangian.append(mul_param_to_list(-C3*G0*G1R,traj_2nd_order))

return flatten(lagrangian)

```

Building on this, we can define the action by applying the integration procedure followed by multiplication with $\omega_C T_R$.

```

def action_list(number_of_ramsey_quanta:int ,number_of_bloch_quanta:int ,time ,
    ↵ initial_height ,initial_velocity ,non_rel_initial_height ,
    ↵ non_rel_initial_velocity ,cutoff:int ,initial_time:TimeParameter ,
    ↵ third_order_gravity_in_potential:bool ,second_order_gravity_in_trajectory:
    ↵ bool ,third_order_gravity_in_trajectory:bool ):
    action_list_of_terms = list()
    prefactor=time.prefactor*time.symbol*omegaC

    lagrangian=lagrangian_list(number_of_ramsey_quanta ,number_of_bloch_quanta ,time ,
        ↵ initial_height ,initial_velocity ,non_rel_initial_height ,
        ↵ non_rel_initial_velocity ,cutoff ,initial_time ,
        ↵ third_order_gravity_in_potential ,second_order_gravity_in_trajectory ,
        ↵ third_order_gravity_in_trajectory)
    lagrangian_with_prefactor=multiply_parameter_to_list(prefactor ,lagrangian)
    action_list_of_terms.append(list(map(custom_integral ,lagrangian_with_prefactor)))
    ↵ )
return flatten(action_list_of_terms)

```

The propagation phase is then determined iteratively by summing this action functional across all interferometry segments.

```

prop_phase_upper_path_symbol = 0
prop_phase_lower_path_symbol = 0
for i in range(number_of_time_intervals):
    prop_phase_upper_path_symbol=prop_phase_upper_path_symbol+action_list(
        ↵ trans_bragg_upper_path[i] ,trans_bloch_upper_path[i] ,time_decomposition[i
        ↵ +1] ,abstract_init_pos_upper_path[i] ,abstract_init_vel_upper_path[i] ,
        ↵ abstract_nr_init_pos_upper_path[i] ,abstract_nr_init_vel_upper_path[i] ,
        ↵ order_cutoff ,time_decomposition[1] ,include_3rd_order_gravity_in_potential
        ↵ ,include_2nd_order_gravity_in_trajectory ,
        ↵ include_3rd_order_gravity_in_trajectory )

```

```

prop_phase_lower_path_symbol=prop_phase_lower_path_symbol+action_list(
    ↪ trans_bragg_lower_path[i], trans_bloch_lower_path[i], time_decomposition[i
    ↪ +1], abstract_init_pos_lower_path[i], abstract_init_vel_lower_path[i],
    ↪ abstract_nr_init_pos_lower_path[i], abstract_nr_init_vel_lower_path[i],
    ↪ order_cutoff, time_decomposition[1], include_3rd_order_gravity_in_potential
    ↪ , include_2nd_order_gravity_in_trajectory ,
    ↪ include_3rd_order_gravity_in_trajectory)

prop_diff_phase = cutoff_symbolic_expression((prop_phase_upper_path_symbol-
    ↪ prop_phase_lower_path_symbol).expand(), order_cutoff)
prop_phase_after_substitution = prop_diff_phase
for i in range(number_of_time_intervals-1):
    prop_phase_after_substitution = cutoff_symbolic_expression(
        ↪ prop_phase_after_substitution .subs(list_of_substitutions[
        ↪ number_of_time_intervals-2-i]).expand(), order_cutoff)

propagation_phase_parameter = prop_phase_after_substitution .subs(c_substitution)

```

Note that we applied various substitutions in the final steps. We continue with the separation phase, which is quite straightforward.

4.4.2 Separation Phase

The separation phase can be easily calculated using the symbolic representations of the final positions and velocities of the atomic ensemble, specifically right after the last interferometry pulse, cf. Eq. (2.14).

```

separation=simp_init_pos_lower_path_symbol[-1]-simp_init_pos_upper_path_symbol[-1]
average_velocity_mod_c_at_output_port=Rational(1,2)*(final_nr_upper_vel+
    ↪ final_nr_upper_vel)
try:
    separation_phase_parameter=time_decomposition[1]*omegaC*separation*
        ↪ average_velocity_mod_c_at_output_port .expand()).subs(c_substitution)
except AttributeError:
    separation_phase_parameter = 0

```

The last step is necessary because if the gravity gradient is disregarded, the separation phase might be zero. Attempting to perform a substitution procedure on an integer is not defined, which can result in an `AttributeError`.

4.4.3 Kick Phase

We define the kick phase contribution in a single function, but include a string argument `bragg_or_bloch` to modify the corresponding contribution based on the selected interaction type. Similar to the propagation phase, we start by initialising the atomic heights and velocities at various levels of accuracy. We then determine how the laser phase should be adjusted due to the Doppler effect and gravitational correction, as explained in Eq. (3.106), for interactions of the Bragg type. If the interaction process is not of Bragg type, the simpler Bloch kick phase is returned.

```

def kick_phase_contribution(bragg_or_bloch:str, number_of_upper_quanta:int,
    ↪ number_of_lower_quanta:int, time_step:int, cutoff_number:int):

    upper_position=magnitude_cutoff_list(init_pos_upper_path_dim_param[time_step],
        ↪ cutoff_number)
    lower_position=magnitude_cutoff_list(init_pos_lower_path_dim_param[time_step],
        ↪ cutoff_number)
    nr_upper_position=magnitude_cutoff_list(nr_init_pos_upper_path_dim_param[
        ↪ time_step], cutoff_number)
    nr_lower_position=magnitude_cutoff_list(nr_init_pos_lower_path_dim_param[
        ↪ time_step], cutoff_number)
    nr_upper_velocity=magnitude_cutoff_list(nr_init_vel_upper_path_dim_param[
        ↪ time_step], cutoff_number)

```

```

nr_lower_velocity=magnitude_cutoff_list(nr_init_vel_lower_path_dim_param[
    ↪ time_step],cutoff_number)

if bragg_or_bloch.lower() == "bragg":
    upper_momentum=number_of_upper_quanta*RR.parameter
    lower_momentum=number_of_lower_quanta*RR.parameter
    upper_frequency=number_of_upper_quanta*FR.parameter
    lower_frequency=number_of_lower_quanta*FR.parameter

    upper_phase_mod_height=upper_momentum*(1 - Rational(1,2)*nr_upper_velocity**2 +
    ↪ gamma*Rational(1,2)*GIR.parameter*nr_upper_position + Rational(1,2)*GIR.
    ↪ parameter*nr_upper_position) + nr_upper_velocity*upper_frequency

    lower_phase_mod_height=lower_momentum*(1 - Rational(1,2)*nr_lower_velocity**2 +
    ↪ gamma*Rational(1,2)*GIR.parameter*nr_lower_position+Rational(1, 2)*GIR.
    ↪ parameter*nr_lower_position)+nr_lower_velocity*lower_frequency

    if number_of_upper_quanta != 0:
        upper_phase = upper_phase_mod_height*upper_position*initial_time
    else:
        upper_phase = 0

    if number_of_lower_quanta != 0:
        lower_phase = lower_phase_mod_height*lower_position*initial_time
    else:
        lower_phase = 0

elif bragg_or_bloch.lower() == "bloch":
    upper_momentum = number_of_upper_quanta*RB.parameter
    lower_momentum = number_of_lower_quanta*RB.parameter

    if number_of_upper_quanta != 0:
        upper_phase = upper_momentum*upper_position*initial_time
    else:
        upper_phase = 0

    if number_of_lower_quanta != 0:
        lower_phase = lower_momentum*lower_position*initial_time
    else:
        lower_phase = 0

else:
    print("There is a typo in the Kick phase formula!")
    quit()

return omegaC * (upper_phase - lower_phase)

```

We then sum over all interaction processes that transfer momentum and use the same substitutions as before.

```

kick_phase_contribution_list = list()
for i in range(number_of_time_intervals+1):
    kick_phase_contribution_list.append(kick_phase_contribution("bragg",
        ↪ trans_bragg_upper_path[i],trans_bragg_lower_path[i],i,order_cutoff))
    kick_phase_contribution_list.append(kick_phase_contribution("bloch",
        ↪ trans_bloch_upper_path[i],trans_bloch_lower_path[i],i,order_cutoff))

kick_phase_after_substitution = cutoff_symbolic_expression(sum(
    ↪ kick_phase_contribution_list).expand(),order_cutoff)
for i in range(number_of_time_intervals-1):
    kick_phase_after_substitution = kick_phase_after_substitution.subs(
        ↪ list_of_substitutions[number_of_time_intervals-2-i])

kick_phase_parameter = cutoff_symbolic_expression(kick_phase_after_substitution.
    ↪ expand(), order_cutoff).subs(c_substitution)

```

4.4.4 Simplified FSL Phase

Lastly, we aim to analyse a simplified version of the FSL phase used for comparing our relativistic findings with those of Dimopoulos et al. [87, 88], as shown in Table 3.4. Instead of computing all the exact time instances detailed in Fig. 2.2 and implemented in Ref. [3], we focus on the temporal component of the Kick phase, which serves as the leading-order contribution. Specifically, this involves the latter part of Eq. (3.106), where τ is set to the laser emission times $0, T_R, 2T_R$. It is worth mentioning that this can also be described as a pure kick phase contribution, given the inherent ambiguity in term nomenclature. The implementation is as follows:

```

upper_FSL_phase = list()
lower_FSL_phase = list()
for index in range(number_of_time_intervals + 1):
    # If the comment is removed the resulting phase shift will coincide with number
    # 9 in Dim. et al.
    fsl_upper_position=mag_cutoff_list(init_pos_upper_path_dim_param[index],
                                         order_cutoff-1) #.subs(RR.param, 0)
    fsl_lower_position=mag_cutoff_list(init_pos_lower_path_dim_param[index],
                                         order_cutoff-1) #.subs(RR.param, 0)
    fsl_upper_velocity=mag_cutoff_list(init_vel_upper_path_dim_param[index],
                                         order_cutoff-1)
    fsl_lower_velocity=mag_cutoff_list(init_vel_lower_path_dim_param[index],
                                         order_cutoff-1)

    omega_1_upper=Rational(1,2)*trans_bragg_upper_path[index]*(FR.param+RR.param)
    omega_2_upper=-Rational(1,2)*trans_bragg_upper_path[index]*(FR.param-RR.param)
    omega_1_lower=Rational(1,2)*trans_bragg_lower_path[index]*(FR.param+RR.param)
    omega_2_lower=-Rational(1,2)*trans_bragg_lower_path[index]*(FR.param-RR.param)

    # These shifted values are then the Doppler/GR compensation needed, in order for
    # the interferometer to operate on resonance
    shifted_omega_1_upper=(1+fsl_upper_velocity-Rational(1,2)*fsl_upper_velocity
                           **2+(gamma+1)*GIR.param*fsl_upper_position)*omega_1_upper
    shifted_omega_2_upper=(1-fsl_upper_velocity-Rational(1,2)*fsl_upper_velocity
                           **2+(gamma+1)*GIR.param*fsl_upper_position)*omega_2_upper
    shifted_omega_1_lower=(1+fsl_lower_velocity-Rational(1,2)*fsl_lower_velocity
                           **2+(gamma+1)*GIR.param*fsl_lower_position)*omega_1_lower
    shifted_omega_2_lower=(1-fsl_lower_velocity-Rational(1,2)*fsl_lower_velocity
                           **2+(gamma+1)*GIR.param*fsl_lower_position)*omega_2_lower

    # Create lists of upper and lower FSL phases.
    upper_FSL_phase.append(shifted_omega_1_upper*fsl_upper_position*TR-
                           shifted_omega_2_upper*fsl_upper_position*TR)
    lower_FSL_phase.append(shifted_omega_1_lower*fsl_lower_position*TR-
                           shifted_omega_2_lower*fsl_lower_position*TR)

    # Full FSL phase gets an overall minus sign, since this is also added in the full
    # phase (see below). This is done to fit most literatures' convention.
    fsl_phase=cutoff_symbolic_expression(-omegaC*(sum(upper_FSL_phase)-sum(
                                         lower_FSL_phase)).expand(), order_cutoff)

for i in range(number_of_time_intervals - 1):
    fsl_phase=fsl_phase.subs(list_of_substitutions[number_of_time_intervals-2-i]).subs(c_substitution)

```

Here, we provide a more detailed explanation of why term #9 in [87, 88] differs, as outlined in Sec. 3.7. By neglecting the atomic recoil transferred by AIF pulses – specifically, setting \mathcal{R}_R to zero in `fsl_upper_position` and `fsl_lower_position`, as noted in the comments – one arrives at the same term #9 as in [87, 88]. Apparently, in that work, only the atomic parabola without any recoils was considered.

4.5 Visualisation

In the following, we will focus on the most basic visualisation of the phase shifts. This involves generating a .txt file and an automatically compiled .tex file, which can then be used to produce a PDF. The algorithm is also capable of creating images of the interferometer in both the lab frame and the freely falling frame, which are included in the PDF as well. We won't delve into the details of this process, as our focus is on the algebraic calculation of phase shifts. We defined the full interferometer phase with a global minus sign, as indicated in the first line. Note that, whenever we analyse partial results – for instance, to understand how the full phase shift is divided into its components – we comment out the corresponding phase shifts at this stage. The `extract_term_from_list` function returns all phase shift terms in an expression that involve the specified powers of dimensionless parameters and is defined in `parameters_and_functions.py`. We illustrate this process using the $O(2)$ terms as an example.

```
full_phase_parameter=-(kick_phase_parameter+separation_phase_parameter+
    ↪ propagation_phase_parameter).expand()

second_order_phase=cutoff_symbolic_expression(full_phase_parameter,3).expand()

list_of_second_order_terms = list()

second_order_RR_G1R=simplify(extract_term_from_list(second_order_phase,[(G1R,1),
    ↪ RR,1])))
list_of_second_order_terms.append(second_order_RR_G1R)

second_order_RR_RR=simplify(extract_term_from_list(second_order_phase,[(RR,2)]))
list_of_second_order_terms.append(second_order_RR_RR)

second_order_RR_RB=simplify(extract_term_from_list(second_order_phase,[(RB,1),(RR
    ↪ ,1)]))
list_of_second_order_terms.append(second_order_RR_RB)

# REST terms of order 2
second_order_REST=simplify(second_order_phase-sum(list_of_second_order_terms))

with open("phases/" + interferometer_name + "_phase_shift.txt","w") as file:

    file.write(interferometer_name+": Phase shift contributions:\n"
    ↪ ~~~~~\n\n")
    file.write("Second order small parameters (non-relativistic phases):\n"
    ↪ ~~~~~\n")

    file.write("1.:\\n" + str(second_order_RR_G1R) + "\\n\\n")
    file.write("2.:\\n" + str(second_order_RR_RR) + "\\n\\n")
    file.write("3.:\\n" + str(second_order_RR_RB) + "\\n\\n")
    file.write("x. Second order rest:\\n" + str(second_order_REST) + "\\n\\n")

file.close()
```

All of these terms are then written into a .txt file, with the corresponding abbreviation, `interferometer_name`, included in the title. We proceed to create a .tex file. For this task, we utilise the previously created pictures of the interferometer and the hard-coded text from the `latex_attributes.py` file. In the `latex_attributes.py` file, a preamble and some macros for the dimensionless parameters are defined. These are then written into the .tex file. Similar to the .txt file process, we write each non-zero¹ phase shift into the .tex file. We use the defined `LATeX` macro substitutions and the built-in `latex()` command for formatting. Finally, we run `pdf-LATeX` to generate a PDF file containing all the results.

¹Since else the substitution would not work.

```

latex_macros_substitution=[(FR.parameter ,FreqR),(G0.parameter ,GZero),(G1R.
    ↪ parameter ,GOneR),(G1B.parameter ,GOneB),(G2R.parameter ,GTwoR),(G2B.parameter
    ↪ ,GTwoB),(G3R.parameter ,GThreeR),(G3B.parameter ,GThreeB),(Z0.parameter ,ZZero
    ↪ ),(V0.parameter ,VZero),(RR.parameter ,RBrigg),(RB.parameter ,RBloch)]
```

```

with open("phases/" + interferometer_name + "_result.tex","w") as file:
```

```

if include_bloch_time:
    file.write(ltx.preamble+ltx.latex_text+ltx.include_geometry_pictures+ltx.
        ↪ include_numerical_pictures_without_Bloch_order_3+ltx.
        ↪ include_numerical_pictures_with_Bloch_order_3)
else:
    file.write(ltx.preamble+ltx.latex_text+ltx.include_geometry_pictures+ltx.
        ↪ include_numerical_pictures_without_Bloch_order_3)
```

```

file.write("\section*{Non-zero phase contributions:} \n\\vspace{1cm}\\underline{\\
    ↪ textbf{Second order small parameters:}} \n\\vspace{0.5cm}")
```

```

if second_order_RR_G1R != 0:
    file.write("\\begin{flalign*}\n")
    file.write("\\text{No. 1:} \\qquad=" + str(latex(second_order_RR_G1R.subs(
        ↪ latex_macros_substitution))))
    file.write("\\end{flalign*}\n")
```

```

if second_order_RR_RR != 0:
    file.write("\\begin{flalign*}\n")
    file.write("\\text{No. 2:} \\qquad=" + str(latex(second_order_RR_RR.subs(
        ↪ latex_macros_substitution))))
    file.write("\\end{flalign*}\n")
```

```

if second_order_RR_RB != 0:
    file.write("\\begin{flalign*}\n")
    file.write("\\text{No. 3:} \\qquad=" + str(latex(second_order_RR_RB.subs(
        ↪ latex_macros_substitution))))
    file.write("\\end{flalign*}\n")
```

```

file.close()
```

```

if compile_latex_file:
    subprocess.check_call(["pdflatex", "phases/" + interferometer_name + "_result.
        ↪ tex"], stderr=subprocess.DEVNULL, stdout=subprocess.DEVNULL)
    try:
        os.remove(interferometer_name + "_result.aux")
        os.remove(interferometer_name + "_result.log")
    except FileNotFoundError:
        print("Could not delete result.aux and result.log!")
else:
    print("Everything completed. Live long and prosper.")
```

The presented algorithm is highly flexible and allows for a variety of different visualisation procedures, such as those used to automatically create figures like Figs. 2.1. For the algorithm in Ref. [3], we neglected the $O(4)$ phase contributions and focussed on the $O(3)$ order, with automated FSL calculations and a numerical simulation of the gravitational field of the VLBAI. The basic code structure is, however, exactly the same as outlined here. The numerical simulation of an interferometer in that reference is also completely analogous to the analytical description provided here and does not require additional explanation. Each code is thoroughly commented and written in a transparent manner, facilitating understanding and use. Potential extensions of this code are discussed in the following outlook.

Chapter 5

Summary and Outlook

"Meine Versuche, den Quanten greifbare Gestalt zu geben, sind allerdings immer wieder gescheitert, aber die Hoffnung gebe ich noch lange nicht auf. Und wenns garnicht gehen will, dann bleibt doch der Trost, daß der Mißerfolg nur an mir liegt."

Albert Einstein in a letter to Max Born

The accuracy of AIFs is improving at an exceptional rate, especially considering how relatively new this field of research is. Most notably, one should highlight once again that the two most recent measurements of the fine-structure constant, α , have achieved an accuracy of parts per trillion [38, 39]. Future experiments aim to detect gravitational waves and rule out certain dark matter models [71–74]. To pursue this path and achieve these goals, a highly accurate theoretical model, including (general) relativistic effects, is essential. This thesis provides the necessary models and considerations for several of the upcoming tasks in this field.

Starting from a post-Newtonian approximation of the Schrödinger equation in a curved spacetime, described by a metric theory of gravity, we have presented a calculation of the phase contributions of a whole class of light-pulse AIFs. The phases are derived from a relativistically-corrected, quantum-optical Hamiltonian for atoms and light in a PPN spacetime and applied to the specific case of AIFs that use elastic scattering processes. After following the standard procedure for calculating phases in AIFs in the presence of relativistic corrections we have expressed all the resulting phase contributions as functions of dimensionless parameters that arise naturally from this description. The computation of all phase contributions up to a desired order in those dimensionless parameters for any AIF geometry consisting of Bragg and Bloch pulses is automated in Python. Using this code one can try to find a suitable interferometer geometry, that may be possible to create new measurement strategies similar to the CGI and its novel implementation. Additionally, we defined a new interferometer geometry capable of measuring gravitational curvature and simulated it numerically within the gravitational field of the VLBAI in Hannover. We discussed how to mitigate unwanted phase shift contributions arising from the finite speed of light and analysed how to interpret the phase shift results. In this process, we defined an estimator for gravitational curvature that shows excellent agreement with the model data.

This analysis can be extended to AIFs that use inelastic scattering processes, e.g., Raman or single photon transitions [68, 69, 90, 148], as it was partially already done in Ref. [3]. There might also be interesting combinations between the CGI and clock interferometry, leveraging the advantages of both methods. In general, the application of CGI will be intriguing to observe, particularly for large-scale interferometer setups worldwide, where gravitational

fields are subject to temporal fluctuations. Designing a gravitational field using cleverly positioned test masses, as proposed and observed in Ref. [103], is likely to yield fascinating new insights into the intricate interplay between gravity and quantum mechanics. These setups may be efficiently described using the processes outlined here, or, even better, they might reveal the limitations of using atoms as "test particles" and show how quantum matter gravitates.

The presented analysis would also be sufficient to describe stationary spacetimes, which could include effects of Earth's rotation and describe gravitomagnetic phenomena such as the Lense-Thirring effect [139], as already indicated in Sec. 3.8. Another interesting approach one could pursue is to start from a Hamiltonian that describes fermionic particles in curved spacetime, cf. Ref. [149], and investigate whether spin-related interactions with gravity might give rise to interesting tests of GR in light-pulse AIFs. In such setups, one could also test whether the vanishing torsion axiom of GR holds true, as spin might break this symmetry, since spin couples to energy and has no classical counterpart.

An interesting extension of the computer algorithm would be to automatically solve the motional ELE for any arbitrary gravitational potential, given as a Taylor series, to any desired order – all while remaining entirely analytical. Currently, the atomic trajectories are hard-coded into the algorithm up to order $\mathcal{O}(3)$, and calculating any higher orders manually could introduce errors. This approach would be particularly useful when a numerical model of the gravitational field, such as in the case of the VLBAI in Hannover, is available [83, 109]. This would allow modelling the data to any desired accuracy, within measurement uncertainty, and directly utilising analytical data. By implementing all of our findings in a freely available computer language and making it open source, we enable the community to incorporate additional systematics and improve the code as needed.

Appendix A

Differential Geometry

In the following, we gather the key concepts of differential geometry necessary to understand the mathematics of GR. A four-dimensional manifold \mathcal{M} is a topological space with charts, which are continuous invertible maps $\phi_i : \mathcal{M} \supseteq U_i \longrightarrow \phi_i(U_i) \subseteq \mathbb{R}^4$, where U_i are open subsets of \mathcal{M} , as depicted in Fig. A.1. Here, I is an arbitrary index set. If the chart transition maps

$$\psi_{ij} = \phi_j \circ \phi_i^{-1} : \mathbb{R}^4 \supseteq \phi_i(U_{ij}) \longrightarrow \phi_j(U_{ij}) \subseteq \mathbb{R}^4 \quad (\text{A.1})$$

are smooth functions on the common domain $U_{ij} = U_i \cap U_j$ for all i and j , we call the manifold smooth, see Fig. A.1. A collection of maps $\{\phi_i\}_{i \in I}$ that cover the whole manifold, i.e., $\mathcal{M} = \bigcup_{i \in I} U_i$ is called an atlas of \mathcal{M} .

For now consider only one chart (U, ϕ) and denote the canonical basis of \mathbb{R}^4 as $\{\mathbf{e}_\alpha\}_\alpha = \{\mathbf{e}_0, \mathbf{e}_1, \mathbf{e}_2, \mathbf{e}_3\}$. If we denote $x^\alpha : \mathcal{M} \supseteq U \longrightarrow \mathbb{R}$ as the component functions of the chart $\phi : U \longrightarrow \mathbb{R}^4, p \mapsto \phi(p) = x^\alpha(p) \mathbf{e}_\alpha$, one can define the notion of differentiability on a manifold, both for functions mapping from and onto a manifold. Let $f : U \longrightarrow \mathbb{R}^n$, then we say that f is a smooth function on U , denoted $C^\infty(U, \mathbb{R}^n)$, if the function $f \circ \phi^{-1} : \mathbb{R}^4 \longrightarrow \mathbb{R}^n$ is smooth. If this holds for every chart in the atlas of \mathcal{M} we say that $f \in C^\infty(\mathcal{M}, \mathbb{R})$. Note that this works analogously for functions mapping from \mathbb{R}^n onto \mathcal{M} . A geometric depiction of the concept of tangent spaces for two-dimensional manifolds can be seen in Fig. A.2.

Building upon this one can define the differential operators on the manifold. Let $\gamma : (-\epsilon, \epsilon) \longrightarrow \mathcal{M}$ with $\gamma(0) = p$ be a smooth curve on \mathcal{M} , e.g., the world line of an observer. We can use this to define a tangent vector $\dot{\gamma}_p$ which maps a function $f \in C^\infty(\mathcal{M}, \mathbb{R})$ into the directional derivative of f in the direction of γ at p by

$$\dot{\gamma}_p(f) = \frac{d}{dt} \Big|_{t=0} (f \circ \gamma)(t) \in \mathbb{R}. \quad (\text{A.2})$$

Note that there is a different, commonly used, way to define a world line on a manifold if one has chosen a chart: Given a smooth curve $\gamma : (-\epsilon, \epsilon) \longrightarrow \mathcal{M}$, one can equivalently describe the curve using the four-tuple of coordinate functions $x^\mu(t) = \gamma \circ x^\mu$. We will use both notions interchangeably. The collection of all such tangent vectors through p is the tangent space will be denoted by $\mathcal{T}_p \mathcal{M}$ and is often depicted geometrically as a vector space attached to the manifold as illustrated in Fig. A.2. Algebraically, however, one views a tangent vector $\gamma_p \in \mathcal{T}_p \mathcal{M}$ as a linear function that maps functions on \mathcal{M} to real numbers. One can show that this $\mathcal{T}_p \mathcal{M}$ is also a four-dimensional vector space and has a canonical basis given by

$$\frac{\partial}{\partial x^\alpha} \Big|_p : C^\infty(\mathcal{M}, \mathbb{R}) \longrightarrow \mathbb{R}, \quad f \mapsto \frac{\partial}{\partial x^\alpha} \Big|_p f = \frac{d}{dt} \Big|_{t=0} f \circ \phi^{-1}(\phi(p) + t \mathbf{e}_\alpha) \quad (\text{A.3})$$

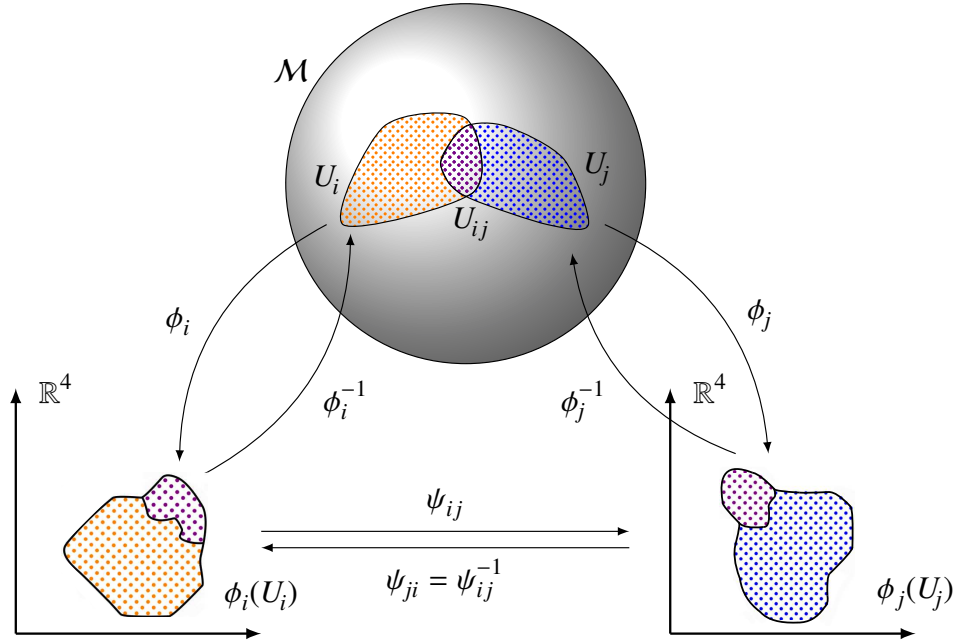


Figure A.1: Schematic depiction of charts (U_i, ϕ_i) and (U_j, ϕ_j) and a chart transition map ψ_{ij} of a manifold \mathcal{M} .

Analogously one can define the cotangent space $\mathcal{T}_p^*\mathcal{M}$ as the dual space of $\mathcal{T}_p\mathcal{M}$ and define its basis via

$$dx^\alpha|_p : \mathcal{T}_p\mathcal{M} \rightarrow \mathbb{R}, \quad dx^\alpha|_p \left(\frac{\partial}{\partial x^\beta}|_p \right) = \delta^\alpha_\beta. \quad (\text{A.4})$$

The notions of the tangent space and its dual are crucial for GR. We will now extend this concept to bundles and fields in the sense that we collect all the (co-) tangent spaces to vector bundles $(\mathcal{T}\mathcal{M}, \pi, \mathcal{M})$ and $(\mathcal{T}^*\mathcal{M}, \tilde{\pi}, \mathcal{M})$ consisting of

$$\mathcal{T}\mathcal{M} = \bigcup_{p \in \mathcal{M}} \mathcal{T}_p\mathcal{M} \times \{p\}, \quad \pi : \mathcal{T}\mathcal{M} \rightarrow \mathcal{M} \text{ with } \mathcal{T}_p\mathcal{M} \ni \mathfrak{x}_p \mapsto \pi(\mathfrak{x}_p) = p \quad (\text{A.5a})$$

$$\mathcal{T}^*\mathcal{M} = \bigcup_{p \in \mathcal{M}} \mathcal{T}_p^*\mathcal{M} \times \{p\}, \quad \tilde{\pi} : \mathcal{T}^*\mathcal{M} \rightarrow \mathcal{M} \text{ with } \mathcal{T}_p^*\mathcal{M} \ni \mathfrak{u}_p \mapsto \tilde{\pi}(\mathfrak{u}_p) = p. \quad (\text{A.5b})$$

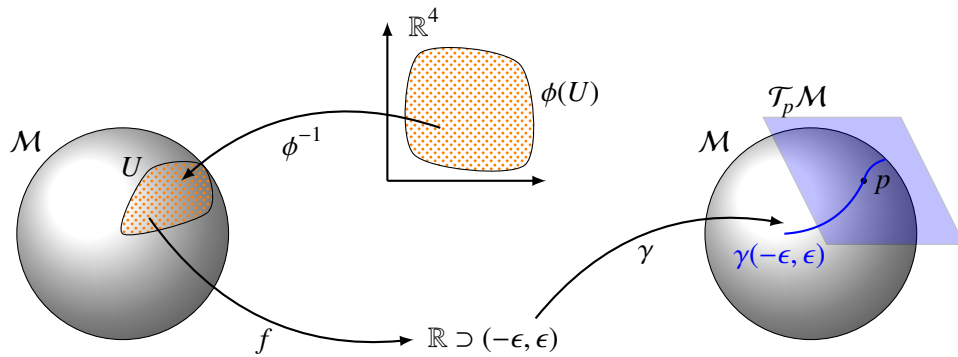


Figure A.2: Schematic depiction of functions on manifolds and visualisation of a tangent space $\mathcal{T}_p\mathcal{M}$ using a path γ through $p \in \mathcal{M}$.

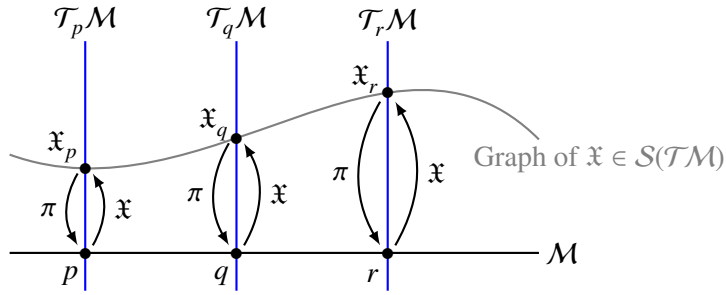


Figure A.3: Schematic depiction the tangent bundle $(\mathcal{T}\mathcal{M}, \pi, \mathcal{M})$ and a section \mathfrak{X} therein, i.e., a vector field. At every point $p \in \mathcal{M}$ in the manifold $\mathfrak{X}(p) = \mathfrak{X}_p \in \mathcal{T}_p \mathcal{M}$ is a tangent vector in the corresponding tangent space.

A section , which generalises the notion of a field, is a map which assigns an element in the (co-) tangent space to each point of the manifold. A vector field \mathfrak{X} is then a section in $\mathcal{T}\mathcal{M}$, denoted by $\mathfrak{X} \in \mathcal{S}(\mathcal{T}\mathcal{M})$, and is a map $\mathfrak{X} : \mathcal{M} \rightarrow \mathcal{T}\mathcal{M}$. The example of a tangent bundle and section therein is depicted schematically in Fig. A.3.

The four basis (co-) vector fields $\partial_\alpha \in \mathcal{S}(\mathcal{T}\mathcal{M})$ and $dx^\alpha \in \mathcal{S}(\mathcal{T}^*\mathcal{M})$ are given by

$$\partial_\alpha : \mathcal{M} \ni p \mapsto \frac{\partial}{\partial x^\alpha} \Big|_p \in \mathcal{T}_p \mathcal{M}, \quad dx^\alpha : \mathcal{M} \ni p \mapsto dx^\alpha \Big|_p \in \mathcal{T}_p^* \mathcal{M}. \quad (\text{A.6})$$

One can use (co-) tangent bundles to construct higher order multilinear maps using the tensor product to obtain "tensors of degree (l, m) " as elements in

$$\mathcal{T}_m^l \mathcal{M} = \mathcal{T}\mathcal{M}^{\otimes l} \otimes \mathcal{T}^*\mathcal{M}^{\otimes m} \quad \text{with} \quad \mathcal{T}_0^1 \mathcal{M} = \mathcal{T}\mathcal{M} \quad \text{and} \quad \mathcal{T}_1^0 \mathcal{M} = \mathcal{T}^*\mathcal{M}, \quad (\text{A.7})$$

and sections therein being corresponding "tensor fields". These fields are the primary focus of Einstein's GR and describe both spacetime curvature and the energy and momentum of gravitating matter.

Acknowledgements

I would like to thank several people, that were involved in writing this thesis. First and foremost, I would like to thank Klemens Hammerer for his patience, advice and the interesting discussions we had. His door was always open, when questions of any kind came up. It was always a pleasure talking to someone, having such a deep understanding of quantum optics and physics in general. His curiosity to learn something new taught me the importance to broaden one's horizons and made me a better scientist in multiple ways. I could not imagine a better supervisor!

Further gratitude goes towards Naceur Gaaloul, being the second examiner of this thesis. Due to him, my curiosity for the numerical simulations of problems, which are analytically impossible – or only very complicated – to solve. This interest significantly guided me in addressing the challenges described in this thesis. I would also like to extend my gratitude to Domenico Giulini and Claus Lämmerzahl. Domenico sparked my interest in gravitational physics and differential geometry, always making the mind-boggling concepts of relativity easily understandable – a rare gift I truly admire. Claus always showed great interest in our work, and I am grateful for the many engaging discussions we had about relativity and quantum mechanics at various conferences. Additionally, I would like to thank Claus for his willingness to examine this thesis.

A big thanks also to my other coauthors, namely Philip Schwartz, Dennis Schlippert, Jan-Niclas Kirsten-Siemß, Ali Lezeik, and Ernst Rasel. I always enjoyed our discussion and am truly impressed by the amount of good ideas, that went into the manuscripts. Thanks to your help, the manuscripts gained a lot of interesting perspectives!

I would also like to thank the entire Hammerer group for providing me with my own office space, great coffee, an incredibly warm welcome, and friendly discussions over the years. The countless cups of coffee we enjoyed together provided much-needed breaks from constant physics discussions. In particular, I want to express my gratitude to Victor, Jan-Niclas, Florian, Kasper, Ivan, Maja, Timm, Erin, Patrik, Ruolin, Julian, and the group's good soul, who keeps everything running smoothly, Birgit Gemmeke!

I must express my gratitude to my friends and family. Particularly, I want to thank my mum for encouraging me on my journey to become a physicist and providing me with the love and support I needed. I also extend my thanks to my dear fellow students, the "Grøbe", for being the best team imaginable when navigating the occasional challenges posed by the university. Without all of you, I'm not sure I could have achieved this. A special thanks also goes to everyone who helped with the proofreading of this work. Your suggestions were invaluable, and you know who you are! A big thanks also to Claudia for sparking my interest in physics at a young age.

Lastly, I want to give a very personal thank you to Nico, Jan, Arne, Julia, Daimien and Julian. You have always been there for me, especially when I struggled to think clearly. You never failed to make me smile, even when I didn't have the strength to do so on my own.

Thank you!

Index

- Action functional, 38
- Atomic trajectory, 25
- Atomic trajectory mean, 60
- Bloch oscillations, 32, 69
- Bragg interactions, 30, 91
- Centrifugal force, 42, 100
- Clock interferometry, 19
- Compton frequency, 25
- Coriolis effect, 42
- Coriolis effect, 100
- Doppler effect, 30, 45, 95
- Equivalence principle
 - Definition, 2
 - LLI, 3
 - LPI, 3
 - UCR, 3
 - UFF, 3
 - UGR, 3
 - WEP, 3
- Fine-structure constant, 68
- Finite speed of light, 28, 45, 50, 51
- General relativity
 - Einstein's field equations, 1, 6
 - Lagrangian, 5
 - Line element, 5
 - Minkowski Spacetime, 6
 - Newtonian Spacetime, 9
 - PPN Spacetime, 10
 - Speed of light, 6
 - Stationary Spacetime, 5
- Geopotential model
 - Definition, 54
 - Tesseral corrections, 55
 - Zonal corrections, 55
- Gravitational Aharonov-Bohm, 56, 66
- Gravitational curvature
 - Curvature phase, 62
 - Definition, 58
 - Estimator, 61
 - Tidal phase, 62
- Gravitomagnetism, 101
- Gravity gradient mitigation schemes, 41
- Hamiltonian, 12, 14–16, 19, 24, 31, 37, 71, 75, 77, 80, 91
- Interferometer
 - ARBI, 22
 - CGI, 46, 59
 - MZI, 22
 - SDDI, 22
 - SRBI, 22
- Lagrangian, 24, 38, 42, 48, 63, 71, 72, 78, 80, 98, 100, 112, 113
- Lense-Thirring, 100
- Light propagation, 28
- Manifold
 - Atlas, 122
 - Chart transitions, 122
 - Christoffel symbols, 5
 - Cotangent space, 123
 - Covariant derivative, 5
 - Curvature scalar, 6
 - Ricci curvature tensor, 6
 - Riemann curvature tensor, 6
 - Smooth manifold, 122
 - Tangent space, 122
 - Tangent vector, 122
- Maxwell's equations, 12, 81
- Maxwell's equations
 - Geometric optics, 84
- Midpoint theorem, 40

Midpoint trajectory, 40

Single photon transitions, 19

Phase

Curvature phase, 62

FSL phase, 51, 64, 117

Kick phase, 32, 49, 64, 94, 115

Propagation phase, 27, 49, 64, 113

Recoil phase, 46

Separation phase, 27, 49, 64, 115

Tensor bundle

Cotangent bundle, 123

Section, 124

Tangent bundle, 123

Tensors of degree (l, m) , 124

Vector field, 124

Raman transitions, 18, 19, 69

Rotating reference frames, 42

VLBAI Hannover, 56, 57

List of Figures

1.1	Simplified visualisation of a setup to test the UGR with two observers on their respective worldlines γ_1, γ_2 and corresponding four-velocities u_1, u_2 interchanging a light ray k for the case of a two-dimensional spacetime.	4
1.2	Two-dimensional depiction of a spacetime diagram of an observer travelling along the timelike curve γ in Minkowski space (blue) with indicated light cone structure (yellow) and corresponding regions of future, past and the absolute elsewhere.	7
1.3	Schematic depiction of an interferometer consisting of two atomic paths, which are the solutions to the ELE for the different initial conditions set by the spacetime events A, B_1, B_2 and C . The upper path $A \rightarrow B_1 \rightarrow C$ is depicted in blue and the lower path $A \rightarrow B_2 \rightarrow C$ in orange.	14
1.4	Schematic depiction of Bragg diffraction using an effective two-level atom with states $ g\rangle, e\rangle$ and two counter propagating light fields with frequencies ω_a (red) and ω_b (blue), namely a DF field \hat{E}_{DF} . The resonant two photon transition (thick red and blue arrows) results in an effective momentum transfer of $\hbar k = \hbar(k_a + k_b)$, where $\omega_R = \frac{\hbar k^2}{2m} = \omega_a - \omega_b$ denotes the corresponding recoil frequency. The dashed lines correspond to off resonant transitions. Both laser frequencies ω_a, ω_b are detuned by Δ to $ e\rangle$, such that there is no coupling to the excited state.	17
1.5	Level scheme of a two-photon Raman diffraction for an effective three-level atom and two counter propagating light fields with frequencies ω_a (red) and ω_b (blue). The resonant transition $ g_1\rangle \rightarrow e\rangle \rightarrow g_2\rangle$ is indicated with thick arrows. The dashed lines correspond to off resonant transitions. Both light fields are far detuned from the excited state $ e\rangle$	18
1.6	Level scheme of a single photon transition for an effective two-level atom and a single light field (red) with frequency ω and wave vector $ k = \omega/c$	19
2.1	Schematic pictures of atomic trajectories (green lines) for four different AIF geometries in the freely falling frame. Interferometry laser (beam splitter/mirror) pulses are depicted in red dashed with a momentum transfer of $\pm \hbar k_R$ and Bloch oscillations in violet with a momentum transfer of $\hbar k_B$. The speed of light is set to infinity for this picture. (a) Mach-Zehnder interferometer (MZI) (b) Symmetric Ramsey-Bordé interferometer (SRBI), (c) Symmetric Double Diffraction interferometer (SDDI), (d) Antisymmetric Ramsey-Bordé interferometer (ARBI). For the case of Bragg scattering (a), (b) and (d) can be realised using single Bragg diffraction, whereas (c) relies on double Bragg diffraction.	23

2.2	Schematic picture of how the finite light speed effects a MZI, which uses two-photon transitions (black dots). The atomic trajectory (green) interacts with two light fields (red, orange), originating by a light sourced at height z_U and retroreflected at z_L . The picture is not to scale in order to highlight the FSL effect. The atoms are launched out of a trap at a time t_0 from a height z_0 with an initial velocity v_0 . At the time t_{BS1} the atomic wave packet is split into a coherent spatial superposition. The mirror interactions happen for the upper path at t_{UM} and for the lower path at t_{LM} . Since gravitational gradients can result in a non-vanishing separation at the output port one can have two distinct time instances $t_{\text{BS2.1}}$ and $t_{\text{BS2.2}}$ for each atomic path to interact with the light fields.	29
2.3	Schematic picture of how the Doppler effect is perceived by an atomic trajectory (green line) for two counter propagating light fields (red, orange). Left: Depicted in the lab frame, where the laser sources rest and the atoms move non-trivially. Right: Atomic rest frame, which is co-accelerated with the atoms are each time instance.	31
2.4	Phase shift contributions in the three AIF geometries SRBI, SDDI, ARBI for a 10 m baseline. Solid curves correspond to phase shifts of order $O(2)$ and dashed curves to $O(3)$. (a) (c), (e): The Bloch time T_B is set to zero and all non-zero phase shift contributions above $1 \mu\text{rad}$ are plotted w.r.t. time $T = 2T_R$. (b), (d), (f): Coloured phase shift contributions depend non-trivially on T_B and are plotted against T_B for fixed time $T = 2T_R + T_B$ of 3 seconds; the grey curves correspond to the Bloch-time independent phase contributions from (a), (c), (e). Assumed numerical values can be found in Table 2.1.	36
2.5	Upper and lower atomic trajectories of a MZI $z_{\text{up}}(t)$, $z_{\text{low}}(t)$ (green) in the lab frame and unpopulated midpoint trajectory $z_{\text{mid}}(t)$ (purple), which is used in the midpoint theorem.	40
2.6	(a) Illustration of a reference frame, Σ (blue), which is fixed to Earth's surface, thus rotating with the planet, alongside a stationary reference frame, Σ' (red), which does not rotate relative to the distant stars. Relative to each other, the origins of these two reference frames trace a circle of latitude θ_{Lab} (purple). (b) A two-dimensional cross-section of a vertical AIF within the Earth-fixed reference frame Σ . Laser pulses, depicted by the red shaded region, are associated with light fields k_a, k_b and are aligned with the z-axis. The Earth's rotation causes the initially vertical atomic trajectories (black dashed arrow) to deviate due to fictitious forces (grey arrows), resulting in a curved path that may lead the atoms out of the laser beam. The effect is exaggerated for illustrative purposes.	43
2.7	A schematic illustration of an interferometer's geometry, designed to isolate phases related to gravity gradients [4]. The atomic paths of the SDDI are depicted in green, while those of the MZI, with a doubled amount of imprinted momenta, are shown in blue. FSL effects are neglected in the picture for illustrative purposes.	45
2.8	A schematic representation of the experimental implementation of the first beam splitter pulse (shown in purple), which is based on an initial MZI. It uses the output ports of this initial system as the inputs for the desired interferometer. Traditional beam splitter pulses are depicted in red.	47

2.9 A schematic illustration that presents the mitigation scheme, which involves applying a detuning Δ_{Det} to the final interferometry pulse. By precisely adjusting the frequency of the last pulse in the AIF, a carefully calculated detuning is introduced to cancel out unwanted phases related to the FSL effect. 51

2.10 Optimal detuning frequency $\nu_{\text{Det}}(\nu_0, T_R) = ck_R\Delta_{\text{Det}}(\nu_0, T_R)$ as a function of T_R for fixed values of ν_0 . Notably, the optimal detuning approaches infinity for pairs (ν_0, T_R) that satisfy Eq. (2.59). 52

2.11 Deviation of the local gravitational acceleration from the mean, based on the JGM-3 model. The figure was created using the open source 3D visualisation tool of the International Centre for Global Earth Models (ICGEM) at the GFZ in Potsdam, see Ref. [116]. The legend has been adapted for better readability. 54

2.12 Comparison of the (dimensionless) magnitudes of several components of the effective gravitational potential as functions of latitude θ from 0 (north pole) to π (south pole): i) constant gravitational potential of a sphere (black) and ii) zonal correction terms from Eq. (2.62b) for different $l \geq 2$ (coloured). 56

2.13 Comparison of the (dimensionless) magnitudes of several components of the effective gravitational potential as functions of colatitude φ for fixed $\theta = \pi/4$: i) constant gravitational potential of a sphere (black) and ii) summed tesseral correction terms $T_n = \sum_{m=1}^n T_{n,m}$ from Eq. (2.62c) (coloured). 57

2.14 Gravitational acceleration $g(z)$ and gravitational gradient $\Gamma(z)$ as functions of height in the ROI of the VLBAI Hannover with a reference acceleration of $g_{\text{ref}} = 9.812 \text{ m/s}^2$. $g(z)$ is interpolated by a polynomial fit. Building cross-section taken from Ref. [83] and adapted. 58

2.15 (a) Graphical depiction of a CGI within the baseline of a large-scale interferometry facility, where the initial height z_0 can be chosen freely. (b) Detailed depiction of the CGI in the laboratory frame. (c) Illustration of the CGI in the freely falling frame, with the current momentum state of each interferometer arm indicated. 59

2.16 Comparison of the measured phase shift $\Delta\Phi$ (black) and the gravitational curvature Γ from Fig. 2.14 (orange), as a function of the initial height z_0 in the ROI for three different values of T_R (and therefore Δh), i.e., different choices of measurement resolution. The pink line highlights the offset between the phase shift and the gravitational curvature. 60

2.17 Comparison of the gravitational curvature Γ from Fig. 2.14 (orange) and the estimator for the gravity gradient $\hat{\Gamma}$ from Eq.(2.70) (red dashed) for three different values of T_R (and therefore Δh), i.e., different choices of measurement resolution. 62

2.18 (a) Difference between the exact scale factor f_3 and the idealised one, f_{ideal} , as a function of the interferometer baseline Δh . (b) Phase shift magnitude for CGIs with varying baselines Δh and corresponding root mean-square error in the estimation of the gravity gradient. $\Delta\hat{\Gamma}$ is averaged over all possible initial heights in the ROI obtainable with a baseline of Δh and $\langle \Gamma \rangle = 2.75 \times 10^3 \text{ E}$ is the magnitude of the mean gravitational gradient of the facility. 63

2.19	Numerical phase shift simulation (blue) of the CGI in the gravitational field of the VLBAI from Fig. 2.14 as a function of T_R for fixed $N_R = 1$, $z_0 = 0$, and $v_0 = 13.8$ m/s. A polynomial of fourth order (orange) is fitted to the phase shift. One can observe that the phase shift is primarily dominated by the propagation and separation phases, with the kick phase contributing at most one order of magnitude lower.	64
2.20	Schematic depiction of a measurement sequence to obtain a time resolved model of the gravitational curvature. Here, the separation between the initial heights of each CGI, Δl , are shown equally spaced, in order to achieve a higher spatial resolution, one can decrease the separation between neighbouring interferometers in certain areas.	65
3.1	A simplified configuration for a double differential measurement involving two ARBI is illustrated in a freely falling reference frame, as similarly presented in Ref. [38]. The illustration includes atomic trajectories (orange and blue), Bloch oscillations (purple), and Bragg lasers (red, dashed). In this setup, the last two Bragg pulses are frequency-detuned by ω_m . The notation used has been adapted for our analysis.	69
3.2	Illustration of the interferometer setup described in Ref. [39]. Atomic trajectories are shown in orange and blue, Bloch oscillations in purple, and Raman lasers in red, dashed. The notation has been adapted to suit our analysis. Depending on the orientations of the Bloch and Raman lasers, up to four different interferometer configurations can be realised. In the two depicted AIF configurations, the Raman pulses impart momentum downward to the initial wave packet, indicated by $\varepsilon_R = -1$, while the Bloch oscillations are presented in both orientations, $\varepsilon_B = \pm 1$	70
3.3	Comparison of the (dimensionless) magnitudes of several components of the effective gravitational potential as functions of latitude θ from 0 (north pole) to π (south pole): i) constant gravitational potential of a sphere (black), ii) zonal correction terms from Eq. (2.62b) for different $l \geq 2$ (coloured), and iii) the Lense-Thirring term for an observer fixed on Earth's surface (red dashed). This figure builds upon Fig. 2.12.	102
3.4	Comparison of the (dimensionless) magnitudes of several components of the effective gravitational potential as functions of colatitude φ for fixed $\theta = \pi/4$: i) constant gravitational potential of a sphere (black), ii) summed tesseral correction terms $T_n = \sum_{m=1}^n T_{n,m}$ from Eq. (2.62c) (coloured), and iii) the Lense-Thirring term for an observer fixed on Earth's surface (red dashed). This figure builds upon Fig. 2.13.	103
3.5	Comparison of the dominant zonal correction term (green) to the Lense-Thirring contribution (red) over the radial distance at the equator	104
4.1	Summary of the algebraic structure within the DimPar-class.	108
4.2	Schematic and simplified overview of the algorithm after initialisation.	110
4.3	Example of the transition between an analytic expression and the computer form in terms of DimPar-class arguments.	111
A.1	Schematic depiction of charts (U_i, ϕ_i) and (U_j, ϕ_j) and a chart transition map ψ_{ij} of a manifold \mathcal{M}	123
A.2	Schematic depiction of functions on manifolds and visualisation of a tangent space $\mathcal{T}_p \mathcal{M}$ using a path γ through $p \in \mathcal{M}$	123

Bibliography

- [1] M. Werner and K. Hammerer, “Dataset: Atom interferometers in weakly curved spacetimes using Bragg diffraction and Bloch oscillations,” 2023.
- [2] M. Werner, P. K. Schwartz, J.-N. Kirsten-Siemß, N. Gaaloul, D. Giulini, and K. Hammerer, “Atom interferometers in weakly curved spacetimes using Bragg diffraction and Bloch oscillations,” *Phys. Rev. D*, vol. 109, p. 022008, Jan 2024.
- [3] M. Werner and K. Hammerer, “Local Measurement Scheme of Gravitational Curvature using Atom Interferometers [Data set],” 2024.
- [4] M. Werner, A. Lezeik, D. Schlippert, E. Rasel, N. Gaaloul, and K. Hammerer, “Local Measurement Scheme of Gravitational Curvature using Atom Interferometers,” 2024.
- [5] A. Einstein, *Zur Allgemeinen Relativitätstheorie*. Akademie der Wissenschaften, in Kommission bei W. de Gruyter, 1915.
- [6] E. Hubble, “A relation between distance and radial velocity among extra-galactic nebulae,” *Proceedings of the national academy of sciences*, vol. 15, no. 3, pp. 168–173, 1929.
- [7] G. Lemaître, “The beginning of the world from the point of view of quantum theory,” *Nature*, vol. 127, no. 3210, p. 706, 1931.
- [8] K. Schwarzschild, “Über das Gravitationsfeld eines Massenpunktes nach der Einsteinschen Theorie,” *Sitzungsberichte der königlich preussischen Akademie der Wissenschaften*, pp. 189–196, 1916.
- [9] D. C. Miller, “Ether-Drift Experiments at Mount Wilson Solar Observatory,” *Physical Review*, vol. 19, no. 4, p. 407, 1922.
- [10] D. C. Miller, “The ether-drift experiment and the determination of the absolute motion of the earth,” *Reviews of modern physics*, vol. 5, no. 3, p. 203, 1933.
- [11] K. Akiyama, A. Alberdi, W. Alef, K. Asada, R. Azulay, A.-K. Bacsko, D. Ball, M. Baloković, J. Barrett, D. Bintley, *et al.*, “First M87 event horizon telescope results. IV. Imaging the central supermassive black hole,” *The Astrophysical Journal Letters*, vol. 875, no. 1, p. L4, 2019.
- [12] J. Wambsganss, “Gravitational lensing in astronomy,” *Living Reviews in Relativity*, vol. 1, pp. 1–74, 1998.
- [13] B. P. Abbott *et al.*, “Observation of Gravitational Waves from a Binary Black Hole Merger,” *Phys. Rev. Lett.*, vol. 116, p. 061102, Feb 2016.

[14] D. Giulini, “Equivalence principle, quantum mechanics, and atom-interferometric tests,” in *Quantum Field Theory and Gravity*, pp. 345–370, Springer, 2012.

[15] P. Touboul, G. Métris, M. Rodrigues, J. Bergé, A. Robert, Q. Baghi, Y. André, J. Bedouet, D. Boulanger, S. Bremer, P. Carle, R. Chhun, B. Christophe, V. Cipolla, T. Damour, P. Danto, L. Demange, H. Dittus, O. Dhuicque, P. Fayet, B. Foulon, P.-Y. Guidotti, D. Hagedorn, E. Hardy, P.-A. Huynh, P. Kayser, S. Lala, C. Lämmerzahl, V. Lebat, F. m. c. Liorzou, M. List, F. Löffler, I. Panet, M. Pernot-Borràs, L. Perraud, S. Pires, B. Pouilloux, P. Prieur, A. Rebray, S. Reynaud, B. Rievers, H. Selig, L. Serron, T. Sumner, N. Tanguy, P. Torresi, and P. Visser, “MICROSCOPE Mission: Final Results of the Test of the Equivalence Principle,” *Phys. Rev. Lett.*, vol. 129, p. 121102, Sep 2022.

[16] S. Herrmann, A. Senger, E. Kovalchuk, H. Müller, and A. Peters, “Test of the Isotropy of the Speed of Light Using a Continuously Rotating Optical Resonator,” *Phys. Rev. Lett.*, vol. 95, p. 150401, Oct 2005.

[17] L. S. Dreissen, C.-H. Yeh, H. A. Fürst, K. C. Grensemann, and T. E. Mehlstäubler, “Improved bounds on Lorentz violation from composite pulse Ramsey spectroscopy in a trapped ion,” *Nature communications*, vol. 13, no. 1, p. 7314, 2022.

[18] F. Di Pumbo, A. Friedrich, C. Ufrecht, and E. Giese, “Universality-of-clock-rates test using atom interferometry with T^3 scaling,” *Phys. Rev. D*, vol. 107, p. 064007, Mar 2023.

[19] R. F. Vessot, M. W. Levine, E. M. Mattison, E. Blomberg, T. Hoffman, G. Nystrom, B. Farrel, R. Decher, P. B. Eby, C. Baugher, *et al.*, “Test of relativistic gravitation with a space-borne hydrogen maser,” *Physical Review Letters*, vol. 45, no. 26, p. 2081, 1980.

[20] T. M. Fortier, N. Ashby, J. Bergquist, M. Delaney, S. Diddams, T. Heavner, L. Hollberg, W. Itano, S. R. Jefferts, K. Kim, *et al.*, “Precision atomic spectroscopy for improved limits on variation of the fine structure constant and local position invariance,” *Physical Review Letters*, vol. 98, no. 7, p. 070801, 2007.

[21] F. Schuller, “A thorough introduction to the theory of general relativity,” 2015. Lecture held at the Wilhelm and Else Heraeus international winter school on gravity and light.

[22] P. R. Berman, *Atom Interferometry*. Academic press, 1997.

[23] C. Brans and R. H. Dicke, “Mach’s Principle and a Relativistic Theory of Gravitation,” *Phys. Rev.*, vol. 124, pp. 925–935, Nov 1961.

[24] K. Nordtvedt Jr and C. M. Will, “Conservation laws and preferred frames in relativistic gravity. II. Experimental evidence to rule out preferred-frame theories of gravity,” *The Astrophysical Journal*, vol. 177, p. 775, 1972.

[25] D. Giulini, A. Großardt, and P. K. Schwartz, *Coupling Quantum Matter and Gravity*, vol. 1017 of *Lecture Notes in Physics*, ch. 16. Cham: Springer, 2023.

[26] C. M. Will, “Gravitation theory,” *Sci. Am.*, v. 231, no. 5, pp. 25-33, 11 1974.

[27] R. M. Wald, *General relativity*. University of Chicago press, 2010.

- [28] B. Bertotti, L. Iess, and P. Tortora, “A test of general relativity using radio links with the Cassini spacecraft,” *Nature*, vol. 425, no. 6956, pp. 374–376, 2003.
- [29] A. S. Konopliv, S. W. Asmar, W. M. Folkner, Ö. Karatekin, D. C. Nunes, S. E. Smrekar, C. F. Yoder, and M. T. Zuber, “Mars high resolution gravity fields from MRO, Mars seasonal gravity, and other dynamical parameters,” *Icarus*, vol. 211, no. 1, pp. 401–428, 2011.
- [30] A. Fienga, J. Laskar, P. Kuchynka, H. Manche, G. Desvignes, M. Gastineau, I. Cognard, and G. Theureau, “The INPOP10a planetary ephemeris and its applications in fundamental physics,” *Celestial Mechanics and Dynamical Astronomy*, vol. 111, no. 3, p. 363, 2011.
- [31] A. Verma, A. Fienga, J. Laskar, H. Manche, and M. Gastineau, “Use of MESSENGER radioscience data to improve planetary ephemeris and to test general relativity,” *Astronomy & Astrophysics*, vol. 561, p. A115, 2014.
- [32] E. Schrödinger, “Die gegenwärtige Situation in der Quantenmechanik,” *Die Naturwissenschaften*, vol. 23, no. 48, pp. 807–812, 1935.
- [33] W. Heisenberg, “Über den anschaulichen inhalt der quantentheoretischen kinematik und mechanik,” *Zeitschrift für Physik*, vol. 43, no. 3, pp. 172–198, 1927.
- [34] S. Hawking, *A brief history of time: from big bang to black holes*. Random House, 2009.
- [35] L. d. Broglie, “XXXV. A tentative theory of light quanta,” *The London, Edinburgh, and Dublin Philosophical Magazine and Journal of Science*, vol. 47, no. 278, pp. 446–458, 1924.
- [36] C. Davisson and L. H. Germer, “Diffraction of Electrons by a Crystal of Nickel,” *Phys. Rev.*, vol. 30, pp. 705–740, Dec 1927.
- [37] R. Colella, A. W. Overhauser, and S. A. Werner, “Observation of Gravitationally Induced Quantum Interference,” *Phys. Rev. Lett.*, vol. 34, pp. 1472–1474, Jun 1975.
- [38] R. H. Parker, C. Yu, W. Zhong, B. Estey, and H. Müller, “Measurement of the fine-structure constant as a test of the Standard Model,” *Science*, vol. 360, no. 6385, pp. 191–195, 2018.
- [39] L. Morel, Z. Yao, P. Cladé, and S. Guellati-Khélifa, “Determination of the fine-structure constant with an accuracy of 81 parts per trillion,” *Nature*, vol. 588, no. 7836, pp. 61–65, 2020.
- [40] P. Storey and C. Cohen-Tannoudji, “The Feynman path integral approach to atomic interferometry. A tutorial,” *Journal de Physique II*, vol. 4, no. 11, pp. 1999–2027, 1994.
- [41] D. Becker, M. D. Lachmann, S. T. Seidel, H. Ahlers, A. N. Dinkelaker, J. Grosse, O. Hellmig, H. Müntinga, V. Schkolnik, T. Wendrich, *et al.*, “Space-borne Bose–Einstein condensation for precision interferometry,” *Nature*, vol. 562, no. 7727, pp. 391–395, 2018.

[42] M. D. Lachmann, H. Ahlers, D. Becker, A. N. Dinkelaker, J. Grosse, O. Hellmig, H. Müntinga, V. Schkolnik, S. T. Seidel, T. Wendrich, *et al.*, “Ultracold atom interferometry in space,” *Nature communications*, vol. 12, no. 1, p. 1317, 2021.

[43] A. O. Jamison, J. N. Kutz, and S. Gupta, “Atomic interactions in precision interferometry using Bose-Einstein condensates,” *Phys. Rev. A*, vol. 84, p. 043643, Oct 2011.

[44] H. Müntinga, H. Ahlers, M. Krutzik, A. Wenzlawski, S. Arnold, D. Becker, K. Bongs, H. Dittus, H. Duncker, N. Gaaloul, C. Gherasim, E. Giese, C. Grzeschik, T. W. Hänsch, O. Hellmig, W. Herr, S. Herrmann, E. Kajari, S. Kleinert, C. Lämmerzahl, W. Lewoczko-Adamczyk, J. Malcolm, N. Meyer, R. Nolte, A. Peters, M. Popp, J. Reichel, A. Roura, J. Rudolph, M. Schiemangk, M. Schneider, S. T. Seidel, K. Sengstock, V. Tamme, T. Valenzuela, A. Vogel, R. Walser, T. Wendrich, P. Windpassinger, W. Zeller, T. van Zoest, W. Ertmer, W. P. Schleich, and E. M. Rasel, “Interferometry with Bose-Einstein Condensates in Microgravity,” *Phys. Rev. Lett.*, vol. 110, p. 093602, Feb 2013.

[45] J. Rudolph, W. Herr, C. Grzeschik, T. Sternke, A. Grote, M. Popp, D. Becker, H. Müntinga, H. Ahlers, A. Peters, *et al.*, “A high-flux BEC source for mobile atom interferometers,” *New Journal of Physics*, vol. 17, no. 6, p. 065001, 2015.

[46] G. Condon, M. Rabault, B. Barrett, L. Chichet, R. Arguel, H. Eneriz-Imaz, D. Naik, A. Bertoldi, B. Battelier, P. Bouyer, and A. Landragin, “All-Optical Bose-Einstein Condensates in Microgravity,” *Phys. Rev. Lett.*, vol. 123, p. 240402, Dec 2019.

[47] J. Günther, J.-N. Kirsten-Siemß, N. Gaaloul, and K. Hammerer, “Squeezing Enhancement in Lossy Multi-Path Atom Interferometers,” *arXiv preprint arXiv:2409.04091*, 2024.

[48] F. Anders, A. Idel, P. Feldmann, D. Bondarenko, S. Loriani, K. Lange, J. Peise, M. Gersemann, B. Meyer-Hoppe, S. Abend, *et al.*, “Momentum entanglement for atom interferometry,” *Physical Review Letters*, vol. 127, no. 14, p. 140402, 2021.

[49] B. K. Malia, Y. Wu, J. Martínez-Rincón, and M. A. Kasevich, “Distributed quantum sensing with mode-entangled spin-squeezed atomic states,” *Nature*, vol. 612, no. 7941, pp. 661–665, 2022.

[50] G. P. Greve, C. Luo, B. Wu, and J. K. Thompson, “Entanglement-enhanced matter-wave interferometry in a high-finesse cavity,” *Nature*, vol. 610, no. 7932, pp. 472–477, 2022.

[51] P. Asenbaum, C. Overstreet, M. Kim, J. Curti, and M. A. Kasevich, “Atom-Interferometric Test of the Equivalence Principle at the 10^{-12} Level,” *Phys. Rev. Lett.*, vol. 125, p. 191101, Nov 2020.

[52] B. K. Malia, J. Martínez-Rincón, Y. Wu, O. Hosten, and M. A. Kasevich, “Free Space Ramsey Spectroscopy in Rubidium with Noise below the Quantum Projection Limit,” *Phys. Rev. Lett.*, vol. 125, p. 043202, Jul 2020.

[53] A. Herbst, H. Albers, K. Stolzenberg, S. Bode, and D. Schlippert, “Rapid generation of all-optical ^{39}K Bose-Einstein condensates using a low-field Feshbach resonance,” *Phys. Rev. A*, vol. 106, p. 043320, Oct 2022.

- [54] H. Albers, A. Herbst, L. L. Richardson, H. Heine, D. Nath, J. Hartwig, C. Schubert, C. Vogt, M. Woltmann, C. Lämmerzahl, *et al.*, “Quantum test of the Universality of Free Fall using rubidium and potassium,” *The European Physical Journal D*, vol. 74, pp. 1–9, 2020.
- [55] S. P. Carman, J. Rudolph, B. E. Garber, M. J. Van de Graaff, H. Swan, Y. Jiang, M. Nantel, M. Abe, R. L. Barcklay, and J. M. Hogan, “Collinear three-photon excitation of a strongly forbidden optical clock transition,” *arXiv preprint arXiv:2406.07902*, 2024.
- [56] J.-N. Siemß, F. Fitzek, S. Abend, E. M. Rasel, N. Gaaloul, and K. Hammerer, “Analytic theory for Bragg atom interferometry based on the adiabatic theorem,” *Physical Review A*, vol. 102, no. 3, p. 033709, 2020.
- [57] E. Giese, “Mechanisms of matter-wave diffraction and their application to interferometers,” *Fortschritte der Physik*, vol. 63, no. 6, pp. 337–410, 2015.
- [58] T. Kovachy, J. M. Hogan, A. Sugarbaker, S. M. Dickerson, C. A. Donnelly, C. Overstreet, and M. A. Kasevich, “Matter Wave Lensing to Picokelvin Temperatures,” *Phys. Rev. Lett.*, vol. 114, p. 143004, Apr 2015.
- [59] S.-w. Chiow, T. Kovachy, H.-C. Chien, and M. A. Kasevich, “102 $\hbar k$ Large Area Atom Interferometers,” *Phys. Rev. Lett.*, vol. 107, p. 130403, Sep 2011.
- [60] B. Plotkin-Swing, D. Gochnauer, K. E. McAlpine, E. S. Cooper, A. O. Jamison, and S. Gupta, “Three-Path Atom Interferometry with Large Momentum Separation,” *Phys. Rev. Lett.*, vol. 121, p. 133201, Sep 2018.
- [61] H. Müller, S.-w. Chiow, Q. Long, S. Herrmann, and S. Chu, “Atom Interferometry with up to 24-Photon-Momentum-Transfer Beam Splitters,” *Phys. Rev. Lett.*, vol. 100, p. 180405, May 2008.
- [62] T. Kovachy, S.-w. Chiow, and M. A. Kasevich, “Adiabatic-rapid-passage multiphoton Bragg atom optics,” *Phys. Rev. A*, vol. 86, p. 011606, Jul 2012.
- [63] E. Giese, A. Roura, G. Tackmann, E. M. Rasel, and W. P. Schleich, “Double Bragg diffraction: A tool for atom optics,” *Physical Review A*, vol. 88, no. 5, p. 053608, 2013.
- [64] H. Ahlers, H. Müntinga, A. Wenzlawski, M. Krutzik, G. Tackmann, S. Abend, N. Gaaloul, E. Giese, A. Roura, R. Kuhl, C. Lämmerzahl, A. Peters, P. Windpassinger, K. Sengstock, W. P. Schleich, W. Ertmer, and E. M. Rasel, “Double Bragg interferometry,” *Phys. Rev. Lett.*, vol. 116, p. 173601, Apr 2016.
- [65] M. Gebbe, J.-N. Siemß, M. Gersemann, H. Müntinga, S. Herrmann, C. Lämmerzahl, H. Ahlers, N. Gaaloul, C. Schubert, K. Hammerer, *et al.*, “Twin-lattice atom interferometry,” *Nature communications*, vol. 12, no. 1, p. 2544, 2021.
- [66] R. Li, V. J. Martínez-Lahuerta, S. Seckmeyer, K. Hammerer, and N. Gaaloul, “Robust double bragg diffraction via detuning control,” 2024.
- [67] J. Küber, F. Schmaltz, and G. Birkl, “Experimental realization of double Bragg diffraction: robust beamsplitters, mirrors, and interferometers for Bose-Einstein condensates,” 2016.

- [68] F. Di Pumbo, C. Ufrecht, A. Friedrich, E. Giese, W. P. Schleich, and W. G. Unruh, “Gravitational Redshift Tests with Atomic Clocks and Atom Interferometers,” *PRX Quantum*, vol. 2, p. 040333, Nov 2021.
- [69] A. Roura, “Gravitational Redshift in Quantum-Clock Interferometry,” *Phys. Rev. X*, vol. 10, p. 021014, Apr 2020.
- [70] C. Ufrecht, F. Di Pumbo, A. Friedrich, A. Roura, C. Schubert, D. Schlippert, E. M. Rasel, W. P. Schleich, and E. Giese, “Atom-interferometric test of the universality of gravitational redshift and free fall,” *Phys. Rev. Res.*, vol. 2, p. 043240, Nov 2020.
- [71] S. Dimopoulos, P. W. Graham, J. M. Hogan, M. A. Kasevich, and S. Rajendran, “Atomic gravitational wave interferometric sensor,” *Phys. Rev. D*, vol. 78, p. 122002, Dec 2008.
- [72] A. Bertoldi, P. Bouyer, and B. Canuel, “Quantum Sensors with Matter Waves for GW Observation,” in *Handbook of Gravitational Wave Astronomy*, pp. 1–43, Springer Singapore, 2021.
- [73] B. Canuel, S. Abend, P. Amaro-Seoane, F. Badaracco, Q. Beaufils, A. Bertoldi, K. Bongs, P. Bouyer, C. Braxmaier, W. Chaibi, *et al.*, “ELGAR—a European laboratory for gravitation and atom-interferometric research,” *Classical and Quantum Gravity*, vol. 37, no. 22, p. 225017, 2020.
- [74] F. Di Pumbo, A. Friedrich, A. Geyer, C. Ufrecht, and E. Giese, “Light propagation and atom interferometry in gravity and dilaton fields,” *Phys. Rev. D*, vol. 105, p. 084065, Apr 2022.
- [75] L. Hu, N. Poli, L. Salvi, and G. M. Tino, “Atom Interferometry with the Sr Optical Clock Transition,” *Phys. Rev. Lett.*, vol. 119, p. 263601, Dec 2017.
- [76] J. S. Schelfhout, T. M. Hird, K. M. Hughes, and C. J. Foot, “A single-photon large-momentum-transfer atom interferometry scheme for Sr or Yb atoms with application to determining the fine-structure constant,” 2024.
- [77] P. W. Graham, J. M. Hogan, M. A. Kasevich, and S. Rajendran, “New Method for Gravitational Wave Detection with Atomic Sensors,” *Phys. Rev. Lett.*, vol. 110, p. 171102, Apr 2013.
- [78] M. Ben Dahan, E. Peik, J. Reichel, Y. Castin, and C. Salomon, “Bloch Oscillations of Atoms in an Optical Potential,” *Phys. Rev. Lett.*, vol. 76, pp. 4508–4511, Jun 1996.
- [79] S. R. Wilkinson, C. F. Bharucha, K. W. Madison, Q. Niu, and M. G. Raizen, “Observation of Atomic Wannier-Stark Ladders in an Accelerating Optical Potential,” *Phys. Rev. Lett.*, vol. 76, pp. 4512–4515, Jun 1996.
- [80] E. Peik, M. Ben Dahan, I. Bouchoule, Y. Castin, and C. Salomon, “Bloch oscillations and an accelerator for cold atoms.,” *Applied Physics B: Lasers & Optics*, vol. 65, no. 6, 1997.
- [81] F. Fitzek, J.-N. Kirsten-Siemß, E. M. Rasel, N. Gaaloul, and K. Hammerer, “Accurate and efficient Bloch-oscillation-enhanced atom interferometry,” 2023.

[82] S. M. Dickerson, J. M. Hogan, A. Sugarbaker, D. M. S. Johnson, and M. A. Kasevich, “Multiaxis Inertial Sensing with Long-Time Point Source Atom Interferometry,” *Phys. Rev. Lett.*, vol. 111, p. 083001, Aug 2013.

[83] M. Schilling, É. Wodey, L. Timmen, D. Tell, K. H. Zipfel, D. Schlipper, C. Schubert, E. M. Rasel, and J. Müller, “Gravity field modelling for the Hannover 10 m atom interferometer,” *Journal of Geodesy*, vol. 94, nov 2020.

[84] L. Zhou, Z. Xiong, W. Yang, B. Tang, W. Peng, K. Hao, R. Li, M. Liu, J. Wang, and M. Zhan, “Development of an atom gravimeter and status of the 10-meter atom interferometer for precision gravity measurement,” *General Relativity and Gravitation*, vol. 43, pp. 1931–1942, 2011.

[85] L. Badurina, E. Bentine, D. Blas, K. Bongs, D. Bortoletto, T. Bowcock, K. Bridges, W. Bowden, O. Buchmueller, C. Burrage, *et al.*, “AION: an atom interferometer observatory and network,” *Journal of Cosmology and Astroparticle Physics*, vol. 2020, no. 05, p. 011, 2020.

[86] M.-S. Zhan, J. Wang, W.-T. Ni, D.-F. Gao, G. Wang, L.-X. He, R.-B. Li, L. Zhou, X. Chen, J.-Q. Zhong, *et al.*, “ZAIGA: Zhaoshan long-baseline atom interferometer gravitation antenna,” *International Journal of Modern Physics D*, vol. 29, no. 04, p. 1940005, 2020.

[87] S. Dimopoulos, P. W. Graham, J. M. Hogan, and M. A. Kasevich, “General relativistic effects in atom interferometry,” *Phys. Rev. D*, vol. 78, p. 042003, Aug 2008.

[88] S. Dimopoulos, P. W. Graham, J. M. Hogan, and M. A. Kasevich, “Testing General Relativity with Atom Interferometry,” *Phys. Rev. Lett.*, vol. 98, p. 111102, Mar 2007.

[89] J. M. Hogan, D. Johnson, and M. A. Kasevich, “Light-pulse atom interferometry,” *arXiv preprint arXiv:0806.3261*, 2008.

[90] M. Kasevich and S. Chu, “Atomic interferometry using stimulated Raman transitions,” *Phys. Rev. Lett.*, vol. 67, pp. 181–184, Jul 1991.

[91] S. Loriani, C. Schubert, D. Schlipper, W. Ertmer, F. Pereira Dos Santos, E. M. Rasel, N. Gaaloul, and P. Wolf, “Resolution of the colocation problem in satellite quantum tests of the universality of free fall,” *Phys. Rev. D*, vol. 102, p. 124043, Dec 2020.

[92] A. Roura, “Circumventing Heisenberg’s Uncertainty Principle in Atom Interferometry Tests of the Equivalence Principle,” *Phys. Rev. Lett.*, vol. 118, p. 160401, Apr 2017.

[93] C. Overstreet, P. Asenbaum, T. Kovachy, R. Notermans, J. M. Hogan, and M. A. Kasevich, “Effective Inertial Frame in an Atom Interferometric Test of the Equivalence Principle,” *Phys. Rev. Lett.*, vol. 120, p. 183604, May 2018.

[94] G. D’Amico, G. Rosi, S. Zhan, L. Cacciapuoti, M. Fattori, and G. M. Tino, “Canceling the Gravity Gradient Phase Shift in Atom Interferometry,” *Phys. Rev. Lett.*, vol. 119, p. 253201, Dec 2017.

[95] C. Ufrecht, “Generalized gravity-gradient mitigation scheme,” *Physical Review A*, vol. 103, no. 2, p. 023305, 2021.

- [96] S. Loriani, A. Friedrich, C. Ufrecht, F. Di Pumbo, S. Kleinert, S. Abend, N. Gaaloul, C. Meiners, C. Schubert, D. Tell, *et al.*, “Interference of clocks: A quantum twin paradox,” *Science advances*, vol. 5, no. 10, p. eaax8966, 2019.
- [97] F. Fitzek, J.-N. Siemß, S. Seckmeyer, H. Ahlers, E. M. Rasel, K. Hammerer, and N. Gaaloul, “Universal atom interferometer simulation of elastic scattering processes,” *Scientific Reports*, vol. 10, no. 1, p. 22120, 2020.
- [98] G. D. McDonald and C. C. Kuhn, “Space-time area in atom interferometry,” *arXiv preprint arXiv:1312.2713*, 2013.
- [99] C. Ufrecht and E. Giese, “Perturbative operator approach to high-precision light-pulse atom interferometry,” *Physical Review A*, vol. 101, no. 5, p. 053615, 2020.
- [100] S. Bade, L. Djadaojee, M. Andia, P. Cladé, and S. Guellati-Khelifa, “Observation of extra photon recoil in a distorted optical field,” *Physical Review Letters*, vol. 121, no. 7, p. 073603, 2018.
- [101] C. J. Bordé, “Atomic clocks and inertial sensors,” *Metrologia*, vol. 39, no. 5, p. 435, 2002.
- [102] C. Overstreet, P. Asenbaum, and M. A. Kasevich, “Physically significant phase shifts in matter-wave interferometry,” *American Journal of Physics*, vol. 89, no. 3, pp. 324–332, 2021.
- [103] C. Overstreet, P. Asenbaum, J. Curti, M. Kim, and M. A. Kasevich, “Observation of a gravitational Aharonov-Bohm effect,” *Science*, vol. 375, no. 6577, pp. 226–229, 2022.
- [104] A. Roura, W. Zeller, and W. P. Schleich, “Overcoming loss of contrast in atom interferometry due to gravity gradients,” *New Journal of Physics*, vol. 16, p. 123012, dec 2014.
- [105] S.-Y. Lan, P.-C. Kuan, B. Estey, P. Haslinger, and H. Müller, “Influence of the Coriolis Force in Atom Interferometry,” *Phys. Rev. Lett.*, vol. 108, p. 090402, Feb 2012.
- [106] A. Sugarbaker, S. M. Dickerson, J. M. Hogan, D. M. S. Johnson, and M. A. Kasevich, “Enhanced Atom Interferometer Readout through the Application of Phase Shear,” *Phys. Rev. Lett.*, vol. 111, p. 113002, Sep 2013.
- [107] J. Glick, Z. Chen, T. Deshpande, Y. Wang, and T. Kovachy, “Coriolis Force Compensation and Laser Beam Delivery for 100-Meter Baseline Atom Interferometry,” 2023.
- [108] P. Asenbaum, C. Overstreet, T. Kovachy, D. D. Brown, J. M. Hogan, and M. A. Kasevich, “Phase Shift in an Atom Interferometer due to Spacetime Curvature across its Wave Function,” *Phys. Rev. Lett.*, vol. 118, p. 183602, May 2017.
- [109] A. Lezeik, D. Tell, K. Zipfel, V. Gupta, É. Wodey, E. Rasel, C. Schubert, and D. Schlipfert, “Understanding the gravitational and magnetic environment of a very long baseline atom interferometer,” in *Proceedings of the Ninth Meeting on CPT and Lorentz Symmetry*, pp. 64–68, World Scientific, 2023.
- [110] D. Pfeiffer, M. Dietrich, P. Schach, G. Birkl, and E. Giese, “Dichroic mirror pulses for optimized higher-order atomic Bragg diffraction,” 2024.

- [111] J. C. Saywell, M. S. Carey, P. S. Light, S. S. Szigeti, A. R. Milne, K. S. Gill, M. L. Goh, V. S. Perunicic, N. M. Wilson, C. D. Macrae, A. Rischka, P. J. Everitt, N. P. Robins, R. P. Anderson, M. R. Hush, and M. J. Biercuk, “Enhancing the Sensitivity of Atom-Interferometric Inertial Sensors Using Robust Control,” *Nature Communications*, vol. 14, p. 7626, Nov. 2023.
- [112] G. Louie, Z. Chen, T. Deshpande, and T. Kovachy, “Robust Atom Optics for Bragg Atom Interferometry,” *New Journal of Physics*, vol. 25, p. 083017, Aug. 2023.
- [113] E. R. Elliott, D. C. Aveline, N. P. Bigelow, P. Boegel, S. Botsi, E. Charron, J. P. d’Incao, P. Engels, T. Estrampes, N. Gaaloul, *et al.*, “Quantum gas mixtures and dual-species atom interferometry in space,” *Nature*, vol. 623, no. 7987, pp. 502–508, 2023.
- [114] A. Landragin, A. Clairon, N. Dimarcq, P. Teyssandier, C. Salomon, E. Rasel, W. Ertmer, C. J. Bordé, P. Tourrenc, P. Bouyer, *et al.*, “Hyper: Atom interferometry in space,” in *Advanced Technology and Particle Physics*, pp. 16–22, World Scientific, 2002.
- [115] J. R. Williams, C. A. Sackett, H. Ahlers, D. C. Aveline, P. Boegel, S. Botsi, E. Charron, E. R. Elliott, N. Gaaloul, E. Giese, W. Herr, J. R. Kellogg, J. M. Kohel, N. E. Lay, M. Meister, G. Müller, H. Müller, K. Oudrhiri, L. Phillips, A. Pichery, E. M. Rasel, A. Roura, M. Sbroscia, W. P. Schleich, C. Schneider, C. Schubert, B. Sen, R. J. Thompson, and N. P. Bigelow, “Interferometry of Atomic Matter Waves in the Cold Atom Lab onboard the International Space Station,” 2024.
- [116] E. S. Ince, F. Barthelmes, S. Reißland, K. Elger, C. Förste, F. Flechtner, and H. Schuh, “ICGEM – 15 years of successful collection and distribution of global gravitational models, associated services, and future plans,” *Earth System Science Data*, vol. 11, no. 2, pp. 647–674, 2019.
- [117] B. D. Tapley, M. Watkins, J. Ries, G. Davis, R. Eanes, S. Poole, H. Rim, B. Schutz, C. Shum, R. S. Nerem, *et al.*, “The joint gravity model 3,” *Journal of Geophysical Research: Solid Earth*, vol. 101, no. B12, pp. 28029–28049, 1996.
- [118] J. Coleman, “MAGIS-100 at Fermilab,” 2018.
- [119] S. Abend, B. Allard, I. Alonso, J. Antoniadis, H. Araújo, G. Arduini, A. S. Arnold, T. Asano, N. Augst, L. Badurina, *et al.*, “Terrestrial very-long-baseline atom interferometry: Workshop summary,” *AVS Quantum Science*, vol. 6, no. 2, 2024.
- [120] T. Rodzinka, E. Dionis, L. Calmels, S. Beldjoudi, A. Béguin, D. Guéry-Odelin, B. Allard, D. Sugny, and A. Gauguet, “Optimal Floquet Engineering for Large Scale Atom Interferometers,” 2024.
- [121] J. Li, T. Kovachy, J. Bonacum, and S. M. Shahriar, “Sensitivity and Bandwidth of a Point-Source-Interferometry-based Inertial Measurement Unit Employing Large Momentum Transfer and Launched Atoms,” 2024.
- [122] P. Asenbaum, C. Overstreet, and M. A. Kasevich, “Matter waves and clocks do not observe uniform gravitational fields,” *Physica Scripta*, vol. 99, no. 4, p. 046103, 2024.
- [123] B. Stray, A. Lamb, A. Kaushik, J. Vovrosh, A. Rodgers, J. Winch, F. Hayati, D. Boddice, A. Stabrawa, A. Niggebaum, M. Langlois, Y.-H. Lien, S. Lellouch, S. Roshamanesh, K. Ridley, G. De Villiers, G. Brown, T. Cross, G. Tuckwell, A. Faramarzi,

N. Metje, K. Bongs, and M. Holynski, "Quantum Sensing for Gravity Cartography," *Nature*, vol. 602, pp. 590–594, Feb. 2022.

[124] J. Mitchell, T. Kovachy, S. Hahn, P. Adamson, and S. Chattopadhyay, "MAGIS-100 environmental characterization and noise analysis," *Journal of Instrumentation*, vol. 17, no. 01, p. P01007, 2022.

[125] M. Abe, P. Adamson, M. Borcean, D. Bortoletto, K. Bridges, S. P. Carman, S. Chattopadhyay, J. Coleman, N. M. Curfman, K. DeRose, *et al.*, "Matter-wave atomic gradiometer interferometric sensor (MAGIS-100)," *Quantum Science and Technology*, vol. 6, no. 4, p. 044003, 2021.

[126] H. Müller, A. Peters, and S. Chu, "A precision measurement of the gravitational redshift by the interference of matter waves," *Nature*, vol. 463, no. 7283, pp. 926–929, 2010.

[127] P. Wolf, L. Blanchet, C. J. Bordé, S. Reynaud, C. Salomon, and C. Cohen-Tannoudji, "Atom gravimeters and gravitational redshift," *Nature*, vol. 467, no. 7311, p. E1, 2010.

[128] P. Wolf, L. Blanchet, C. J. Bordé, S. Reynaud, C. Salomon, and C. Cohen-Tannoudji, "Does an atom interferometer test the gravitational redshift at the Compton frequency?," *Classical and Quantum Gravity*, vol. 28, no. 14, p. 145017, 2011.

[129] M. A. Hohensee, S. Chu, A. Peters, and H. Mueller, "Comment on: 'Does an atom interferometer test the gravitational redshift at the Compton frequency?'," *Classical and Quantum Gravity*, vol. 29, no. 4, p. 048001, 2012.

[130] P. Wolf, L. Blanchet, C. J. Bordé, S. Reynaud, C. Salomon, and C. Cohen-Tannoudji, "Reply to comment on: 'Does an atom interferometer test the gravitational redshift at the Compton frequency?'," *Classical and Quantum Gravity*, vol. 29, no. 4, p. 048002, 2012.

[131] P. J. Mohr and B. N. Taylor, "CODATA recommended values of the fundamental physical constants: 1998," *Journal of Physical and Chemical Reference Data*, vol. 28, no. 6, pp. 1713–1852, 1999.

[132] P. K. Schwartz and D. Giulini, "Post-Newtonian Hamiltonian description of an atom in a weak gravitational field," *Phys. Rev. A*, vol. 100, p. 052116, Nov 2019.

[133] T. Morishima, T. Futamase, and H. M. Shimizu, "The general relativistic effects on the magnetic moment in Earth's gravity," *Progress of Theoretical and Experimental Physics*, vol. 2018, no. 6, p. 063B07, 2018.

[134] M. Visser, "Post-Newtonian particle physics in curved spacetime," *arXiv preprint arXiv:1802.00651*, 2018.

[135] D. Venhoek, "Analyzing "magnetic moments in curved spacetime": pitfalls in GR," *arXiv preprint arXiv:1804.09524*, 2018.

[136] H. Nikolic, "Can effective muon g-2 depend on the gravitational potential?," *arXiv preprint arXiv:1802.04025*, 2018.

[137] V. J. Martínez-Lahuerta, S. Eilers, T. E. Mehlstäubler, P. O. Schmidt, and K. Hammerer, "Ab initio quantum theory of mass defect and time dilation in trapped-ion optical clocks," *Phys. Rev. A*, vol. 106, p. 032803, Sep 2022.

- [138] T. Chiba and S. Kinoshita, “Quantum clocks, gravitational time dilation, and quantum interference,” *Phys. Rev. D*, vol. 106, p. 124035, Dec 2022.
- [139] S. Wajima, M. Kasai, and T. Futamase, “Post-Newtonian effects of gravity on quantum interferometry,” *Phys. Rev. D*, vol. 55, pp. 1964–1970, Feb 1997.
- [140] C. W. Misner, K. S. Thorne, and J. A. Wheeler, *Gravitation*. San Francisco: W. H. Freeman, 1973.
- [141] J. Kijowski, “On electrodynamical self-interaction,” *Acta Physica Polonica-Series A General Physics*, vol. 85, no. 4, p. 771, 1994.
- [142] L. B. Okun, “Photons and static gravity,” *Modern Physics Letters A*, vol. 15, no. 31, pp. 1941–1947, 2000.
- [143] M. Sonnleitner and S. M. Barnett, “The Röntgen interaction and forces on dipoles in time-modulated optical fields,” *The European Physical Journal D*, vol. 71, no. 12, pp. 1–13, 2017.
- [144] S. Barnett and P. M. Radmore, *Methods in theoretical quantum optics*, vol. 15. Oxford University Press, 2002.
- [145] H. Müller, S.-w. Chiow, and S. Chu, “Atom-wave diffraction between the Raman-Nath and the Bragg regime: Effective Rabi frequency, losses, and phase shifts,” *Phys. Rev. A*, vol. 77, p. 023609, Feb 2008.
- [146] E. Poisson and C. M. Will, *Gravity: Newtonian, post-Newtonian, Relativistic*. Cambridge University Press, 2014.
- [147] C. M. Will, *Theory and experiment in gravitational physics*. Cambridge university press, 2018.
- [148] C. J. Bordé, “Atomic interferometry with internal state labelling,” *Physics letters A*, vol. 140, no. 1-2, pp. 10–12, 1989.
- [149] A. Alibabaei, P. K. Schwartz, and D. Giulini, “Geometric post-Newtonian description of massive spin-half particles in curved spacetime,” 2023.

Academic Curriculum Vitae

Personal Information

Name	Michael Werner
Born	7. December 1994 in Bückeburg, Germany
Nationality	German

Education

2019 – 2024	PhD candidate , Institute of Theoretical Physics, Leibniz University Hannover
2016 – 2019	Master of Science , Leibniz University of Hannover, Grade: 1.2
2013 – 2016	Bachelor of Science , Leibniz University of Hannover, Grade: 1.0 Honours Degree

Theses

2024	PhD Thesis: <i>Gravitational Curvature And Relativistic Effects In Atom Interferometers</i> , Supervisor: Prof. Dr. Klemens Hammerer
2019	Master Thesis: <i>One-Dimensional Field Theories Arising From Continuous Measurement</i> , Supervisor: Prof. Dr. Reinhard Werner
2016	Bachelor Thesis: <i>Wigner Functions For Arbitrary Operator Tuples</i> , Supervisor: Prof. Dr. Reinhard Werner

Publications

1. S. Abend et al., *Terrestrial very-long-baseline atom interferometry: Workshop summary* [\[119\]](#)
2. **M. Werner** and K. Hammerer, *Dataset: Atom interferometers in weakly curved spacetimes using Bragg diffraction and Bloch oscillations* [\[1\]](#)
3. **M. Werner**, P. Schwartz, J.-N. Kirsten-Siemß, N. Gaaloul, D. Giulini, and K. Hammerer, *Atom interferometers in weakly curved spacetimes using Bragg diffraction and Bloch oscillations* [\[2\]](#)
4. **M. Werner** and K. Hammerer, *Local Measurement Scheme of Gravitational Curvature using Atom Interferometers [Data set]* [\[3\]](#)
5. **M. Werner**, A. Lezeik, D. Schlippert, E. M. Rasel, N. Gaaloul and K. Hammerer, *Local Measurement Scheme of Gravitational Curvature using Atom Interferometers* [\[4\]](#)

